The Application of Multiple-Quantum MAS NMR to Materials

Dem Fachbereich 6 (Chemie-Geographie)

der

Gerhard-Mercator-Universität-Gesamthochschule Duisburg

zur Erlangung des akademischen Grades eines

Doktor rer. nat.

genehmigte Dissertation

von

Guangxin Lin

aus China

Duisburg 1999

Die vorliegende Arbeit entstand in der Zeit von 11. 1995 bis 11. 1999 an der Gerhard-Mercator-Universität-Gesamthochschule Duisburg im Fachgebiet Physikalische Chemie des Fachbereiches 6 (Chemie-Geographie).

Referent:	Prof. Dr. Wiebren. S. Veeman
Koreferent:	Prof. Dr. Werner Wenig
Tag der mündlichen Prüfung:	22. 12. 1999

Preface

This work is completed under the guidance of Prof. Dr. Wiebren S. Veeman in the Institute of Theoretical and Physical Chemistry from November 1995 to August 1999. It is my great pleasure to have worked with Prof. Dr. Wiebren S. Veeman in the last several years. He has directed me into a challenging, interesting, and important field-the Application of Multiple-Quantum MAS NMR to Materials. I appreciate his financial support, and his patience in reading and correcting my thesis. His kindness, helpfulness and encouragement leave me a profound impression. I have learned so much from him through our conversation. Through this work, I have got a solid understanding of solid-state NMR and gained experience in NMR instrument operation. I really enjoyed my NMR research during my Ph.D. study and found many funs in the last three years.

My special thanks goes to Prof. Dr. W. Wenig for accepting me doing research work in the Laboratory for Applied Physics from August, 1994 to October, 1995 and as the coreferent of my thesis.

I would like to thank all of the friends and colleagues from the Institute of Physical Chemistry, without their help, I would not have finished my thesis. I am especially indebted to Dr. M. Hess, Prof. Dr. C. Mayer for their kindly generous help. I thank Mr. Frank Hamacher, Dr. Yong Ba, Mr. Marco Miles for discussion of the MQC theories. Dr. Yong Ba and Mr. M. Miles have patiently read and corrected the manuscript.

I acknowledge Dipl. Ing. Mansfred Zähres, and Dipl. Ing. Uwe Bachorski for their help in performing the NMR experiments.

I heartily thank Miss Claudia Feldhüsen for her kindly help in preparing the HDPE sample.

For our Badminton team, I appreciate Dr. W. Sutter, Mr. R. Schreiber, Mr. Uwe Großpietch, Mr. Daniel Lattner, and Mr. Michael Kischel, during the playing times I relaxed from the work and enjoined so much at the same time.

I would like to thank my wife, my son and my parents for their help and encouragement in finishing my thesis.

CONTENTS

Chapter 1. Introduction

The NMR phenomenon was discovered at the end of 1945 independently by Purcell et al.[1] at Harvard University and by Bloch et al.[2] at Stanford University. Since then its use has spread with great success to chemistry, biochemistry, physiology, medicine, materials science, finding many applications in every discipline.

In the earliest experiments, the NMR signals were detected by continuous wave (CW) methods. In the 1960s and 1970s, the CW method was replaced by the pulse method, which not only reduced the time needed for an experiment, but also allowed many new types of experiments.

In the pulsed, or Fourier transform, experiment the spin resonance frequencies are revealed through the transient response of the spins following a disturbance from equilibrium. The diversity of local magnetic fields and spin interactions adds to the complexity of the response and makes the NMR spectrum a rich source of information concerning the structure, and dynamical behaviour, of molecules in all phases of matter. Yet beyond this diversity NMR is additionally favoured by a particular set of circumstances, among them the phase coherence of radio frequency sources and the magnitude and time scale of nuclear spin interactions, that combine to offer extraordinary opportunities for external manipulation and control of the spin Hamiltonian: where desired, the effective operator structure of a Hamiltonian or the direction of a local field can be altered, a selected interaction attenuated or eliminated, the sense of time reversed. Moreover, the Hamiltonian governing the spin dynamics can be switched rapidly between different forms during different periods of an experiment.

A characteristic feature of solid-state NMR spectroscopy is the anisotropy of the internal interactions. On the one hand, this is an advantage because the anisotropic parameters carry important information, which is inaccessible from solution-state NMR. On the other hand, if neither the space- nor the spin-part of these interactions is manipulated, the anisotropic interactions produce broad and often featureless NMR spectra. Obtaining high-resolution liquidlike spectra, while still preserving information about anisotropic properties, is thus one of the key goals of solid-state NMR.

There are many techniques which average and eliminate certain internal interactions in order to obtain high-resolution spectra of solids, for example, the magic angle sample spinning (MAS)[3] can eliminate the broadening due to the anisotropy of the chemical shift, while the multiple pulse sequence[4] can eliminate the dipolar interactions between homonuclear spins, provided that the cycle frequency of the multiple-pulse sequence exceeds the static width of the NMR spectrum.

The phenomena of multiple-quantum coherences were first observed as early as 1956 by a continuous-wave NMR experiment, later, after the development of the Fourier transform experiment, the average Hamiltonian theory and the two-dimensional spectroscopic methods, the popularity of multiple-quantum NMR has steadily increased since the mid 1970s.

Initially, the excitation of the multiple-quantum transitions in scalar-coupled spin systems was used in liquid-state NMR spectroscopy for the characterization of spin coupling topologies and for the simplification of complicated spectra[5].

For exciting the multiple-quantum transitions in abundant spins-1/2 systems, such as ^{1}H in solids, it is necessary to design multiple-pulse sequences which generate a suitable effective Hamiltonian and avoid the loss of signal by dipolar dephasing in both the excitation and reconversion time period. In 1983, Yen and Pines[6] showed the excitation and detection of high-order multiple-quantum coherences (MQC) in strongly dipolar-coupled, abundant nuclear spin-1/2 systems in solids, corresponding to nuclear magnetic resonance transitions in which more than 30 nuclei simultaneously flip their spins. The time-reversible radio-frequency (rf) pulse sequence was designed to generate a time-reversible evolution of the coupled spin system and thereby minimize destructive interference among MQC. Then, MQ NMR was further developed as a tool for estimating the sizes of nuclear spin clusters in solids[7-10]. Applications in structural studies of a wide variety of systems have been reported, including amorphous silicon hydride[11,12], diamond films and powder [13,14], doped synthetic polymers[15-17], catalyst supports[18], and zeolites[19]. The dynamics of multispin systems have also been investigated[20-22], homonuclear dipole-dipole couplings of the abundant nuclei with large magnetic moments such as ^{1}H dominate nuclear spin interactions in such systems, resulting in homogeneously broadened line shapes.

Recently, much progress[23-25] has been made towards exciting multiple-quantum coherences amongst abundant spins in solids under magic angle spinning for getting high-resolution

MQC spectra. Especially the high-resolution of the double-quantum[26-28]and triple-quantum[29] coherences were obtained under fast MAS.

The aim of this thesis is the application of multiple-quantum MAS NMR to materials, including inorganic and organic macromolecules. The direct goal of this work is to investigate whether the multiple quantum coherence technique can be used to enhance the effective resolution of solid state NMR spectra. To clarify this let us look at the following case. In a material single, isolated proton spins and spin pairs are found. The silica surface, which is treated in chapter 6, would be an example. The single proton spins are then found in isolated silanol groups, spin pairs for instance in associated silanols (Fig. 6.1). The proton NMR spectrum of such a material is the sum of the contribution from the single spins and from the spin pairs. Due to the low resolution of solid state proton NMR spectra the spectral contributions of both spin types overlap. The idea of the MQC technique is now that a spectrum that is obtained using a double-quantum filtration technique, can only reveal the contribution from the proton spin pairs, while single, isolated spins can never take part in double-quantum coherence. The contents of the thesis are as follows: In chapter 2 a basic description of the quantum mechanics is given. Chapter 3 reviews the basic principles and methods of high-resolution solid-state NMR spectroscopy. Chapter 4 presents the principles and methods of multiple-quantum MAS NMR. Chapter 5 describes multiple-quantum experiments on the static adamantane sample. The surface structure of silica gel is investigated in chapter 6. Chapter 7 illustrates the application of the double-quantum MAS filtering method to the phase separation of some polymers, copolymers, and polymer blends. The semicrystalline polyethylene is studied by multiple-quantum MAS NMR together with other high-resolution solid-state NMR methods in chapter 8. Finally, the results are summarized in chapter 9.

References

(1) E. M. Purcell, H. C. Torrey and R. V. Pound, Phys. Rev. **69**, 37 (1946).

(2) F. Bloch, W. W. Hansen and M. E. Packard, Phys. Rev. **69**, 127 (1946).

(3) E. R. Andrew, A. Bradbury, R. G. Eades, Nature **182**, 1659 (1958).

(4) J. S. Waugh, L. M. Huber, and U. Haeberlen, Phys. Rev. Lett. **20**, 180 (1968).

(5) R. R. Ernst, G. Bodenhausen, and A. Wokaum, Principles of Nuclear Magnetic Resonance in One and Two Dimensions, Volume 14 of International Series of Monographs on Chemistry, **1990**, Oxford University Press, New York.

(6) Y. S. Yen and A. Pines, J. Chem. Phys. **78**, 3579 (1983).

(7) J. Baum and A. Pines, J. Am. Chem. Soc. **108**, 7447 (1986).

(8) D. Suter, S. B. Liu, J. Baum, and A. Pines, Chem. Phys. **114**, 103 (1987).

(9) D. N. Shykind, J. Baum, S. B. Liu, And A. Pines, J. Magn. Reson. **76**, 149 (1988).

(10) W. V. Gerasimowicz, A. N. Garroway, and J. B. Miller, J. Am. Chem. Soc. **112**, 3726 (1990).

(11) J. Baum, K. K. Gleason, A. Pines, A. N. Garroway, and J. A. Reimer, Phys. Rev. Lett. **56**, 1377 (1986).

(12) M. A. Petrich, K. K. Gleason, and J. A. Reimer, Phys. Rev. **B 36**, 9722 (1987).

(13) D. H. Levy and K. K. Gleason, J. Phys. Chem. **96**, 8125 (1992).

(14) B. E. Scruggs and K. K. Gleason, J. Phys. Chem. **97**, 9187 (1993).

(15) S. J. Limb, B. E. Scruggs, and K. K. Gleason, Macromolecules **25**, 3750 (1993).

(16) B. E. Scruggs and K. K. Glason, Macromolecules **25**, 1864 (1992).

(17) G. Buntkowsky, E. Roessler, M. Taupitz, and H. M. Vieth, J. Phys. Chem. **A 101**, 67 (1997).

(18) S. J. Hwang, D. O. Uner, T. S. King, M. Pruski, and B. C. Gerstein, J. Phys. Chem. **99**, 3697 (1995).

(19) J. G. Person, B. F. Chemlka, D. N. Shykind, and A. Pines, J. Phys. Chem. **96**, 8517 (1992).

(20) M. Munowitz, A. Pines, and M. Mehring, J. Chem. Phys. **86**, 3172 (1987).

(21) M. Tomaselli, S. Hediger, D. Suter, and R. R. Ernst, J. Chem. Phys. **105**, 10672 (1996).

(22) S. Lacelle, S. J. Hwang, and B. C. Gerstein, J. Chem. Phys. **99**, 8407 (1993).

(23) B. H. Meier and W. L. Earl, J. Chem. Phys. **85**, 4905 (1986).

(24) B. H. Meier and W. L. Earl, J. Am. Chem. Soc. **109**, 7937 (1987).

(25) Y. Ba, Ph.D. Dissertation, University of Duisburg, Germany, **1995**.

(26) H. Geen, J. J. Titman, J. Gottwald, H. W. Spiess, Chemical Physics letters **227**, 79 (1994).

(27) J. Gottwald, D. E. Demco, R. Graf, H. W. Spiess, Chemical Physics Letters **243**, 314 (1995).

(28) H. Geen, J. J. Titman, J. Gottwald, and H. W. Spiess, J. Magn. Reson., Series A **114**, 264 (1995).

(29) U. Friedrich, I. Schnell, D. E. Demco, H. W. Spiess, Chemical Physics letters **285**, 49 (1998).

Chapter 2. Basic principles of the quantum mechanics of spins-1/2 nuclei

2.1 Introduction

Many magnetic resonance phenomena can be described by the classical Bloch equations[1,2]. However, the discussion of many NMR experiments requires the knowledge of the quantum mechanics of spin systems. In quantum mechanics, the density operator can exactly predict the average state of a spin system, while the Hamilton operator can represent the interactions. This chapter will provide a brief discussion of time-dependent quantum mechanics of spin-1/2 systems which will provide the basic knowledge for describing multiple-quantum NMR in the later chapters. More specified information and completely detailed description of the concepts and theories can be found in the references[1-6] of this chapter.

2.2 The spaces in quantum mechanics

Normally three linear spaces are used in describing the quantum mechanics of spins, i.e., (1) the Hilbert space in which spin state vectors span a state vector space of dimension n, (2) the Liouville space (Operator algebra) in which the operators span a vector space of dimension n×n, (3) the Superoperator space in which the superoperators span a vector space of dimension $n^2 \times n^2$. There is some similarity between the Hilbert space H spanned by the state functions and the Liouville space L spanned by the corresponding linear operators. However, in addition to having the properties of a unitary vector space, the Liouville space L forms an operator algebra where the product of two operators is defined as well.

2.3 State vectors and superposition in Hilbert space

Let us consider a simple case of a spin-1/2 two-level system in quantum mechanics. When one spin-1/2 is placed in a magnetic field, the two possible states are: $|\alpha\rangle$ and $|\beta\rangle$, the former represents the spin aligned with the magnetic field and has lower energy (on the assumption of $\gamma > 0$, $E = \langle\alpha|-\gamma B_0 I_z|\alpha\rangle$), the latter represents the spin aligned against the magnetic field and

has a higher energy. The value of ΔE (i.e. the energy difference between these two states) is dependent on the strength of the magnetic field: $\Delta E = \gamma\eta B_0$. If we apply a radiofrequency (r.f.) field, B_1, with frequency ω perpendicular to the main magnetic field, B_0, so that $\eta\omega$ equals ΔE, a transition between the two states can occur. In this case we can say that a coherence has been established between the two states. For a 90° r.f. pulse, the spin state evolves into the following state under the radiofrequency field:

$$|\psi>=\frac{1}{\sqrt{2}}|\alpha>+\frac{1}{\sqrt{2}}|\beta>, \tag{2.1a}$$

or

$$|\psi>=\frac{1}{\sqrt{2}}|\alpha>-\frac{1}{\sqrt{2}}|\beta>, \tag{2.1b}$$

depending on the phase of the B_1-field, the spin is then in the superposition state of $|\alpha>$ and $|\beta>$ (using the Dirac "ket" vector and "bra" vector[3] representation).

In the case of a single spin-1/2, an arbitrary state |ψ> or <ψ| can be constructed as a linear superposition of the two basis states |α> and |β>:

$$|\psi>=c_\alpha(t)\,|\alpha> + c_\beta(t)|\beta>, \tag{2.2a}$$

$$<\psi|=<\alpha|c_\alpha^*(t) + <\beta|c_\beta^*(t), \tag{2.2b}$$

where $c_\alpha(t)$ and $c_\beta(t)$ are complex numbers, and the basis kets |α> and |β> eigenstates of the Zeeman Hamiltonian, and <α|β> = 0. Therefore, just like the description of a vector in real space, the spin state |ψ> or <ψ| can be described as a vector in Hilbert space, as shown in Figure 2.1[4]. The norm of the vector is interpreted as the statistical probability of finding the system in the particular state.

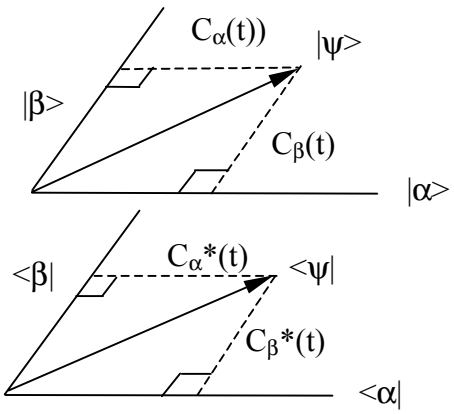

***Figure 2.1**: The representation of states |ψ> and <ψ| in Hilbert space.*

As mentioned above, once we have chosen a basis set of wave functions, we can describe any state vector as a linear combination of these wave functions. All the information about the

state vector is in the coefficients of this linear combination. In general, any state vector $|\psi>$ can be described by the following equation:

$$|\Psi>=\sum_i c_i|i>, \tag{2.3}$$

where the coefficient c_i is the contribution of the eigenstate $|i>$ to the state vector and can be obtained through the scalar product of $<i|\psi>$.

In summary, a spin state vector can be described by linear combinations of a set of orthonormal eigenstates in Hilbert space. We cannot change its length, i.e., the sum of the squares of the coefficients in (2.3) must be equal to 1: By applying pulses to the spins we can change the orientation of vectors in Hilbert space by operating on the present state and causing it to rotate to another state.

2.4 The basic spin-1/2 operators and its representations [5]

In quantum mechanics, operators operate on wave functions. The wave function describes the spin system, while the operator, which corresponds to a physical observable, represents the action that we are going to perform to the system. For an operator $\hat{A}$ representing a physical observable, a special group of wave functions, $|\psi_i>$, exists, which satisfies the condition:

$$\hat{A}|\psi_i>=a_i|\psi_i>, \tag{2.4}$$

where a_i is a real number. Then we can say that $|\psi_i>$ is the eigenfunction or eigenstate of the operator $\hat{A}$ and a_i is the corresponding eigenvalue.

The operators for spin angular momentum are $\hat{F}_x, \hat{F}_y$ and $\hat{F}_z$. The rules which describe how each angular momentum operator acts on each wave function in our chosen orthonormal basis set $|\alpha>$ and $|\beta>$ are given as follows:

$$\begin{aligned}
&\hat{F}_x|\alpha>=\frac{\eta}{2}|\beta>,\ \hat{I}_y|\alpha>=\frac{i\eta}{2}|\beta>,\ \hat{I}_z|\alpha>=\frac{\eta}{2}|\alpha>,\\
&\hat{F}_x|\beta>=\frac{\eta}{2}|\alpha>,\ \hat{I}_y|\beta>=-\frac{i\eta}{2}|\alpha>,\ \hat{I}_z|\beta>=-\frac{\eta}{2}|\beta>.
\end{aligned} \tag{2.5}$$

The first equation of (2.5) will be explained as an example for the interpretation of these rules: the operator $\hat{F}_x$ operating on the state vector $|\alpha>$ gives back the value of $\frac{\eta}{2}$ and rotates the state vector to $|\beta>$. It is usually convenient to write the angular momentum operators in a matrix form:

$$\hat{I}_x = \frac{\eta}{2}\begin{bmatrix} 0 & 1 \\ 1 & 0 \end{bmatrix},\ \hat{I}_y = -\frac{i\eta}{2}\begin{bmatrix} 0 & 1 \\ -1 & 0 \end{bmatrix},\ \hat{I}_z = \frac{\eta}{2}\begin{bmatrix} 1 & 0 \\ 0 & -1 \end{bmatrix}, \tag{2.6}$$

which operate on the vector $\begin{pmatrix} |\alpha> \\ |\beta> \end{pmatrix}$. Other rules such as the effect of the square of the operator or of a product of operators can be obtained through a matrix calculation, for example:

$$\bar{I}_x^2|\alpha> = \bar{I}_x \frac{\eta}{2}|\beta> = \frac{\eta^2}{4}|\alpha>,\ \bar{I}_x^2|\beta> = \bar{I}_x \frac{\eta}{2}|\alpha> = \frac{\eta^2}{4}|\beta>. \tag{2.7}$$

So the square operators can be written:

$$\bar{I}_x^2 = \frac{\eta^2}{4}\bar{E},\quad \bar{I}_y^2 = \frac{\eta^2}{4}\bar{E},\quad \bar{I}_z^2 = \frac{\eta^2}{4}\bar{E}, \tag{2.8}$$

where $\bar{E}$ is the identity matrix, $\begin{bmatrix} 1 & 0 \\ 0 & 1 \end{bmatrix}$.

The other products of the operators can be represented as follows:

$$\begin{aligned} &\bar{I}_x\bar{I}_y = \frac{i\eta}{2}\bar{I}_z, && \bar{I}_y\bar{I}_z = \frac{i\eta}{2}\bar{I}_x, && \bar{I}_z\bar{I}_x = \frac{i\eta}{2}\bar{I}_y, \\ &\bar{I}_y\bar{I}_x = -\frac{i\eta}{2}\bar{I}_z, && \bar{I}_z\bar{I}_y = -\frac{i\eta}{2}\bar{I}_x, && \bar{I}_x\bar{I}_z = -\frac{i\eta}{2}\bar{I}_y. \end{aligned} \tag{2.9}$$

From (2.9) we can see that the order in which the operators are applied, matters. The commutation operation allows us to decide mathematically whether two operators commute. The commutator $[\hat{A}, \hat{B}]$ is defined as:

$$[\bar{A}, \bar{B}] = \bar{A}\bar{B} - \bar{B}\bar{A}\ . \tag{2.10}$$

If the result of $[\hat{A}, \hat{B}]$ is zero, then the two operators commute. For commuting operators, this means that there is no difference in which order we apply these two operators to the system. The angular momentum operators, $\bar{I}_x, \bar{I}_y$ and $\bar{I}_z$, do not commute with each other and they have the following important commutation rules:

$$[\bar{I}_x, \bar{I}_y] = \bar{I}_x\bar{I}_y - \bar{I}_y\bar{I}_x = \frac{i\eta}{2}\bar{I}_z - \frac{-i\eta}{2}\bar{I}_z = i\eta\bar{I}_z, \tag{2.11a}$$

$$[\bar{I}_y, \bar{I}_z] = \bar{I}_y\bar{I}_z - \bar{I}_z\bar{I}_y = \frac{i\eta}{2}\bar{I}_x - \frac{-i\eta}{2}\bar{I}_x = i\eta\bar{I}_x\ , \tag{2.11b}$$

$$[\bar{I}_z, \bar{I}_x] = \bar{I}_z\bar{I}_x - \bar{I}_x\bar{I}_z = \frac{i\eta}{2}\bar{I}_y - \frac{-i\eta}{2}\bar{I}_y = i\eta\bar{I}_y, \tag{2.11c}$$

and $$[\bar{I}^2, \bar{I}_z] = \bar{I}^2\bar{I}_z - \bar{I}_z\bar{I}^2 = 0. \tag{2.11d}$$

From (2.11d) we see that the operators $\bar{F}_z$ and $\bar{F}^2$ commute, so they have the same eigenstates |I,M>, where I is the spin quantum number of the nucleus and M is the magnetic quantum number that takes one of the values I, I-1, ..., -I:

$$\bar{F}_z|I,M>=M|I,M>, \tag{2.12a}$$

$$\bar{F}^2|I,M>=I(I+1)|I,M>. \tag{2.12b}$$

In addition to the spin operators $\bar{F}_x, \bar{F}_y, \bar{F}_z$, there are two very useful spin operators, i.e., the so-called raising and lowering operators, $\hat{I}_+$ and $\hat{I}_-$:

$$\bar{F}_+ = \bar{F}_x + i\bar{F}_y,\ \bar{F}_- = \bar{F}_x - i\bar{F}_y, \tag{2.13}$$

with the following effect on the eigenstates of $\bar{F}_z$:

$$\bar{F}_+|I,M>=\sqrt{I(I+1)-M(M+1)}|I,M+1>, \tag{2.14a}$$

$$\bar{F}_-|I,M>=\sqrt{I(I+1)-M(M-1)}|I,M-1>. \tag{2.14b}$$

2.5 Density operator in Liouville space [1, 2, 6]

2.5.1 Definition and physical meaning of the density operator

The density operator is a standard quantum mechanical tool for dealing with coherence and mixed states. In a pure state, all spin systems of the ensemble are in the same state, the corresponding density operator, $\bar{\rho}(t)$, is defined by:

$$\bar{\rho}(t)=|\psi(t)><\psi(t)|=\sum_i\sum_j c_i(t)c_j^*(t)|i><j|. \tag{2.15}$$

The matrix elements of $\hat{\rho}$, ρ_{rs}, can be written as follows:

$$\rho_{rs}=<r|\hat{\rho}(t)|s>=\sum_i\sum_j c_i(t)c_j^*(t)<r|i><j|s>=c_r(t)c_s^*(t). \tag{2.16}$$

In a mixed state, for example for an ensemble in thermal equilibrium, the density operator is defined as a weighed average of the projection operators, $|\Psi^k><\Psi^k|$:

$$\begin{aligned}\hat{\rho}(t)&=\sum_k P^k\left|\psi^k(t)\right\rangle\left\langle\psi^k(t)\right|\\&=\sum_k P^k\sum_i\sum_j C_i^k(t)C_j^{k*}(t)|i\rangle\langle j|\\&=\sum_i\sum_j\overline{C_i(t)C_j^*(t)}|i\rangle\langle j|,\end{aligned} \tag{2.17}$$

where P^k is the probability that a spin system of the ensemble is in one of several possible states $|\psi^k(t)>$, $\sum_k P^k = 1$, and the bar denotes the ensemble average. The matrix elements, ρ_{rs}, can be expressed as:

$$\rho_{rs} =< r \mid \hat{\rho}(t) \mid s >= \sum_k p^k c_r^k(t) c_s^{k*}(t) = \overline{c_r(t) c_s^*(t)}. \qquad (2.18)$$

The density operator is a Hermitian operator, i.e., $< r \mid \hat{\rho}(t) \mid s >=< s \mid \hat{\rho}(t) \mid r >^*$ and its matrix elements are the products of the expansion coefficients of the state function $|\psi>$. The physical meaning of the density operator may be visualized by examination of its matrix elements in the orthonormal eigenbase of the Hamiltonian H. For example, we can see that the diagonal element, ρ_{rr},

$$\rho_{rr} =< r \mid \hat{\rho}(t) \mid r >= \overline{|c_r(t)|^2} = P_r, \qquad (2.19)$$

is equal to the probability that the spin system is found in the eigenstate |r> of the Hamiltonian H and P_r is associated with the population of state |r>; and the off-diagonal element, ρ_{rs},

$$\rho_{rs} =< r \mid \hat{\rho}(t) \mid s >= \overline{|c_r(t) c_s^*(t)|}, \qquad (2.20)$$

expresses a "coherent superposition" (or simply "coherence") of eigenstates |r> and |s>. In general, ρ_{rs} is the complex amplitude of the coherence |r><s|, it represents an n-quantum coherence ($n=M_r-M_s$, is defined as the difference in Zeeman quantum number between any two states |r> and |s> in coherent superposition). For $n=\pm 1$, it is related to the transverse magnetization components and can be directly observed; but for $n\neq\pm 1$, it does not lead to observable magnetization and can only be detected indirectly. This indirect detection of non-observable coherences forms the main line throughout this dissertation.

2.5.2 Expectation value

With knowledge of the density operator, the expectation value of any observable A can be evaluated from the trace of the product of the observable operator $\hat{A}$ and the density operator as follows:

$$< A >= tr\{\hat{A}\hat{\rho}(t)\}. \qquad (2.21)$$

The trace can be evaluated either from the matrix representations of A and $\rho(t)$ in an arbitrary base $\{|r>\}$ or via an expansion of the two operators A and $\rho(t)$ in terms of orthogonal base operators.

2.5.3 The density operator at equilibrium

The density operator in thermal equilibrium at temperature T, $\hat{\rho}_{eq}$, can be expressed by the Boltzmann distribution:

$$\hat{\rho}_{eq} = \frac{\exp(-\eta \hat{H}_0 / kT)}{tr\{\exp(-\eta \hat{H}_0 / kT)\}} , \qquad (2.22)$$

where H_0 is the time-independent Hamiltonian (in angular frequency units) for the spin system. It consists of the Zeeman interaction $\hat{H}_z$ and the other secular portions of the internal interactions in a strong magnetic field. k is the Boltzmann constant. Usually the Zeeman interaction $\hat{H}_z$ dominates and (2.22) can be simplified:

$$\hat{\rho}_{eq} = \frac{\exp(-\eta \hat{H}_z / kT)}{tr\{\exp(-\eta \hat{H}_z / kT)\}} = \frac{\exp(-\eta \hat{H}_z / kT)}{\sum_m < m|\exp(-\eta \hat{H}_z / kT)|m>} . \qquad (2.23)$$

Provided that $|\eta \hat{H}_z| << kT$, an assumption usually valid down to temperatures as low as 1 K, the eq.(2.23) can be further simplified:

$$\hat{\rho}_{eq} \approx \frac{\hat{1} + \gamma \eta B_0 \hat{I}_z / kT}{\sum_{M=I}^{-I} (1 + \gamma \eta B_0 M / kT)} \approx \frac{\hat{1}}{2I+1} + \frac{\gamma \eta B_0}{(2I+1)kT} \hat{I}_z , \qquad (2.24)$$

where $-\gamma B_0 \hat{I}_z = \hat{H}_z$, B_o is the external magnetic field, M=I, I-1, ..., -I describes the z component of the total spin angular momentum I. Because the term, $\frac{\hat{1}}{2I+1}$, is proportional to the unit operator, it commutes with all the operators and consequently can not influence the time development of ρ. For simplicity we will usually suppress this term, as well as the constant $\frac{\gamma \eta B_0}{(2I+1)kT}$ in eq. (2.24), so the equilibrium density operator at high temperature (above 1 K) can be approximately expressed as follows:

$$\hat{\rho}_{eq} \approx \hat{I}_z = \sum_{i=1}^{N} \hat{I}_{iz} . \qquad (2.25)$$

2.5.4 Expansion of the density operator in orthonormal base

The density operator $\hat{\rho}(t)$ can be expanded in a complete set of orthonormal base operators $\{B_s\}$ in the Liouville space of dimension n×n:

$$\hat{\rho}(t) = \sum_{s=1}^{n^2} b_s(t)\hat{B}_s , \tag{2.26}$$

where the coefficient $b_s(t)$ in the expansion can be determined by the scalar product:

$$b_s(t) = \frac{<\hat{B}_s|\hat{\rho}(t)>}{<\hat{B}_s|\hat{B}_s>} = \frac{tr\{\hat{B}_s^+\hat{\rho}(t)\}}{tr\{\hat{B}_s^+\hat{B}_s\}} , \tag{2.27}$$

where $\hat{B}_s^+$ is the adjoint operator of $\hat{B}_s$. For normalized base operators, the denominator is unity. The scalar product of two operators is equivalent to the scalar product of two n^2-dimensional vectors consisting of the sets of elements $\{A_{lk}]$ and $\{B_{lk}\}$:

$$<\hat{A}|\hat{B}>= tr\{\hat{A}^+\hat{B}\} = \sum_{kl}\hat{A}_{kl}^+\hat{B}_{lk} = \sum_{kl}\hat{A}_{lk}^*\hat{B}_{lk} . \tag{2.28}$$

Below we will give some sets of base operators which have been proven to be useful for the expansion of the density operator in the context of pulse Fourier spectroscopy.

(1). Products of Cartesian spin operators: based on the angular momentum operators $\hat{I}_{kx}$, $\hat{I}_{ky}$ and $\hat{I}_{kz}$ of the individual spins and its cyclic commutation rules, $[\hat{I}_{k\alpha}, \hat{I}_{k\beta}] = i\hat{I}_{k\gamma}$, where α, β, γ = x, y, z and cyclic permutations, the base operators $\hat{B}_s$ can be defined by the products:

$$\hat{B}_s = 2^{(q-1)}\prod_{k=1}^{N}(\hat{I}_{k\alpha})^{a_{ks}} , \tag{2.29}$$

where N is the total number of I=1/2 nuclei in the spin system, k is the index of the individual nucleus, α = x, y, or z, q is the number of operators in the products, a_{ks} = 1 for q of the spins, and a_{ks} = 0 for the N-q remaining spins. The complete base set $\{\hat{B}_s\}$ for a system with N spin-1/2 consists of 4^N product operators $\hat{B}_s$. There are 16 product operators $\hat{B}_s$ for a two spin-1/2 system:

$$\begin{aligned}
&q = 0,\ \hat{B}_s = 1/2\,\hat{E}\ (\hat{E} = \text{unity operator}),\\
&q = 1,\ \hat{B}_s = \{\hat{I}_{1x}, \hat{I}_{1y}, \hat{I}_{1z}, \hat{I}_{2x}, \hat{I}_{2y}, \hat{I}_{2z}\},\\
&q = 2,\ \hat{B}_s = \{2\hat{I}_{1x}\hat{I}_{2x},\ 2\hat{I}_{1x}\hat{I}_{2y},\ 2\hat{I}_{1x}\hat{I}_{2z},\\
&\qquad 2\hat{I}_{1y}\hat{I}_{2x},\ 2\hat{I}_{1y}\hat{I}_{2y},\ 2\hat{I}_{1y}\hat{I}_{2z},\\
&\qquad 2\hat{I}_{1z}\hat{I}_{2x}, 2\hat{I}_{1z}\hat{I}_{2y}, 2\hat{I}_{1z}\hat{I}_{2z}\}.
\end{aligned} \tag{2.30}$$

(2). Shift operators: raising and lowering operators are sometimes more straightforward to use for multiple-quantum coherence descriptions than ($\hat{I}_x, \hat{I}_y$), their definitions are given in eq. (2.13). As an example, we use them to express ±2-quantum and zero quantum coherence in a two spin-1/2 system:

$$\hat{I}_k^+ \hat{I}_l^+ = 1/2[2\hat{I}_{kx}\hat{I}_{lx} - 2\hat{I}_{ky}\hat{I}_{ly} + i2\hat{I}_{kx}\hat{I}_{ly} + i2\hat{I}_{ky}\hat{I}_{lx}] \ , \tag{2.31a}$$

$$\hat{I}_k^- \hat{I}_l^- = 1/2[2\hat{I}_{kx}\hat{I}_{lx} - 2\hat{I}_{ky}\hat{I}_{ly} - i2\hat{I}_{kx}\hat{I}_{ly} - i2\hat{I}_{ky}\hat{I}_{lx}] \ , \tag{2.31b}$$

$$\hat{I}_k^+ \hat{I}_l^- = 1/2[2\hat{I}_{kx}\hat{I}_{lx} + 2\hat{I}_{ky}\hat{I}_{ly} - i2\hat{I}_{kx}\hat{I}_{ly} + i2\hat{I}_{ky}\hat{I}_{lx}] \ , \tag{2.31c}$$

$$\hat{I}_k^- \hat{I}_l^+ = 1/2[2\hat{I}_{kx}\hat{I}_{lx} + 2\hat{I}_{ky}\hat{I}_{ly} + i2\hat{I}_{kx}\hat{I}_{ly} - i2\hat{I}_{ky}\hat{I}_{lx}]. \tag{2.31d}$$

2.6 Equation of motion

In quantum mechanics, the density operator, $\hat{\rho}(t)$, describes the state of the spin system, while the Hamiltonian represents the forces or interactions that try to change the state of the system. The motion of $\hat{\rho}(t)$ may be derived from the Schrödinger equation which describes the evolution of the spin system[1,4]:

$$\frac{d}{dt}|\psi(t)\rangle = -\frac{i}{\eta}\hat{H}(t)|\psi(t)\rangle, \text{ (Schrödinger equation)} \tag{2.32}$$

where $\hat{H}(t)$ (having energy unit) is the Hamiltonian or total energy operator of the system. From eq. (2.32) one obtains the well-known Liouville-von Neumann equation, which is of central importance for calculating the dynamical systems:

$$\frac{d}{dt}\hat{\rho}(t) = -\frac{i}{\eta}[\hat{H}(t), \hat{\rho}(t)]. \tag{2.33}$$

The commutator $[\hat{H}(t), \hat{\rho}(t)]$ in the expression represents that the outcome of two consecutive operators depends on the order in which the operators act. Only when the commutator is zero can the two corresponding observables be measured simultaneously, or, alternatively, consecutively but in any order, in this case. The two operators are said to commute with each other. So the presence of the commutator in the Liouville-von Neumann equation shows that there must exist some fundamental incompatibility between the density operator and the Hamiltonian if the system is to change with time. Its formal solution may be written[6]:

$$\hat{\rho}(t) = \hat{U}(t)\hat{\rho}(0)\hat{U}(t)^{-1}, \tag{2.34}$$

and $$\hat{U}(t) = T\exp\{-\frac{i}{\eta}\int_0^t \hat{H}(t')dt'\}, \tag{2.35}$$

where T is the Dyson time ordering operator which ensures that operators that act at earlier times on $\hat{\rho}(0)$ are always at the right of operators that act at later times on $\hat{\rho}(0)$. $\hat{U}(t)$ is the propagator which pushes the density operator ahead in time. We can observe from eq. (2.34) that $\hat{\rho}(t)$ is always related to $\hat{\rho}(0)$ by a unitary transformation in Liouville space, this means that the norm of the density operator is conserved during the evolution of the spin system. When the Hamiltonian $\hat{H}$ is time-independent, then eq. (2.34) can be re-written as:

$$\hat{\rho}(t) = \exp[-\frac{i}{\eta}\hat{H}t]\hat{\rho}(0)\exp[\frac{i}{\eta}\hat{H}t], \tag{2.36}$$

using the Baker-Campbell-Hausdorff expansion, $\hat{\rho}(t)$ can be expanded in terms of t:

$$\hat{\rho}(t) = \hat{\rho}(0) + \frac{i}{\eta}t[\hat{\rho}(0),\hat{H}] - \frac{1}{\eta}\frac{t^2}{2!}[[\hat{\rho}(0),\hat{H}],\hat{H}] - \frac{i}{\eta}\frac{t^3}{3!}[[[\hat{\rho}(0),\hat{H}],\hat{H}],\hat{H}] + \cdots. \tag{2.37}$$

Since knowledge of the density operator permits calculation of the expectation value, <A(t)>, of any operator according to the relationship: $<\mathrm{A(t)}> = \mathrm{tr}\{\hat{\mathrm{A}}\hat{\rho}(\mathrm{t})\}$, prediction and control of the time development of $\hat{\rho}(t)$ are always the central problem for pulsed NMR in general and multiple-quantum NMR in particular.

Usually it is facilitated to solve the Livouville-von Newmann equation in the rotating frame. In the rotating frame, the Liouville-von Neumann equation takes the same form as in the laboratory frame: $\frac{d\hat{\rho}^R}{dt} = -\frac{i}{\eta}[\hat{H}^R, \hat{\rho}^R]$, wherein only those components of the Hamiltonian that remain independent of time in the rotating frame are retained (the secular terms). We will later omit the superscript R on ρ and H, with the understanding that the laboratory frame has been replaced by a suitable rotating frame in which external time-dependent interactions are absent.

2.7 Summary

Based on the previous discussion we can conclude this chapter by shortly repeating the main points. The state vector |ψ> which describes N interacting spins, is a superposition of $(2I+1)^N$ basis states |r> in Hilbert space, each corresponding to one magnetic energy. The density operator |ψ><ψ| which carries all the statistical information relevant to the measurement of

observables is a superposition of $(2I+1)^N \times (2I+1)^N$ orthogonal base operators in Liouville space. Each base operator corresponds to one of the $[(2I+1)^N \times (2I+1)^N - 1]$ linearly independent modes. If the density operator is regarded as a symbol for the entire system, then its base operators represent the noninteracting components into which the whole may be decomposed. Implicit in each component is the statistical property of the coherence, the net interference between two basis states over the ensemble. A given component of the density operator representing a mode of coherence, evolves independently of the rest, its transformation into other components is determined by the Liouville-von Neumann equation of motion.

References

(1) R. R. Ernst, G. Bodenhausen, and A. Wokaum, Principles of Nuclear Magnetic Resonance in One and Two Dimensions, Volume 14 of International Series of Monographs on Chemistry, Oxford University Press, New York, 1990.

(2) B. C. Gerstein and C. R. Dybowski, Transient Techniques in NMR of Solids, An Introduction to Theory and Practice, Academic Press, 1985.

(3) P. A. M. Dirac, The Principles of Quantum Mechanics, Oxford University Press, Fourth Edition 1958, reprinted 1974.

(4) M. Munowitz, Coherence and NMR, Wiley, New York, 1988.

(5) W. S. Veeman, NMR Lecture.

(6) M. Munowitz, A. Pines, and M. Mehring, J. Chem. Phys. **86**, 3172(1987).

Chapter 3. Basic principles and methods of high-resolution solid-state NMR experiments

In order to understand the principles and methods of high-resolution solid-state NMR, in this chapter I begin with the description of the basic spin interactions in solids, and then I will briefly outline the average Hamiltonian theory and its applications. Following this magic angle sample spinning (MAS) will be introduced. Finally, two-dimensional NMR spectroscopy and ^{1}H-WISE experiment are summarised. For more detailed treatment of these solid-state NMR principles and methods, some excellent monographs, books and reviews [1-10] are recommended.

3.1 The NMR interactions

We know that nuclei with a spin possess a magnetic moment $\vec{\mu}$, which interacts with its surroundings in several ways. These interactions can be described by an external and an internal Hamiltonian according to the type of its interactions: $\hat{H} = \hat{H}_{ext} + \hat{H}_{int}$. The first term includes the interaction of a spin system with the external static magnetic field $\vec{B}_0$ (Zeeman interaction) and the pulsed oscillating radio-frequency (r.f.) fields. These interactions cause a common motion of the spin system and contain no structural information about the nucleus of interest. The second term includes the interactions of a spin system with internal local fields produced through the chemical shift interaction, direct dipole-dipole interaction, quadrupole interaction, and indirect J-coupling. These interactions give the structural information. In comparison with the external static magnetic field, the internal or local interactions are very small, so they act only as a first-order perturbation in the high field (secular) limit and produce small shifts and splittings of the Zeeman energy levels which depend on the nature and extent of the couplings and on the number of interacting spins. In this thesis we will focus on a strongly coupled spins-1/2 solid system, so the quadrupole interaction and indirect J-coupling will not be dealt with in this chapter.

3.1.1 The Zeeman interaction

We know that some nuclei possess a spin ($\vec{I}$). This is associated with an angular momentum $\vec{J}$, which can be written as:

$$\vec{J} = \eta\vec{I}, \tag{3.1}$$

where η is Planck's constant h divided by 2π. When a nucleus has charge and spin, it also has a magnetic moment, $\vec{\mu}$, which is given by:

$$\vec{\mu} = \gamma\vec{J} = \gamma\eta\vec{I}, \tag{3.2}$$

where γ (with unit of rad T^{-1} s^{-1}) is the gyromagnetic ratio of the nuclear spin $\vec{I}$. When placed in an external magnetic field, the magnetic moments of the nuclei will align, either with or against the external magnetic field, and precess about the z axis of the field with the so-called Larmor frequency. Figure 3.1a gives a classical picture which represents the motion of a spin in a magnetic field. Aligned with the field represents a lower energy than that against the field. The energy for the interaction between the spin and the static magnetic field is classically expressed by:

$$E = -\vec{\mu}\cdot\vec{B}_0 = -\gamma\eta\vec{I}\cdot\vec{B}_0. \tag{3.3}$$

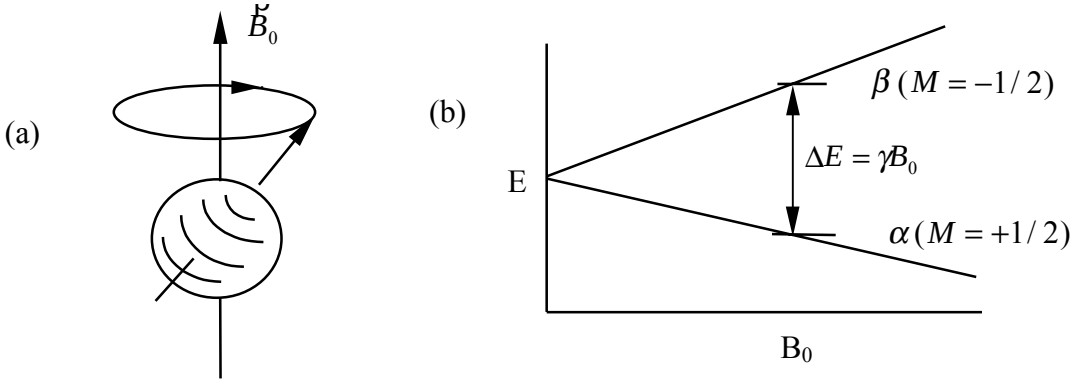

Figure 3.1*. (a) Schematic representation of the motion of a nucleus in a magnetic field. (b) The relationship between the magnitude of the magnetic field and the energy difference of the two states for a single spin 1/2.*

In the quantum mechanical description, this interaction is called Zeeman interaction and is represented by the Zeeman Hamiltonian operator:

$$\hat{H} = -\gamma\eta\hat{I}\cdot\vec{B}_0, \tag{3.4}$$

where $\hat{I} = (\hat{I}_x, \hat{I}_y, \hat{I}_z)$, $\vec{B}_0$ is the static magnetic field, which is normally chosen along the z-axis of the laboratory frame $\vec{B}_0 = (0,0,B_0)$. The Zeeman Hamiltonian operator can then be written as:

$$\hat{H}_z = -\gamma\eta\hat{I}_z B_0. \tag{3.5}$$

The eigenstates of this Hamiltonian are the states |I, M>, as defined previously in eq.(2.12). The energy of the spin system can be calculated by applying the Zeeman Hamiltonian to the spin wave function |I, M>:

$$\hat{H}_z \mid I,M >= -\gamma\eta B_0 \hat{I}_z \mid I,M > = -\gamma\eta B_0 M \mid I,M > . \tag{3.6}$$

The resulting (2I+1) energy levels generated by the Zeeman Hamilonian in the external static magnetic field are equally spaced, which is separated by the Larmor frequency ω_0 times η:

$$\omega_0 = \gamma B_0. \tag{3.7}$$

For the single spin-1/2, the Zeeman energies are $E=\pm 1/2\gamma\eta B_0$, so the energy difference between the upper energy level, which is often referred to as the "spin down" state (M=-1/2) described by wave function |1/2, -1/2> or |β>, and the lower level, which is referred to as the "spin up" state (M=+1/2) with wave function |1/2, +1/2> or |α>, is represented as follow:

$$\Delta E = -\gamma\eta B_0 (-1/2 - 1/2) = \gamma\eta B_0. \tag{3.8}$$

From (3.8) we can see that the energy difference ΔE is proportional to the magnitude of the magnetic field. As the external magnetic field strength increases, the energy difference between the two quantum states also increases. This relationship is illustrated in Figure 3.1b. Transition from the lower energy state to the higher energy state and vice verse will occur only if the incident photon has an energy equal to the energy difference between the two states.

For an ensemble of spins-1/2, the two energy states |α> and |β> will be unequally populated, the ratio being given by the Boltzmann equation:

$$\frac{N_\beta}{N_\alpha} = e^{-\Delta E/kT}, \tag{3.9}$$

where N_α and N_β are the populations of the α and β energy states, k the Boltzmann constant, and T the temperature. For NMR the frequencies are in the megahertz range which gives an $N_\beta/N_\alpha = 0.99998$ at room temperature. Therefore the population difference between the two states is small or we can say that the probabilities of being in either state is almost the same, 0.500005 for N_α and 0.499995 for N_β. At thermal equilibrium, due to the surplus population in the lower energy state according to the Boltzmann distribution, a net magnetization exists parallel to the static magnetic field. Meanwhile, all the contributing spins have components precessing in the x-y plane with a random phase, so there will be no net magnetization in the x-y plane. The total magnetization of the sample is stationary and aligned along the z-axis.

For an ensemble of spins, the corresponding Zeeman Hamiltonian is written as:

$$\hat{H}_z = -\sum_i \eta\gamma_i B_0 \hat{F}_{zi}, \tag{3.10}$$

where γ_i is the gyromagnetic ratio of the nuclear spin i, and $\hat{F}_{zi}$ is the operator for the z-component of the spin angular momentum of the ith spin.

3.1.2 The radio-frequency field induced interaction

The radio-frequency field is of essential importance in NMR, especially in the multiple pulse experiments, because the radio-frequency fields are used to manipulate the effective Hamiltonian of the spin system. Usually the r.f. field is generated by the probe coil in a suitable resonant electronic circuit. If an oscillating radio frequency (r.f.) magnetic field is applied along the x-axis perpendicular to the static magnetic field in the laboratory frame, the interaction of a nuclear spin with this field can be expressed by the Hamiltonian:

$$\hat{H}_{rf} = -2\gamma\eta B_1 \cos(\omega_{rf} t + \varphi)\hat{I}_x. \tag{3.11}$$

Transitions between the spin states will occur when the r.f. field oscillates close to the resonance frequency ω_0 which matches the Zeeman energy splitting. The amplitude of the oscillating fields is substantially smaller than that of the static magnetic field (thousands of times smaller), so H_{rf} acts as a perturbation on the spin system, which does not change the energy levels but only induces transitions between them.

Now the motion of the spin becomes very complicated in the magnetic field during the r.f. pulse. On the one hand, the spin precesses around the B_0 field with the Larmor frequency, and on the other hand, it nutates under the action of the r.f. field. At this moment it is useful to introduce the "rotating frame", which rotates with frequency ω_{rf} around the z-axis of the applied static magnetic field. In this rotating frame, the r.f. Hamiltonian is time-independent. At the same time, transformation into the rotating frame introduces a fictitious magnetic field $\vec{B}_f = -\omega_{rf}/\gamma$, which is opposite to the direction of the static magnetic field $\vec{B}_0$. The effective Hamiltonian in the rotating frame becomes:

$$\begin{aligned}\hat{H}_{eff} &= -\gamma\eta(\vec{B}_0 - \vec{B}_f)\hat{I}_z + \gamma\eta\vec{B}_1\hat{I}_x \\ &= (\omega_0 - \omega_{rf})\eta\hat{I}_z - \omega_{rf}\eta\hat{I}_x\end{aligned} \tag{3.12}$$

where $(\omega_0-\omega_{rf})$ is defined as the resonance offset, when $\omega_0=\omega_{rf}$ the irradiation is said on resonance.

In multiple-quantum experiments on-resonance $90°_{\varphi}$ ($\varphi=\pm x, \pm y$) pulses with different phases are used, where the duration of the irradiation of the pulse t_{pulse} is adjusted to satisfy the following condition:

$$\frac{\pi}{2} = \gamma B_1 t_{pulse}. \tag{3.13}$$

A $90°_x$ pulse applied on x axis in the rotating frame rotates the magnetization by 90° from the +z direction into the -y axis according to a right-handed rotation.

3.1.3 The chemical shielding interaction

The chemical shift, or shielding, interaction arises from the coupling of the spins with local fields generated by the interplay of B_0 and the electron cloud surrounding a nucleus. The electron cloud precesses about the external magnetic field. Thus, additional magnetic fields are induced. The induced field normally opposes the external magnetic field for diamagnetic materials, so the nucleus experiences the superposition of the external magnetic field and the induced internal fields. The nuclear resonance frequency is thus shifted from the external magnetic field value. Usually the chemical shift, relative to a reference substance, is expressed in ppm (parts per million) of the Larmor frequency. It is customary to represent the spectrum as follows: the frequency increases from right to left along an horizontal axis, and resonances with large ppm values are said to be “downfield shifted” or “least shielded”. Otherwise, they are said to be “upfield shifted” or “most shielded”.

Because the electronic environment is usually different for different directions in the molecule, the nucleus experiences a different shielding, and hence has a different chemical shift, in different directions. The chemical shift can be expressed by a second-rank tensor:

$$\hat{H}_{cs} = \gamma \hbar \vec{I} \cdot \vec{\vec{\sigma}} \cdot \vec{B}_0, \tag{3.14}$$

where $\vec{\vec{\sigma}}$ is the chemical shielding tensor. The chemical shift interaction is an anisotropic interaction, which results from the fact that the electronic distribution in molecules is not spherical symmetric. In the principal axis system (PAS) fixed in the molecule (see Figure 3.2), the chemical shift tensor is diagonal. The secular part of $\hat{H}_{CS}$, or the projection of the chemical shift tensor along the z axis, can be expressed in terms of the principal values of σ, σ_{ii} (here i=1, 2 ,3), and the respective direction cosines with respect to $\vec{B}_0$:

$$\sigma_{zz} = \sigma_{11}\sin^2\theta\cos^2\phi + \sigma_{22}\sin^2\theta\sin^2\phi + \sigma_{33}\cos^2\theta, \tag{3.15}$$

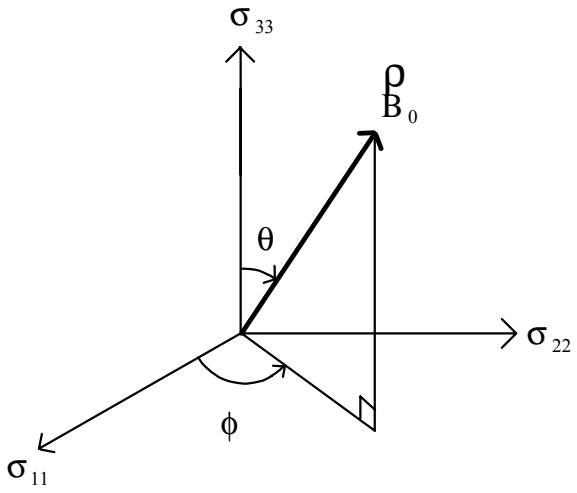

Figure 3.2*. The relationship between the external magnetic field and principal axis system.*

where σ_{11}, σ_{22} and σ_{33} are the principal values of the tensor in three mutually perpendicular directions in the molecule. The secular component of the chemical shift Hamiltonian has the form:

$$\hat{H}_{cs} = -\gamma\eta\sigma_{zz}B_0\hat{I}_z = \sigma_{zz}\omega_0\eta\hat{I}_z . \tag{3.16}$$

For a single crystal, one can obtain a single, relatively narrow signal. The position of this signal depends on the orientation of the principal axes of σ, and hence of the crystal, with respect to $\vec{B}_0$. Through a study of the chemical shift as a function of orientation of a single crystal, one can map out the shift anisotropy and its orientation in the molecule. For a powder sample, all orientations of the principal axes with respect to the magnetic field are present, usually a typical powder pattern is obtained. Fig. 3.3(a) shows a generalized chemical shift anisotropy (CSA) powder pattern for a common nonsymmetrical case, and Fig. 3.3(b) depicts the theoretical line shape for a powder solid when $\sigma_{11} = \sigma_{22} \equiv \sigma_{\perp} \neq \sigma_{33} \equiv \sigma_{//}$, where $\sigma_{//}$ and

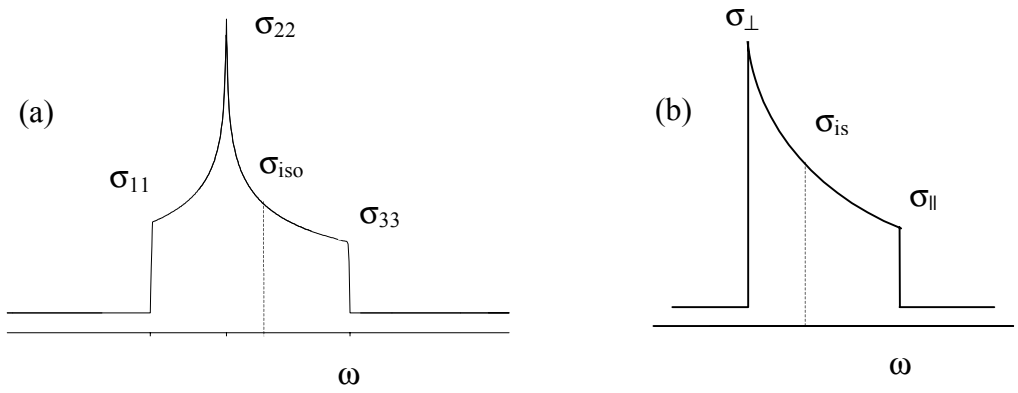

Figure 3.3*. Schematic representation of chemical shift tensor powder patter for an axially asymmetric (a) and axially symmetric (b) tensor. The isotropic chemical shift values σ_{iso} are indicated as dashed lines.*

$\sigma_{\perp}$ represent B_0 is aligned $\parallel$ and $\perp$ to the principle axes, respectively. Molecular motion will narrow the chemical shift tensor, by partial averaging, and the resulting powder pattern will then contain information concerning the axis and angular range of the motion. In a solution, the rapid, essentially isotropic motion of the molecule or molecular segments averages the shielding tensor to its isotropic value σ_{iso}:

$$\sigma_{iso} = \frac{1}{3} Tr\bar{\sigma} = \frac{1}{3}(\sigma_{11} + \sigma_{22} + \sigma_{33}). \tag{3.17}$$

From above we can see that the chemical shift is a direct consequence of the electronic structure, so the chemical shift tensor gives information on the structure of the molecule, and therefore, can serve to verify calculations of the electronic structure of molecules. In addition it potentially provides motional and orientation information of molecules. The chemical shift tensor powder pattern contributes significantly to the line broadening of solid state NMR spectra, and this effect often obscures the structural information available from the isotropic chemical shifts. This line broadening of the resonances in the solid state can be eliminated by high speed sample spinning at the magic angle (see later section). Magic angle spinning (MAS) reduces the anisotropic chemical shift tensor powder pattern to the isotropic average.

Another important feature is that conformational effects play an important role in the chemical shifts in solids. Structure information can be extracted from the so-called γ-gauche effect for methylene groups in aliphatics structures, e.g., the carbon atoms at the γ position from the $^{13}CH_2$ group under consideration be in a trans or gauche conformation relative to the ^{13}C-α bond. For a gauche conformation of ^{13}C-γ, the signal of ^{13}C-α is shifted upfield by about 5 ppm compared to the trans conformation of ^{13}C-γ. Packing effects, in contrast, are found empirically to amount to only 1 ppm in aliphatics.

3.1.4 The direct dipole-dipole interaction

If we consider two dipolar coupled spins i and j, one nuclear spin will experience a local dipolar field from the other. The magnitude of this dipole-dipole interaction depends on the distance between the two spins and the direction of the internuclear vector with respect to the external magnetic field as schematically depicted in Figure 3.4. The dipole-dipole Hamiltonian between the two spins i and j can be expressed as follows:

$$\hat{H}_{D,ij} = \frac{\vec{\mu}_i \cdot \vec{\mu}_j}{r_{ij}^3} - \frac{3(\vec{\mu}_i \cdot \vec{r}_{ij})(\vec{\mu}_j \cdot \vec{r}_{ij})}{r_{ij}^5}$$

$$= \frac{\gamma_i \gamma_j \eta^2}{r_{ij}^3}\left(\hat{I}_i \cdot \hat{I}_j - 3\frac{(\hat{I}_i \cdot \vec{r}_{ij})(\hat{I}_j \cdot \vec{r}_{ij})}{r_{ij}^2}\right), \qquad (3.18)$$

where $r_{ij} = |\vec{r}_{ij}|$ is the vector joining the two spins, γ_i and γ_j are nuclear gyromagnetic ratios. The general expression of (3.18) has the form:

$$\hat{H}_D = \hat{I}_i \cdot \vec{\vec{D}} \cdot \hat{I}_j = \frac{\gamma_i \gamma_j \eta^2}{r_{ij}^3}(\hat{I}_{xi}, \hat{I}_{yi}, \hat{I}_{zi}) \times$$

$$\begin{pmatrix} (1-3\cdot\Delta x_{ij}^2)/r_{ij}^2 & -3\cdot\Delta x_{ij}\cdot\Delta y_{ij}/r_{ij}^2 & -3\cdot\Delta x_{ij}\cdot\Delta z_{ij}/r_{ij}^2 \\ -3\cdot\Delta x_{ij}\cdot\Delta y_{ij}/r_{ij}^2 & (1-3\cdot\Delta y_j^2)/r_{ij}^2 & -3\cdot\Delta y_{ij}\cdot\Delta z_j/r_{ij}^2 \\ -3\cdot\Delta x_{ij}\cdot\Delta z_{ij}/r_{ij}^2 & -3\cdot\Delta y_{ij}\cdot\Delta z_{ij}/r_{ij}^2 & (1-3\cdot\Delta z_{ij}^2)/r_{ij}^2 \end{pmatrix} \begin{pmatrix} \hat{I}_{xj} \\ \hat{I}_{yj} \\ \hat{I}_{zj} \end{pmatrix}, \qquad (3.19)$$

where $\Delta x_{ij} = x_j - x_i$, $\Delta y_{ij} = y_j - y_i$, and $\Delta z_{ij} = z_j - z_i$. $\vec{\vec{D}}$ is the dipolar coupling tensor, it is traceless and symmetric. Through transforming the Cartesian coordinate (x, y, z) to the corresponding spherical coordinate (r, θ, ϕ) (see Figure 3.4) and using the raising and

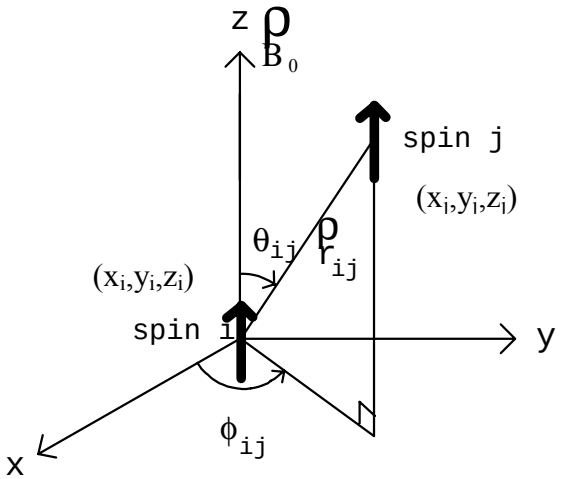

Figure 3.4. *Schematically representation of a coupled spin pair in a magnetic field* $\vec{B}_0$.

lowering operators $\hat{I}_+$ and $\hat{I}_-$ to express $\hat{I}_x$ and $\hat{I}_y$ in eq.(3.19), the dipolar Hamiltonian can be written in a convenient "dipolar alphabet" form:

$$\hat{H}_D = \frac{\gamma_i \gamma_j \eta^2}{r_{ij}^3}(\hat{A} + \hat{B} + \hat{C} + \hat{D} + \hat{E} + \hat{F}), \qquad (3.20)$$

where

$$\hat{A} = (1 - 3\cos^2\theta_{ij})\hat{I}_{zi}\hat{I}_{zj},$$

$$\hat{B} = -\frac{1}{4}\left(1-3\cos^2\theta_{ij}\right)\left[\hat{I}_{+i}\hat{I}_{-j} + \hat{I}_{-i}\hat{I}_{+j}\right],$$

$$\hat{C} = -\frac{3}{2}\sin\theta_{ij}\cos\theta_{ij}e^{-i\phi_{ij}}\left[\hat{I}_{zi}\hat{I}_{+j} + \hat{I}_{+i}\hat{I}_{zj}\right],$$

$$\hat{D} = -\frac{3}{2}\sin\theta_{ij}\cos\theta_{ij}e^{i\phi_{ij}}\left[\hat{I}_{zi}\hat{I}_{-j} + \hat{I}_{-i}\hat{I}_{zj}\right], \qquad (3.21)$$

$$\hat{E} = -\frac{3}{4}\sin^2\theta_{ij}e^{-i2\phi_{ij}}\left[\hat{I}_{+i}\hat{I}_{+j}\right],$$

$$\hat{F} = -\frac{3}{4}\sin^2\theta_{ij}e^{i2\phi_{ij}}\left[\hat{I}_{-i}\hat{I}_{-j}\right].$$

This "dipolar alphabet" form is quite useful in describing the effect of the dipolar coupling, because the terms $\hat{A}$ to $\hat{F}$ have a different effect on the eigenfunctions of the Zeeman Hamiltonian. There are two distinguishable cases: homonuclear coupling (coupling between the same type of nuclei) and heteronuclear coupling (coupling between different types of nuclei). In the case of homonuclear coupling, because the terms $\hat{A}$ and $\hat{B}$ commute with the $\hat{I}_z$ operator of the Zeeman term, they form the secular part of the Hamiltonian. The terms $\hat{C}$, $\hat{D}$, $\hat{E}$ and $\hat{F}$ form the non-secular part. Only the secular part, which is the cause of the shifting and splitting of the Zeeman energy levels, is taken into account, the non-secular part is involved in the spin-lattice relaxation process of spins. It is more usual to write the secular part of the dipolar interaction as:

$$\hat{H}_D = -2D_{ij}\left[\hat{I}_{zi}\hat{I}_{zj} - \frac{1}{4}\left(\hat{I}_{+i}\hat{I}_{-j} + \hat{I}_{-i}\hat{I}_{+j}\right)\right] = -D_{ij}\left(3\hat{I}_{zi}\hat{I}_{zj} - \hat{I}_i\cdot\hat{I}_j\right), \qquad (3.22)$$

with the coupling constant:

$$D_{ij} = -\frac{\gamma_i\gamma_j\eta^2}{2r_{ij}^{\ 3}}\left(1-3\cos^2\theta_{ij}\right). \qquad (3.23)$$

The first spin term $I_{zi}I_{zj}$ in eq.(3.22) represents the interaction of one spin with the z-component of the local field generated by the other spin, which causes line broadening. Considering an isolated dipolar coupled two spins-1/2 pair i and j, the resonance line of spin i will be split into a doublet with a separation of $1.5D_{ij}$ due to the two possible values of the static local field. In a powder sample all spins are coupled together and each spin feels a superposition of many local magnetic fields due to the coupling to its neighbours, and each local field resulted from the neighbouring coupled spin gives a contribution to the resonance frequencies of the observed spin. Since the size and direction of the local field varies from

spin to spin due to the distance and angle dependence, the dipolar coupling causes a distribution of resonance frequencies and leads to very broad lines in solid, for example, up to 70 kHz for protons.

The second term in eq.(3.22) is known as the flip-flop term, which induces flip-flop transitions. The flip-flop process is energy conserving, i.e. the energy required to flip spin i (down to up) matches the energy needed to flop spin j (up to down). In particular, for a rigid-lattice system, this term causes mutual energy-conserving flip-flop transitions which can be described as a diffusion process.

In the case of heteronuclear interaction, only the $\hat{A}$ term commutes with the $\hat{I}_z$ operator of the Zeeman Hamiltonian. Usually the abundant spins, such as ^{1}H and ^{19}F are referred as the I-spin, while the rare spins, such as ^{13}C and ^{29}Si are designed as the S-spin. The secular part of the heteronuclear dipolar Hamiltonian is given by:

$$\hat{H}_D^{IS} = -\frac{\gamma_I \gamma_S \eta^2}{r_{IS}^3}(3\cos^2\theta_{IS} - 1)\hat{I}_z\hat{S}_z . \qquad (3.24)$$

Now let us consider dipolar coupled isolated C-H pairs in a powder. For each angle θ between the internuclear vector and the external magnetic field, there is a corresponding dipolar coupling containing the term $(3\cos^2\theta\text{-}1)$. Each spin in the presence of the local field of the other gives rise to a distribution of lines with the same qualitative shape as that of the chemical shift in an axially symmetric molecule. This gives a characteristic powder pattern, the Pake doublet, with a separation of D_{CH} as shown in Figure 3.5. The angle θ_m corresponding to the point where the two curves cross, is called the "magic angle" and is equal to 54.7°, as required by the condition $(3\cos^2\theta\text{-}1)=0$.

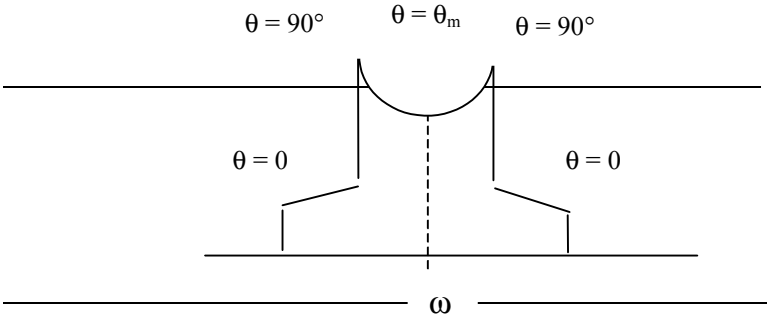

Figure 3.5. *Pake doublet pattern expected for isolated C-H pairs distributed at all angles as in a powder.*

The dipolar tensor is an irreducible second-rank tensor, the isotropic value of the dipolar coupling tensor is zero. Since the term D_{ij} depends on θ_{ij} and r_{ij} as seen in eq.(3.23), it supplies a wealth of structural information: for example, dipolar couplings permit the measurement of distances, either via the distance-dependent strength of the coupling of spin pairs or through

the diffusive transfer of magnetization (spin diffusion). The latter allows the determination of domain sizes in heterogeneous samples. The dipole-dipole interaction can also give structure information such as spin connectivities, spin distributions and polarization transfer. The dipolar interaction plays a very important role in this thesis because multiple-quantum coherences are created by this kind of through space interaction.

3.1.5 Summary

We know from the above discussion that for most experiments in solid-state NMR, the internal interactions of multispin systems, such as the dipole-dipole interactions and the anisotropy of the chemical shift, are usually causes of line broadening, so manipulating and modifying the nuclear spin Hamiltonian is necessary to achieve liquid-like high-resolution spectra in solid-state NMR. In practice, the usual tools for manipulation the spin Hamiltonian are time-dependent perturbations. These include mechanical sample spinning and multiple-pulse sequences for coherent averaging of the couplings in "real space" and in "spin space", respectively. In the case of magic angle sample spinning, the inhomogeneous and anisotropic interactions, such as magnetic field inhomogeneities, dipolar interactions and anisotropic chemical shifts, can be eliminated by sufficiently rapid spinning. Multiple pulse sequences or trains of r.f. pulses are found to be very useful for the suppression or scaling of selected interactions. In both cases the effect of a periodic perturbation can be described by a modified time-independent Hamiltonian. This will be treated in the following sections.

3.2. Average Hamiltonian theory

Average Hamiltonian theory was initially introduced by Haeberlen and Waugh[9,11] to interpret the effect of cyclic multiple-pulse sequences. The basic idea of average Hamiltonian theory is that it uses a time-independent average Hamiltonian, $\overline{H}$, which causes an "average" motion of the spin system, to describe the effects of a time-dependent perturbation applied to the spin system. The following conditions have to be fulfilled: (a) the sequence of r.f. pulses is cyclic; (b) the Hamiltonian H(t) is periodic; (c) the NMR observation is stroboscopic and synchronized with the period of the Hamiltonian; (d) the time interval over which the Hamiltonian acts between observations is short compared to T_2, characterizing the

homogeneous broadening. The average Hamiltonian[5] may be expressed by an exact calculation or by an expansion which is known as Baker-Campbell-Hausdorff expansion (or Magnus expansion).

From the previous chapter we know that at any time the expectation value of any observable can be obtained from the trace of the scalar product of the observable operator and the density operator (see eq. (2.21)). The spin density operator can be obtained from the Liouville equation:

$$\frac{d\hat{\rho}(t)}{dt} = -i[\hat{H}, \hat{\rho}(t)], \tag{3.25}$$

with the solution:

$$\hat{\rho}(t_c) = \hat{U}(t_c)\hat{\rho}(0)\hat{U}(t_c)^{-1}. \tag{3.26}$$

The propagator $\hat{U}(t_c)$ in the time interval (0, t_c) can be solved according to the properties of the Hamiltonian:

(1) If the Hamiltonian is time-independent, for example, $\hat{H}$ equal to the internal Hamiltonian $\hat{H}_{\text{int}}$ of the spin system, then the propagator can be expressed as:

$$\hat{U}(t_c) = \exp(-i\hat{H}t_c) = \exp(-i\hat{H}_{\text{int}}t_c). \tag{3.27}$$

(2) If the Hamiltonian $\hat{H}$ is piecewise constant in successive time intervals $\hat{H}(t) = \hat{H}_k$ for ($\tau_1 + \tau_2 + ... + \tau_{k-1} < t < (\tau_1 + \tau_2 + ... + \tau_k)$, then the propagator $U(t_c)$ can be represented:

$$\hat{U}(t_c) = \exp\{-i\hat{H}_n\tau_n\}...\exp\{-i\hat{H}_1\tau_1\} = T\exp\{-i\sum_k^n \hat{H}_k\tau_k\} = \exp\{-i\hat{\bar{H}}t_c\}, \tag{3.28}$$

where T is the Dyson time-ordering operator and $t_c = \sum_{k=1}^{n}\tau_k$. Based on the Baker-Campbell-Hausdorff relation:

$$e^B e^A = \exp\{A + B + \frac{1}{2}[B, A] + \frac{1}{12}[B,[B, A]] + [[B, A], A+...\}, \tag{3.29}$$

the average Hamiltonian for a piecewise constant Hamiltonian changing (n-1) times in the time interval $t_c=\tau_1+\tau_2+\tau_3+...+\tau_n$, H={$H_1$, τ_1; H_2, τ_2; H_3, $\tau_{3,...}$}, can be expressed:

$$\hat{\bar{H}}(t_c) = \hat{\bar{H}}^{(0)} + \hat{\bar{H}}^{(1)} + \hat{\bar{H}}^{(2)} + ... \tag{3.30}$$

with

$$\hat{\bar{H}}^{(0)} = \frac{1}{t_c}\{\hat{H}_1\tau_1 + \hat{H}_2\tau_2 + ... + \hat{H}_n\tau_n\}, \tag{3.31a}$$

$$\bar{\hat{H}}^{(1)} = -\frac{i}{2t_c}\{[\hat{H}_2\tau_2, \hat{H}_1\tau_1] + [\hat{H}_3\tau_3, \hat{H}_1\tau_1] + [\hat{H}_3\tau_3, \hat{H}_2\tau_2] + ...\}, \quad (3.31b)$$

$$\bar{\hat{H}}^{(2)} = -\frac{1}{6t_c}\{[\hat{H}_3\tau_3, [\hat{H}_2\tau_2, \hat{H}_1\tau_1]] + [[\hat{H}_3\tau_3, \hat{H}_2\tau_2], \hat{H}_1\tau_1]$$

$$+\frac{1}{2}[\hat{H}_2\tau_2, [\hat{H}_2\tau_2, \hat{H}_1\tau_1]] + \frac{1}{2}[[\hat{H}_2\tau_2, \hat{H}_1\tau_1], \hat{H}_1\tau_1] + ...\}. \quad (3.31c)$$

(3) If the Hamiltonian continuously changes, the corresponding propagator becomes:

$$\hat{U}(t_c) = T\exp\{-i\int_0^{t_c}\hat{H}(\tau)d\tau\} = \exp\{-i\bar{\hat{H}}t_c\}. \quad (3.32)$$

Using the Magnus expansion, the average Hamilonian can be expanded into the following form:

$$\bar{H} = \int_0^{t_c}\hat{H}(t')dt' = \sum_{k=0}^{\infty}\bar{\hat{H}}^{(k)}, \quad (3.33)$$

where

$$\bar{\hat{H}}^{(0)} = \frac{1}{t_c}\int_0^{t_c}\hat{H}(t)dt, \quad (3.34a)$$

$$\bar{\hat{H}}^{(1)} = \frac{-i}{2t_c}\int_0^{t_c}dt_2\int_0^{t_2}dt_1\left[\hat{H}(t_2), \hat{H}(t_1)\right], \quad (3.34b)$$

$$\bar{\hat{H}}^{(2)} = \frac{-1}{6t_c}\int_0^{t_c}dt_3\int_0^{t_3}dt_2\int_0^{t_2}dt_1\left\{\left[\hat{H}(t_3), \left[\hat{H}(t_2), \hat{H}(t_1)\right]\right] + \left[\hat{H}(t_1), \left[\hat{H}(t_2), \hat{H}(t_3)\right]\right]\right\}. \quad (3.34c)$$

These are the basic forms of the average Hamiltonian theory.

The expressions in equations (3.31a) and (3.34a) for the average Hamiltonian remain valid, if the time modulation of the Hamiltonian is so fast that:

$$\hat{H}_k\tau_k << 1, \ \sum_k \hat{H}_k\tau_k << 1. \quad (3.35)$$

If these conditions are fulfilled, we may say that the spin system appears to evolve during the time interval t_c under the effect of the zeroth-order average Hamiltonian. If the conditions in equation (3.35) are not fulfilled, higher order terms $\hat{H}^{(1)}$, $\hat{H}^{(2)}$, ... , must be taken into account in the development of the average Hamiltonian.

3.2.1 Averaging by time-dependent perturbations

Based on the above descriptions, let us treat a general case in which the Hamiltonian is periodically modified by time-dependent perturbations. Consider the internal Hamiltonian H_{int} of the spin-1/2 system modified by introduction of a time dependent perturbation $\hat{H}_1(t)$ such as in the multiple-pulse experiments. In this case, the total Hamiltonian of the system can be divided into a time independent term $\hat{H}_{\text{int}}$ and a time dependent term $\hat{H}_1(t)$:

$$\hat{H}(t) = \hat{H}_{\text{int}} + \hat{H}_1(t). \tag{3.36}$$

The corresponding propagator $\hat{U}(t)$ can be written as:

$$\hat{U}(t) = T\exp\{-i\int_0^t (\hat{H}_{\text{int}} + \hat{H}_1(t))dt_1\}. \tag{3.37}$$

Now we can separate the effects of H_{int} and $H_1(t)$ and divide the propagator into two factors:

$$\hat{U}(t) = \hat{U}_1(t)\hat{U}_0(t), \tag{3.38}$$

where

$$\hat{U}_1(t_c) = T\exp\{-i\int_0^t \hat{H}_1(t_1)dt_1\}\ , \tag{3.39}$$

and

$$\hat{U}_0(t_c) = T\exp\{-i\int_0^t \hat{\tilde{H}}_{\text{int}}(t_1)dt_1\}. \tag{3.40}$$

$\hat{U}_1(t)$ describes the direct effect of the perturbation $H_1(t)$. $\hat{\tilde{H}}_{\text{int}}(t)$ is the time dependent Hamiltonian in the toggling frame, which is a new frame of reference (or interaction representation) transformed from the rotating frame and in which the radiofrefrequency Hamiltonian is absent. It can be determined by the following transformation:

$$\hat{\tilde{H}}_{\text{int}}(t) = \hat{U}_1^{-1}(t)\hat{H}_{\text{int}}\hat{U}_1(t). \tag{3.41}$$

When the perturbation $\hat{H}_1(t)$ is periodic with period t_c and cyclic as well, this means that for the former condition, the following relation is satisfied: $\hat{H}_1(t+nt_c) = \hat{H}_1(t)$, for n=0, 1, 2, ..., and for the latter condition gives the result: $\hat{U}_1(t_c)$=1. Under these conditions, it appears that $\hat{H}_1(t)$ has no direct effect in the course of one full cycle and $\hat{\tilde{H}}_{\text{int}}(t)$ becomes also periodic. This gives the simple propagator $\hat{U}(t_c) = \hat{U}_0(t_c)$ for one cycle and $\hat{U}(nt_c) = \hat{U}(t_c)^n$ for n cycles. In analogy to eq (3.31), $\hat{U}_0(t_c)$ can be expressed as:

$$\hat{U}_0(t_c) = \exp\{-i\hat{\bar{H}}t_c\}. \tag{3.42}$$

Using the Magnus expansion, the average Hamiltonian can be written as follows:

$$\bar{\hat{H}} = \int_0^{t_c} \hat{H}(t')dt' = \sum_{k=0}^{\infty} \bar{\hat{H}}^{(k)} \tag{3.43}$$

where

$$\bar{\hat{H}}^{(0)} = \frac{1}{t_c}\int_0^{t_c} \hat{\tilde{H}}_{\text{int}}(t)dt \tag{3.44a}$$

$$\bar{\hat{H}}^{(1)} = \frac{-i}{2t_c}\int_0^{t_c} dt_2 \int_0^{t_2} dt_1 \left[\hat{\tilde{H}}_{\text{int}}(t_2), \hat{\tilde{H}}_{\text{int}}(t_1)\right] \tag{3.44b}$$

$$\bar{\hat{H}}^{(2)} = \frac{-1}{6t_c}\int_0^{t_c} dt_3 \int_0^{t_3} dt_2 \int_0^{t_2} dt_1 \left\{\left[\hat{\tilde{H}}_{\text{int}}(t_3), \left[\hat{\tilde{H}}_{\text{int}}(t_2), \hat{\tilde{H}}_{\text{int}}(t_1)\right]\right]\right.$$
$$\left. + \left[\hat{\tilde{H}}_{\text{int}}(t_1), \left[\hat{\tilde{H}}_{\text{int}}(t_2), \hat{\tilde{H}}_{\text{int}}(t_3)\right]\right]\right\} \tag{3.44c}$$

The average Hamiltonian of zero order has a particular simple form, which is just the time average of the toggling frame Hamiltonian $\hat{\tilde{H}}_{\text{int}}(t)$ given by eq.(3.39) and (3.41). Usually the higher order terms contain undesired cross-terms between the various terms of the Hamiltonian, so, in most cases, the removal of certain higher order terms $\bar{\hat{H}}_{\text{int}}^{(1)}$, ... is necessary to achieve an efficient suppression of the unwanted interactions.

The "average Hamiltonian theory" developed by Haeberlen and Waugh facilitates the analysis of the action of pulse sequences. The effect of the local fields can be calculated to zero order as a simple average in an interaction representation, which can be visualised as a transformation into a frame "toggling" with the pulses. As an example we discuss the multiple-pulse sequence for homonuclear decoupling below.

3.2.2 Application of average Hamiltonian theory to the Multiple-pulse sequences

In cases of strong (> 25 kHz) homonuclear dipole-dipole interactions MAS spinning rates ν_R are too small for efficient decoupling. Multiple-pulse techniques can be employed in this case, which, depending on the pulse sequence, selectively average different interactions. Multipulse sequences[1,8,9,12] are mainly used for homonuclear decoupling of protons and consist of specifically designed cycles of several pulses, possibly separated by windows without

irradiation. They are repeated many times with stroboscopic observation of the magnetization in certain windows.

Homonuclear decoupling by multiple-pulse irradiation can be regarded as "MAS in spin space". The pulses produce rotations on the spin operators, so the dipolar Hamiltonian is rotated around a (1, 1, 1) axis, which makes the "magic angle" with the z axis. Subject to this motion in spin space, the average of the dipolar couplings produces the "magic zero" equation:

$$\underbrace{(3\hat{I}_{xi}\hat{I}_{xj}-\hat{\vec{I}}_i\cdot\hat{\vec{I}}_j)}_{\hat{H}^{II}_{xx}}+\underbrace{(3\hat{I}_{yi}\hat{I}_{yj}-\hat{\vec{I}}_i\cdot\hat{\vec{I}}_j)}_{\hat{H}^{II}_{yy}}+\underbrace{(3\hat{I}_{zi}\hat{I}_{zj}-\hat{\vec{I}}_i\cdot\hat{\vec{I}}_j)}_{\hat{H}^{II}_{zz}}=0, \tag{3.45}$$

and is removed.

Now we deal with the famous WAHUHA (Waugh-Huber-Haeberlen) four-pulse sequence using the average Hamiltonian theory discussed in the previous section. It consists of two solid-echo pulse pairs, i.e., four 90° pulses separated by windows of duration τ and 2τ as represented in Figure 3.6. Here, for simplicity, we assume that the pulses are all ideal δ pulses, that is to say that the pulse widths are negligible. The density operator at the end of the sequence (cycle time 6τ) can be written as:

$$\hat{\rho}(t_0+6\tau)=\hat{U}(6\tau)\,\hat{\rho}(t_0)\,\hat{U}^{-1}(6\tau), \tag{3.46}$$

where the propagator $\hat{U}(6\tau)$ results from the sequence of the interactions (from right to left):

$$\hat{U}(6\tau)=\hat{E}_z\hat{P}_x\hat{E}_z\hat{P}_{-y}\hat{E}_z\hat{E}_z\hat{P}_y\hat{E}_z\hat{P}_{-x}\hat{E}_z. \tag{3.47}$$

The propagators of the r.f. pulses are designed by $\hat{P}_\alpha$ and those of the internal Hamiltonians by $\hat{E}_z=\exp(-i\hat{H}_z\tau)$. Inserting the relation $\hat{1}=\hat{P}_\alpha^{-1}\hat{P}_\alpha$ and using the identities:

$$\hat{P}_x\hat{E}_z\hat{P}_x^{-1}=\hat{P}_x e^{-i\hat{H}_z\tau}\hat{P}_x^{-1}=e^{-i\hat{P}_x\hat{H}_z\hat{P}_x^{-1}\tau}=e^{-i\hat{H}_y\tau}=\hat{E}_y, \tag{3.48}$$

equation (3.47) can be rewritten as follows:

$$\begin{aligned}\hat{U}(6\tau)&=\hat{L}_z\hat{P}_x\hat{L}_z(\hat{P}_x^{-1}\hat{P}_x)\hat{P}_{-y}\hat{L}_z\hat{L}_z(\hat{P}_{-y}^{-1}\hat{P}_{-y})\hat{P}_y\hat{L}_z(\hat{P}_y^{-1}\hat{P}_y)\hat{P}_{-x}\hat{L}_z(\hat{P}_{-x}^{-1}\hat{P}_{-x})\\&=\hat{L}_z(\hat{P}_x\hat{L}_z\hat{P}_x^{-1})\hat{P}_x(\hat{P}_{-y}\hat{L}_z\hat{L}_z\hat{P}_{-y}^{-1})\hat{P}_{-y}(\hat{P}_y\hat{L}_z\hat{P}_y^{-1})\hat{P}_y(\hat{P}_{-x}\hat{L}_z\hat{P}_{-x}^{-1})\hat{P}_{-x}\\&=\hat{E}_z\hat{E}_y\hat{P}_x\hat{E}_x\hat{E}_x\hat{P}_{-y}\hat{E}_{-x}\hat{P}_y\hat{E}_{-y}\hat{P}_{-x},\end{aligned} \tag{3.49}$$

repetition of this procedure finally yields:

$$\hat{U}(6\tau)=\hat{L}_z\hat{L}_y\hat{L}_x\hat{L}_x\hat{L}_y\hat{L}_z\hat{P}_x\hat{P}_{-y}\hat{P}_y\hat{P}_{-x}=\hat{E}_z\hat{E}_y\hat{E}_x\hat{E}_x\hat{E}_y\hat{E}_z. \tag{3.50}$$

The product of the pulses cancels itself ($\hat{P}_x\hat{P}_{-y}\hat{P}_y\hat{P}_{-x}=1$) on the bases of $\hat{P}_{-\alpha}=\hat{P}_{\alpha}^{-1}$, so WAHUHA is a cyclic sequence. On the condition of short τ, the equation (3.50) can be further simplified:

$$\hat{U}(6\tau)=\hat{E}_z\hat{E}_y\hat{E}_x\hat{E}_x\hat{E}_y\hat{E}_z=e^{-i\hat{H}_z\tau}e^{-i\hat{H}_y\tau}e^{-i\hat{H}_x\tau}e^{-i\hat{H}_x\tau}e^{-i\hat{H}_y\tau}e^{-i\hat{H}_z\tau}$$

$$\cong\hat{1}-i(\hat{H}_z+\hat{H}_y+2\hat{H}_x+\hat{H}_y+\hat{H}_z)\tau+Order(\tau^2)\cong e^{-i\hat{\bar{H}}\cdot 6\tau}. \qquad (3.51)$$

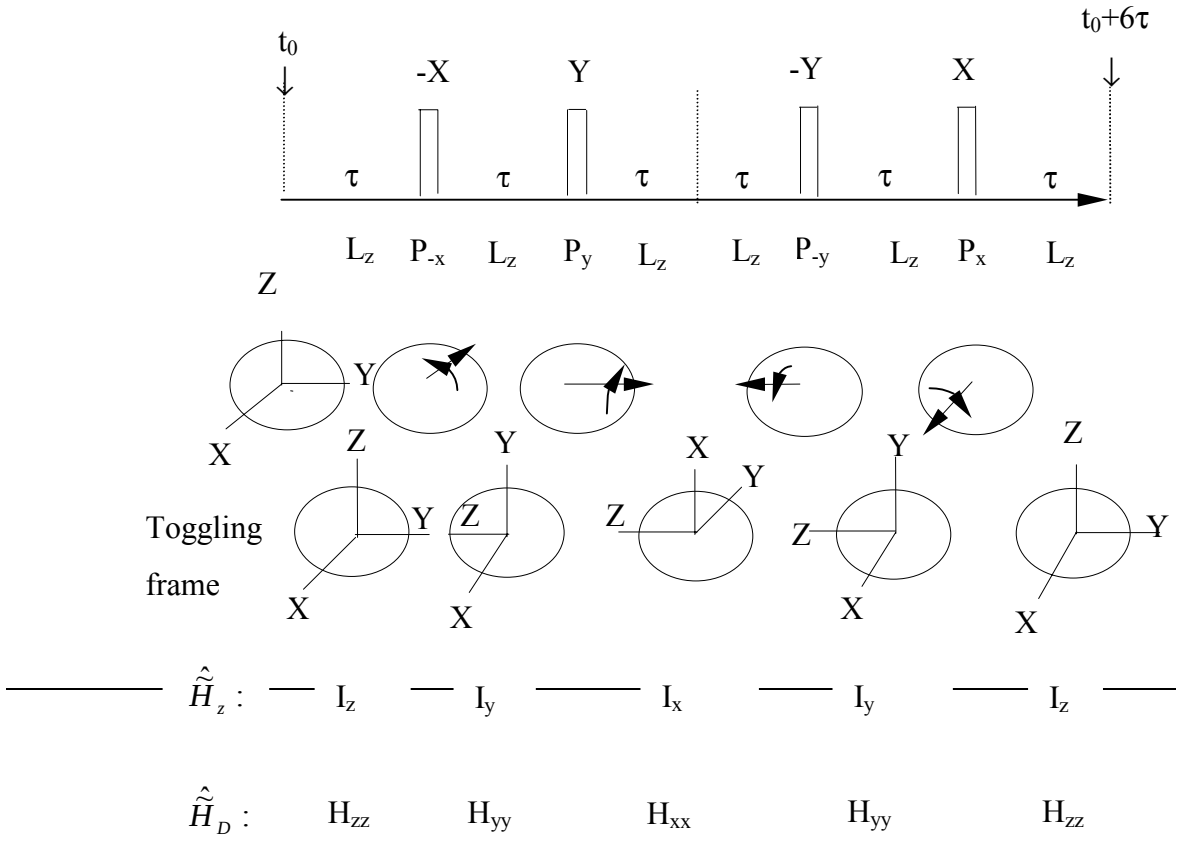

***Figure 3.6**. Schematic representation of the WAHUHA four-pulse sequence for homonuclear decoupling and the determination of the average Hamiltonian in the toggling frame. In each cycle of total length $t_c=6\tau$, the four pulses spaced by τ and 2τ lead to a rotated coordinate system, known as toggling frame. The average Zeeman Hamiltonian $\hat{\bar{\bar{H}}}_z$ and the dipolar Hamiltonian $\hat{\bar{\bar{H}}}_D$ are obtained by averaging the transformed Hamiltonian in the toggling frame.*

This illustrates that for sufficiently short pulse-spacings τ, the spins effectively evolve under the average Hamiltonian:

$$\hat{\bar{H}}=(\hat{H}_z+\hat{H}_y+2\hat{H}_x+\hat{H}_y+\hat{H}_z)/6$$

$$= -\frac{1}{3}\sum_j \omega_j (\hat{I}_{zj} + \hat{I}_{yj} + \hat{I}_{xj}) + \frac{1}{3}(\hat{H}^{II}_{zz} + \hat{H}^{II}_{yy} + \hat{H}^{II}_{xx}). \qquad (3.52)$$

The homonuclear dipolar terms yield the "magic zero" (see eq.(3.45)) and are averaged out by the multiple pulse sequence. This is valid for completely arbitrary spatial prefactors $\omega_{II} = (-\mu_0 \eta / 4\pi)(\gamma^2 / \gamma_{ij}^3) \times \frac{1}{2}\{3\cos^2(\theta_{ij}) - 1\}$. Thus, at observation windows n×6τ the propagators do not exhibit dipolar couplings up to terms of order τ^2. Stroboscopic detection at these times therefore produces a time signal that is to a first approximation modulated only by terms linear in $\vec{I}_{zj}$: the chemical shift, frequency offset, and the heteronuclear dipolar couplings, but they are all scaled by a factor $1/\sqrt{3}$.

In order to remove higher order terms and the effects of pulse imperfections, more effective multiple pulse sequences based on the WAHUHA four-pulses were developed, such as MREV-8, BR-24, the detailed descriptions are found in references[13, 14].

Above we gave a detailed calculation of the average Hamiltonian of the WAHUHA four-pulse sequence which is used for homonuclear decoupling, now we use another method to quickly and easily estimate the average Hamiltonian, here again we use the "toggling frame", which is flipped with the pulses in the rotating frame such that in this frame the pulses are transformed away, we write this as an interaction representation with the subscript T representing the operators seen from the toggling frame:

$$\vec{\rho}_T(t) := \vec{P}^{-1}(t)\,\vec{\rho}(t)\,\vec{P}(t), \qquad (3.53a)$$

$$\vec{H}(t) := \vec{P}^{-1}(t)\,\vec{H}_z\,\vec{P}(t) = (\vec{H}_{z,rot})_T, \qquad (3.53b)$$

$$\dot{\vec{\rho}}_T = -i[\vec{H}_T, \vec{\rho}_T], \qquad (3.53c)$$

$\vec{P}(t)$ expresses the product of the pulse propagators at time t. Due to $\hat{P}(n \times 6\tau) = \hat{1}$ for the WAHUHA four-pulse sequence, we have $\hat{\rho}(n \times 6\tau) = \hat{\rho}_T(n \times 6\tau)$. The magnetization detected in the observation windows, where the rotating frame and the toggling frame are coinciding, it looks as if the magnetization had evolved in the toggling frame under the action of $\vec{H}_T$, which is the Hamiltonian of the rotating frame seen from the toggling frame. Thus the average Hamitonian is the average of $\vec{H}_T$. With this in mind, we can readily determine the average Hamiltonian. First we flip the toggling frame with the pulses in the rotating frame (right-handed rotations). Then, check out the axis of the toggling frame (on which the z axis of the rotating frame is located) between the intervals of the pulses. This determines the direction $(\vec{I}_{\pm x}, \vec{I}_{\pm y}, \vec{I}_{\pm z})$ that $\vec{I}_{z,rot}$ has acquired in the toggling frame. Finally, the Hamiltonian $\vec{H}_T$ with

these rotated $\vec{I}_{z,rot}$ states are summed up for the average, taking into account the magic zero equation (3.45). For pulses of finite length, the duration of the pulses, where the toggling frame changes continuously, must also be included in the average.

Figure 3.6 shows that the pulses rotate the toggling frame sequentially through the indicated orientations. At the start and end of the cycle, rotating frame and toggling frame coincide, in between the toggling frame is toggled by the pulses applied in the rotating frame. The Hamiltonian as seen from the toggling frame is determined by reading the axis of the toggling frame that points along the z direction of the rotating frame. In this figure, the sequence of these axes is z,y,x,x,y,z. These are the states that are taken by $(\hat{I}_{z,rot})$ as seen from the toggling frame. The Zeeman Hamiltonian in the toggling frame can be determined by inspection, its average $\hat{\bar{H}}_Z^0$ corresponds to a new axis of quantization z'=(1,1,1) and involves a Larmor frequency scaled by a factor $1/\sqrt{3}$. The dipolar Hamiltonian goes through the three forms H_{xx}, H_{yy}, and H_{zz} in the toggling frame, and the resulting average Hamiltonian $\hat{\bar{H}}_D^0$ is zero.

3.3 Magic angle sample spinning

In addition to the multiple-pulse sequence, another fundamental line-narrowing technique is magic angle sample spinning (MAS). It was independently invented by Andrew[15,16] and Lowe[17]. Nowadays, it is a standard NMR method. The procedure of this technique consists of rotating the solid specimen about an axis inclined at the angle 54.7° to the direction of the magnetic field of the NMR magnet. Sufficiently rapid rotation about this particular axis removes most broadening interactions from the NMR spectra and gets the liquid-like high resolved NMR spectra.

Magic angle spinning may be used on its own, and may also be combined with other line-narrowing techniques. For example, it may be combined with multiple pulse sequence (CRAMPS) to obtain high resolution NMR spectra, especially of hydrogen and fluorine nuclei, in solids; it may be combined with cross-polarization and high power heteronuclear decoupling methods to obtain the high resolution spectra from ^{13}C, ^{29}Si and other nuclei of low abundance. Of most importance in this dissertation is the combination with multiple quantum NMR spectroscopy.

We know from the previous section that the line broadening in spin-1/2 solids mainly comes from the following anisotropic internal interactions: (1) Direct (homonuclear and heteronuclear) dipolar interactions, (2) Electron shielding interactions such as chemical shift. Below we will discuss the effect of MAS on each of them.

3.3.1 Magic angle spinning and dipolar interactions

The secular dipolar interaction Hamiltonian $\hat{H}_D$, for all nuclear pairs i and j is given:

$$\hat{H}_D = \sum_{i<j} \frac{1}{2} \gamma_i \gamma_j \eta^2 r_{ij}^{-3} (\hat{I}_i \hat{I}_j - 3\hat{I}_{zi}\hat{I}_{zj})(3\cos^2\theta_{ij} - 1), \qquad (3.54)$$

where γ_i and γ_j are the nuclear magnetogyric ratios, r_{ij} is the internuclear displacement, and θ_{ij} is the angle between r_{ij} and the Zeeman magnetic field B_0, which is along the z axis in the laboratory frame.

If a solid specimen is rotated uniformly with angular velocity ω_r about an axis inclined to B_0 at angle θ_m, every internuclear vector r_{ij} in the solid describes a conical figure about the rotation axis, retracing the same path during each complete circuit (see Figure 3.7(a)).

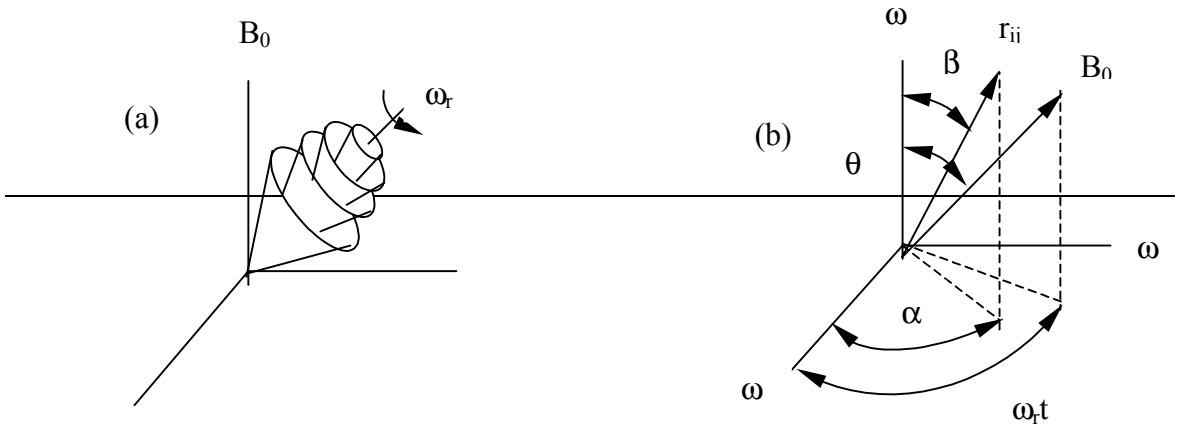

Figure 3.7. *Schematic representation of magic angle sample spinning. (a) The unique internuclear vector r_{ij} moves along a cone whose axis is always inclined at θ_m relative B_0. (b) r_{ij} and B_0 viewed in the rotor frame ω_x-ω_y-ω_z.*

Figure 3.7(b) shows the relationship between r_{ij} and B_0 in a frame of reference where z is along the rotation axis. The direction of r_{ij} is fixed in this rotor based frame with a polar angle β and an azimuthal angle α as shown. B_0 appears to precess about the z axis of the rotor frame, maintaining a fixed angle θ_m while sweeping out an azimuth angle $\omega_r t$. Hence the

instantaneous angle θ_{ij} between B_0 and r_{ij} becomes time dependent and the factor $(3\cos^2\theta_{ij}-1)$ in eq. (3.54) runs through a range of values that may be positive or negative. Its average value may be made zero by a judicious choice of θ_m. Expressing $\cos\theta_{ij}$ in terms of the other angles in the system can be obtained by the spherical law of cosines as:

$$\cos\theta_{ij}(t)=\cos\theta_m\cos\beta+\sin\theta_m\sin\beta\cos(\alpha-\omega_r t). \tag{3.55}$$

As $\theta_{ij}(t)$ becomes time dependent, so does the dipolar Hamiltonian:

$$\hat{H}_D=\sum_{i<j}\frac{1}{2}\gamma_i\gamma_j\eta^2 r_{ij}^{-3}(\hat{I}_i\hat{I}_j-3\hat{I}_{zi}\hat{I}_{zj})\{\frac{1}{2}(3\cos^2\theta_m-1)(3\cos^2\beta-1)$$

$$+\frac{3}{2}\sin 2\theta_m\sin 2\beta\cos(\alpha-\omega_r t)+\frac{3}{2}\sin^2\theta_m\sin^2\beta\cos 2(\alpha-\omega_r t)\}. \tag{3.56}$$

Note that the first term in the curly bracket is constant, which gives a reduced dipolar interaction and the narrowed spectrum, while the second and the third term are periodic in ω_r and $2\omega_r$ with zero mean value and give rise to rotational sidebands at multiples of ω_r.

From eq. (3.56), we can consider three special conditions: (1) when $\theta_m=0$, then the factor $(3\cos^2\theta_m-1)=1$, so the rotation about the B_0 has no effect on the dipolar interactions; (2) when $\theta_m=\pi/2$, $|(3\cos^2\theta_m-1)|=1/2$, that means that rotation about an axis normal to B_0 halves the spectral width; (3) when $\theta_m=\cos^{-1}(1/\sqrt{3})=54.7°$, $(3\cos^2\theta_m-1)=0$, so rotation about an axis making the magic angle 54.7° should reduce the dipolar broadening to zero.

Providing the magic angle spinning rate ω_r is larger than the linewidth resulting from the dipolar interaction, the dipolar broadening may be eliminated. In practice, however, it is usually not possible to spin faster than the dipolar linewidth and only magic angle spinning with very high frequencies (> 30 kHz) or in combination with other line narrowing techniques has any use for dipolar line narrowing.

3.3.2 Magic angle spinning and chemical shift

Now we consider the effect of MAS on the anisotropic chemical shift interactions. Unlike the dipolar interaction tensor which is traceless, the second-rank shift tensor is not traceless, the secular chemical shift can be written as:

$$\hat{H}_{CS}=\eta\gamma\hat{I}_z\sigma_{zz}B_0, \tag{3.57}$$

with $\sigma_{zz} = \sum_p \lambda_p^2 \sigma_{pp}$, where σ_{pp}(p=1, 2, 3) are the principal values of σ and λ_p are the direction cosines of the principal axes with respect to B_0. Since the isotropic average of each λ_p^2 is 1/3, the average value of σ_{zz} is its isotropic value σ_{iso}, i.e., $\bar{\sigma}_{zz} = \sigma_{iso} = \frac{1}{3} tr\sigma$.

When a rigid array of nuclei in a solid is rotated with angular velocity ω_r about an axis inclined at angle θ_m to B_0 and at angles χ_p to the principal axes of σ, the following relationship can be obtained:

$$\lambda_p = \cos\theta_m \cos\chi_p + \sin\theta_m \sin\chi_p \cos(\omega_r t + \psi_p) . \quad (3.58)$$

The chemical shift Hamiltonian $\hat{H}_{CS}$ in eq. (3.57) becomes time dependent and can be decomposed into its mean value and terms periodic in ω_r which generate spinning sidebands. So the average σ_{zz} for every nucleus can be written as follows:

$$\bar{\sigma}_{zz} = \frac{3}{2}\sigma_{iso} \sin^2\theta_m + \frac{1}{2}(3\cos^2\theta_m - 1)\sum_p \sigma_p \cos^2\chi_p . \quad (3.59)$$

Consequently, when θ_m is the magic angle, $\bar{\sigma}_{zz}$ reduces to the isotropic chemical shift value and the shift anisotropy is removed from the NMR spectrum. The time averaged shift in eq. (3.59) can be expressed in terms of the anisotropy parameter $\delta = \sigma_{33} - \sigma_{iso}$ and the asymmetry parameter $\eta = (\sigma_{22} - \sigma_{11})/\delta$:

$$\bar{\sigma}_{zz} = \sigma_{iso} + \frac{1}{2}(3\cos^2\theta_m - 1)\delta\{\frac{1}{2}(3\cos^2\theta - 1) + \frac{1}{2}\eta\sin^2\theta\cos 2\phi\} , \quad (3.60)$$

where θ and ϕ are polar angles relating the rotation axis to the principal axes of the shift tensor.

When the spinning rate is not fast enough to exceed the width of the static powder line shape, the situation becomes more complicated, the powder pattern breaks up into relatively narrow lines at the isotropic chemical shift (center band) and sidebands at multiples of ω_r from the center band.

3.4 Two-dimensional NMR spectroscopy

The course of a 2D experiment in the time domain can be partitioned into four time periods[1,5]: preparation (τ_p), evolution (t_1), mixing (τ_m), and detection (t_2), as depicted in Figure 3.8.

Generally, the changes of the density operator during the evolution period t_1, which is incremented in successive subexperiments, are detected indirectly as modulations of the nuclear signal that is observed during the detection period t_2. Here we briefly describe the basic features of the whole process: (1) In the preparation period τ_p, the spin system is prepared into a coherent non-equilibrium state by a single pulse or multi-pulse sequence in a fixed time interval τ_p; (2) In the course of the evolution period t_1, the density operator evolves freely under the action of the Hamiltonian $\hat{H}_e$ which may be modified by spin decoupling, sample spinning or multiple pulse sequences. This evolution determines the frequencies in the ω_1 dimension, which is obtained from a series of experiments with systematic incrementation of t_1; (3) The mixing period with a fixed time interval τ_m transforms the resulted density operator including single- or multiple-quantum coherences, into observable transverse magnetization; and (4) in the course of the detection period t_2, the desired signals are monitored. The system evolves under the influence of the Hamiltonian $\hat{H}_d$ which may be also modified.

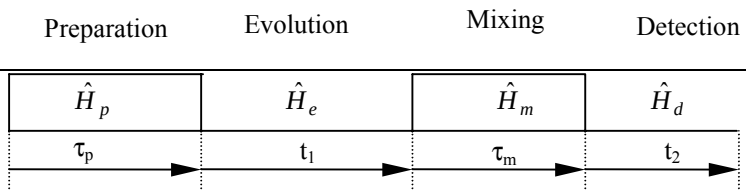

Figure 3.8. *Schematic representation of 2D time-domain NMR, the four distinct time intervals represent the preparation τ_p, evolution t_1, mixing τ_m and detection t_2 time intervals.*

3.5 ^{1}H -WISE (Wideline Separation) experiment

An example of a two-dimensional experiment is the WISE-experiment. The proton wide lines, which are induced by the homonuclear dipolar couplings, can be used to give qualitative information on molecular dynamics in materials. Rigid materials exhibit broad ^{1}H lines resulting from the static dipolar couplings, while often in amorphous polymer materials molecular mobility averages these couplings and produces narrower lines. These different lines representing the dynamics of the individual components of a polymer can be separated by using the ^{1}H WISE experiment via ^{13}C isotropic chemical shifts (see Figure 3.9)[4,18,19]. In this experiment, there is an incremented delay t_1 after the initial ^{1}H 90° pulse, the evolution or

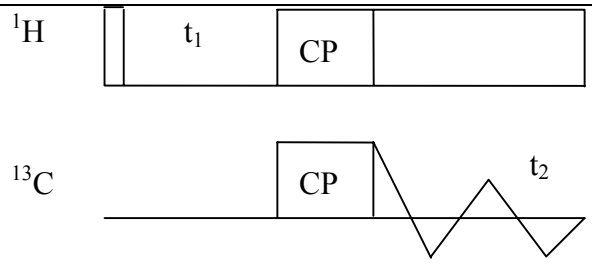

***Figure 3.9**. Schematic representation of pulse sequence for ^{1}H-WISE 2D NMR.*

decay of the proton magnetization can be detected because the ^{13}C signal produced by cross-polarization is modulated in amplitude by the change of the proton signal during t_1. Fourier transformations over t_1 and t_2 give ^{1}H wideline spectra in the ω_1-demension, while the corresponding ^{13}C isotropic chemical shifts are found in the ω_2-demension.

References

(1) M. Mehring, Principles of High Resolution NMR in Solids, **1983**, 2nd. Ed. Springer Verlage, New York.

(2) C. P. Slichter, Principles of Magnetic Resonance, **1992**, 3rd ed., Springer Verlage, Oxford.

(3) A. Abragam, Principles of Nuclear Magnetism, **1961**, Clarendon Press, Oxford.

(4) K. Schmidt-Rohr and H. W. Spiess, Multidimensional Solid State NMR and Polymers, **1994**, Academic Press, London.

(5) R. R. Ernst, G. Bodenhausen, and A. Wokaum, Principles of Nuclear Magnetic Resonance in One and Two Dimensions, Volume 14 of International Series of Monographs on Chemistry, **1990**, Oxford University Press, New York.

(6) M. Munowitz, Coherence and NMR, Wiley, New York, **1988**.

(7) E. Fukushima, S. B. W. Roeder, Experimental Pulse NMR: A Nuts and Bots Approach, Addison-Wesley Publishing Company, Inc., **1981**.

(8) B. C. Gerstein and C. R. Dybowski, Transient Techniques in NMR of Solids, An Introduction to Theory and Practice, Academic Press, **1985**.

(9) U. Haeberlen, High Resolution NMR in Solids, Academic, New York, **1976**.

(10) W. S. Veeman, PAON-course, Solid State NMR, June 14-16, **1989**, Berg en Dal.

(11) U. Haeberlen and J. S. Waugh, Phys. Rev. **175**, 453 (1968).

(12) A. Abragam, M. Goldmann, Nuclear magnetism: Order and disorder, Clarendon, Oxford, **1982**.

(13) W.-K. Rhim, D. D. Elleman, and R. W. Vaugh, J. Chem. Phys. **59**, 3740 (1973).

(14) D. P. Burum, and W. –K. Rhim, J. Chem. Phys.**71,** 944 (1979).

(15) E. R. Andrew, A. Bradbury, and R. G: Eades, Nature (London) **182**, 1659 (1958).

(16) E. R. Andrew, A. Bradbury, and R. G. Rades, Nature (London) **183**, 1802 (1959).

(17) I. J. Lowe, Phys. Rev. Lett. **2**, 285 (1959).

(18) K. Schmidt-Rohr, J. Clauss and H. W. Spiess, Macromolecules **25**, 3273 (1992).

(19) J. Clauss, K. Schmidt-Rohr, A. Adam, C. Boeffel and H. W. Spiess, Macromolecules **25**, 5208 (1992).

Chapter 4. The principles and methods of multiple-quantum (MQ) MAS NMR

4.1 Introduction

In strongly dipolar coupled spin-1/2 rigid solids, dipole-dipole interactions and their manipulation in multiple-quantum (MQ) NMR experiments induce multiple spin correlations. The temporal and spatial development of these collective modes give information about the structure and the dynamics of the spin system. There are many excellent reviews and books[1-12] which summarize work in this area. In this chapter, we examine the fundamental aspects of the growth of multiple-spin multiple-quantum coherences in extended dipolar coupled spin networks driven by r.f. fields.

4.2 The physical meaning and properties of multiple-quantum coherences (MQC)

4.2.1 The physical meaning and definition of MQC

First we give a clear definition and description of the basic concept “coherence”, it refers to the superposition of states of a spin or group of spins with a coherent phase relationship. In terms of energy levels, a coherence exists between levels available to a spin or group of spins when the spin or group of spins populates each level and the phases of the coefficients for the state functions of each level have a coherent relationship. Coherences are often termed transitions, because a spin can be thought of as making transitions between energy levels in order to populate both levels. In terms of density operators, the off-diagonal elements of the density matrix represent the superposition of the states involved in the coherence.

Coherence is a very abstract concept. For its physical meaning, Munowitz[5,6,10] gave a vivid description of the single quantum coherence using a vector model (Figure 4.1): for an ensemble of identical, noncoupled spins-1/2 nuclei, each spin precesses around the external magnetic field with the same frequency and amplitude but with a different phase with respect

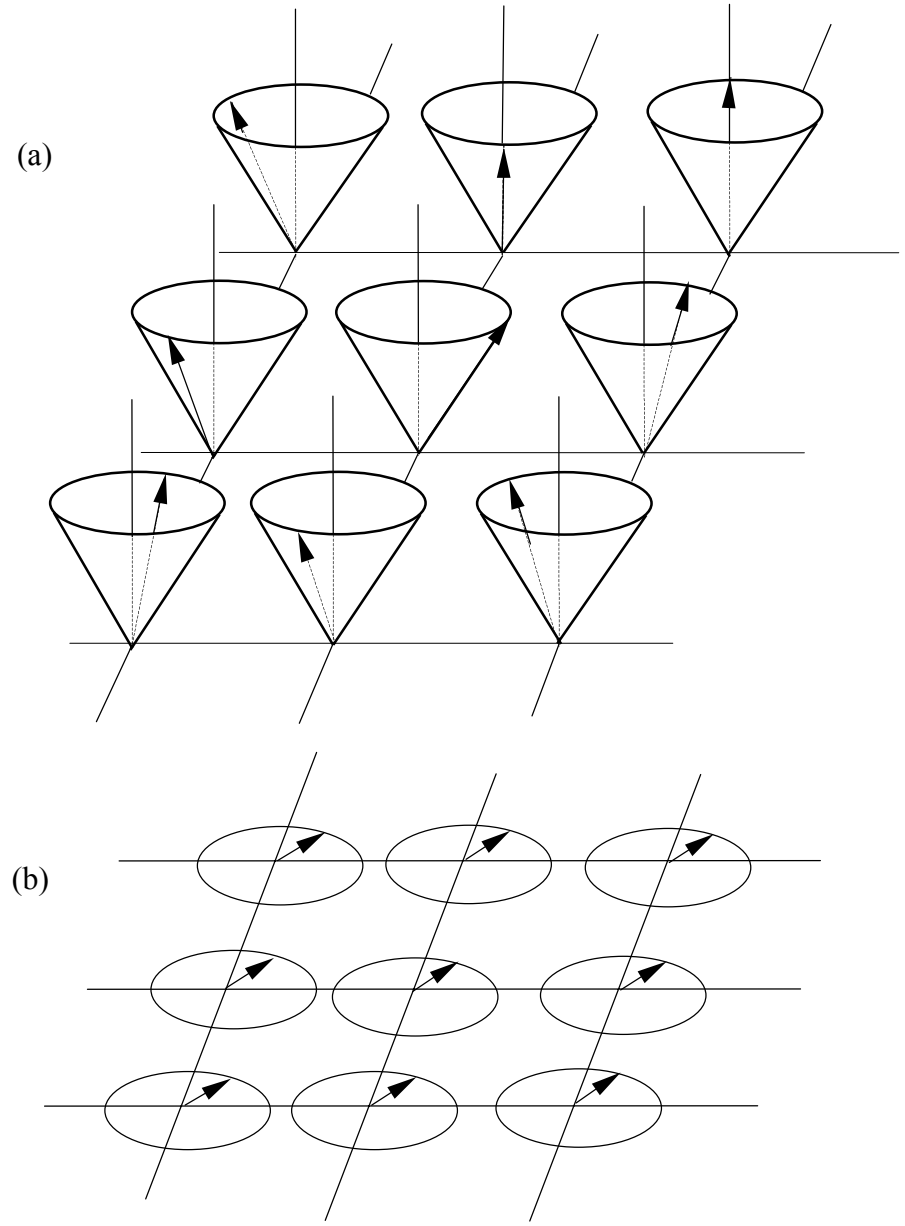

Figure 4.1. *Diagram representation of (a) incoherent and (b) coherent phase relationships in an ensemble of two-level system.*

to each other. The net magnetization arising as the sum of these separate contributions is determined entirely by the phase relationships among the different vectors. In a case where the phases are randomly distributed between 0 and 2π, as shown in Figure 4.1(a), the transverse components vanish owing to destructive interference. Only a time independent longitudinal component along the magnetic field direction remains. We say there is no coherence in this case, and it is associated with thermal equilibrium. While the coherent oscillations of the spins having the same phase resulting from a 90° pulse, as shown in Figure 4.1(b), gives a net

transverse magnetization (i.e. single-quantum coherence) which can be detected in the plane perpendicular to the magnetic field. We say that in this case there is full transverse coherence or single-quantum coherence.

The latter case can be quantum mechanically described as a coherent superposition (or linear combination) of the spin-up and spin-down states, $|\alpha>$ and $|\beta>$, for which the difference in Zeeman quantum numbers $(\frac{1}{2},-\frac{1}{2})$ is one unit. The phase of precession appears as a phase in the wave function, and in this way the physical picture of magnetization is translated into a more abstract, yet more general concept of single-quantum coherence.

Using this method, we can describe the state of one spin-1/2 represented as:

$$|\Psi>= c_1 |\alpha> + c_2 |\beta>, \tag{4.1}$$

using the density operator $\hat{\rho}$ whose three linearly independent and orthogonal components form a vector in a three dimensional Liouville space:

$$\rho_x = c_1 c_2^* + c_1^* c_2 \ , \tag{4.2a}$$

$$\rho_y = -i(c_1 c_2^* - c_1^* c_2)\,, \tag{4.2b}$$

$$\rho_z = c_1^* c_1 - c_2^* c_2\,. \tag{4.2c}$$

The equation (4.2) can be represented by the Pauli matrix:

$$\hat{\rho}_x = |\alpha><\beta| + |\beta><\alpha|\,, \tag{4.3a}$$

$$\hat{\rho}_y = -i(|\alpha><\beta| - |\beta><\alpha|)\,, \tag{4.3b}$$

$$\hat{\rho}_z = |\alpha><\alpha| - |\beta><\beta|\,. \tag{4.3c}$$

If the Hamiltonian matrix elements $H_{rs} = <r|\hat{H}|s>$ are similarly combined into the vector:

$$\Omega_x = H_{12} + H_{21}\,,\ \Omega_y = -i(H_{12} - H_{21})\,,\ \Omega_z = H_{11} - H_{22}\,, \tag{4.4}$$

the Schrödinger equation can be rewritten as follows:

$$\frac{d\hat{\rho}}{dt} = \hat{\rho} \times \hat{\Omega}\,. \tag{4.5}$$

The density vector ρ thus can be viewed as precessing about Ω in analogy to the precession of a spin-1/2 magnetization about an applied field. When ρ_x and ρ_y are combined to give a single transverse component, $\rho_{xy}=\rho_x+i\rho_y$, equation (4.5) can be represented as:

$$\frac{d\rho_{xy}}{dt} = -i\Omega_z \rho_{xy}\,, \tag{4.6}$$

with solution:

$$\rho_{xy}(t)=\rho_{xy}(0)\exp(-i\Omega t). \quad (4.7)$$

The longitudinal population, ρ_z, remains constant.

Associate with the density vector ρ the physical magnetization: its z component is proportional to the population difference, and the x and y components correspond to the transverse magnetization in the rotating frame. The usual angular momentum operators can be expressed:

$$\hat{I}_x = \frac{1}{2}(|\alpha><\beta| + |\beta><\alpha|), \quad (4.8a)$$

$$\hat{I}_y = -\frac{i}{2}(|\alpha><\beta| - |\beta><\alpha|), \quad (4.8b)$$

$$\hat{I}_z = \frac{1}{2}(|\alpha><\alpha| - |\beta><\beta|). \quad (4.8c)$$

This representation can be applied to the multilevel spin system, where the wave functions are generalized to:

$$|\psi> = c_1|1>+c_2|2>+\cdots+c_N|N>, \quad (4.9)$$

so the density operator $|\psi><\psi|$ contains N^2 elements of the form $|r><s|$. For any pair of levels r and s we can describe them by using the fictitious spin-1/2 operators:

$$\hat{I}_x^{r-s} = \frac{1}{2}(|r><s| + |s><r|), \quad (4.10a)$$

$$\hat{I}_y^{r-s} = -\frac{i}{2}(|r><s| - |s><r|), \quad (4.10b)$$

$$\hat{I}_z^{r-s} = \frac{1}{2}(|r><s| - |s><r|). \quad (4.10c)$$

This expression is very useful for treating a transition between any two states |r> and |s>: the x and y components describe the phase coherence, and the z component supplies the population difference between the two states. With each state |r> understood to be a Zeeman eigenstate having z component equal to M_r, there is no restriction on the order of coherence $n=M_r-M_s$. The multiple-quantum coherence is just the physical manifestation of the uniform phase relationship between states |r> and |s>, driving from the particular linear combinations specified by c_r and c_s. Viewed in this way, multispin, multiple-quantum processes are more the rule than exception.

The fictitious spin-1/2 operators, along with equivalent representations such as the product operator basis, thus bring out a fundamental characteristic of all complex spin system: there exist orthogonal modes of coherence which can be excited individually and monitored

dynamically. Each mode is a coherent superposition of a certain order, rendered graphically as an independent vector precessing in an abstract three-dimensional space. With frequency selective excitation, e.g., one can theoretically excite a particular pair of levels within the large spin system.

A mode of coherence in high field may be classified according to its order, n, the difference in Zeeman quantum numbers between the states |r> and |s> it connects, $n=M_r-M_s$. The existence of an n-quantum coherence means that the spins have interacted with at least n quanta of electromagnetic radiation at some earlier time. The effect of the r.f. pulse is to bring the two states, |r> and |s>, into coherent superposition, and at the same time there may be other modes of coherences. Each pair of coherently superposed states may be described by an autonomous (i.e. fictitious) two-level system. There are many modes of coherences, such as total-spin and partial-spin multiple-quantum coherences. A coherence between levels of an N-spin-1/2 system where all N spins are involved in the coherence are said total-spin multiple-quantum coherence, while where only a portion of the coupled spins are involved in a coherence is denoted as partial-spin multiple-quantum coherence.

In general, collective modes of coherence involve n active spins (which "flip" collectively and can be regarded as "superspin") and q passive spins (which "watch"). The order of coherence is obtained by algebraic summation of the Zeeman quantum numbers of the active participants, while the local field is determined by the remaining passive spins. The spectrum of a multiple-quantum coherence, which reflects all the algebraic combinations of the q passive spins, becomes progressively simpler as more spins are allowed to participate actively. The limit is reached with N-quantum coherence in an N-spin system, where the local field vanishes except only for combined chemical shifts and resonance offsets.

4.2.2 The properties of MQC

In the previous section we gave a description of physical meaning of MQC, now we turn to discuss some important properties of MQC.

4.2.2.1 The "invisibility" of MQC

The first property associated with MQC is their "invisibility". We know that in conventional NMR spectroscopy one observes only the single-quantum coherences. For a group of

interacting spins, by definition the individual spins are no longer isolated. If one spin is perturbed, the measured result reflects the presence of the other interacting spins. So multiple-spin multiple-quantum transitions are possible in extended spin networks. Because multiple-quantum coherences are not associated with magnetization, it is not possible to directly observe the MQC with simple single-pulse excitation. Experiments to explore the possibilities for indirect detection of MQC can be cast in the general formulation of two-dimensional NMR experiments, as shown in Figure 3.8, which may be divided into four periods: preparation τ, evolution t_1, mixing τ' and detection t_2 time periods.

In the preparation period the desired MQC are pumped under a multiple-pulse sequence, such as the three-pulse and eight-pulse sequences as discussed later in this chapter. Following this period, the MQC evolve in the presence of the internal Hamiltonian in the evolution period. During this period, MQC respond to their environment and oscillate at their characteristic spectral frequencies, at the same time relaxation of the MQC also occur in this period. Then these unobservable MQC are converted into single-quantum coherences in the conversion (mixing) period. Finally, the created single-quantum coherences, which are modulated by MQC as a function of t_1, are detected in the detection period t_2.

In the MQC experiments, one usually halts the evolution of MQC after a specified interval t_1, converts them to observable single-quantum coherences, and then monitors the free induction decays in the detection period t_2. The first point of the FID depends on the prior history of the MQC, and thus through this way the progress of MQC is reflected in the observed spectra. An entire MQC "interferogram" can be mapped out in this way, point by point, through systematic incrementation of the evolutionary period t_1. Fourier transformation with respect to t_2 separates the various transverse magnetization components which precess during the detection period whose initial amplitude or phase is modulated by the MQC as a function of t_1. Fourier transformation of the MQC interferogram in t_1 reveals the spectral response of the MQC.

In practice, the number N_1 of different points t_1 for which the pulse sequence is repeated, is determined by the range of transition frequencies and the attainable or desired resolution. The sampling rate (Nyquist) theorem states that each sinusoidal component of the time domain signal must be sampled at least twice per cycle to avoid losing information or aliasing high-frequency components to lower frequency. The Nyquist frequency ν_N is chosen to be greater than the expected line frequencies and will depend on the internal Hamiltonian H_{int} and on the

offset terms. The increment in t_1 between shots is $\Delta t_1=(2\nu_N)^{-1}$. When a resolution R(Hz/point) is required the number N_1 is then: $N_1 = 2\nu_N/R$.

4.2.2.2 The response of MQC to resonance offsets and chemical shifts

The second property of MQC is their response to resonance offsets and chemical shifts. The response of an n-quantum coherence $\hat{\rho}^n$=|r><s| to a uniform resonance offset $\hat{H}_{off} = -\Delta\omega\hat{I}_z$ can be represented as:

$$\hat{\rho}^n(t) = \hat{\rho}^n(0)\exp(in\Delta\omega t)\ , \tag{4.11}$$

it can be rewritten in terms of their quadrature components:

$$\hat{\rho}_x^{[n]}(t) = \hat{\rho}_x^{[n]}(0)\cos(n\Delta\omega t) + \hat{\rho}_y^{[n]}(0)\sin(n\Delta\omega t)\,, \tag{4.12}$$

and

$$\hat{\rho}_y^{[n]}(t) = \hat{\rho}_y^{[n]}(0)\cos(n\Delta\omega t) - \hat{\rho}_x^{[n]}(0)\sin(n\Delta\omega t)\,. \tag{4.13}$$

From equation (4.12) and (4.13) we can see that the n-quantum coherences oscillate at n times the actual frequency offset, thereby enhance the effect of a static magnetic field inhomogenity when |n| > 1 and eliminating it when n = 0. Similarly the response of MQC to the chemical shifts can be constructed as:

$$\hat{\rho}_x^{[n]}(t) = \hat{\rho}_x^{[n]}(0)\cos(\Omega_{eff}t) + \hat{\rho}_y^{[n]}(0)\sin(\Omega_{eff}t)\,, \tag{4.14}$$

in the absence of strong couplings the effective precession frequency, given by:

$$\Omega_{eff} = \sum_j \Delta M_j \Omega_j\ , \tag{4.15}$$

is a sum over all the chemical shifts, weighted by ΔM_j=1, −1, or 0, depending on the change in quantum number for each spin. Thus for a pair of spins a zero-quantum coherence oscillates at the difference of the two chemical shifts, and a double-quantum coherence oscillates at their sum. The form of the effective precession frequency results from the products of independent trigonometric factors expressed in eq. (4.15).

4.2.2.3 The response of MQC to dipolar couplings

As we know the dipolar couplings play an important role in creating MQC, at the same time they also affect the response of MQC after the excitation, the evolution of the n-quantum coherences $\hat{\rho}_x^{[n]}$ under the effect of dipolar interaction D_{eff} can be written:

$$\hat{\rho}_x^{[n]}(t) = \hat{\rho}_x^{[n]}(0)\cos(\frac{3}{2}D_{eff}t) + 2\hat{I}_{zk}\hat{\rho}_y^{[n]}(0)\sin(\frac{3}{2}D_{eff}t), \quad (4.16)$$

where the effective dipolar constant D_{eff} which is the sum of the dipolar interactions between the active spins ($\hat{I}_{\alpha j}$, α = x, y, or z) and the passive spins $\hat{I}_{zk}$:

$$D_{eff} = \sum_j \Delta M_j D_{jk}, \quad (4.17)$$

influences the dynamical evolution of a previously existing coherence, determining not only the frequency of oscillation but introducing new modes as well. In general the effect of the bilinear dipolar coupling is to expand the number of spins participating either directly or indirectly in a coherence as time progresses.

4.2.2.4 The response of MQC to r.f. pulses and phase shift

A coherence mode can be transferred into others under the action of 90° pulses, this coherence transfer process, i.e., the process of transferring coherence among the possible coherences available to the spin system is very useful in multiple-quantum spectroscopy. Two important types of coherence transfer can be distinguished for groups of coupled spins: 1) coherence transfer to an active spin, and 2) coherence transfer to a passive spin.

The effect of the phase shift ϕ of a 90° pulse at time τ, e.g., with respect to the x axis in the rotating frame, on the n-quantum coherence can be represented as:

$$\hat{\rho}_x^{[n]}(\tau^+;\phi) = \hat{\rho}_x^{[n]}(\tau^-)\cos(n\phi) + \hat{\rho}_y^{[n]}(\tau^-)\sin(n\phi), \quad (4.18)$$

where τ^- and τ^+ represent just before and just after the pulse at time τ. Equation (4.18) shows that when the phase of the r.f. pulse is shifted by ϕ, an n-quantum coherence sees an apparent phase shift of $n\phi$. This behaviour is very useful in separating different orders of MQC, as seen later in this chapter the method of time proportional phase incrementation is rooted in this phase behaviour.

4.3 The generation and detection of MQC within spins-1/2 dipolar coupled solid systems

From definition we know that multiple-quantum transitions are termed "forbidden transitions" in sense of the selection rule ΔM=1 and are only excited[*] under multiple-pulse sequences, and usually detected by using of two-dimensional spectroscopy methods. In this case, the spin system which was prepared into a state containing MQC evolves for a stepped interval and then MQC are transferred to observable single-quantum coherences. There are many pulse sequences for generating multiple-quantum transitions. For simplicity and clarity we will use short intense r.f. pulses. i.e. nonselective pulses, to excite MQC within spins-1/2 dipolar coupled nuclei systems, and we will use product operators to describe the full processes of generation, evolution and detection of MQC. In this thesis we will use two pulse sequences for excitation of MQC, i.e., the three-pulse sequence and the time-reversible eight-pulse sequence. Below we give a detailed discussion of their mechanism in generation of MQC in strongly dipolar coupled spin-1/2 systems.

4.3.1 Three-pulse sequence

4.3.1.1 MQC generated within two spin-1/2 system

First we consider an isolated system of two spin-1/2 dipolar coupled nuclei, I_1 and I_2, which have the same chemical shift and possess a dipolar coupling constant $D_{12} = \frac{\eta^2 \gamma_I \gamma_S}{r^3}(3\cos^2\theta_{12} - 1)$. The truncated dipole-dipole interaction is represented as:

$$\hat{H}_D = -D_{12}(3\hat{I}_{z1}\hat{I}_{z2} - \hat{\vec{I}}_1 \cdot \hat{\vec{I}}_2) = -D_{12}(2\hat{I}_{z1}\hat{I}_{z2} - \hat{I}_{x1}\hat{I}_{x2} - \hat{I}_{y1}\hat{I}_{y2}), \qquad (4.19)$$

and the spin energy levels are shown in Figure 4.2. The three-pulse sequence used to excite the MQC in the two-spin system is shown in Figure 4.3. The MQC generation, evolution, mixing and detection processes will be discussed in the following.

(1) The generation of MQC

[*] Multiple-quantum transitions between two energy levels E_i and E_j can also be excited with one photon with a frequency equal to $\Delta E = |Ei - Ej|$. With the exception of single-quantum coherences, the probability for such transitions is very small and this excitation of MQC is neglected here.

To avoid the complexity of non-ideal pulses we make the assumption that the 90° pulses used in the three-pulse and later eight-pulse sequences are strong and infinitely short δ pulses*. Here strong means that the r.f. magnetic field γB_1 far exceeds the spectral width, $\Delta\omega$, of the spectrum: B_1 is larger than the spectral splittings arising from chemical shifts or spin-spin couplings. Under these condition we can assume that during the pulses, the effect of the internal Hamiltonian can be neglected. Compared with the dipolar interaction, the chemical shift usually is small for protons and will be neglected in the excitation period. Provided that

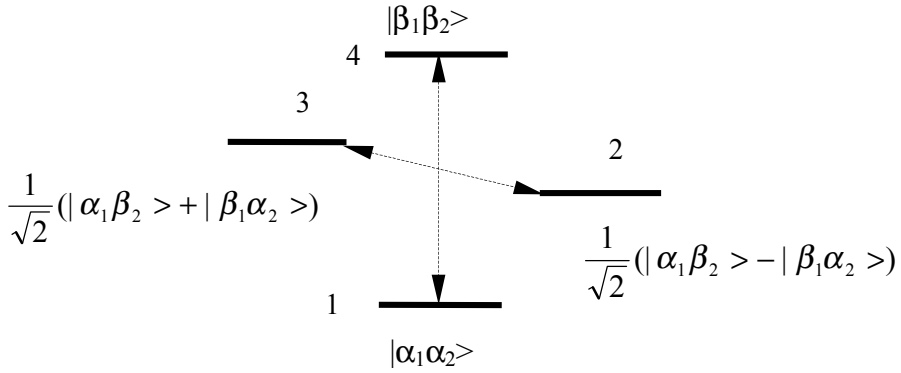

Figure 4.2. *The energy levels for a two-dipolar-coupled-spin-1/2 system.*

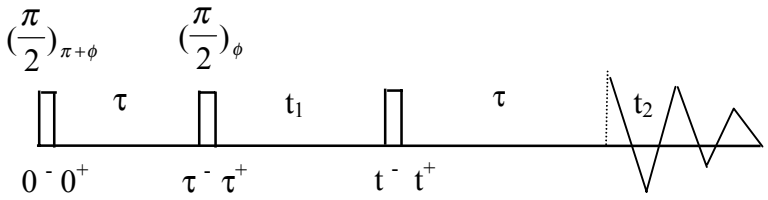

Figure 4.3. *Schematic representation of the three-pulse sequence used for the excitation of multiple-quantum transitions.*

We excite the spin system on resonance, the resonance offset term will also not be considered here. If the excitation period is short enough we can also avoid the relaxation effect.

We use the product operator description to follow the development of the density operator $\hat{\rho}(t)$, and denote times labelled as, 0^-, 0^+, τ^- and τ^+, etc., as illustrated in Figure 4.3 to represent the times just before and just after the pulses at time t = 0, τ, etc.. Supposing the spin system is at equilibrium before the first pulse:

$$\hat{\rho}(0^-) = (\hat{I}_{z1} + \hat{I}_{z2}), \tag{4.20}$$

* 90° pulses which are infinitely short, must be infinitely strong!

where in equation (4.20) the proportionality constant is omitted and only the spin density operator is used. The first 90° pulse applied along the x-axis in the rotating frame rotates the equilibrium density operator into a single-quantum coherence. The effect of the internal Hamiltonian during the pulse can be neglected, so the effect of the hard pulse on the density matrix is dominated by the unitary transformation:

$$\hat{\rho}(0^+) = \exp[-i\frac{\pi}{2}(\hat{I}_{x1} + \hat{I}_{x2})]\hat{\rho}(0^-)\exp[i\frac{\pi}{2}(\hat{I}_{x1} + \hat{I}_{x2})] = -(\hat{I}_{y1} + \hat{I}_{y2}). \qquad (4.21)$$

The single-quantum coherence components then evolve under the influence of the internal Hamiltonian, which is dominated by the dipolar interaction $\hat{H}_D$ (see equation (4.19)), into the following components at the end of the preparation period of τ:

$$\hat{\rho}(\tau^-) = -(\hat{I}_{y1} + \hat{I}_{y2})\cos(\frac{3}{2}D_{12}\tau) - 2(\hat{I}_{x1}\hat{I}_{z2} + \hat{I}_{z1}\hat{I}_{x2})\sin(\frac{3}{2}D_{12}\tau), \qquad (4.22)$$

where the relationship $[\hat{\vec{I}}_1 \cdot \hat{\vec{I}}_2, \hat{I}_{y1} + \hat{I}_{y2}] = 0$ is used. At this stage the spin density operator $\hat{\rho}(\tau^-)$ consists of entirely single-quantum coherences, e.g., one-spin single-quantum coherence terms like $(\hat{I}_{y1} + \hat{I}_{y2})$ and two-spin single-quantum coherence terms like $(\hat{I}_{x1}\hat{I}_{z2} + \hat{I}_{z1}\hat{I}_{x2})$.

The second 90° pulse applied along the x-axis in the rotating frame transforms the corresponding spin density operator into the following components:

$$\hat{\rho}(\tau^+) = -(\hat{I}_{z1} + \hat{I}_{z2})\cos(\frac{3}{2}D_{12}\tau) + 2(\hat{I}_{x1}\hat{I}_{y2} + \hat{I}_{y1}\hat{I}_{x2})\sin(\frac{3}{2}D_{12}\tau). \qquad (4.23)$$

In order to make the result more transparent, we expand the equation (4-23) in terms of raising and lowering operators, $\hat{I}_x = \frac{1}{2}(\hat{I}_+ + \hat{I}_-)$ and $\hat{I}_y = \frac{1}{2i}(\hat{I}_+ - \hat{I}_-)$:

$$\hat{\rho}(\tau^+) = -(\hat{I}_{z1} + \hat{I}_{z2})\cos(\frac{3}{2}D_{12}\tau) + \frac{1}{2i}(\hat{I}_{+1}\hat{I}_{+2} - \hat{I}_{-1}\hat{I}_{-2})2\sin(\frac{3}{2}D_{12}\tau), \qquad (4.24)$$

where the first term at the right side of the equation represents a longitudinal magnetization or the zero-quantum coherence components, the second term represents the double-quantum coherence components. All these terms can be separately detected by using a proper method, such as TPPI (time proportional phase increment), which will be discussed in a later section. A specific order of coherence can be eliminated or selected by using phase cycling, as described in a later section.

From equation (4.24) one can see that the intensity of the double-quantum coherences is proportional to $\sin(\frac{3}{2}D_{12}\tau)$. This means that double-quantum coherences do not arise in a system of uncoupled spins. On the other hand, if the time period τ between the two pulses in the preparation period goes to zero, the double-quantum terms also disappear. Then the effect of the two 90° pulses is equivalent to a single 180° pulse which flips the magnetization $(\hat{I}_{z1}+\hat{I}_{z2})$ into the negative z-direction. Therefore, in order to generate double-quantum coherences, one must choose a proper time τ such that $\sin(\frac{3}{2}D_{12}\tau)$ is appreciable; when we choose $\frac{3}{2}D_{12}\tau \approx \pi/2,\ 3\pi/2$, etc., we get the maximum intensity of the double-quantum coherences. Because the dipolar coupling is proportional to $1/r^3$, where r is the distance between spins I_1 and I_2, by selecting suitable τ values, one can distinguish the coupling between two spins, e.g. two protons, in the same molecule from coupling of protons in different molecules.

(2) MQC evolving during the evolution period

Above, we have already seen how two pulses which are separated by a delay τ can produce zero-, and double-quantum coherences within a two spin-1/2-dipolar-coupled system. Once the multiple-quantum coherences are excited, they will evolve under the action of the internal Hamiltonian, $\hat{H}_0 = -\eta\Omega(\hat{I}_{z1}+\hat{I}_{z2}) - \eta D_{12}(3\hat{I}_{z1}\hat{I}_{z2} - \hat{\vec{I}}_1\hat{\vec{I}}_2)$, where $\Omega \equiv \gamma B_0 - \omega$ is the off-resonance offset frequency. (This offset is purposefully introduced here to separate different coherence orders, but in practice this is done by a phase shift of the pulses in the preparation period as seen in section 4.3.3.3). Here for simplicity we consider the evolution process of zero-, and double-quantum coherences separately, and do not consider relaxation (T_1 and T_2) effects.

Firstly, consider the evolution of the zero-quantum coherences in the t_1 interval. The first terms in equation (4.23) $-(\hat{I}_{z1}+\hat{I}_{z2})\cos(\frac{3}{2}D_{12}\tau)$ commute with the internal Hamiltonian and so they remain the same throughout the evolution period.

The evolution of the double-quantum coherence terms in the equation (4-23), $+2(\hat{I}_{x1}\hat{I}_{y2}+\hat{I}_{y1}\hat{I}_{x2})\sin(\frac{3}{2}D_{12}\tau)$, during the evolution period t_1 only depends on the resonance offset and is independent of the dipolar couplings between them, due to $[\hat{I}_{z1}\hat{I}_{z2},\hat{I}_{\alpha1}\hat{I}_{\beta2}]=0$, for α,β=x, y, or z. This evolution process can be expressed as follows:

$$\exp(-i\hat{H}_0t_1)[+2(\hat{I}_{x1}\hat{I}_{y2}+\hat{I}_{y1}\hat{I}_{x2})\sin(\frac{3}{2}D_{12}\tau)]\exp(i\hat{H}_0t_1)$$

$$=2(\hat{I}_{x1}\hat{I}_{y2}+\hat{I}_{y1}\hat{I}_{x2})\sin(\frac{3}{2}D_{12}\tau)\cos(2\Omega t_1)+2(\hat{I}_{y1}\hat{I}_{y2}-\hat{I}_{x1}\hat{I}_{x2})\sin(\frac{3}{2}D_{12}\tau)\sin(2\Omega t_1), \quad (4.25)$$

using the raising and lowering operators this can be written as:

$$[\frac{1}{2i}(\hat{I}_{+1}\hat{I}_{+2}-\hat{I}_{-1}\hat{I}_{-2})]\,2\sin(\frac{3}{2}D_{12}\tau)\cos(2\Omega t_1)\text{ - }[\frac{1}{2}(\hat{I}_{+1}\hat{I}_{+2}+\hat{I}_{-1}\hat{I}_{-2})]\,2\sin(\frac{3}{2}D_{12}\tau)\sin(2\Omega t_1)$$

$$=\{2QC\}_y2\sin(\frac{3}{2}D_{12}\tau)\cos(2\Omega t_1)\text{ - }\{2QC\}_x2\sin(\frac{3}{2}D_{12}\tau)\sin(2\Omega t_1). \quad (4.26)$$

As discussed already before, we see that the double-quantum coherence develops with twice the offset frequency during t_1.

(3) The mixing and detection of the MQC

Since it is not possible to directly observe orders of coherences other than single-quantum coherences, one must transfer the MQC to observable single-quantum coherences with a mixing period before detection.

Let us check the changes of the density operator components after the mixing period τ' (which consists of one 90°$_x$ pulse and a delay τ') using the product operator description.

a) The zero-quantum coherence terms

The zero-quantum coherence terms, $-(\hat{I}_{z1}+\hat{I}_{z2})\cos(\frac{3}{2}D_{12}\tau)$, are converted to the single-spin single-quantum coherence after the mixing 90°$_x$ pulse:

$$(\hat{I}_{y1}+\hat{I}_{y2})\cos(\frac{3}{2}D_{12}\tau), \quad (4.27)$$

which is then converted into the two-spin and one-spin single-quantum coherences under the action of the internal Hamiltonian, $\hat{H}_D = -D_{12}(3\hat{I}_{z1}\hat{I}_{z2} - \hat{\vec{I}}_1 \cdot \hat{\vec{I}}_2)$, in the following delay time τ':

$$(\hat{I}_{y1} + \hat{I}_{y2})\cos(\frac{3}{2}D_{12}\tau)\cos(\frac{3}{2}D_{12}\tau') - 2(\hat{I}_{x1}\hat{I}_{z2} + \hat{I}_{z1}\hat{I}_{x2})\cos(\frac{3}{2}D_{12}\tau)\sin(\frac{3}{2}D_{12}\tau'), \quad (4.28)$$

where the relationship $[\hat{\vec{I}}_1 \cdot \hat{\vec{I}}_2, (\hat{I}_{y1} + \hat{I}_{y2})] = 0$ was used. Then the first terms corresponding to the single-quantum coherence in above equation are detected in the detection period. The second terms are two-spin single-quantum coherences which are undetectable in the signal acquisition period, their traces are zero, that is: $Tr[(\hat{I}_{1+} + \hat{I}_{2+})\hat{I}_{x1}\hat{I}_{z2}] = 0$, and $Tr[(\hat{I}_{1+} + \hat{I}_{2+})\hat{I}_{z1}\hat{I}_{x2}] = 0$.

b) The two-spin double-quantum coherence terms

The two-spin double-quantum coherence terms in eq.(4.25),

$2(\hat{I}_{x1}\hat{I}_{y2} + \hat{I}_{y1}\hat{I}_{x2})\sin(\frac{3}{2}D_{12}\tau)\cos(2\Omega t_1)$ and $2(\hat{I}_{y1}\hat{I}_{y2} - \hat{I}_{x1}\hat{I}_{x2})\sin(\frac{3}{2}D_{12}\tau)\sin(2\Omega t_1)$,

are converted into the following two-spin zero-, single-, and double-quantum coherence terms by the mixing $90°_x$ pulse:

$$2(\hat{I}_{x1}\hat{I}_{z2} + \hat{I}_{z1}\hat{I}_{x2})\sin(\frac{3}{2}D_{12}\tau)\cos(2\Omega t_1), \quad (4.29)$$

and

$$2(\hat{I}_{z1}\hat{I}_{z2} - \hat{I}_{x1}\hat{I}_{x2})\sin(\frac{3}{2}D_{12}\tau)\sin(2\Omega t_1), \quad (4.30)$$

and then under the effect of the dipolar Hamiltonian $\hat{H}_D$ in the following mixing period τ', the terms in eq. (4.29) are changed into the following components:

$$2(\hat{I}_{x1}\hat{I}_{z2} + \hat{I}_{z1}\hat{I}_{x2})\sin(\frac{3}{2}D_{12}\tau)\cos(2\Omega t_1)\cos(\frac{3}{2}D_{12}\tau')$$

$$+ 2(\hat{I}_{x1} + \hat{I}_{x2})\sin(\frac{3}{2}D_{12}\tau)\cos(2\Omega t_1)\sin(\frac{3}{2}D_{12}\tau'), \quad (4.31)$$

and the terms in eq. (4.30) are not affected by the dipolar Hamiltonian and stay unchanged. They are two-spin zero- and double-quantum coherences which are not detected in the detection period. The second terms in eq.(4.31) correspond to the one-spin single-quantum

coherences and are detected in the acqusition period. The others are the two-spin single-quantum coherences and not detectable.

(4) Summary

We have discussed that the nonselective pulse sequence $90°_x\cdots\cdots\tau\cdots\cdots 90°_x$ can produce zero-, and double-quantum coherences within a two spin-1/2 system from the equilibrium state. We can see from the eq.(4.28) and eq.(4.31) that the intensities of the detectable single-quantum coherence are maximum when $\tau = \tau$‘. This means that when we make a symmetrized excitation and mixing, we can get the maximum intensity.

As can be seen from the above discussion, it is the combination effect of the dipolar coupling and the 90° pulses that lead to the generation of multiple-quantum coherences: the pulses change the order of coherences, whereas the dipolar Hamiltonian reserves the order of coherences and only changes the number of involved spins.

4.3.1.2 Three and more spin-1/2 systems

We have discussed the generation of multiple-quantum coherences within a pair of spins, now we turn into discussion of three and more spin-1/2 systems.

(1) Three spin-1/2 system

First let us consider a dipolar coupled three spins-1/2 I_1, I_2, and I_3 system, which has a coupling of the form $\hat{H}_D = \sum_{i,j=1,i\neq j}^{3} D_{ij}(3\hat{I}_{zi}\hat{I}_{zj} - \hat{\vec{I}}_i \cdot \hat{\vec{I}}_j)$. For simplicity we also assume that we irradiate the spin system on resonance, and do not consider relaxation effects.

As in eq.(4-20), we take $\hat{\rho}(0^-)$ just before the first pulse, as

$$\hat{\rho}(0^-) = \hat{I}_{z1} + \hat{I}_{z2} + \hat{I}_{z3}, \tag{4.32}$$

so that at $t = 0^+$, just after the $90°_x$ pulse,

$$\hat{\rho}(0^+) = -(\hat{I}_{y1} + \hat{I}_{y2} + \hat{I}_{y3}). \tag{4.33}$$

Then under the influence of the dipolar interaction the density operator becomes:

$$\hat{\rho}(\tau^-) = \exp(-\frac{i}{\eta}\hat{H}_D\tau)\hat{\rho}(0^+)\exp(\frac{i}{\eta}\hat{H}_D\tau)$$

$$= \exp[-i \sum_{i,j=1,i\neq j}^{3} D_{ij}(3\hat{I}_{zi}\hat{I}_{zj} - \hat{\vec{I}}_i \cdot \hat{\vec{I}}_j)\tau][-(\hat{I}_{1y} + \hat{I}_{2y} + \hat{I}_{3y})]\exp[i \sum_{i,j=1,i\neq j}^{3} D_{ij}(3\hat{I}_{zi}\hat{I}_{zj} - \hat{\vec{I}}_i \cdot \hat{\vec{I}}_j)\tau], \quad (4.34)$$

since all three spin-spin terms commute with each other and $[\hat{I}_{z1}\hat{I}_{z2}, \hat{I}_{3y}] = 0$, $[\hat{I}_{z2}\hat{I}_{z3}, \hat{I}_{1y}] = 0$, $[\hat{I}_{z3}\hat{I}_{z1}, \hat{I}_{y2}] = 0$, eq.(4.34) can be simplified as:

$$\begin{aligned}\hat{\rho}(\tau^-) = {} & \exp[-(D_{12}3\hat{I}_{z1}\hat{I}_{z2} + D_{31}3\hat{I}_{z3}\hat{I}_{z1})\tau](-\hat{I}_{y1})\exp[(D_{12}3\hat{I}_{z1}\hat{I}_{z2} + D_{31}3\hat{I}_{z3}\hat{I}_{z1})\tau] \\ & + \exp[-(D_{12}3\hat{I}_{z1}\hat{I}_{z2} + D_{23}3\hat{I}_{z2}\hat{I}_{z3})\tau](-\hat{I}_{y2})\exp[(D_{12}3\hat{I}_{z1}\hat{I}_{z2} + D_{23}3\hat{I}_{z2}\hat{I}_{z3})\tau] \\ & + \exp[-(D_{23}3\hat{I}_{z2}\hat{I}_{z3} + D_{31}3\hat{I}_{z3}\hat{I}_{z1})\tau](-\hat{I}_{3y})\exp[(D_{23}3\hat{I}_{z2}\hat{I}_{z3} + D_{31}3\hat{I}_{z3}\hat{I}_{z1})\tau]. \quad (4.35)\end{aligned}$$

We can compute it separately. As an example, we analyse for spin I_1:

$$\begin{aligned}& \exp[-(D_{12}3\hat{I}_{z1}\hat{I}_{z2} + D_{31}3\hat{I}_{z3}\hat{I}_{z1})\tau](-\hat{I}_{y1})\exp[(D_{12}3\hat{I}_{z1}\hat{I}_{z2} + D_{31}3\hat{I}_{z3}\hat{I}_{z1})\tau] \\ & = \exp[-(D_{12}3\hat{I}_{z1}\hat{I}_{Z2})\tau]\exp[-D_{31}(3\hat{I}_{z3}\hat{I}_{z1})\tau](-\hat{I}_{y1})\exp[(D_{12}3\hat{I}_{z1}\hat{I}_{Z2})\tau]\exp[D_{31}(3\hat{I}_{z3}\hat{I}_{z1})\tau] \\ & = -\hat{I}_{y1}\cos(\frac{3}{2}D_{12}\tau)\cos(\frac{3}{2}D_{13}\tau) + 2\hat{I}_{x1}\hat{I}_{z2}\sin(\frac{3}{2}D_{12}\tau)\cos(\frac{3}{2}D_{31}\tau) \\ & + 2\hat{I}_{x1}\hat{I}_{z3}\sin(\frac{3}{2}D_{13}\tau)\cos(\frac{3}{2}D_{12}\tau) + 4\hat{I}_{y1}\hat{I}_{z2}\hat{I}_{z3}\sin(\frac{3}{2}D_{13}\tau)\sin(\frac{3}{2}D_{12}\tau). \quad (4.36)\end{aligned}$$

Here we can see that only spin I_1 has either x- or y-components, which are in-phase or anti-phase and represent single-quantum coherences, and only the coupling constants involving spin I_1 occur. The contributions from I_2 and I_3 can be easily obtained by cyclic permutation of the indices in eq.(4.36).

At the end of the τ, the density operator is affected by the second $90°_x$, (or $90°_y$) pulse. In order to see what spin coherences are generated, we need only examine what happens to the spin parts, the result is represented in table 4.1.

Table 4.1. *Effect of the second $90°_x$, (or $90°_y$) pulse on the three spin system*

Operators before $90°_x$ [or $90°_y$] pulse	Operators after $90°_x$ [or $90°_y$] pulse	Orders of MQC, n
$\hat{I}_{y1}$	$\hat{I}_{z1}$ $[\hat{I}_{y1} = \frac{1}{2i}(\hat{I}_{+1} - \hat{I}_{-1})]$	0 (±1)
$\hat{I}_{x1}\hat{I}_{z2}$	$-\hat{I}_{x1}\hat{I}_{y2} = -\frac{1}{4i}(\hat{I}_{+1} + \hat{I}_{-1})(\hat{I}_{+2} - \hat{I}_{-2})$	±2, 0 (±1)

	$[-\hat{I}_{z1}\hat{I}_{x2} = -\frac{1}{2i}\hat{I}_{z1}(\hat{I}_{+2} + \hat{I}_{-2})]$	
$\hat{I}_{x1}\hat{I}_{z3}$	$-\hat{I}_{x1}\hat{I}_{y3} = -\frac{1}{4i}(\hat{I}_{+1} + \hat{I}_{-1})(\hat{I}_{+3} - \hat{I}_{-3})$ $[-\hat{I}_{z1}\hat{I}_{x3} = -\frac{1}{2i}I_{1z}(I_3^+ + I_3^-)]$	±2, 0 (±1)
$\hat{I}_{y1}\hat{I}_{z2}\hat{I}_{z3}$	$\hat{I}_{z1}\hat{I}_{y2}\hat{I}_{y3} = \frac{1}{4i}\hat{I}_{z1}(\hat{I}_{+2} - \hat{I}_{-2})(\hat{I}_{+3} - \hat{I}_{-3})$ $[\hat{I}_{y1}\hat{I}_{x2}\hat{I}_{x3} = \frac{1}{8i}(\hat{I}_{+1} - \hat{I}_{-1})(\hat{I}_{+2} + \hat{I}_{-2})(\hat{I}_{+3} + \hat{I}_{-3})]$	±2, 0 (±1, ±3)

From table 4.1 and eq.(4.36) we can get the following conclusions:

(1) The three spins give MQC ranging from +3 to -3 under the attack of the sandwiched excitation sequence. The amount of coherence created depends on the sine of the coupling between the two spins involved in the coherence and the cosine of all other couplings;

(2) If all three spins are close together, we can quickly produce single-, double-, and triple-quantum coherences when all the strong coupling D_{ij} satisfy the condition: $\sin(\frac{3}{2}D_{ij}\tau) \cong 1$ or $\frac{3}{2}D_{ij}\tau/2 \cong \pi/2$; If, however, two spins are close, the third is far away, two of the coupling constants are small, so that while double-quantum coherence can be excited quickly, triple-quantum coherence is produced slowly;

(3) The particular coherence created from the product operators depends on the relative phase of the second pulse, e.g. the term $\hat{I}_{y1}\hat{I}_{z2}\hat{I}_{z3}$ containing the product of three operators can be converted into either zero- and double-quantum coherence or single-, triple-quantum coherence and total-spin single-quantum coherence by using $90°_x$ pulse and $90°_y$ pulse, respectively.

(2) More than three spin-1/2 system

When we treat more than three dipolar coupled spin-1/2 systems, the above described method is also valid for the analysis of the generating and detection of MQC. In general, in a group of

N coupled spins, analogous to the eq.(4.35), the density operator for one of the spins, for example, spin 1, can be written as:

$$\begin{aligned}\hat{\rho}(\tau^-) &= \exp(-\frac{i}{\eta}\hat{H}_D\tau)[-\hat{I}_{y1}]\exp(\frac{i}{\eta}\hat{H}_D\tau)\\ &= \exp(-\frac{i}{\eta}\sum_j D_{1j}\hat{I}_{z1}\hat{I}_{zj})[-\hat{I}_{y1}]\exp(\frac{i}{\eta}\sum_j D_{1j}\hat{I}_{z1}\hat{I}_{zj})\\ &= -\hat{I}_{y1}\prod_{j=2}^{N}\cos(\frac{3}{2}D_{1j}\tau) + 2\hat{I}_{x1}\sum_{j\neq 1}^{N}[\hat{I}_{zj}\sin(\frac{3}{2}D_{1j}\tau)\prod_{k\neq 1,j}^{N}\cos(\frac{3}{2}D_{1k}\tau)]\\ &\quad + 4\hat{I}_{y1}\sum_{j,k\neq 1}^{N}\hat{I}_{zj}\hat{I}_{zk}\sin(\frac{3}{2}D_{1j}\tau)\sin(\frac{3}{2}D_{1k}\tau)\prod_{l\neq 1,j,k}^{N}\cos(\frac{3}{2}D_{1l}\tau)\\ &\quad \pm 2^{N-1}\hat{I}_{\varepsilon 1}\hat{I}_{z2}\cdots\hat{I}_{zN}\sin(\frac{3}{2}D_{12}\tau)\cdots\sin(\frac{3}{2}D_{1N}\tau),\end{aligned} \tag{4.37}$$

where ε=x for N=even integer and ε=y for N=odd integer. The signs of the terms in the expansion follow $+--++--++\cdots$ and consequently the sign of the last term depends on the number of coupled spins.

This form of the density operator contains product operator terms which represent transverse magnetization of spin 1 modulated by coupling to the other spins in the coupled network. The terms can be divided into two general types as:

$$\hat{I}_{x1}\hat{I}_{z2}\cdots\hat{I}_{zN}, \qquad \text{N=even integer,} \tag{4.38}$$

and

$$\hat{I}_{y1}\hat{I}_{z2}\cdots\hat{I}_{zN}, \qquad \text{N=odd integer.} \tag{4.39}$$

In each case the coefficient of the product operator term is proportional to the product of the sines of the coupling constant between spin 1 and the other spins involved in the product operator, and to the product of the cosines of the coupling constants between spin 1 and all the other spins in the network.

The second pulse in the preparation sequence can transfer multiple-spin single-quantum coherence expressed in equation (4.38) and (4.39) into MQC. The exact result is dependent on the relative phase of this second pulse with respect to the first pulse in the sequence. When the creation pulse is in phase with the first pulse, say $90°_x$, it transforms the single-quantum coherences represented in eq.(4-38) and (4-39) into the following components, respectively:

$$\hat{I}_{x1}\hat{I}_{y2}\cdots\hat{I}_{yN}, \qquad \text{N=even number,} \tag{4.40}$$

and

$$-\hat{I}_{z1}\hat{I}_{y2}\cdots\hat{I}_{yN}, \qquad \text{N=odd number,} \tag{4.41}$$

by expanding the final product operator terms above in terms of raising and lowering operators, it can be shown that only even orders of coherences are created. In general, product operator terms with an even or odd number of transverse angular momentum operators contain even or odd orders of coherence, respectively.

When the second pulse is 90° out of phase with respect to the first pulse in the sequence, say $90°_{y,}$ the second pulse converts the single-quantum coherence in eq.(4-38) and (4-39) into the following terms:

$$-\hat{I}_{z1}\hat{I}_{x2}\cdots\hat{I}_{xN}, \qquad \text{N=even number,} \tag{4.42}$$

and

$$\hat{I}_{y1}\hat{I}_{x2}\cdots\hat{I}_{xN}, \qquad \text{N=odd number.} \tag{4.43}$$

When expanded in terms of raising and lowering operators, the above terms are seen to represent only odd-orders of coherence.

In the general case of N coupled spin-1/2 nuclei without any coupling symmetry, the 2^N energy levels are partitioned into N+1 Zeeman manifolds, each containing:

$$\Omega = \frac{N!}{\left(\frac{1}{2}N+M\right)!\left(\frac{1}{2}N-M\right)!}, \tag{4.44}$$

distinct states. The magnetic quantum number M may take one of the values -L, -L+1, ...,L-1, L, where the total spin quantum number L is the sum of the spin quantum numbers of the component nuclei:

$$\mathrm{L}=\sum_{\mathrm{i}}^{\mathrm{N}}\mathrm{I_i}=\frac{1}{2}N\text{ , for I = 1/2.} \tag{4.45}$$

The energy levels are shown in Fig.4.4.

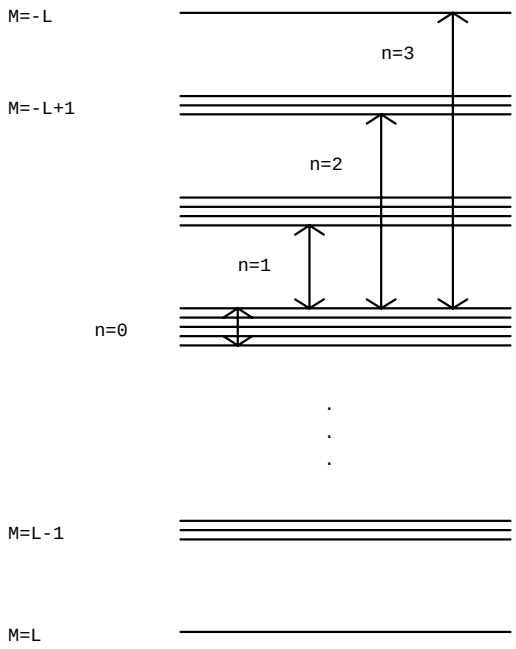

Fig. 4.4. Schematic representation of the energy levels for a system of N coupled spin-1/2 nuclei without any coupling symmetry.

The levels within a manifold are shifted and split by the internal interactions, thereby making a large number of spectroscopic transitions or coherences possible. The number of pairs of levels Z_n over which coherence of order n can develop is obtained as:

$$Z_n = \binom{2N}{N-n} = \frac{(2N)!}{(N-n)!(N+n)!}, \quad n \neq 0 \tag{4.46}$$

and

$$Z_0 = \frac{1}{2}\left[\binom{2N}{N} - 2^N\right], \quad n = 0. \tag{4.47}$$

4.3.2 Time-reversible eight-pulse sequence

4.3.2.1 Pulse sequence and average Hamiltonian

In the previous sections we have discussed a three-pulse sequence. Although it can excite all orders of multiple-quantum coherence within strongly dipolar coupled spin-1/2 systems, the generating rate of the higher order coherences is slow. This point will be further treated in a later section. We first discuss the generation of multiple-quantum coherences within strongly dipolar coupled spin-1/2 systems using the cyclic time-reversible eight-pulse sequence, which is illustrated in Figure 4.5. This sequence consists of eight 90° pulses with phases as indicated

and separated by delays Δ and Δ' = 2Δ+t_p, here t_p is the duration of the 90° pulse. The delay Δ'=2Δ+t_p instead of Δ'=2Δ is based on the belief that the finite length of the 90° pulses will affect the average Hamiltonian of the sequence. Using average Hamiltonian theory[4,7,9,13,14], we can calculate the effective Hamiltonian of the cyclic time-reversible eight-pulse sequence to be $\hat{H}_{yx}$:

$$\hat{H}_{yx} = -\frac{1}{2}\sum_{i<j} D_{ij}(\hat{I}_{+i}\hat{I}_{+j}+\hat{I}_{-i}\hat{I}_{-j}) = -\frac{1}{4}\sum_{i\neq j} D_{ij}(\hat{I}_{+i}\hat{I}_{+j}+\hat{I}_{-i}\hat{I}_{-j}). \tag{4.48}$$

In contrast to the dipolar Hamiltonian, this average Hamiltonian is a pure double-quantum Hamiltonian[15-19]. When the coupled spin-1/2 nuclei are excited under the integer cycles of one of the pulse sequences in Fig. 4.5, the development of the density operator of the spin system is governed by this average Hamiltonian $\hat{H}_{yx}$ and can be predicted by the following equation:

$$\frac{d\hat{\rho}(t)}{dt} = -i\left[\hat{H}_{yx}, \hat{\rho}(t)\right], \tag{4.49}$$

which has the formal solution:

$$\hat{\rho}(t) = \exp(-i\hat{H}_{yx}t)\hat{\rho}(0)\exp(i\hat{H}_{yx}t), \tag{4.50}$$

where relaxation terms are not considered.

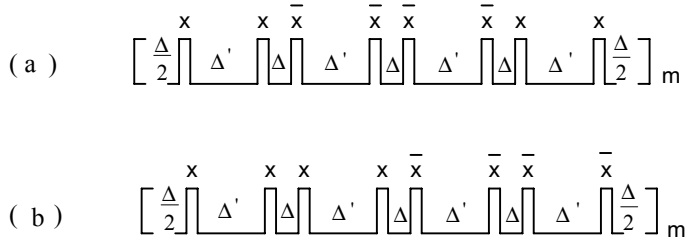

Figure 4.5*. Schematic representation of the time-reversible eight-pulse sequences possessing a pure double-quantum average Hamiltonian.*

4.3.2.2 Generation of MQC

For a discussion of the MQC development under the excitation of $\hat{H}_{yx}$, it is better to treat spin systems from simple to complex. Below we will separately discuss the two-, three- and multiple-spins-1/2 systems using an analytical method. In all the cases studied here, we

assume that the spin systems are excited from the equilibrium state, i.e. one-spin zero-quantum coherence, $\hat{\rho}(0) = \hat{I}_z = \sum_{i=1}^{N} \hat{I}_{zi}$.

(1) Two-spin-1/2 case. Let us first consider the simplest spin system: isolated spin-1/2 pairs (N=2) with identical internuclear separation and orientations with respect to the external magnetic field. This situation can occur in a single crystal or a liquid crystal. In this case all the intrapair dipolar coupling constants D_{ij}=D are identical and much stronger than any interpair coupling constants. Only zero- and double-quantum coherences are excited in this spin system by using the even-order selective excitation Hamiltonian $\hat{H}_{yx}$. The normalized zero- and double-quantum coherence intensities, $I_0(t)$ and $I_{|2|}(t)$, can be obtained by using the equation (4.50)[20,25]:

$$I_0(t) = \frac{1}{2} + \frac{\cos(2Dt)}{2}, \tag{4.51a}$$

$$I_{|2|}(t) = I_2(t) + I_{-2}(t) = \frac{1}{2} - \frac{\cos(2Dt)}{2}. \tag{4.51b}$$

In the absence of relaxation, the oscillatory exchange of MQC intensity between the different orders (zero- and double-quantum coherences) will continue indefinitely. But in practice polycrystalline powders are the most commonly used samples for MQ NMR. In this case, even for isolated pairs with identical internuclear spacings, the angular dependence of the dipolar coupling interaction leads to destructive interference among the characteristic frequencies which contribute to the MQ intensity development, leading to steady state values of I_n at long excitation t. The appearance of oscillations which are damped at long times, is characteristic for the powder average of a small number of coupled spins.

For calculating the MQ intensities of polycrystalline powder samples, equation (4.51) must be appropriately averaged over all possible orientations. The resulting solutions for the normalized zero- and double-quantum intensities for a polycrystalline sample containing isolated dipolar coupled spin pairs are approximated as follows [20,25]:

$$I_{0,powder} \sim \frac{1}{2} + \frac{1}{2}\sqrt{\frac{\pi}{24D_0t}}[\cos(D_0t) + \sin(D_0t)], \tag{4.52a}$$

$$I_{|2|,powder} \sim \frac{1}{2} - \frac{1}{2}\sqrt{\frac{\pi}{24D_0t}}[\cos(D_0t) + \sin(D_0t)], \tag{4.52b}$$

for large values of $(D_0t/\pi)^{1/2}$, where $D_0 = |D_{ij}(\theta = 0)| = \frac{\gamma^2\eta}{r_{ij}^3}$. In approaching their long-term limit the intensities of the powder therefore undergo a series of damped oscillations about the value ½, following a brief introduction period. The intensities oscillate with frequency of about $2\pi\times(1/D_0)$, while the envelope function $(\pi/D_0t)^{1/2}$ slowly decays to zero, at the same time shifting the extrema in the trigonometric functions.

(2) Three-spin-1/2 case. For three dipolar coupled spin–1/2 nuclei, there are three pairwise dipolar coupling constants D_{12}, D_{13}, and D_{23}. The normalized zero- and double-quantum coherence intensities can be expressed as follows[20,25]:

$$I_0(t) = \frac{2}{3} + \frac{1}{3}\cos(2D_{eff}t), \tag{4.53a}$$

$$I_{|2|}(t) = \frac{1}{3} - \frac{1}{3}\cos(2D_{eff}t), \tag{4.53b}$$

where $D_{eff} = (D_{12}^2 + D_{13}^2 + D_{23}^2)^{1/2}$. Similarly for a polycrystalline sample containing isolated three spin clusters, the normalized zero- and double-quantum coherence intensities averaged over all powder orientations can be expressed as follows:

$$I_{0,powder} \sim \frac{2}{3} + \frac{1}{3}\sqrt{\frac{\pi}{24D_0t}}[\cos(D_0t) + \sin(D_0t)], \tag{4.54a}$$

$$I_{|2|,powder} \sim \frac{1}{3} - \frac{1}{3}\sqrt{\frac{\pi}{24D_0t}}[\cos(D_0t) + \sin(D_0t)], \tag{4.54b}$$

where $D_0=2D_{eff}/(1-3\cos^2\theta)$.

(3) Multiple-spin-1/2 systems. In the case of multiple-spin coupled system, the above analytical method would become very complicated and intractable. It is advantageous to use the power expansion of equation (2.39), equation (4.50) can then be rewritten as follows:

$$\begin{aligned}\hat{\rho}(t) &= \exp(-i\hat{H}_{yx}t)\hat{\rho}(0)\exp(i\hat{H}_{yx}t)\\ &= \hat{\rho}(0) + it[\hat{\rho}(0), \hat{H}_{yx}] - \frac{t^2}{2!}[\,[\hat{\rho}(0), \hat{H}_{yx}\,], \hat{H}_{yx}\,]\\ &\quad - i\frac{t^3}{3!}[\,[\,[\hat{\rho}(0), \hat{H}_{yx}\,], \hat{H}_{yx}\,], \hat{H}_{yx}\,] + \cdots.\end{aligned} \tag{4.55}$$

The nested commutators provide the possible product operators with the number of correlated spins and the order of multiple-quantum coherences. These can be seen clearly by inserting $\hat{\rho}(0)=\hat{I}_z=\sum_{i=1}^{N}\hat{I}_{zi}$ into equation (4-55) and expanding it to the following form [19]:

$$\hat{\rho}(t)=\sum_k \hat{I}_{zk} - \frac{it}{2}\sum_{i\neq j} D_{ij}(\hat{I}_{+i}\hat{I}_{+j}-\hat{I}_{-i}\hat{I}_{-j}) - \frac{t^2}{2}\sum_{i\neq k\neq m} D_{kj}D_{km}(\hat{I}_{zk}\hat{I}_{+j}\hat{I}_{-m}+\hat{I}_{zk}\hat{I}_{-j}\hat{I}_{+m})$$
$$-i\frac{t^3}{3}\sum_{j\neq k\neq m\neq l} D_{kj}D_{km}D_{jl}(\hat{I}_{zj}\hat{I}_{zk}\hat{I}_{+m}\hat{I}_{+l}-\hat{I}_{zj}\hat{I}_{zk}\hat{I}_{-m}\hat{I}_{-l})$$
$$+i\frac{t^3}{6}\sum_{j\neq k\neq m\neq l} D_{kj}D_{km}D_{kl}(\hat{I}_{+j}\hat{I}_{+k}\hat{I}_{+l}\hat{I}_{-m}-\hat{I}_{-j}\hat{I}_{-k}\hat{I}_{-l}\hat{I}_{+m})+\cdots. \quad (4.56)$$

In this calculation the raising and lowering operators and their commutation rules $[\hat{I}_z,\hat{I}_\pm]=\pm\hat{I}_\pm$, and $[\hat{I}_\pm,\hat{I}_\mu]=\pm 2\hat{I}_\pm$ were used for obtaining the result. In this expression, every product operator represents a family of coupled spins characterized by a spin number K and a coherence order n, e.g. the product operator, $\hat{I}_{+j}\hat{I}_{+k}\hat{I}_{+l}\hat{I}_{-m}$, expresses a four-spin +2 (n = +1+ 1+1−1 = +2)-quantum coherence. A 4-spin +2-QC includes other combinations such as $\hat{I}_{+j}\hat{I}_{+k}\hat{I}_{-l}\hat{I}_{+m}$, $\hat{I}_{+j}\hat{I}_{-k}\hat{I}_{+l}\hat{I}_{+m}$, $\hat{I}_{-j}\hat{I}_{+k}\hat{I}_{+l}\hat{I}_{+m}$. This equation shows that higher order coherences are generated under excitation of the time-reversible eight-pulse sequence from the equilibrium spin state. From equation (4-56) we can also see the sequential growth and development of coherences with time, e.g. at the time order t = 0 only single-spin zero-quantum coherence, $\hat{I}_{kz}$, is present, then 2-spin double-quantum coherence $\left(\hat{I}_{+i}\hat{I}_{+j}-\hat{I}_{-i}\hat{I}_{-j}\right)$ develops proportional to time t, followed by the appearance of 3-spin zero-quantum coherence at the time order t^2, and finally 4-spin double-quantum coherences are generated when the time progressively increased to the order t^3. This shows that the K-spin coherence grows with t^{K-1}.

4.3.3.3 Detection of MQC

Having discussed the generation of MQC in section 4.3.3.2, now in this section we will focus our attention upon the detection of MQC. For this goal, let us first follow the change of MQC in the whole process of our two-dimensional time-domain multiple-quantum experiments. As

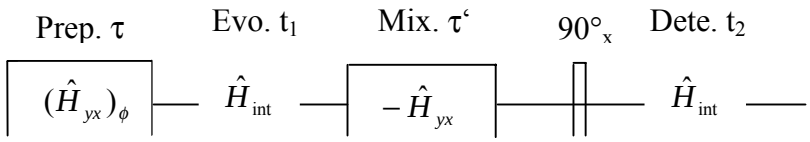

Figure 4.6*. General form of multiple-quantum pulse sequence. Multiple-quantum coherences are created by the preparation period propagator U(τ) and respond to local fields during the evolution period t_1. The mixing period propagator V(τ') transfers multiple-quantum coherences into single-spin zero-quantum coherence. The 90° read pulse rotates the magnetizations into transverse magnetization in detection period for acquisition of the signals modulated by the multiple-quantum coherences as a function of t_1.*

shown schematically in Figure 4.6, our two-dimensional time-domain multiple-quantum experiment is divided into the preparation period (τ), evolution period (t_1), mixing period (τ') and detection period (t_2). For a simple description, at the moment we neglect relaxation effects on the MQC generation and detection, later we will discuss its effects in the MQC dynamics section. During the preparation period, the multiple-quantum coherences are excited from $\hat{\rho}(0)=\hat{I}_z$. The average Hamiltonian $\hat{H}_{yx}$ governs the time evolution of the spin system, the density operator of the spin system at the end of the preparation period $\hat{\rho}(\tau)$ has evolved into the following form:

$$\hat{\rho}(\tau)=\hat{U}(\tau)\hat{\rho}(0)\hat{U}^{-1}(\tau)=\hat{U}(\tau)\hat{I}_z\hat{U}^{-1}(\tau)\,, \tag{4.57}$$

directed by the preparation propagator:

$$\hat{U}(\tau)=\exp(-i\hat{H}_{yx}\tau)\,. \tag{4.58}$$

During the evolution period t_1, the MQC generated in the preparation period τ evolve at their characteristic frequencies determined by the internal Hamiltonian $\hat{H}_{\text{int}}$. At the end of the evolution period, the density operator of the spin system can be written as follows:

$$\hat{\rho}(\tau,t_1)=\hat{U}(t_1)\hat{U}(\tau)\hat{I}_z\hat{U}^{-1}(\tau)\hat{U}^{-1}(t_1)\,, \tag{4.59}$$

where

$$\hat{U}(t_1)=\exp(-i\hat{H}_{yx}t_1)\,. \tag{4.60}$$

During the mixing period, the MQC are forced back to single-spin zero-quantum coherences. This is done by using the same pulse sequence as in the preparation period but all the 90° pulses are 90° phase shifted which change the effective Hamiltonian to $-\hat{H}_{yx}$. By doing so we get an effective mixing propagator,

$$\hat{V}(\tau')=\hat{U}^{-1}(\tau')=\exp(i\hat{H}_{yx}\tau')\,, \tag{4.61}$$

which undoes the effect of the preparative propagator on the spin system and pushes the spin system back to single-spin zero-quantum coherences. At the end of the mixing period τ', the density operator develops into the following state:

$$\hat{\rho}(\tau,t_1,\tau') = \hat{V}(\tau')\hat{U}(t_1)\hat{U}(\tau)\hat{I}_z\hat{U}^{-1}(\tau)\hat{U}^{-1}(t_1)\hat{V}^{-1}(\tau') . \qquad (4.62)$$

The mixing propagator would completely transfer the coherences back to the initial single-spin zero-quantum coherence when $\tau' = \tau$ and if there had been no evolution period (i.e. if t_1=0) and relaxation. This process is called the "time reversal" procedure[7], which ensures that all generated multiple-quantum coherences in the preparation period return to their initial coherences and enables all transition lines to be phased with respect to each other, thereby avoiding any cancellations due to differences in sign and enhancing the signal-to-noise ratio. Very high order coherence in solid such as adamantane can be obtained through the incorporation of the time-reversible pulse sequence. The final $\pi/2$ pulse rotates the z magnetization (the observable $\hat{S}_{ob} = \hat{I}_z$) into the transverse plane for acquisition during the detection period t_2. All multiple-quantum coherences, possibly modified in amplitude and/or phase during the evolution period t_1, contribute to the amplitude of the detected single-spin single-quantum coherences. In the density operator formalism, the observable $S_{zz}(\tau, t_1,\tau')$ (or the intensity of the signal) at the end of the mixing period is proportional to the trace of the product of the observable $\hat{S}_{ob} = \hat{I}_z$ and the density operator developed at this time (equation (4.62))[19]:

$$\begin{aligned} S_{zz}(\tau,t_1) &= Tr\{(\hat{S}_{ob})\hat{V}(\tau)\hat{U}(t_1)\hat{U}(\tau)\hat{\rho}(0)\hat{U}^{-1}(\tau)\hat{U}^{-1}(t_1)\hat{V}^{-1}(\tau))\} \\ &= Tr\{\hat{U}(\tau)\hat{I}_z\hat{U}^{-1}(\tau)\exp(-i\hat{H}_{\text{int}}t_1)\hat{U}(\tau)\hat{I}_z\hat{U}^{-1}(\tau)\exp(i\hat{H}_{\text{int}}t_1)\} \\ &= \sum_{i,j}\langle i|\hat{U}(\tau)\hat{I}_z\hat{U}^{-1}(\tau)|\,j\rangle\langle j|\exp(-i\hat{H}_{\text{int}}t_1)\hat{U}(\tau)\hat{I}_z\hat{U}^{-1}(\tau)\exp(i\hat{H}_{\text{int}}t_1)|\,i\rangle \\ &= \sum_{i,j}\langle i|\hat{U}(\tau)\hat{I}_z\hat{U}^{-1}(\tau)|\,j\rangle\langle j|\hat{U}(\tau)\hat{I}_z\hat{U}^{-1}(\tau)|\,i\rangle\exp(-i(\omega_j-\omega_i)t_1), \end{aligned} \qquad (4.63)$$

where |i> and |j> are eigenfunctions of $\hat{H}_{\text{int}}$ with eigenvalues ω_i and ω_j. The term $\hat{U}(\tau)\hat{I}_z\hat{U}^{-1}(\tau)$ is self-conjugate, i.e. $(\hat{U}(\tau)\hat{I}\,\hat{U}^{-1}(\tau))^+ = \hat{U}(\tau)\hat{I}_z\hat{U}^{-1}(\tau)$, so equation (4.63) can be simplified as follows:

$$S_{zz}(\tau,t_1) = \sum_{i,j}\left|\langle i|\hat{U}(\tau)\hat{I}_z\hat{U}^{-1}(\tau)|\,j\rangle\right|^2\exp(-i\omega_{ji}^{(1)}t_1) \qquad (4.64)$$

where $\omega_{ji}^{(1)}=\omega_j-\omega_i$ is the transition frequency. In the above equation, the invariance of the trace to cyclic permutation, i.e. the following relationships: $(ABC)^+ = C^+B^+A^+$, $Tr(ABC)=Tr(CAB)=Tr(BCA)$, and $1=\sum_j |j\rangle\langle j|$ have been utilized for getting the result.

The obtained signal expressed above contains theoretically all the information about the frequencies of the rotating frame multiple-quantum transitions, but in practice we do the MQC experiment on resonance, so the contributions of the various coherence orders can not be separated due to the broad distribution of the energy levels in the strongly coupled spin system of a solid. Usually the TPPI [23,24] (time proportional phase incrementation) method is used to separate the different coherence orders. It is achieved by phase shifting the pulses in the preparation period τ in concert with the time increment t_1 in the evolution time period. This effects as a rotation of the preparation propagator around the z-axis in the rotating frame:

$$\hat{U}_\phi(\tau)=\exp(i\phi\hat{I}_z)\hat{U}(\tau)\exp(-i\phi\hat{I}_z)\,, \tag{4.65}$$

where ϕ is the phase of the pulses in the preparation period. Thus an artificial offset term is introduced into the evolution period. The density operator developed at the end of mixing period has the form:

$$\begin{aligned}\hat{\rho}(\tau,t_1,\phi)&=\hat{V}(\tau)\hat{U}(t_1)\hat{U}_\phi(\tau)\hat{\rho}(0)\hat{U}_\phi^{-1}(\tau)\hat{U}^{-1}(t_1)\hat{V}^{-1}(\tau)\\&=\hat{V}(\tau)\hat{U}(t_1)\hat{U}_\phi(\tau)\hat{I}_z\hat{U}_\phi^{-1}(\upsilon)\hat{U}^{-1}(t_1)\hat{V}^{-1}(\tau)\,,\end{aligned} \tag{4.66}$$

and the final signal can be expressed as[19]:

$$\begin{aligned}S_{zz}(\tau,t_1,\phi)&=Tr\{(\hat{S}_{ob})(\hat{V}(\tau)\hat{U}(t_1)\hat{U}_\phi(\tau)\hat{\rho}(0)\hat{U}_\phi^{-1}(t_1)\hat{V}^{-1}(\tau))\}\\&=Tr\{(\hat{U}(\tau)\hat{I}_z\hat{U}^{-1}(\tau))(\exp(-i\hat{H}_{\text{int}}t_1)\exp(i\phi\hat{I}_z)\hat{U}(\tau)\hat{I}_z\hat{U}^{-1}(\tau)\exp(-i\phi\hat{I}_z)\exp(i\hat{H}_{\text{int}}t_1))\}\\&=\sum_n\sum_{i,j}\left|\langle i|\hat{U}(\tau)\hat{I}_z\hat{U}^{-1}(\tau)|j\rangle\right|^2\exp(in_{ji}\phi)\exp(-i\omega_{ji}^{(1)}t_1)\\&=\sum_n\sum_{i,j}\left|\langle i|\hat{U}(\tau)\hat{I}_z\hat{U}^{-1}(\tau)|j\rangle\right|^2\exp\left[-i\left(\omega_{ji}^{(1)}-n_{ji}\frac{\Delta\phi}{\Delta t_1}\right)t_1\right],\end{aligned} \tag{4.67}$$

where $n_{ji}=M_j-M_i$ is the coherence order, $\Delta\phi$ and Δt_1 are the phase increment in the preparation period and the time increment in the evolution period, respectively. In the TPPI experiment, the phase and time dimensions are collapsed into one through the relation $\phi=\frac{\Delta\phi}{\Delta t_1}t_1=\Delta\omega t_1$, Fourier transformation with respect to t_1 gives the spectrum of each order with apparent offset $n\times\Delta\omega$. All lines within a given order n have the same additional artificial

frequency $n\frac{\Delta\phi}{\Delta t_1}$, and the line of neighbouring order differs in this artificial frequency by $\pm\frac{\Delta\phi}{\Delta t_1}$. The artificial frequencies allow the separation of the different coherence orders. The spectral width of the multiple-quantum spectrum is given by $1/\Delta t_1$, and the number of orders detected, $\pm n_{max}$, is determined by the phase increment, $\Delta\phi = 2\pi / 2n_{max}$[17,19]. Thus small Δt_1 and large $\Delta\phi$ give better separation of different orders of multiple-quantum coherences and for detecting very high coherence orders Δt_1 should be very small.

There are cases in which the MQC evolution period can be kept to zero or to a constant time in the MQC experiment such as in MQC filtration experiments[21,22]. In this case only one cycle of the phase increment need to be done. Thus experimental time can be saved. Every coherence order is then presented by a point in the spectrum. In the case $t_1 = 0$, the signal expression of (4.67) becomes:

$$\begin{aligned} S_{zz}(\tau,\phi) &= Tr\{(\hat{S}_{ob})(\hat{V}(\tau')\hat{U}_{\phi}(\tau)\hat{\rho}(0)\hat{U}_{\phi}^{-1}(\tau)\hat{V}^{-1}(\tau'))\} \\ &= Tr\{(\hat{U}(\tau)\hat{I}_z\hat{U}^{-1}(\tau))(\exp(i\phi\hat{I}_z)\hat{U}(\tau)\hat{I}_z\hat{U}^{-1}(\tau)\exp(-i\phi\hat{I}_z))\} \\ &= \sum_n\sum_{i,j}\left|< i \mid \hat{U}(\tau)\hat{I}_z\hat{U}^{-1}(\tau) \mid j >\right|^2 \exp(in_{ji}\phi). \end{aligned} \tag{4.68}$$

Instead of the Fourier-Transformation-pair time and frequency, now the Fourier-Transformation-pair becomes phase and multiple-quantum coherence order.

In detection period t_2 either one point or many may be sampled to obtain the modulated signal. When a complete single-quantum signal is recorded, the development of the density operator in the detection period under the effect of the internal Hamiltonian can be described:

$$\hat{\rho}(\tau,t_1,\tau',t_2) = \hat{U}(t_2)\hat{\rho}(\tau,t_1,\tau')\hat{U}^{-1}(t_2), \tag{4.69}$$

where $\hat{U}(t_2) = \exp(-i\hat{H}_{int})$ is the propagator in the detection period. From equation (4.71) the two-dimensional time domain signal can be obtained:

$$S(\tau,t_1,\tau',t_2) = \sum_{jilm} Z_{jilm}\exp(-i\omega_{ji}^{(1)}t_1)\exp(-i\omega_{lm}^{(2)}t_2), \tag{4.70}$$

where Z_{jilm} is the coherence amplitude which is a real number in the case of time-reversal condition. Fourier transformation with respect to both time variables produces a two-dimensional frequency map showing the connection between the multiple-quantum frequencies during evolution and the single-quantum frequencies in the detection period. Peaks appearing at the intersection of two frequencies indicate a transfer of coherence

between multiple-quantum and single-quantum components oscillating at $\omega_{ji}^{(1)}$ and $\omega_{lm}^{(2)}$. The projection of the spectrum in either direction, accomplished by summing all cross sections parallel to the desired axis, yields either the complete multiple-quantum spectrum $S[\omega^{(1)}]$, or the single-quantum spectrum, $S[\omega^{(2)}]$, "filtered" through the various orders of multiple-quantum coherences.

4.4. Multiple-spin multiple-quantum spin-1/2 dynamics

4.4.1 Excitation dynamics of MQC

From equation (4.55) and (4.56) we can see two features of the MQC development: one is the sequential growth of multiple-spin coherences in the ascending terms of the density operator $\hat{\rho}(t)$ with increasing excitation time, the other is that the dipolar coupling constants appear as a multiplicative manner accompanying the formation of the multiple-spin coherences, so the lattice parameters r_{ij} and θ_{ij} will ultimately control and distinguish between the various n-quantum coherences. At early excitation times, the generation of MQC are dominated by the largest dipolar coupling and their products[26]. Thus for a finite excitation time, coherences can not be treated equally as assumed in the Gaussian statistical mode[6,27-29] as discussed sooner later, only in the limit of an infinite excitation time will all the coherences contribute equally to the spin dynamics[26, 30].

Murdoch et al.[31] computed numerically the average coherence magnitude as a function of the excitation times for n = 2, 3 and 6 using the three-pulse sequence, they had found that the initial development of each order proceeds according to the expected power law, with the higher orders requiring longer excitation times to attain their limiting values, after an induction time, when $2\pi\tau \times$ (average dipolar coupling in Hz) $\approx \pi/2$ or $\tau \approx (4 \times$ average dipolar coupling$)^{-1}$, all orders of coherences are excited.

The inverse relationship between the duration of excitation and the magnitude of the coupling reflects the propagation time that must elapse before any two spins becomes fully aware of each other. A network of interactions thus develops around each initially independent spin, expanding with the passage of time as partners with smaller and smaller coupling constants are added. The network may radiate outward from a shared central spin, or develop as a chain of couplings along the lines as depicted in Figure 4.7 (a) and (b), respectively.

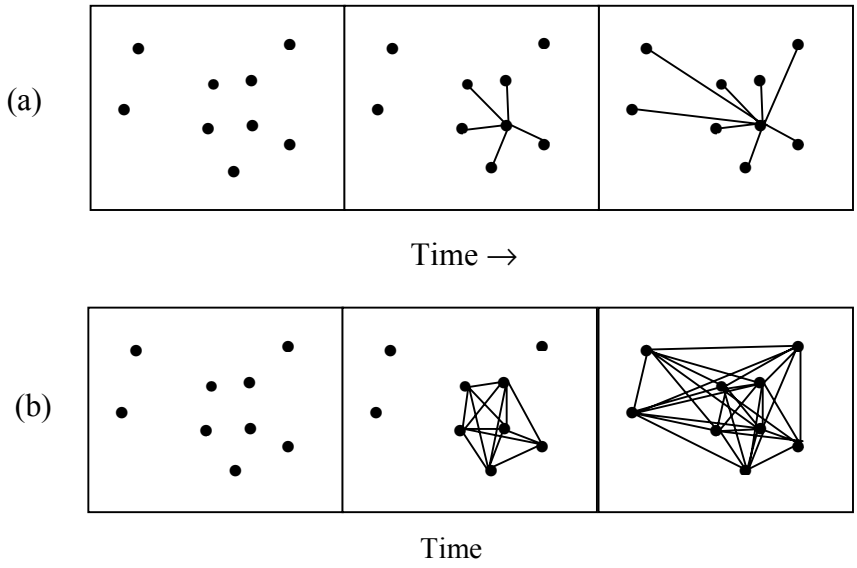

Figure 4.7*. Symbolic representation of the growth of a coupling network with time. Pairwise couplings gradually become effective as time passes, either (a) developing from a central spin and expanding outward, or (b) moving from spin to spin , or both of them.*

From above we know that the higher order of multiple-spin multiple-quantum coherences require longer time to develop, more spins become correlated with increasing excitation time. The intensities of MQC at long excitation time are determined by coherence magnitudes attained during the preparation and mixing periods, their frequencies are determined by the eigenvalues of the Hamiltonian during the evolution period. To predict the effective size, $N_{eff}(t)$, of the spin system, i.e. the number of correlated spins at time t, a statistical model was developed[6,17,27-29,31-33]: it is assumed that under excitation all allowed n-quantum coherences in a complicated system (the spin number N>6) can be excited with equal amplitudes but with

random phases, and the intensity of the n-quantum coherences, I[n, N_{eff}(t)] at long excitation time t, can be described by a Gaussian distribution[6]:

$$I[n, N_{eff}(t)] = \frac{4^{N_{eff}}}{\sqrt{N_{eff}\pi}} \exp[-n^2 / N_{eff}(t)\}], \qquad (4.71)$$

from which the instantaneous effective size of the system can be inferred. In the absence of relaxation, the theoretically N_{eff}(t) would approach the true number N of the spins in the system. Using the detection of the effective number of dynamically coupled spins, the distribution of nuclei in a solid can be investigated. Usually three generic classes of behaviour have been observed for N_{eff}(t): (1) saturation in N_{eff}(t) implies the presence of isolated clusters of spins, (2) unbounded growth of the correlated spins are observed in extended spin networks, and (3) saturation behaviour seen at early excitation times, followed by unbounded growth, indicates the occurrence of coupled clusters of spins. This model tell us the end results of the response, but it fails to give a picture about the formation process of multiple-quantum coherences in a large dipolar spin system. To this end one approach (random walk model)[6, 34] is to replace the Liouville-von Neumann equation which has oscillatory solutions, with a modified equation that has exponential solutions instead. In this condensed or reduced Liouville space the number of degrees of freedom is reduced and the remaining degrees of freedom are collected into a vector g, the evolution of the system is described by the following equation[6]:

$$dg/dt=Rg, \qquad (4.72)$$

this formulation is equivalent to a generalized multisite exchange model in which the elements of R give the rate of change from one component of g to another. The components g_{Kn} of the vector g represent the coherence modes: K stands for the number of single-spin operators and n for the number of quanta involved in that coherence mode, for example, in a two spin system, the two kinds of the coherence modes $\hat{I}_{+1}\hat{I}_{z2}$ and $\hat{I}_{z1}\hat{I}_{+2}$ regarding two-spin one-quantum coherences can be represented as g_{21}. In this representation the Liouville space is reduced into a two-dimensional grid plane in which each point denotes an entire family g_{Kn}. K runs from 1 through N, and |n| runs from 0 through K for each set.

The Hamiltonian determines the selection rules and rates which control the migration through the reduced Liouville space: a bilinear q-quantum Hamiltonian adds or subtracts one spin at a time to a multiple-spin mode, and connects states differing by q quanta. In this case, a given

set of coherence modes g_{Kn} can develop into the four new sets $g_{K\pm1;n\pm q}$. The corresponding selection rules can be summarized as follows:

$$\Delta K = \pm 1,\ \Delta n = \pm 2 \text{ for } \hat{H}_{yx}, \tag{4.73}$$

$$\Delta K = \pm 1,\ \Delta n = 0, \pm 2 \text{ for } \hat{H}_{xx} \text{ and } \hat{H}_{yy}, \tag{4.74}$$

$$\Delta K = \pm 1,\ \Delta n = 0 \text{ for } \hat{H}_{zz}. \tag{4.75}$$

In Figure 4.8 the pathways through the reduced Liouville space under the three different Hamiltonians are diagrammed, in which the initial condition $\hat{\rho}(0)$ is taken to be equal to $\hat{I}_+$ (K=1, n=1) for the secular operator $\hat{H}_{zz}$ (a) and nonsecular operator $\hat{H}_{yx}$ (d) and equal to $\hat{I}_z$

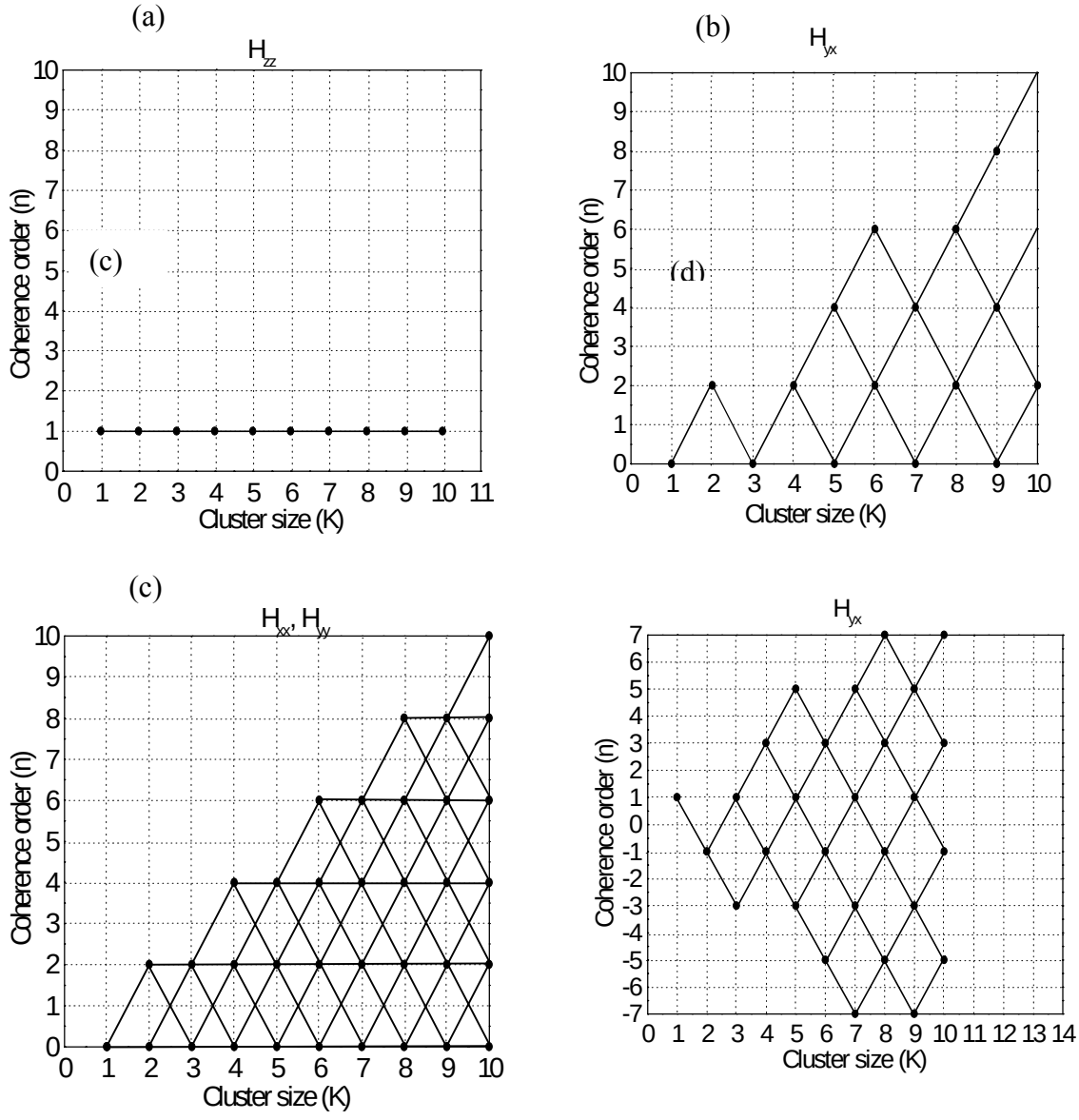

Figure 4.8*. Schematic representation of the routes through the reduced Liouville space under* $\hat{H}_{zz}$ *(a)* $\hat{H}_{xx}, \hat{H}_{yy}$ *(b), and* $\hat{H}_{yx}$ *(c) (d).*

(K=1, n=0) for the nonsecular operators $\hat{H}_{xx}, \hat{H}_{yy}$ (b), and $\hat{H}_{yx}$ (c). From Figure 4.8(c) and (d) we can see that in the case of the nonsecular operator $\hat{H}_{yx}$ to excite the MQC, two different processes occur: when the initial density operator $\hat{\rho}(0)$ is proportional to $\hat{I}_z$ before the attacking of $\hat{H}_{yx}$, only the even-order MQC are developed from the spin system under the effect of the bilinear raising and lowering operators $\hat{I}_{+i}\hat{I}_{+j}$ and $\hat{I}_{-i}\hat{I}_{-j}$, while the odd-order MQC can be excited from the spin system when the initial density operator $\hat{\rho}(0)$ is proportional to $\hat{I}_+$ before the attacking of $\hat{H}_{yx}$[19, 35]. (d)

Make a closer examination of Figure 4.8(c), we can find the following limitation in application for spin counting in small spin systems: the highest order n (n-quantum) = N (the total spin number in spin network) coherence can not be excited from an initial density operator $\hat{\rho}(0)$ proportional to $\hat{I}_z$ under the nonsecular Hamiltonian $\hat{H}_{yx}$, the ability to achieve N quantum coherence via other MQ propagators can be even more restrictive; that is means that n-quantum coherence cannot be achieved among n = 4k (k is a positive integer) dipolar coupled spins. Thus four-quantum coherence cannot be developed among an isolated cluster of four coupled spins. This situation is improved[35] in Figure 4.8(d) in which a prepulse creates an initial density matrix proportional to single-quantum coherence $\hat{I}_+$. For such spin counting experiments it would be desirable to use the two-spin single-quantum Hamiltonian[36] $\hat{H}_{zx} = \frac{D_{ij}}{3}(\hat{I}_{z1}\hat{I}_{x2} + \hat{I}_{x1}\hat{I}_{z2})$ to excite all orders of multiple-quantum transitions except the highest-order transitions, from an initial condition one-spin zero-quantum coherence $\hat{I}_{zi}$. Using the same pulse sequence the highest possible transition can be excited by changing the initial condition to one-spin single-quantum coherence $\hat{I}_{xi}$.

The rate of MQ coherence development depends on the strength and time dependence of each pairwise homonuclear dipolar coupling as well as the number of such pairs. In addition to this, it also depends on the effective Hamiltonian which are used to excite the MQC, e.g. higher orders develop more quickly under $\hat{H}_{yx}$[25], maximizing the number of spins that can be

correlated before relaxation effects become significant. But in practice, the time-reversible eight-pulse sequence has a too long cycle time. In our laboratory we only reached a shortest cycle time t_c = 54 μs and 67.2 μs for static and MAS experiments, respectively. Usually condensed materials, e.g., semicrystalline polymers have a typical T_2 time of the crystalline phases in the range of 8-12 μs. In this case, after only one cycle time, the coherences from spins in the rigid phases have completely relaxed during the early excitation time. So we cannot observe a response from rigid phases, we will treat this point in later chapters.

4.4.2 The distribution of dipolar coupling constants and their products

From equation (4.56) we can see that the multiple-spin coherences are weighed by products of dipolar coupling constants. In recognition that the distributions of dipolar coupling constants and their products are extremely wide, Lacelle et al.[12,26,30] made a detailed investigation of the properties of these distributions and their effect on the MQC generation. They found that in spin networks the distributions of dipolar coupling constants and their products are characterized by asymmetry associated with extreme widths, this is very important for understanding MQ NMR spin dynamics.

In one-dimensional solids, the sum of dipolar coupling constants can be obtained analytically, for example, for an infinite crystalline one-dimensional chain of spins with lattice parameter r oriented perpendicular to the Zeeman field, the average dipolar coupling constants per spin $<D_s>$ is as follows:

$$< D_s >= 2\sum_{k=1}^{\infty} \frac{1}{2}\gamma^2\eta^2 (kr)^{-3} \approx 1.20\gamma^2\eta^2 / r^3 . \qquad (4.76)$$

In this case, 83% of the average is determined by the value of two nearest neighbor couplings out of an infinity of couplings.

In three-dimensional solids, the sum of dipolar coupling constants can be approximated by:

$$\sum_{i>j}^{N} D_{ij} \propto \int_r (1/r^3) r^2 dr = \ln r . \qquad (4.77)$$

For an infinite large sample, the lattice sum diverges, while for finite spin networks the sum is conditionally convergent, i.e., it depends on the sample shape.

The distribution of dipolar coupling constants is depicted in Figure 4.9, it shows the distribution of the absolute values of dipolar coupling constants. One can find the following feature: the average <|D|> is sensitive to the largest coupling constant and determined by the

coupling constants in the tail of the distribution, while the most probable value $|D|_{MPV}$ depends mainly on the small and numerous long-range couplings. Products of the dipolar coupling constants show similar features, except the distributions are even wider.

So Lacelle[30] reached the following conclusion: In multiple-quantum NMR experiments, the conditions assumed by the Gaussian model is never really achieved. Dipolar coupling constants and their products contribute to the time development of the density operator according to their magnitude. Hence, while the strongest coupling constants are fewest in number, they should nevertheless dominate the spin dynamics at early excitation times. MQC measurements were interpreted to probe either the most probable (usually in large spin networks) or average (usually in small spin system) values of products of coupling constants in multiple correlations.

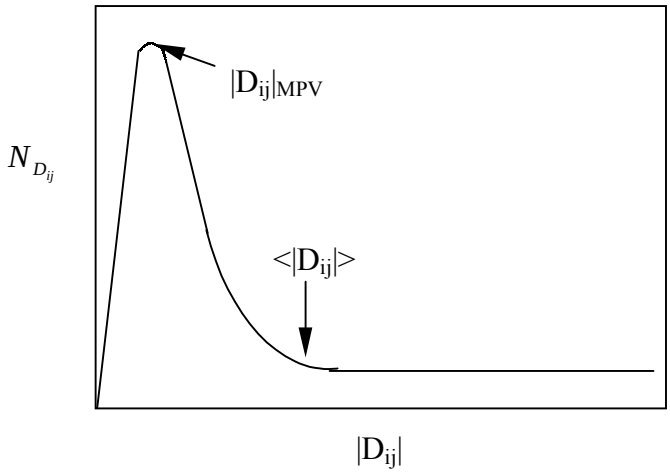

Figure 4.9*. Schematic representation of the distribution of the absolute values of dipolar coupling constants in an N-spin system.*

4.4.3 The relaxation effect on the MQC development

Till now in our discussion of MQC generation and detection we have ignored the relaxation processes that restore a perturbed spin system to its original state of equilibrium. In reality coherences and nonequilibrium population differences inevitably disappear, which often decay exponentially (but not always) with characteristic time constants. Theoretically, every coherence term in the density operator has associated with it an individual transverse relaxation time T_2, while every population term has associated with it a longitudinal relaxation time T_1. These relaxation processes, arising typically from the motions of the spins or lattice,

are often referred to as irreversible relaxation. The local fields vary randomly with time and reduce the norm of the density operator. These can be accounted for by the addition of specific relaxation terms to the Liouville-von Neumann equation.

Multiple-quantum coherences are affected in different ways by the various relaxation mechanisms: zero-quantum coherences are invariant to any time dependent Hamiltonians linear in $\hat{I}_z$, whereas all other coherences are affected by such Hamiltonian in a way, increasing linearly with n; the total-spin coherences are also invariant to any fluctuations of a bilinear Hamiltonian. Since the multiple-quantum coherences involve many spins, their relaxation is sensitive to correlated local field differences at all the nuclear sites concerned, and therefore provides a measure of the degree to which motion in the system is correlated.

In practice the relaxation processes, especially the transverse relaxation time T_2, constrain the multiple-quantum experiment in diverse ways[12]. One obvious limitation is that it sets an upper limit on the useful length of t_1 (the evolution time), which must vary over several times T_2 to allow an accurate linewidth. Another problem is that the T_2 processes limit the length of the preparation and mixing periods and consequently the number of quanta n. Murdoch and co-workers[11] calculated for dipolar coupled systems of up to eight protons, that with a three-pulse sequence the highest-order coherence typically reaches a maximum in a time τ of less than several times $M_2^{-1/2}$, where M_2 is the second moment of the line. For larger systems, since the distribution of the dipolar couplings affect the generation of higher-order coherence, it is not clear that an estimate with a single parameter like $M_2^{-1/2}$ will be generally useful. In general the smaller the range of the parameters D_{ij}, the easier it is to create high-order coherences, e.g. in adamantane where $\hat{H}_{II}^{D}$ is dominated by only a few near-neighbor intermolecular couplings, very high order MQC are observed using a time reversible sequence[19].

4.5 Coherence transfer pathways and phase cycling

Above we have discussed that all orders of coherence can be excited within the strongly coupled spin-1/2 system. In order to clearly see the processes of MQC generation, it is better to describe the coherence transfer pathways. For this sake, first some notions and properties of MQC are reviewed: in high-field NMR, each eigenstate |r> of the Hamiltonian is characterized by a magnetic quantum number M_r, and each coherence |r><s| is associated with a coherence order of $n_{rs}=M_r-M_s$. Each transition between eigenstates is associated with two

coherences |r><s| and |s><r| which have coherence orders n_{rs} and n_{sr} of opposite sign. In the course of free precession, the quantum number n_{rs} is conserved, while r.f. pulses may cause a coherence transfer from |r><s| to |t><u| and induce a change in coherence order $n_{rs} \rightarrow n_{tu.}$ The density operator terms can be classified by their order n: $\hat{\rho}(t) = \sum_n \hat{\rho}^n(t)$, the summation extends over $-2L \le n \le 2L$, where $L = \sum I_k$ is the sum of the spin quantum numbers of all spins. With this in mind, we can represent the sequence of events in various experiments by coherence transfer pathways such as shown in Figure 4.10. In this representation, free precession proceeds within the levels of this diagram, while pulses induce transition between different coherence orders. All coherence transfer pathways start at thermal equilibrium with n=0 and must end with single-quantum coherence ($n = \pm 1$) to be detectable.

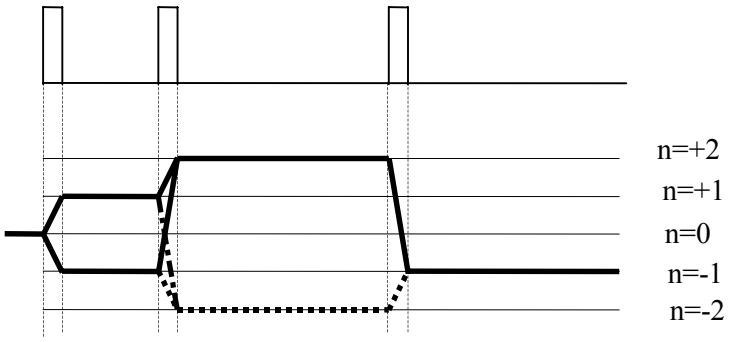

Figure 4.10*. Basic schema of coherence transfer pathways in a three-pulse sequence.*

We know that, the pulse or pulse trains in the preparation period, $\hat{U}_i$, cause a transfer of a particular order of coherence, $\hat{\rho}^n(t_i^-)$, into numerous different orders, $\hat{\rho}^{n'}(t_i^+)$, leading to a branching of the transfer pathways:

$$\hat{U}_i \hat{\rho}^n(t_i^-)\hat{U}_i^{-1} = \sum_{n'} \hat{\rho}^{n'}(t_i^+), \tag{4.78}$$

where t_i^- and t_i^+ refer to the state just before and just after the transformation. Under the phase shifted pulse sequence, the transformation in eq. (4.78) is modified:

$$\hat{U}_i(\varphi_i)\hat{\rho}^n(t_i^-)\hat{U}_i(\varphi_i)^{-1} = \sum_{n'} \hat{\rho}^{n'}(t_i^+)\exp(-i\Delta n_i \varphi_i), \tag{4.79}$$

where $\Delta n_i = n'(t_i^+) - n(t_i^-)$ corresponds to the change in coherence order under the propagator $\hat{U}_i$. Thus the phase shift of a coherence which has undergone a change of order n $\rightarrow$ n' under a propagator $\hat{U}_i(\varphi_i)$ is given:

$$\hat{\rho}(\Delta n_i, \varphi_i) = \hat{\rho}(\Delta n_i, \varphi_i = 0)\exp(-i\Delta n_i \varphi_i). \quad (4.80)$$

This phase-shift will be carried over to n=–1 that is observed in the detection period. The corresponding contribution to the time-domain signal therefore reflects the change Δn_i under the phase-shifted propagator $\hat{U}_i(\varphi_i)$:

$$S(\Delta n_i, \varphi_i, t)=S(\Delta n_i, \varphi_i=0, t)\exp(-i\Delta n_i\varphi_i). \quad (4.81)$$

The total signal is made up of contributions from all pathways:

$$S(\varphi_i, t)=\sum_{\Delta n_i} S(\Delta n_i, \varphi_i, t)= \sum_{\Delta n_i} (\Delta n_i, \varphi_i = 0, t)\exp(-i\Delta n_i \varphi_i). \quad (4.82)$$

To restrict the coherence transfer under $\hat{U}_i$ to a particular change Δn_i in coherence order, we may perform N_i experiments with systematic increments of the r.f. phase φ_i of the propagator:

$$\varphi_i = k_i 2\pi/N_i,\ k_i = 0, 1, ..., N_i-1. \quad (4.83)$$

Each of the N_i signal $S(\varphi_i, t)$ observed in the detection period consists of a superposition, as expressed in equation (4-82). This superposition can be unravelled by a discrete Fourier analysis with respect to the phase φ_i:

$$S(\Delta n_i, t)=\frac{1}{N_i}\sum_{k_i=0}^{N_i-1} S(\varphi_i, t)\exp(i\Delta n_i \varphi_i). \quad (4.84)$$

This weighted linear combination of the signals retains only contributions associated with coherence that has undergone a change Δn_i under the propagator $\hat{U}_i$. However, the procedure does not automatically reject all other pathways, by carrying out a series of N_i experiments, one selects a series of values:

$$\Delta n_i^{(selected)} = \Delta n_i^{(desired)} \pm kN_i,\ k = 0, 1, 2, \ldots. \quad (4.85)$$

Clearly, if a unique Δn_i value must be selected from a range of possible values, N_i must be sufficiently large, and the phase increment $\Delta\varphi = 2\pi/N_i$ correspondingly small.

The weighing of the signals in equation (4-84), which is the key to the selection procedure, can be achieved by one of three strategies: (1) multiplication of the complex recorded signals with complex phase factors $\exp(i\Delta n_i\varphi_i)$, (2) phase-shifting of all pulses in the sequence by an additional phase increment $\varphi = \Delta n\varphi_i$, and addition of the signals without weighing, (3)

shifting of the phase of the receiver reference channel through $\varphi^{ref} = -\Delta n_i \varphi_i$. The selection of double-quantum coherences by using method (2) will be described as an example in next section.

4.6 Double-quantum filtering

For selecting the double-quantum coherences, a suitable phase cycling of the r.f. pulses in the preparation period with respect to the mixing period is necessary. According to the basic principles discussed above, the basis of the phase cycling procedures is the behaviour of multiple-quantum coherences of order n under the influence of a phase shift of ϕ[37, 38]:

$$(n\text{-}QC)_x \xrightarrow{\phi I_z} (n\text{-}QC)_x \cos(n\phi) + (n\text{-}QC)_y \sin(n\phi). \qquad (4.86)$$

Thus a 90° phase shift rotates single-quantum coherences through 90°, double-quantum coherences through 180°, triple-quantum coherences through 270°, and so on. Zero-quantum coherences are invariant to a phase shift. Thus if we use the three-pulse sequence (Fig. 4.3) or the eight-pulse sequence (Fig. 4.5) with the phase ϕ of the pulses in the preparation time period with respect to the mixing period initially at 0° (say at the x-axis of rotating frame), and then increment it by 90° in the next experiment, we obtain the following cycling:

phases (ϕ) of the pulses in the preparation time period with respect to the mixing period:	0°(+x)	90°(+y)	180°(-x)	270°(-y)
phases of zero-quantum coherences:	0°(+x)	0°(+x)	0°(+x)	0°(+x)
phases of double-quantum coherences:	0°(+x)	180°(-x)	0°(+x)	180°(-x)
phases of 4-quantum coherences:	0°(+x)	0°(+x)	0°(+x)	0°(+x)
phases of 6-quantum coherences:	0°(+x)	180°(-x)	0°(+x)	180°(-x)
phases of the pulses in the mixing time period:	0°(+x)	0°(+x)	0°(+x)	0°(+x)
phases of the receiver:	0°(+x)	180°(-x)	0°(+x)	180°(-x)

Subtraction of each alternate experiment achieves selection of order 2 and 6. The contribution of the sixth-order coherences is very small due to the low excitation efficiency compared with

that of the double-quantum coherences, so this phase cycling scheme can be considered as double-quantum selective. This cycle can be repeated four times with incrementation of CYCLOPS phase cycling at every fourth transient, giving a minimum of 16n scans. For further rejection of the sixth-order coherence, an eight-step phase cycling can be used, in this case the phases of the pulses in the preparation time period incremented by 45° in each experiment.

If we are interested only in the double-quantum coherence intensity or only in the 2-QC modulated single-quantum coherences, the pulse sequence can be simplified as an 1-D pulse experiment: it is then an 1-D double-quantum coherence filtered experiment, with the evolution time period t_1 being constant. By doing so experiment time is saved.

If double-quantum coherence line shapes are required, then it is necessary to use the TPPI (time proportional phase incrementation) method in the evolution t_1 time domain in order to get pure phase lineshapes, in addition to the suitable phase cycling to select the desired double-quantum coherences. This can be carried out in the following way: the phase of the pulses in the preparation time period is incremented in steps of 45° with every incrementation of t_1 value in the consecutive experiments. Fourier transformation with respect to t_1 yields the double-quantum coherence linshapes.

4.7 Combination of multiple-pulse sequences with MAS

As discussed in section 3.3, magic angle sample spinning can be used to remove the line broadening due to dipole-dipole interaction and chemically shift anisotropy and to enhance the spectral resolution. It can also be used to obtain high-resolution MQC spectra through suitable adjusting the multiple-pulse sequences.

4.7.1 Combination of the three-pulse sequence with MAS

For short excitation times, usually when the excitation time is shorter than 1/4 revolution period, e.g. when the excitation time is shorter than 25 μs in the case of a MAS frequency of 10 kHz, it is not necessary to synchronize the three-pulse sequence with the MAS. No special precaution or modifications are needed in this case to generate the MQC under the MAS condition. The MQC experiments can be carried out as in the case of a static sample.

Because the cycle time can be adjusted to arbitrary values the three-pulse sequence can excite multiple-quantum coherences for a wide range of ratios between the spin interaction strength and the rotor frequency. But in the case of rotational echos, i.e., when the cycle time is equal to a multiple of the rotation period, multiple-quantum coherences can not be created, due to the fact that the dipolar integral vanishes after one rotor period (see eq. (3.56)). On the other hand, when the cycle time is equal to a multiple of the half rotation period, the efficiency of generating multiple-quantum coherences is low, in this case, only the $\sin\omega_r t$ term in eq. (3.56) is effective in exciting the multiple-quantum coherences.

4.7.2 Synchronization of the eight-pulse sequence with MAS

Although the time-reversible eight-pulse sequence has successfully been applied to static samples, it does not effectively excite multiple-quantum coherence in solids during MAS. This is because magic angle spinning during the preparation and mixing periods causes a "self-time reversal"[39,40], and multiple-quantum coherences disappear after each full rotor period. This is a consequence of the interference of the modulation of the spatial part of the Hamiltonian by MAS and of the modulation of the spin part of the Hamiltonian by the multiple pulse sequence. Much effort has been devoted to trying to overcome this difficulty, such as making the preparation time much shorter than a spinning period, as discussed in previous section, rotor synchronised phase modulation of the pulses, MQ-coherence preparation at off-magic-angle spinning, and use of dipolar-recoupling schemes such as rotational/rotary resonance and dipolar recovery at the magic angle.

In eq. (3.56) we can see that two terms, $\cos(\omega_r t)$ and $\cos(2\omega_r t)$, which modulate the spatial part of the coupling, can be selected to recover the dipolar coupling and excite the multiple-quantum coherences. It is necessary to synchronize the eight-pulse sequence with the sample rotation, which can be carried out through 90° phase shifting of the pulses after each half-rotor period. For example, when the $\sin(\omega_r t)$ term is selected to modulate the Hamiltonian, the eight-pulse sequence should be modified through phase shifting as shown in Figure 4.11 in the case of $t_r = t_c$ (a), $t_r = 2t_c$ (b) and $t_r = 4t_c$ (c), where t_r stands for the time needed for one revolution of the rotor and t_c represents the cycle time of the eight-pulse sequence. This phase shift results in a change in the sign of the spin part of the Hamiltonian which counteracts the

sign change in the spatial part of the Hamiltonian resulting from the action of magic-angle spinning on the dipolar Hamiltonian.

4.8 Combination of multiple pulse sequences with cross-polarization (CP)

For getting high-resolution MQC spectra, another line-narrowing technique, cross-polarization together with high power heteronuclear decoupling, can be combined with the multiple-pulse sequences, as seen in Figure 4.12: after the preparation and mixing periods, the

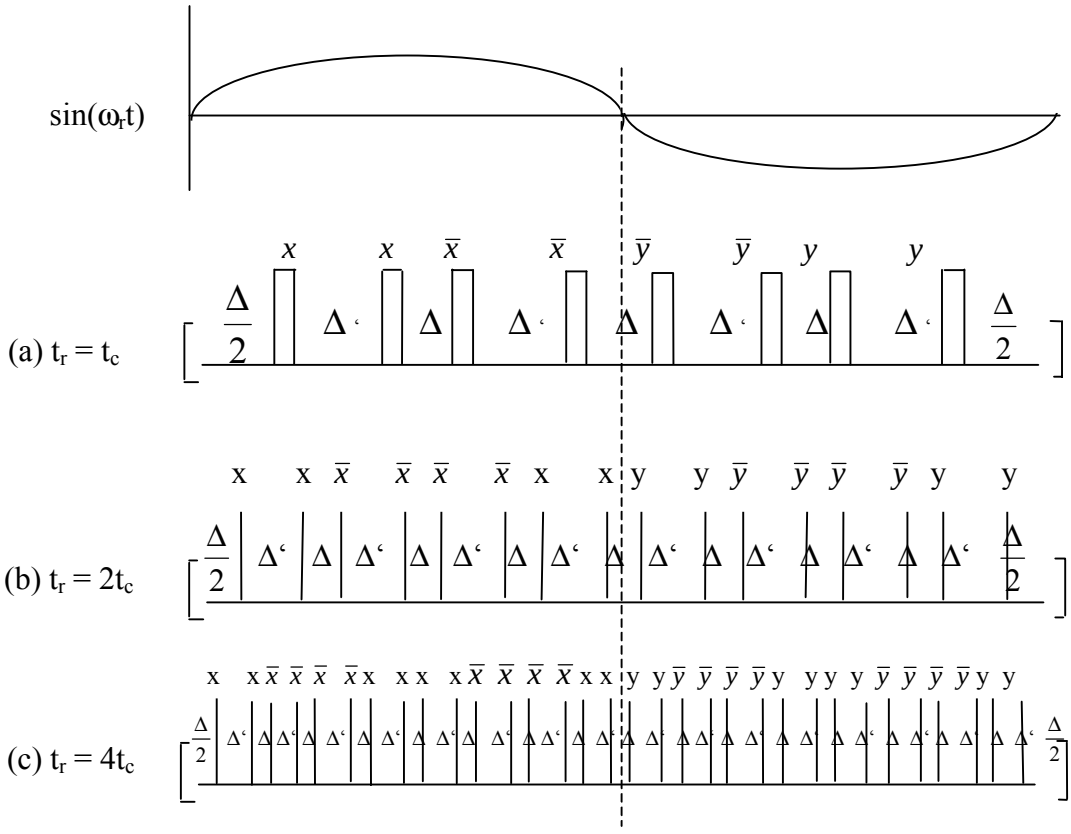

Figure 4.11*. The synchronization of the eight-pulse sequence with the sample rotation in the case of $t_r = t_c$ (a), $t_r = 2t_c$ (b) and $t_r = 4t_c$ (c). During the second half rotation period, the phase of the pulses in the second cycle are 90° shifted with respect to the first cycle.*

Prep. τ Evo. t_1 Mix. τ‘ $90°_x$ Dete. t_2

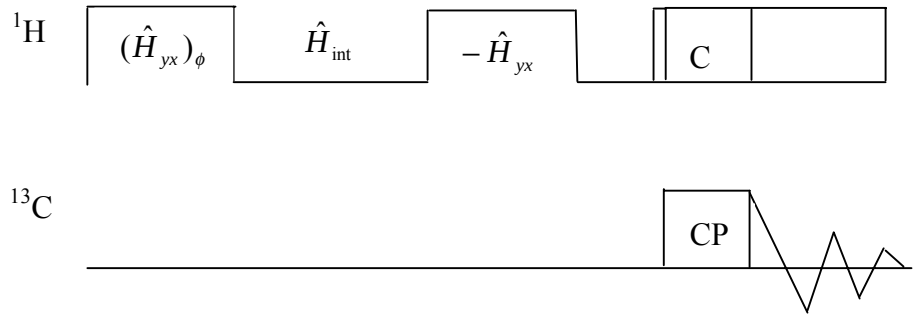

***Figure 4.12**. The schematic representation of the combination of the multiple-pulse sequence with CP. After the mixing period, the desired ^{1}H MQC are transferred to ^{13}C through a cross-polarization process and then detected under the high power proton decoupling during the detection period.*

obtained ^{1}H MQC are then transferred to the ^{13}C through cross-polarization and then under the heteronuclear proton high power decoupling the ^{13}C signal is recorded during the detection period. Fourier transformation of the two-dimensional data set generates a spectrum with proton MQC along the direction F_1, and carbon-13 spectrum in the F_2 direction. This method can be applied to the cases both with and without sample rotation.

References

(1) G. Bodenhausen, Prog. NMR Spectrosc. **14**, 137 (1981**)**.

(2) D. P. Weitekamp, Adv. Magn. Reson.**11**, 111 (1983).

(3) G. P. Drobny, Ann. Rev. Phys. Chem. **36**, 451 (1985**)**.

(4) R. R. Ernst, G. Bodenhausen, and A. Wokaum, Principles of Nuclear Magnetic Resonance in One and Two Dimensions, Volume 14 of International Series of Monographs on Chemistry, **1990**, Oxford University Press, New York.

(5) M. Munowitz and A. Pines, Adv. Chem. Phys. **66**, 1 (1987**)**.

(6) M. Munowitz, Coherence and NMR. JOHN WILEY & SONS, **1988**.

(7) C. P. Slichter, Principles of Magnetic Resonance, Third Enlarged and Updated Edition, Springer-Verlage, **1990**.

(8) T. J. Norwood., Prog. NMR Spectrosc. **24**, 295 (1992).

(9) M. Mehring, Principles of High Resolution NMR in Solids, Springer Verlage, Berlin/New York. **1983**.

(10) M. Munowitz, Encyclopedia of Nuclear Magnetic Resonance, ed. by David M. Grant and Robin K. Harris, **1996**, 1731.

(11) K. K. Gleason, Concepts Magn. Reson. **5**, 199 (1993).

(12) S. Lacelle, Adv. Magn. Opt. Reson. **16**, 173 (1991).

(13) B. C. Gerstein and C. R. Dybowski, Transient Techniques in NMR of Solids, An Introduction to Theory and Practice, Academic Press, **1985**.

(14) U. Haeberlen, High Resolution NMR in Solids, Academic, New York, **1976**.

(15) W. S. Warren, D. P. Weitekamp and A. Pines, J. Chem. Phys. **73,** 2084 (1980).

(16) Y. S. Yen and A. Pines, J. Chem. Phys. **78,** 3579 (1983).

(17) J. Baum, M. Munowitz, A. N. Garroway, and A. Pines, J. Chem. Phys. **83,** 2015 (1985).

(18) Y. Ba and W. S. Veeman, Solid state Nuclear Magnetic Resonance **3,** 249 (1994).

(19) Y. Ba, PhD Thesis, Gerhard-Mercator University of Duisburg, Germany, **1995**.

(20) A. K. Roy and K. K. Gleason, J. Magn. Reson., Series A **120**, 139 (1996).

(21) S. Emid, Physica **128B**, 79 (1985).

(22) S. N. Shykind, J. Baum, S.-B- Liu, A. Pines, A. N. Garroway, J. Magn. Reson. **76**, 149 (1988).

(23) G. Drobny, A. Pines, S. Sinton, D. P. Weitekamp, and D. Wemmer; Faraday Symp. Chem. Soc. **13**, 49 (1979).

(24) G. Bodenhausen, R. L. Vold, and R. R. Vold, J. Magn. Reson. **37**, 93 (1980).

(25) M. Munowitz, Molecular Physical, **71**, 959 (1990).

(26) S. Lacelle, Encyclopedia of Nuclear Magnetic Resonance, ed. by David M. Grant and Robin K. Harris, **1996**, 3154.

(27) J. Baum, M. Munowitz, A. N. Garroway, A. Pines, J. Chem. Phys. **78**, 2015 (1985).

(28) J. Baum, A. Pines, J. Am. Chem. Soc. **108**, 7447 (1986).

(29) B. E. Scruggs, K. K. Gleason, J. Magn. Reson. **99**, 149 (1992).

(30) S. Lacelle and L. Tremblay, J. Chem. Phys. **98**, 3642 (1993).

(31) J. B. Murdoch, W. S. Warren, D. P. Weitekamp, and A. Pines, J. Magn. Reson. **60**, 205 (1984).

(32) M. Munowotz and M. Mehring, Chem. Phys. **116**, 79 (1987).

(33) M. Munowitz and M. Mehring, Solid State Commun. **64**, 605 (1987).

(34) M. Munowitz, A. Pines, and M. Mehring, J. Chem. Phys. **86**, 3172 (1987).

(35) Y. Ba and W. S. Veeman, Israel Journal of Chemistry **32**, 173 (1992).

(36) D. Suter, S. B. Liu, J. Baum and A. Pines, Chemical Physics **114**, 103 (1987).

(37) G. Bodenhausen, H. Kogler, and R. R. Ernst, J. Magn. Reson. **58**, 370 (1984).

(38) S. W. Homans, A Dictory of Concepts in NMR, Clarendon Press, **1992**.

(39) B. H. Meier and W. L. Earl, J. Chem. Phys. **85**, 4905 (1986).

(40) B. H. Meier and W. L. Earl, J. Am. Chem. Soc. **109**, 7937 (1987).

Chapter 5. Multiple-quantum (MQ) NMR experiments on Adamantane

In the previous chapter we have discussed the general principles and methods of multiple-quantum NMR. In this chapter we will study the general features of the multiple-quantum coherences (MQC).

Adamantane ($C_{10}H_{16}$) is chosen as a model sample because it is a typical plastic crystal material and has been intensively investigated. The molecule has a nearly spherical form and performs at room temperature fast and isotropic rotation and tumbling. Thus the interactions between the intra-molecular protons are completely averaged. This leaves sixteen uncoupled protons pro molecule behaving as an effective spin located in the center of each $C_{10}H_{16}$ molecule. These centers form a body-centered tetragonal lattice such that each center has twelve nearest neighbor-centers each at a distance of 6.6 Å, six more intermediate neighbor-centers at 9.34 Å, and an additional sixteen at 11.4 Å[1-3]. This sample forms an uniformly coupled spin cluster of unlimited size. The intermolecular proton-proton pair coupling has a value of about 430 Hz[4] for spin pairs with a distance of 6.6 Å, of 151.7 Hz for spin pairs with a distance of 9.34 Å, and of 83.4 Hz for spin pairs with a distance of 11.4 Å. An effective coupling value of 6.3 kHz for an intermolecule pair protons can be obtained by adding all the squared pair couplings and taking the square root of the sum. The high mobility of the adamantane reduces the rate of relaxational processes among the protons, which would otherwise disturb the development and the observation of high order coherences. Accordingly, adamantane is well suited to be a model sample.

5.1 Experimental

All the experiments were performed at room temperature on a Bruker ASX-400 spectrometer which operates at 400 MHz for ^{1}H. In the MQC experiments, the time-reversible eight-pulse sequence was used to excite the ^{1}H MQC. The 4 mm double-resonance MAS probe was used in the experiments. Adamantane was loaded into a zirconia MAS rotor. The 90° pulses were set to 3.5 μs. Other experimental parameters are given in figure captions.

5.2 Results and discussions

5.2.1 Dipolar coupling measurement

The static ^{1}H spectrum of adamantane (the ^{1}H single quantum spectrum, "SQC or 1QC") shows a broad and featureless Gaussian lineshape, with a linewidth at half height of 13 kHz, as shown in Figure 5.1(a). Figure 5.1(b) shows the static ^{1}H-2QC-filtered-^{1}H-1QC spectrum. It was recorded under the eight-pulse sequence with a short excitation time of 54 μs, other parameters were $t_1 = 0$ and $t_d = 1\mu s$. The ^{1}H-2QC-filtered-1QC spectrum has a doublet pattern. From the selection rule of the eight-pulse sequence as discussed in chapter 4 (Figure 4.8c), we know that the ^{1}H 2QC can be excited from the equilibrium state of the even number spin clusters, such as two-spin, four-spin, six-spin and so on. For two spins, we know from equation (4.58) that the ^{1}H two-spin double-quantum coherences are created during the preparation period under the dipolar coupling D_{ij}, then during the mixing period, the generated two-spin double-quantum coherences are reconverted into 0QC under the effect of the same dipolar coupling D_{ij}. So the intensity of the two-spin 2QC-filtered spectrum is proportional to the square of the dipolar coupling constant, i.e., $I_{2\text{-spin }2QC} \propto (D_{ij})^2$. Similarly, the intensity of the four-spin 2QC-filtered-1QC spectrum is proportional to the square of the

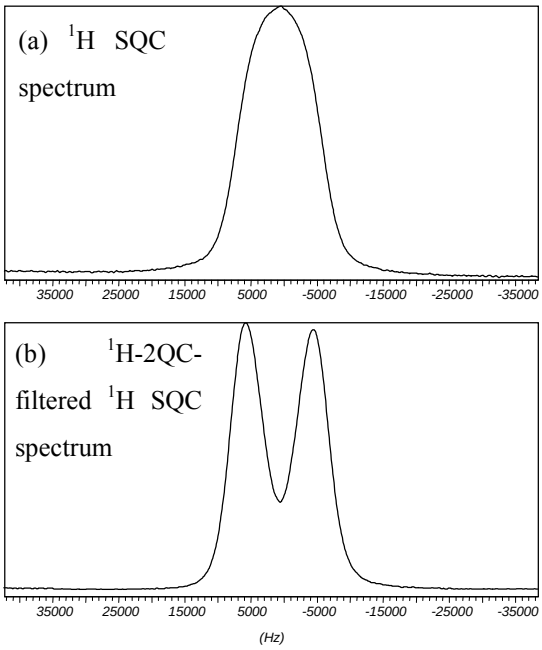

***Figure 5.1**. Static ^1H spectra of adamantane, the length of the 90° pulses were 3.5 μs. (a) Single 90° pulse spectrum, (b) ^1H 2QC filtered ^1H SQC spectrum which was recorded under the eight-pulse sequence with a short excitation time of 54 μs, other parameters were $t_1 = 0$ and $t_d = 1$ μs.*

products of the three dipolar couplings between the active spins, i.e., $I_{4\text{-spin }2QC} \propto (D_{ij} \times D_{im} \times D_{jl})^2$.

We know that the dipolar coupling D_{ij} has an angular term $(3\cos^2\Theta_{ij}-1)$, where Θ_{ij} is the angle between the internuclear vector r_{ij} of the two spins and the external magnetic field B_0. So the strength of the dipolar coupling D_{ij} and the orientation of the vector r_{ij} play an important role in determining the growth of the multiple spin correlations and the intensities of the MQC. As discussed later in section 8.3.1.2, an anisotropic development of MQC is expected due to this angular dependence of the dipolar coupling constant. For constant distances of the proton spin pairs, the growth process in the direction with angles satisfying $0° \leq \Theta_{ij} \leq 35.3°$ and $144.7° \leq \Theta_{ij} \leq 180°$, is expected to be greater than for those with $35.3° < \Theta_{ij} < 144.7°$.

Firstly, we assume that the ^{1}H-2QC-filtered spectrum results from two-spin clusters, the simulated powder ^{1}H-2QC-filtered-1QC spectra are presented in Figure 5.2 (middle column) with different line broadenings from 10.954 to 2190.8 Hz. None of the simulated spectra fits the experimental spectrum, so in this case the ^{1}H-2QC-filtered-1QC spectrum must have contributions from more than two spins.

For more than two spins, it is difficult to simulate the line shape due to the distribution of the dipolar coupling constants and the vector directions of the spin pairs. For simplicity, we assume a polycrystalline sample containing four isolated spins located on a line with the same dipolar coupling constants between the spin pairs. Under this simplified condition, we get the simulated ^{1}H four-spin 2QC-filtered spectra with different line broadenings from 10.954 to 2190.8 Hz as shown in Figure 5.2 (right column). We find that the line shape of the simulated spectrum with line broadening 2190.8 Hz is close to the experimental spectrum (left column).

5.2.2 Spin-diffusion effect after MQC filtering

Spin-diffusion normally occurs when there are spatial magnetization gradients. Spatial magnetization gradients can be generated in heterogeneous solids, when an excitation sequence of pulses and delays has different effects on spins at different locations, for instance because of different relaxation times. After such a sequence spin diffusion will try to even out the magnetization gradient. In the MQC experiment on adamantane we have a slightly different situation while the sample can be considered to be homogeneous, consisting of microcrystallites. In the previous section we saw that spin pairs with small dipolar interactions, while their internuclear axes make an angle with the external magnetic field

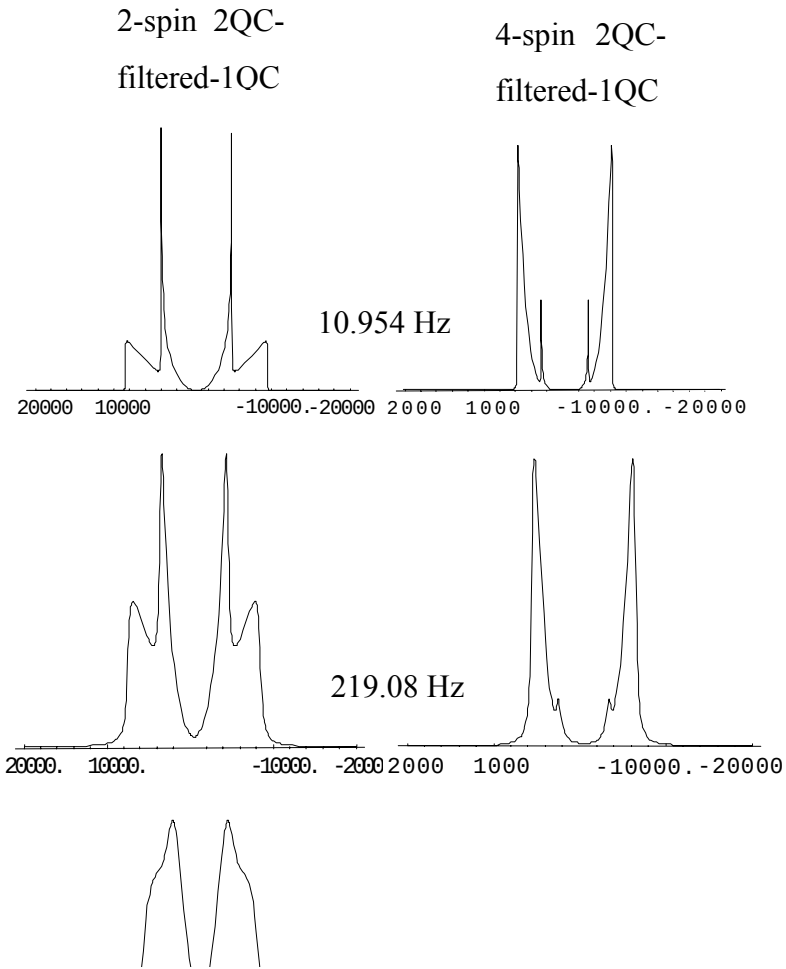

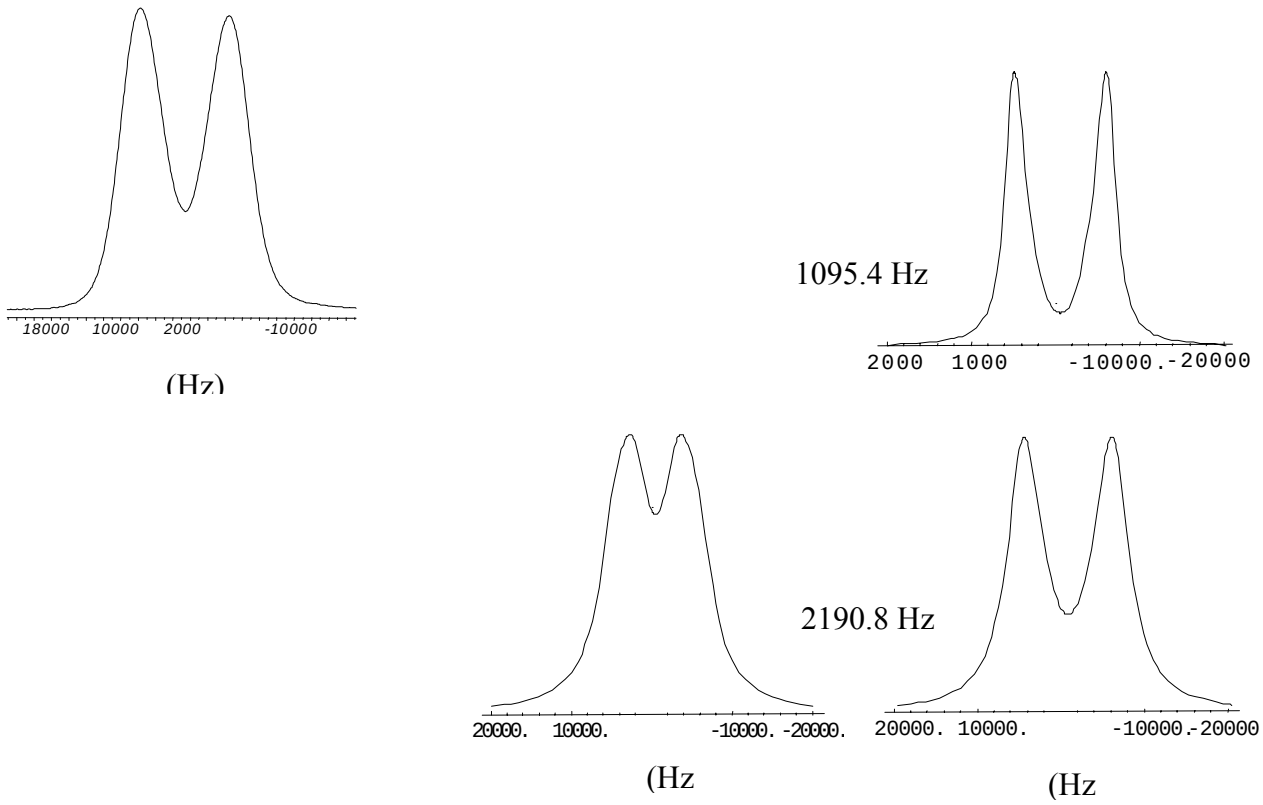

Figure 5.2. *The comparison of the experimental ^{1}H-2QC-filtered-1QC spectrum (left column) with the simulation of the two-spin (middle column) and four-spin (right column) double-quantum filtered spectra by using the different line broadenings as shown in the figure.*

close to the magic angle, contribute little to the 2QC-filtered 1QC-spectrum. The 2QC-filtered 1QC-spectrum results thus mainly from spin pairs with internuclear axes that make angles θ with the external magnetic field unequal to the magic angle $\theta \neq 54.7°$. Spin pairs with $\theta \sim 0$, for instance, will contribute strongly. The magnetization gradient that results from the 2QC-filtering therefore has an orientational instead of a spatial character. Spin diffusion after the filtering process will try to even out these gradients. This effect can be easily detected by inserting a delay time, t_d, between the mixing time period and the last 90° detection pulse[5]. This is also often used in previous work to dephase and eliminate undesired coherences resulting from imperfect pulses during the preparation and the mixing time period. In our case, we checked for the presence of unwanted coherences through the following experiment, in which the 90° read pulse was omitted, and the free induction decay was directly acquired after the mixing time period. We did not find any signal. This indicates that there are no one-spin single-quantum coherences directly after the mixing time period and shows that our

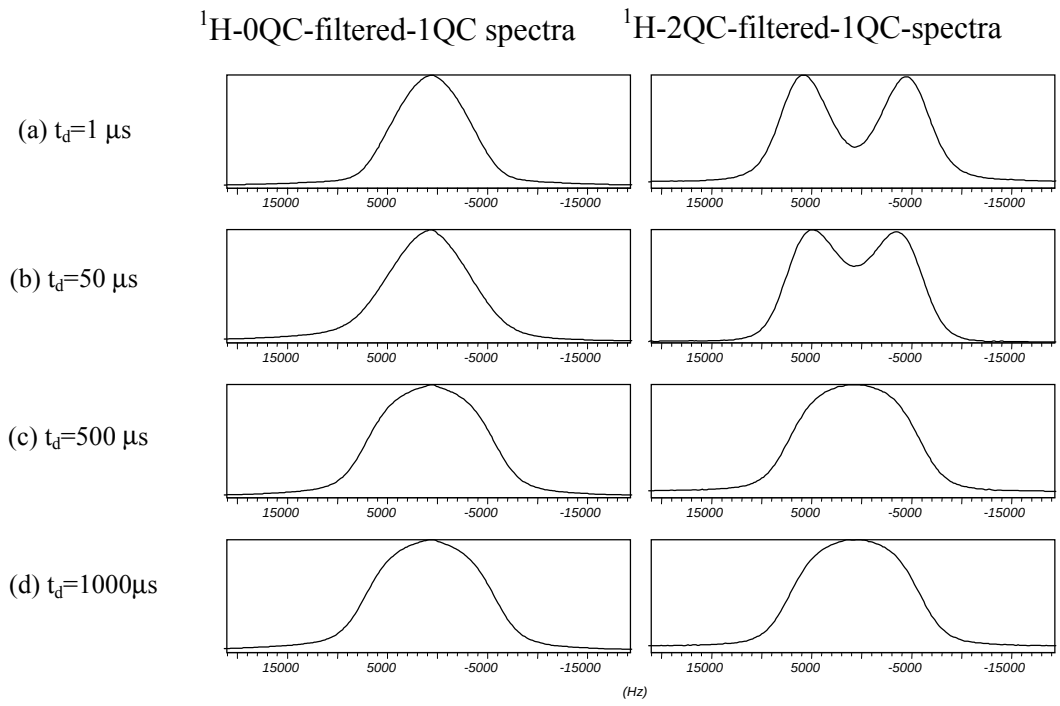

***Figure 5.3**. The effect of ^{1}H spin-diffusion on the MQC development in adamantane. The eight-pulse sequence with an excitation time of 54 μs was used. The delay time t_d was varied: t_d=1 μs (a), t_d=50 μs (b), t_d=500 μs (c), and t_d=1000 μs (d). The left column is the stack plot of ^{1}H SQC spectra obtained from the zero-quantum coherence filtration, the right column is the stack plot of ^{1}H SQC spectra after double-quantum coherence filtration.*

pulses are sufficiently perfect. Figure 5.3 shows the effect of spin-diffusion on the MQC generation. The spectra were recorded under the eight-pulse sequence with an excitation time of 54 μs and varying the delay times after the mixing period from 1 μs to 1000 μs. The effect of the spin-diffusion is obvious: with increasing delay time t_d, the zero-quantum coherences filtered spectra in the left column in Figure 5.3 are broadened; while the doublet components of the ^{1}H SQC obtained from ^{1}H 2QC filtration are gradually broadened and smeared out.

5.2.3 The effect of the excitation time on the MQC generation

From the MQC dynamics, we know that the individual spins become correlated with one another by virtue of their dipolar couplings and show collective behavior as a group of spins ("superspins")**.** To establish this collective behaviour, the spins need time to communicate with each other on the order of the inverse of the size of their mutual coupling. Since the dipolar interaction between spins is proportional to the inverse cube of their distance, spins

with a greater distance need more time to communicate with each other than spins separated by smaller distances. Also, of course, as discussed in the previous sections, the orientation of the internuclear axes is crucial. In the limit of a cycle time within the range of T_2, more and more higher order coherences are generated with increasing excitation time. This feature can be observed from Figure 5.4. Figure 5.4 shows the ^{1}H MQC development vs. excitation time (μs) under the time-reversible eight-pulse sequence. The time increment of the excitation times can be carried out in two ways: (1) through repeating the basic cycle with the same Δ and Δ', such as in Figure 5.4 (a), (c) and (d); or (2) through increasing the delay values Δ and Δ' in one basic cycle such as in Figure 5.4 (a), (b), (d) and (e). More high-order MQC are obtained with increasing excitation time for both methods.

When the cycle time is much longer than the T_2 time, such as in Figure 5.4(f), where the excitation time is τ_{exc} = 1242 μs, only the zero-quatum coherences remain, other coherence orders have completely disappeared.

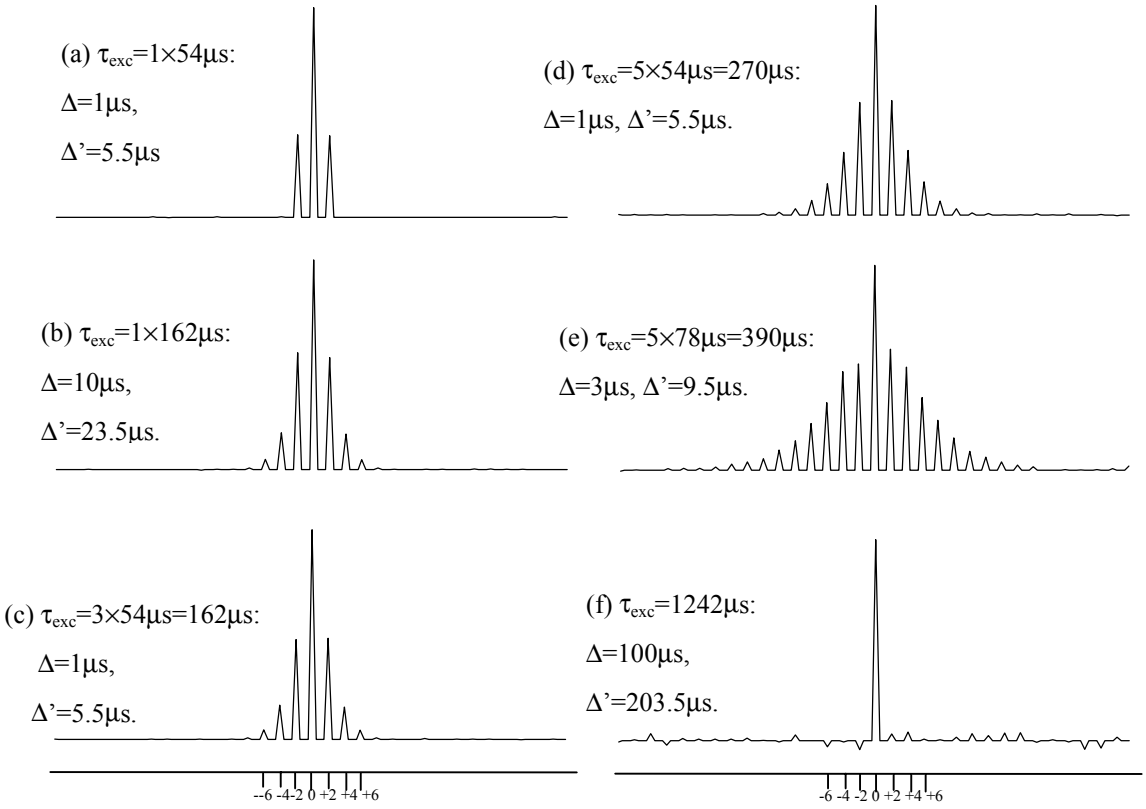

Figure 5.4*. The development of ^{1}H MQC vs. excitation time (μs). The spectra were recorded by the following parameters: t_1 = 0, t_d = 1ms, excitation times were varied, from (a) τ_{exc} = 1×54 μs, to (f) τ_{exc} = 1×1242 μs.*

5.2.4 **The effect of the finite pulse length on the MQC development**

In real experiments, the 90° pulses are not infinitely short δ pulses, they have lengths comparable to the delay times (Δ and Δ') in the sequence. In this case, they will contribute to the higher order correction terms in the average Hamiltonian of the sequence. This will have a destructive effect on the MQC development of the spin system. Therefore in the MQC experiments, the finite length of the pulse duration should be taken into account. In order to compensate for the destructive effect of the finite pulse length in the MQC generation, the setting of the delay time should be $\Delta' = 2\Delta + t_p$, where t_p is the duration of the 90° pulse length[6]. Figure 5.5 shows this effect, the 90° pulses were set to t_p=3.5 μs: in Figure 5. 5(a) the finite pulse length was taken into account and the delay was set to $\Delta' = 2\Delta + t_p$, while in Figure 5.5(b) the delay was set to $\Delta' = 2\Delta$. It is obvious that the former has a higher efficiency for MQC generation than the latter experiment, even though the latter has a longer excitation time. The same conclusion can be obtained from the comparison with Figure 5.5(c) and (d).

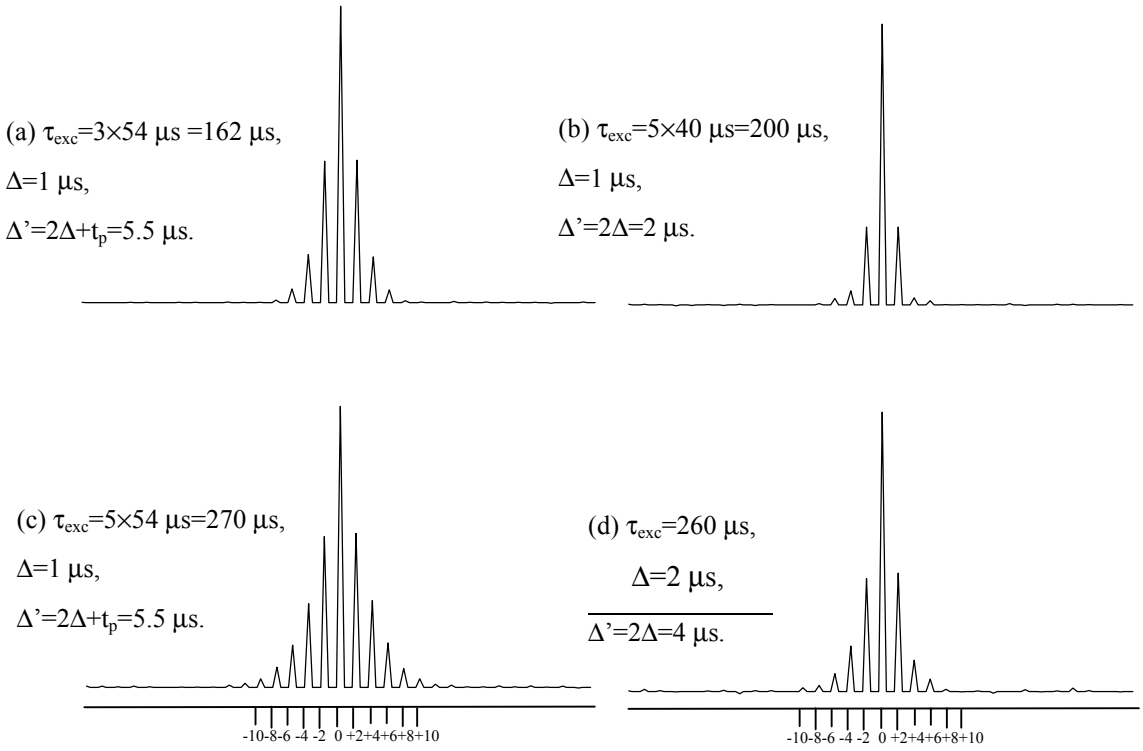

Figure 5.5*. The effect of the finite length of the 90° pulses on the MQC development.*

Also in the case when the finite length of the 90° pulse was not taken care of, the general tendency of the MQC development is the same as discussed before, i.e., with increasing excitation time, more higher orders are generated. Figure 5.5(b) and (d) show this feature:

with short excitation time (200 μs in Figure 5.5(b)), only the 0, ±2, and ±4-order coherences are pumped from the equilibrium state of the spin system, while with longer excitation time (260 μs in Figure 5.5(d)), higher order MQC to ±6 are present.

5.2.5 **The effect of the dipolar modulation on the MQC development**

Figure 5.6 shows that a series of MQC produced by using the eight-pulse sequence with an excitation time of 5×54 μs evolve under the effect of the dipolar Hamiltonian for different lengths of t_1. In the time course of the evolution period, the MQC evolve and dephase under the dipolar modulations which arise from dipolar couplings between the active spins and the passive spins, somewhat like the free induction decay process for single-quantum coherences. With increasing dipolar modulation time, the MQC gradually decay. With long decay times only the zero-quantum coherences remain, as shown in Figure 5.6(e) and (f) after a decay

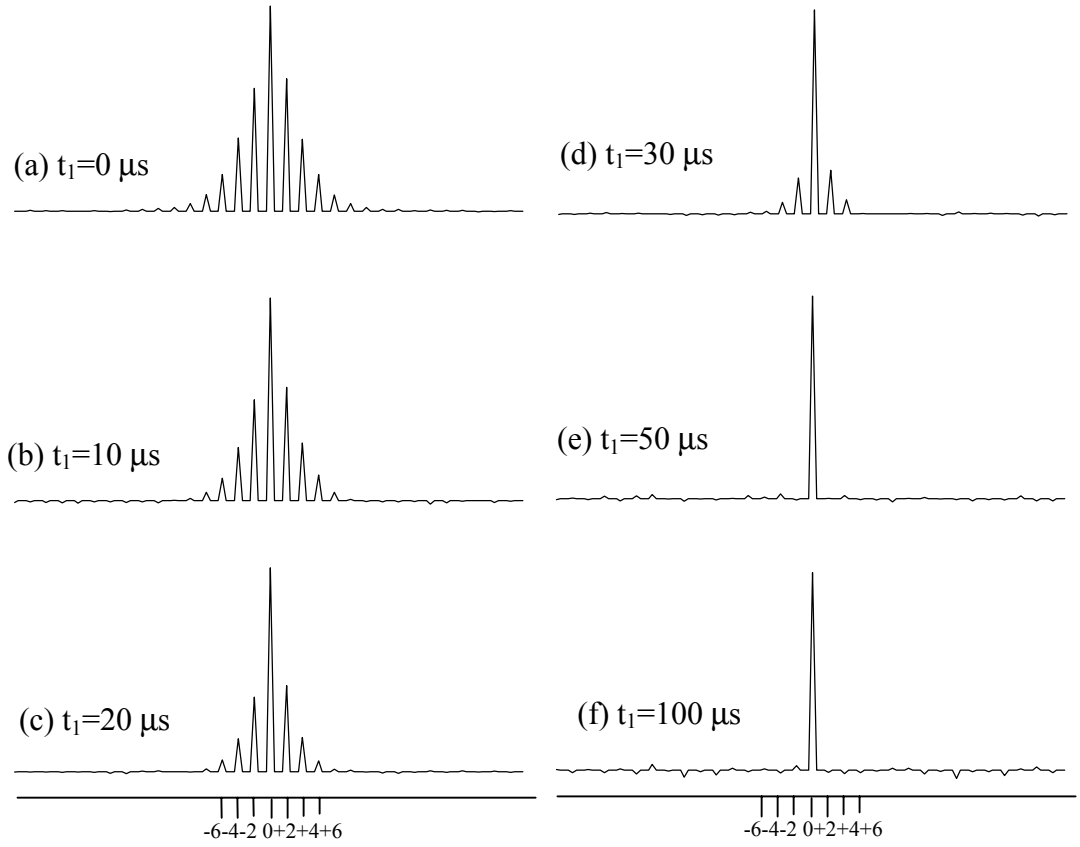

Figure 5.6*. The effect of the dipolar modulation on the MQC development.*

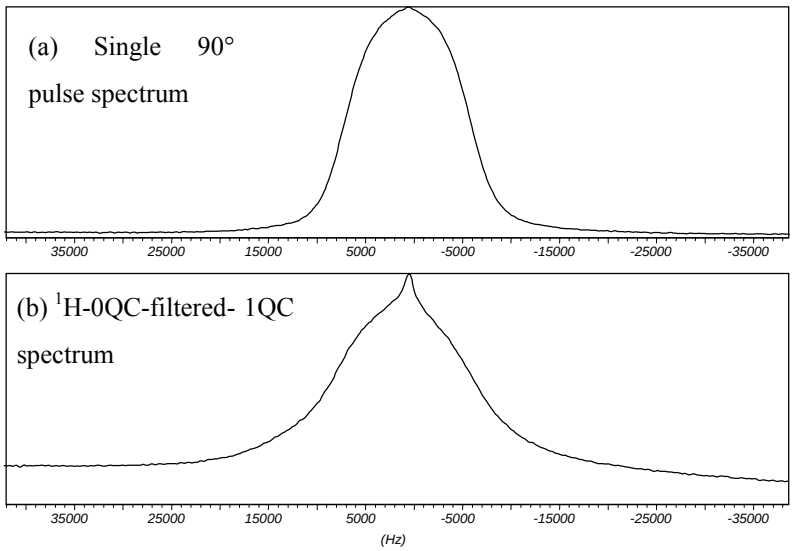

Figure 5.7*. The ^{1}H spectra of adamantane. (a) ^{1}H spectrum arises from the response of a single 90° pulse, (b) ^{1}H-0QC-filtered-^{1}H-SQC using eight-pulse sequence.*

time of 50 μs and 100 μs, respectively. It is very interesting to observe the ^{1}H zero-quantum coherence (after long time dipolar modulation, t_d = 100 μs) filtered ^{1}H SQC spectrum, as shown in Figure 5.7 (b): it corresponds to the zero-quantum coherence of Figure 5.6(f). Compared to the normal static ^{1}H spectrum in Figure 5.7(a), one can note the difference between them: while the ^{1}H single pulse spectrum is broad and featureless, the ^{1}H-0QC-filtered spectrum consists of one broad and one narrow line, which may arise from the different dipolar couplings between the ^{1}H spin pairs, the narrow line may be ascribed to the response of the ^{1}H spin pairs with small dipolar couplings and the broad line to the response of those with great dipolar couplings.

5.3 Conclusions

From the results and discussions above, the following conclusions can be drawn:

(1) The time-reversible eight-pulse sequence can be used to generate MQC from a dipolar coupled solid spin-1/2 system.

(2) Under the effect of the eight-pulse sequence with a short excitation time, the ^{1}H-2QC-filtered spectrum of adamantane has a doublet pattern, it can be simulated by using isolated four spin groups, with the assumption that the dipolar couplings between the spin pairs are the same and the four spins are located on a line.

(3) Spin-diffusion effects are observed through varying the delay time inserted between the mixing and detection time period.

(4) With increasing excitation time, higher orders of coherences are generated. When the excitation time is much longer than the T_2 time, higher order coherences relax away due to the T_2 process, only zero-quantum coherences remain.

(5) The ^1H MQC decays very fast in the evolution time period under the effective dipolar interactions between the active and passive spins.

References

(1) Y. Ba and W. S. Veeman, Isr. J. Chem**. 32,** 173 (1992).

(2) J. Baum, M. Munowitz, A. N. Garroway and A. Pines, J. Chem. Phys. **83**, 2015 (1985).

(3) Y. Ba, Ph.D. Thesis, University of Duisburg, **1995**.

(4) C. Filip, S. Hafner, and I. Schnell, D. E. Demco, H. W. Spiess, J. Chem. Phys., **110**, 423 (1999).

(5) Y. Ba and J. A. Ripmeester, J. Chem. Phys., **108**, 8589 (1998).

(6) P. Slichter, Principles of Magnetic Resonance, Third Enlarged and Updated Edition, Springer-Verlag, **1990**.

Chapter 6. The application of MQ MAS NMR to the study of the silica gel surface

6.1 Introduction

Silica is used for many applications, for instance, as fillers in rubber tires, as stationary phases for chromatography, and as solid absorbents. In these applications the organization, structure and silanol group distribution of the silica, especially on its surface, play an important role. To control and modify these properties it is necessary to study the surface of this material and particularly to determine the properties of the hydroxyl sites. Much work has been devoted to this area in the past years, with techniques such as IR[1,2,3], ^{1}H - ^{29}Si CP MAS NMR[3-5], ^{1}H NMR[6], CRAMPS[4, 7] and multiple-quantum NMR[8].

In general there are three typical species on the silica surface, i.e., surface hydroxyl groups, siloxane groups and physically adsorbed water. The surface hydroxyl groups can be subdivided into different types according to their coordination to the silicon atoms, such as single silanol groups, geminal silanol groups, and associated single and geminal silanol groups[9,10]. The different hydroxyl groups on the silica surface are represented in Figure 6.1. The siloxane groups are mainly formed by dehydroxylation of hydroxyl groups. By using ^{29}Si CPMAS NMR one can usually distinguish siloxane bridges, single and geminal silanol groups (denoted as Q^4, Q^3 and Q^2 according to the silica sites having four, three or two Si-O-Si bridges to neighbouring centers, respectively).

A further distinction can be made between free and bound hydroxyl groups at the silica surface[10]. A major criterion of these two types is the relative distance between adjacent free and bound groups, respectively. Adjacent free hydroxyl groups are assumed to be separated by a distance considerably more than 3.1 Å between the oxygen atoms. Bound hydroxyl groups exhibit a $d_{o\text{-}o}$ distance less than 3.1 Å and hence can interact via hydrogen bonding. As a result of the surface heterogeneity, one can expect the distance between bound hydroxyl groups to vary over a range between 2.4 and 3.1 Å. Consequently, this leads to a wide variation in the strength of O-H···O interactions.

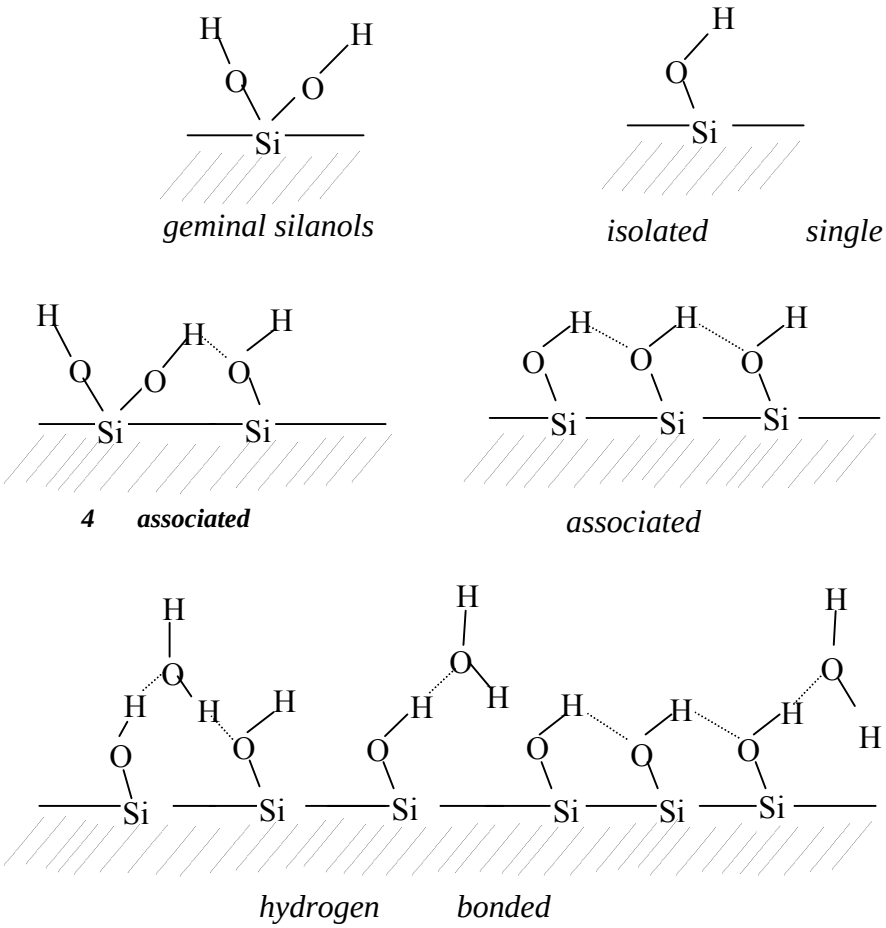

Figure 6.1*. Site occupancies and local organization of silanols in association with water.*

According to the ß-cristobalite model described by Maciel[11], there are three main kinds of the silanol groups on the silica gel surface, i.e., single, geminal and hydrogen-bonded silanol groups.

The single silanol groups are situated on the (111) faces as shown in Figure 6.2. Figure 6.2a is the side view of a (111)-type plane (dashed line representing an edge of such a plane) of the β-cristobalite structure with single silanols. Figure 6.2b is the short-hand notation for a (111)-type face and its single silanols. Two neighbouring single silanol groups located on the same (111) face cannot form hydrogen bonds with each other because of the 5 Å separation between adjacent hydroxyl groups[11], but they can be involved in hydrogen-bonding by the physisorbed water molecules located between them and bridging them to form hydrogen-bonding as shown in Figure 6.2c. Two vicinal single silanol groups located on two concavely intersected nonparallel (111) faces are favourable for hydrogen-bonding.

The geminal silanol groups are situated on the (100) faces as represented in Figure 6.3a, the

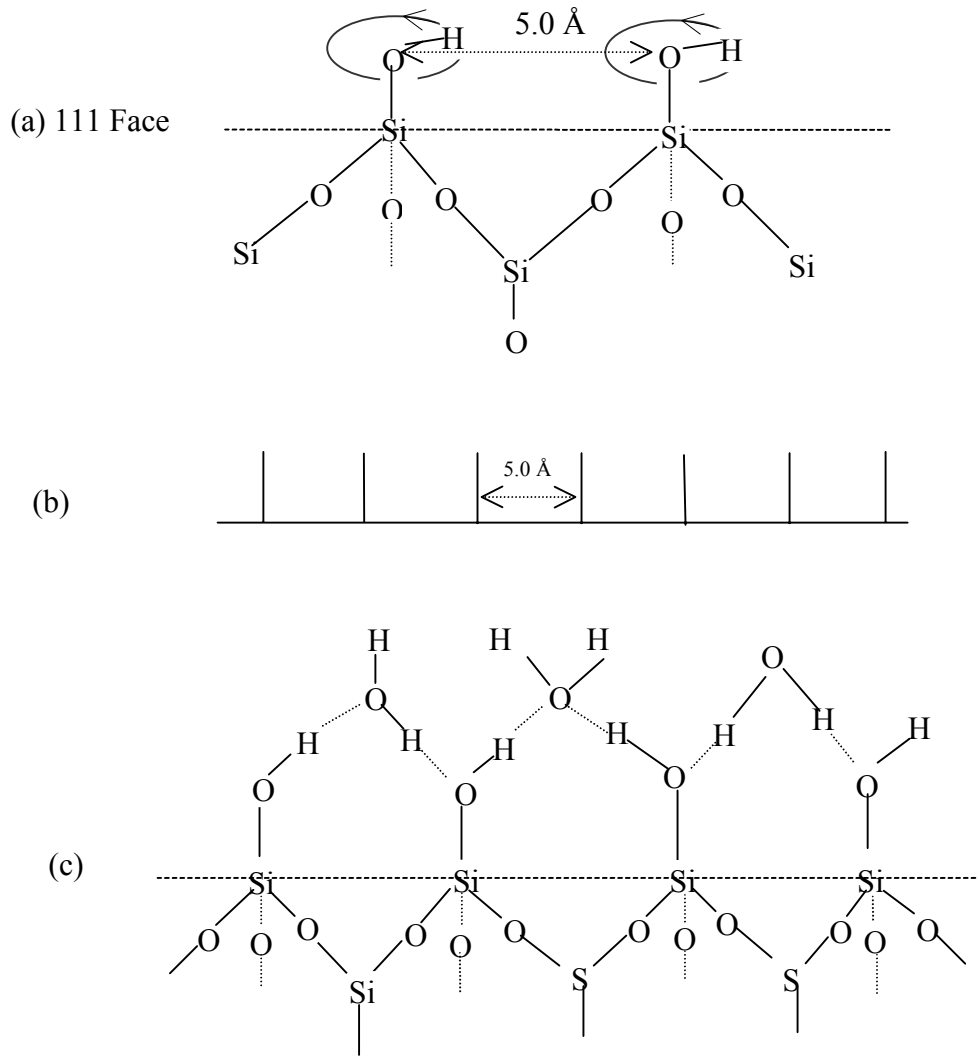

Figure 6.2. *The schematic representation of the single silanol groups on the (111)-type plane. (a) Side view of the (111)-type plane (dashed line representing an edge of such a plane) of the β-cristobalite structure with single silanol groups. (b) Short-hand notation for a (111)-type face and its single silanol groups, the short line representing the silanol groups. (c) Single silanol groups hydrogen-bonding to water molecules.*

two hydroxyl groups of the same geminal silanols cannot form a hydrogen bond with each other because the orientation of these two hydroxyl groups is not suitable for effective hydrogen-bonding, regardless of the internuclear distance of 2.7 Å between them[11]. Two adjacent geminal silanol groups of neighbouring geminal silanols, situated on the same (100) face, can form hydrogen-bonding because of the favourable internuclear distance of 2.3 Å and the orientation between them, which is shown in Figure 6.3b with a short-hand representation. In addition to these, there are other combination possibilities between single and genimal

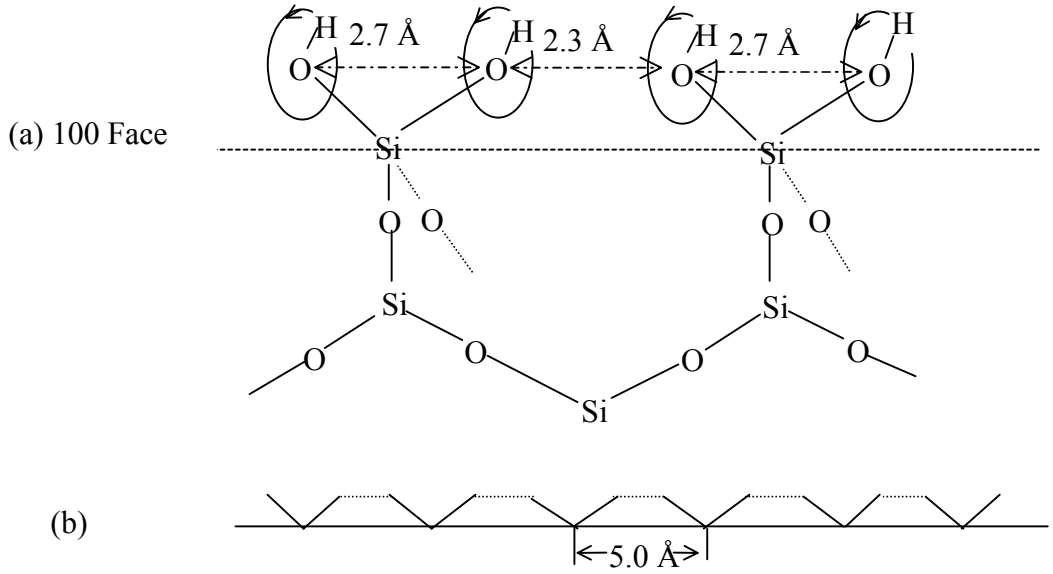

Figure 6.3*. The schematic representation of the (100)-type β-cristobalite face with geminal silanol groups. (a) Side view of the (100)-type plane(dashed line representing an edge of such a plane) of the β-cristobalite structure with geminal silanol groups. (b) Short-hand representation for a (100)-type face and its geminal silanol groups in the same row, the dashed short line indicating hydrogen bonds.*

silanol groups for them to form hydrogen-bonding, e.g., when one (111) face intersects concavely with one (100) face, at the intersection between them one single silanol group located on (111) face can form hydrogen-bonding with adjacent geminal silanol group located on (100) face.

Normally, all these kinds of silanol groups and physisorbed water molecules are present on the surface of the as-received sample. Some water molecules are partially hydrogen-bonded onto the surface of the silica, some of them can penetrate into the micropores near or beneath of the silica surface. The two latter types of water are present as small amounts compared to the adsorbed amounts of the water, and they are very difficult to remove from the surface under mild dehydration conditions. The first physically adsorbed layer of water molecules are hydrogen-bonded on the top of and/or between the silanol groups. The freedom of water molecules in this layer is somewhat restrained through the rigid hydrogen-bonding. They are strongly adsorbed on the surface compared to the second and third absorption layers, while water molecules in the outer absorption layers are very mobile.

The physically adsorbed water at the silica surface usually hampers a quantitative study of the silanol properties. It can be removed from the surface by heating; thermogravimetry is often used for evaluating the water content. Heating above 100 °C first removes physisorbed water[10]. Above 200 °C hydroxyl groups may also start to condense to siloxane groups, yielding water[10]. Condensation proceeds with increasing temperature until at 1200 °C, the concentration of hydroxyl groups will be vanishingly small. Many methods are developed, such as infrared spectroscopy[12,13] combined with thermogravimetry and other related techniques, to distinguish between the physically adsorbed water and the hydroxyl groups. A chemical method[14] based on the well-known Karl Fischer titration procedure is also used to estimate the amount of physically adsorbed water: the adsorbed water reacts rapidly with the Karl Fischer reagent (KFR), while the surface hydroxyl groups undergo a very slow reaction.
Nevertheless, for a quantitative study of the silica surface enough difficulties remain. Firstly, the silica surface is not structured, although some models based on small crystalline domains have been proposed[4,15,16]. Surface irregularity leads to a dispersion of the physicochemical properties of the hydroxyl sites. Secondly, a quantitative determination of structure and adsorbed water by the thermogravimetric method is difficult as hydration and dehydration overlaps with hydroxylation and dehydroxylation processes. Thirdly, the silica surface is heavily reconstructed during the treatment of the sample.
In this chapter the time-reversible-eight-pulse sequence combined with magic-angle sample spinning was used to study the silica surface of a commercial silica gel.

6.2 Experimental

Sample. The silica gel SG254 is commercially available from Grace company. It has the following properties: specific surface area S_{BET} = 570 m^2/g, pore volume = 0.93 ml/g, particle size = 250-355 μm, chemical compositions: SiO_2, 99,5%, Na_2O, 0.10 %, Al_2O_3, 0.15 %, Fe_2O_3, 0.008%, CaO, <0.005 %. For the study and investigation of the silica gel surface, the silica was treated in different ways: (1) the silica gel was dehydrated at 100°C under air atmosphere for 16 hours (Sample A); (2) the silica gel was dehydrated at 120°C under a nitrogen atmosphere in a quartz glass tube for 64 hours (Sample B); (3) the silica gel was dehydroxylated at 500°C under vacuum in a tube furnace for 20 hours (Sample C). After

treatment, Sample C was carefully loaded into a 7 mm zirconia rotor in a glove-box to prevent contamination with water.

NMR measurements. ^{1}H NMR spectra were recorded at 400 MHz by using a Bruker ASX-400 spectrometer equipped with a magic-angle spinning and double-resonance probe. The rotors were made of zirconia and spun by compressed air and/or nitrogen depending on the requirement of the experiments. All ^{1}H chemical shifts were calibrated using water as a second external reference, (4.8 ppm with respect to TMS). The magic-angle sample spinning method was used to enhance the resolution. The ^{1}H MQC were detected using the two-dimensional NMR method, in which the F_1 axis represents the ^{1}H MQC, while the F_2 axis represents the normal 1D ^{1}H spectrum.

The time-reversible-eight-pulse sequence was used to excite the ^{1}H multiple-quantum coherences. According to the selection rule, it can excite only the even-order ^{1}H MQC from the equilibrium spin state. For avoiding interference with the sample rotation, the time-reversible-eight-pulse sequence was synchronized with the sample rotation, as described in section 4.7.2. In the following experiments the Fourier component of $\sin\omega_r t$ (here ω_r stands for the sample rotating rate) in the rotating sample was selected. Both the 4 and 7 mm probe heads were used. In the case of the 4 mm probe head, the synchronization condition $t_r = t_c$ with a MAS frequency of 14881 Hz was used (see Figure 4.11a). In the case of the 7 mm probe head, the conjunction condition $t_r = 4t_c$ under a MAS frequency of 4098 Hz was adopted (see Figure 4.11c). The phase increment was $2\pi/16$, so the highest observable coherence order was 8. For saving experiment time, the evolution time period t_1 was omitted ($t_1 = 0$), and in the ^{1}H-MQC-filtered spectra only the integrated intensities instead of the lineshapes of the coherences were recorded in the F_1 dimension. Other experimental parameters are given in the text and figure captions.

6.3 Results and discussion

6.3.1. ^{29}Si spectrum

Figure 6.4 is the ^{29}Si CPMAS spectrum of the as-received silica gel. It has three resolved peaks, the one at -110 ppm is the resonance from the siloxane groups Q^4, the peak at -100

ppm is for the single or associated silanols Q^3, and the other at -90 ppm is for geminal silanols Q^2. The siloxanes close to the surface of silica form a type of crust of the silica and can be observed via the cross-polarization through the silanol groups in the vicinity. It was Sindorf and Maciel[17-19] in 1980 who first used the $^1H \rightarrow ^{29}Si$ cross-polarization to distinguish the different moieties on the silica gel surface. Since then the $^1H \rightarrow ^{29}Si$ CP has remained the most popular application for surface-selective ^{29}Si detection of the surface structures. But $^1H \rightarrow ^{29}Si$ heteronuclear chemical shift correlations are not easily obtained in a two-dimensional correlation experiment, due to the fact that in the rotating frame ^1H spin diffusion among the protons in a typical silica gel during the spin lock state in a $^1H \rightarrow ^{29}Si$ CP experiment can substantially scramble the intrinsic $^1H \leftrightarrow ^{29}Si$ correlations in the time (>200 μs) required for relatively efficient CP transfer.

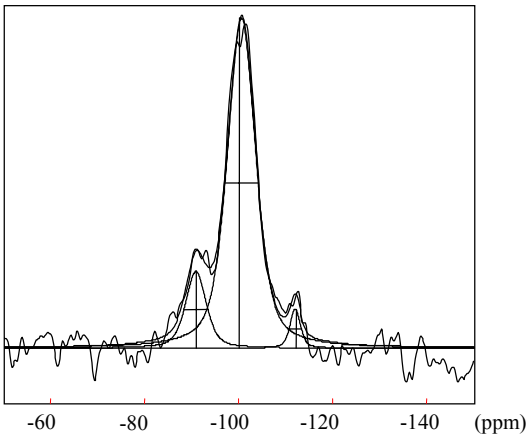

Figure 6.4. *^{29}Si spectrum of the as received silica gel obtained by CPMAS with a contact time of 500 μs under a MAS frequency of 14881 Hz, the length of the 90° pulses was 3.5 μs, the recycle time was 3 s.*

6.3.2 ^1H spectra

^1H spectra of silica gel are shown in Figure 6.5. The corresponding chemical shifts are tabulated in Table 6.1. The experimental parameters are given in the figure caption.

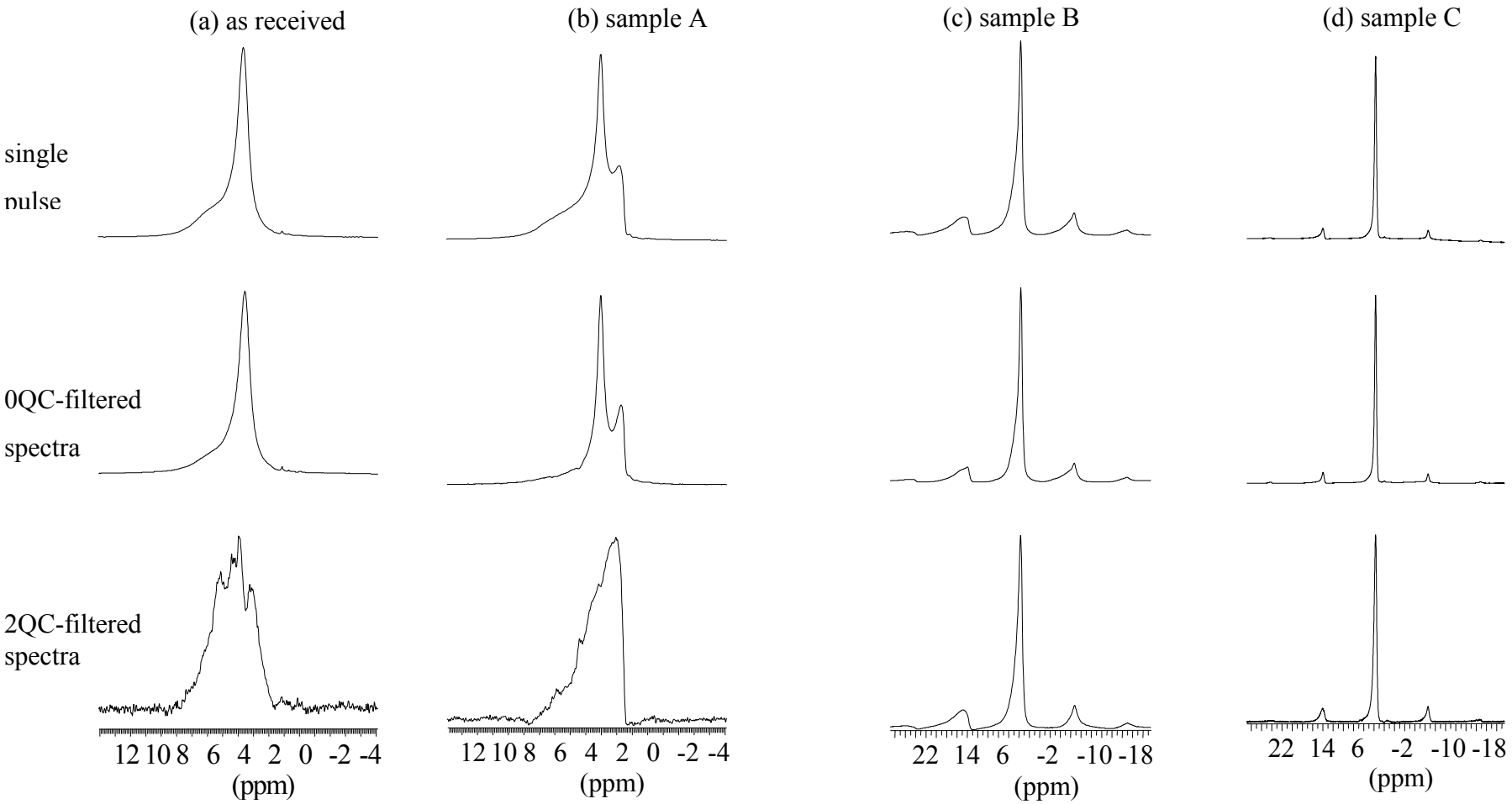

Figure 6.5. *^{1}H spectra of silica gel. (a) as-received, (b) sample A, (c) sample B and (d) sample C. (Top row) single 90° pulse spectra, (middle row) ^{1}H-0QC-filtered-^{1}H-1QC spectra and (bottom row) ^{1}H-2QC-filtered-^{1}H-1QC spectra. The spectra in (a) and (b) were recorded by using a 4 mm double-resonance MAS probe under a MAS frequency of 14881 Hz, the duration of the 90° pulses was 3.5 μs, the ^{1}H-MQC-filtered spectra were acquired under the eight-pulse sequence with an excitation time of $t_{exc} = 3 \times 67.2$ μs. The spectra in (c) and (d) were obtained by using a 7 mm double-resonance MAS probe under a MAS frequency of 4098 Hz, the length of 90° pulses was 4 μs, the ^{1}H-MQC-filtered spectra were produced under the eight-pulse sequence with an excitation time of $t_{exc} = 244$ μs.*

Table 6.1*. The chemical shifts of the ^{1}H spectra of silica gel in Figure 6.5.*

	As-received	A	B	C
^{1}H MAS spectra	3.6 ppm 1 – 8 ppm	1.8 ppm 3.13 ppm 1 – 8 ppm	1.60 ppm 1.87 ppm 2.59 ppm	1.64 ppm 1.80 ppm 2.59 ppm
^{1}H-0QC-filtered spectra	3.7 ppm 1 – 8 ppm	1.8 ppm 3.13 ppm 1 – 8 ppm	1.60 ppm 1.87 ppm 2.59 ppm	1.64 ppm 1.80 ppm 2.55 ppm
^{1}H-2QC-filtered spectra	3.1 – 3.3 ppm 3.9 – 4.1 ppm 4.3 –4.5 ppm 5.05 – 5.5 ppm	2.15 ppm 1.5 – 7.5 ppm	1.60 ppm 1.87 ppm 2.65 ppm	1.65 ppm 1.82 ppm 2.57 ppm

As-received silica gel

First let us examine the ^{1}H spectra of the as-received silica gel in Figure 6.5(a) and Table 6.1. The single pulse ^{1}H MAS spectrum consists of one peak at 3.6 ppm with a low-field unresolved broad shoulder (from 1 ppm to 8 ppm). The peak at 3.6 ppm can be assigned to the physisorbed water on the silica gel surface according to Bronnimann et al[20]. The unresolved broad peak can be assigned to the silanol protons involved in a variety of hydrogen-bonding environments[20]. Considering the similarity of the chemical and physical environments of hydrogen-bonded silanol protons and any associated hydrogen-bonded protons of water molecules, it is reasonable to infer that this broad peak overlaps with those from the first monolayer of strongly hydrogen-bonded water.

Like the one-pulse spectrum in Figure 6.5a (top), the ^{1}H zero-quantum coherence filtered spectrum in Figure 6.5a (middle) is dominated by a narrow peak centered at 3.7 ppm, which may be due to the physisorbed water on the silica gel surface[20], and one broad peak ranging from 1 ppm to 8 ppm, which is attributed to silanol protons in various hydrogen-bonding environments and very strongly hydrogen-bonded (relatively rigid) water molecules [20-22].

More interesting and surprising, the ^{1}H-2QC-filtered spectrum (see Figure 6.5a, bottom) has four resolved peaks which resonate at 3.1 – 3.3 ppm, 3.9 – 4.1 ppm, 4.3 – 4.5 ppm and 5.05 – 5.5 ppm. According to previous work[23,24], these four resolved lines may be assigned to the

structured water molecules close to the surface of the silica gel and hydrogen bonded to the surface silanol groups.

We know that, normally the silica surface is covered with silanol groups and physically adsorbed water, the latter adsorbed on top of and/or between the silanol groups through hydrogen-bonding to form a mono- or multilayer[9]. Bogdan et al.[25] have studied the state of the physisorbed water on the silica surface. They found that on the surface of the silica there are structured monolayers, clusters, and weakly bound liquid-like water molecules. Maciel and co-workers [4,7] found that the resonances of water, bound silanols and isolated silanols are at about 3.5 ppm, 3.0 ppm and 1.7 ppm, respectively. Legrand et al[24] studied the pyrogenic silica surface, they found five distinguishable ^{1}H resonances at the pyrogenic silica surface, i.e., (1) weakly coupled (long T_2), water inaccessible, isolated internal silanols at 1.8 ppm; (2) weakly coupled, external free silanols which are revealed upon dehydration and resonating at 2.5 ppm, (3) strongly coupled external hydrogen-bonded silanols with an unresolved broad line between 3 and 7 ppm; (4) a resonance of water between 2.6 ppm and 4.6 ppm, depending on water content. The last resonance is due to two unresolved species of slightly different T_1, i.e., the first layer of strongly hydrogen bound water resonates at 2.7 ppm, while the liquid-like free water resonates at 5 ppm. Based on this, they made the assumption that there exists an 1:1 ratio between surface hydroxyls and the first layer of physisorbed water.

All this previous research suggests that the silica surface is intrinsically very heterogeneous. To further investigate the heterogeneity of the surface, the bound water and the silanol groups were investigated by studying the change of the lineshapes of the ^{1}H-MQC-filtered spectra with increasing excitation time

Figure 6.6 shows the ^{1}H-0QC-filtered spectra vs. the excitation time t_{exc}. No change in line shapes was observed, only the intensity of the ^{1}H 0QC decreased with increasing excitation time of t_{exc}=1×67.2 μs to t_{exc}=5×67.2 μs, as shown in Figure 6.6b. The decrease of the refocussed signal with increasing excitation time is a general behaviour. There are many factors[26], such as MQC relaxation and development dynamics, multiple-pulse imperfection and molecular motions, which can affect the refocussed signal. For instance zero-quantum magnetization could transform into double-quantum and higher-order coherences with increasing excitation time. From Figure 6.7 one can, however, see that the intensity of the 2QC and 4QC are very small, the sum of the double- and higher-order coherences intensities does not balance the decay of the 0QC intensity. So in this case, the decrease of the ^{1}H 0QC intensities with increasing excitation time may be due to the molecular motion. Random

variations of the internuclear proton vectors resulting from the molecular motions during the course of the experiment hamper the time reversal, so to some extent the intensity of the refocussed signal can be used as a measure of the effectiveness of time reversal[27].

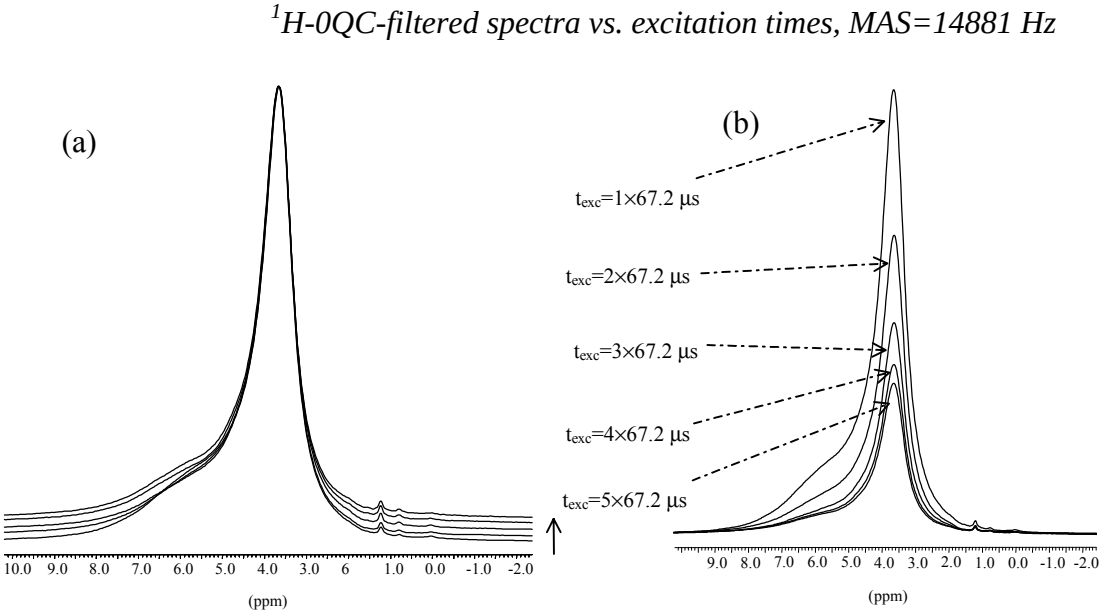

Figure 6.6*. The ^{1}H-0QC-filtered spectra of the as received silica gel vs. excitation times (μs) under MAS frequency of 14881 Hz. The duration of the 90° pulses was 3.5 μs, the recycle time was 3 s. (a) The stack plot of the ^{1}H-0QC spectra which were normalized to the same height, the arrow indicates the increasing direction of the excitation time. (b) The overlay plot of the ^{1}H-0QC spectra with different excitation times.*

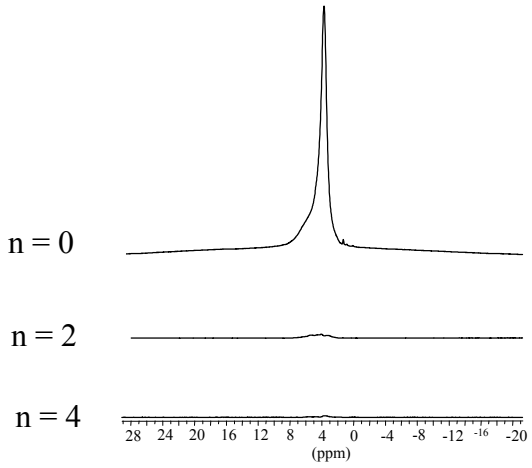

Figure 6.7*. The stack plot of the ^{1}H-detected-^{1}H-even-order-MQC-filtered spectra of the as received silica gel. The spectra were recorded with an excitation time of t_{exc}=3×67.2 μs under a MAS frequency of 14881 Hz. The different orders of the MQC-filtered spectra are denoted as n = i (i = 0, 2 and 4).*

In contrast to the ^{1}H-0QC-filtered spectra, changes in both lineshapes and intensities of the ^{1}H-2QC-filtered spectra are observed, as shown in Figure 6.8. Two interesting changes in the lineshape of the ^{1}H-2QC-filtered spectra are worth mentioning (see Figure 6.8a). Firstly, the

linewidth of the ^{1}H-2QC-filtered spectra are narrowed with increasing excitation time. Secondly, with increasing excitation time, the resolved peaks of the ^{1}H-2QC-filtered spectrum have changed: the peak at 1.8 ppm in the spectrum observed with a short excitation time has disappeared when the excitation time was increased, the other two resolved peaks at about 3.9 ppm and 5.1 ppm have further increased to four resolved peaks. This phenomenon can be interpreted by using the dipolar filter effect of the eight-pulse sequence. We know that the molecular motions modulate the effective Hamiltonian of the spin system through the spatial part of the Hamiltonian. When the molecular motion is described by a correlation time, the double-quantum Hamiltonian is a good approximation when the correlation time is longer than the cycle time of the multiple-pulse sequence, i.e., the slow motion limit. When the correlation time is shorter than the cycle time, i.e., in the fast motion limit, the dipolar couplings are averaged by the molecular motion, in this case no MQC will be generated. When the correlation time is comparable to the cycle time of the eight-pulse sequence, the molecular motion will interfere with the multiple-pulse and the refocussed MQC will drop seriously in intensity. With this in mind, we can explain the observed phenomenon of the 2QC development. With increasing excitation time, more and more rigid dipolar couplings are filtered out, the intrinsically different structured water molecules adsorbed at the surface are revealed. At the same time, the broad line caused by the strong dipolar interactions are narrowed through the elimination of the rigid dipolar couplings.

The development of the ^{1}H 2QC is plotted in Figure 6.8b. In the experimental time scale from $t_{exc} = 1\times67.2$ μs to $t_{exc} = 5\times67.2$ μs, the ^{1}H 2QC intensity first increases and then decreases with the excitation time. As previously discussed in chapter 4, with a short excitation time, the generation of the ^{1}H 2QC is dominated by the nearest neighbour spins with the strongest dipolar couplings. In the course of the experimental time, more and more proton spins are correlated and involved into the 2QC, so the intensity of the resulted ^{1}H 2QC first increases when increasing excitation time from $t_{exc} = 1\times67.2$ μs to $t_{exc} = 3\times67.2$ μs. When excitation time is further increased to a value which is comparable or longer than the correlation time of the molecular motion, the generation of the ^{1}H 2QC is hampered by the molecular motions, therefore the ^{1}H 2QC intensity decreases again with further increase of excitation time.

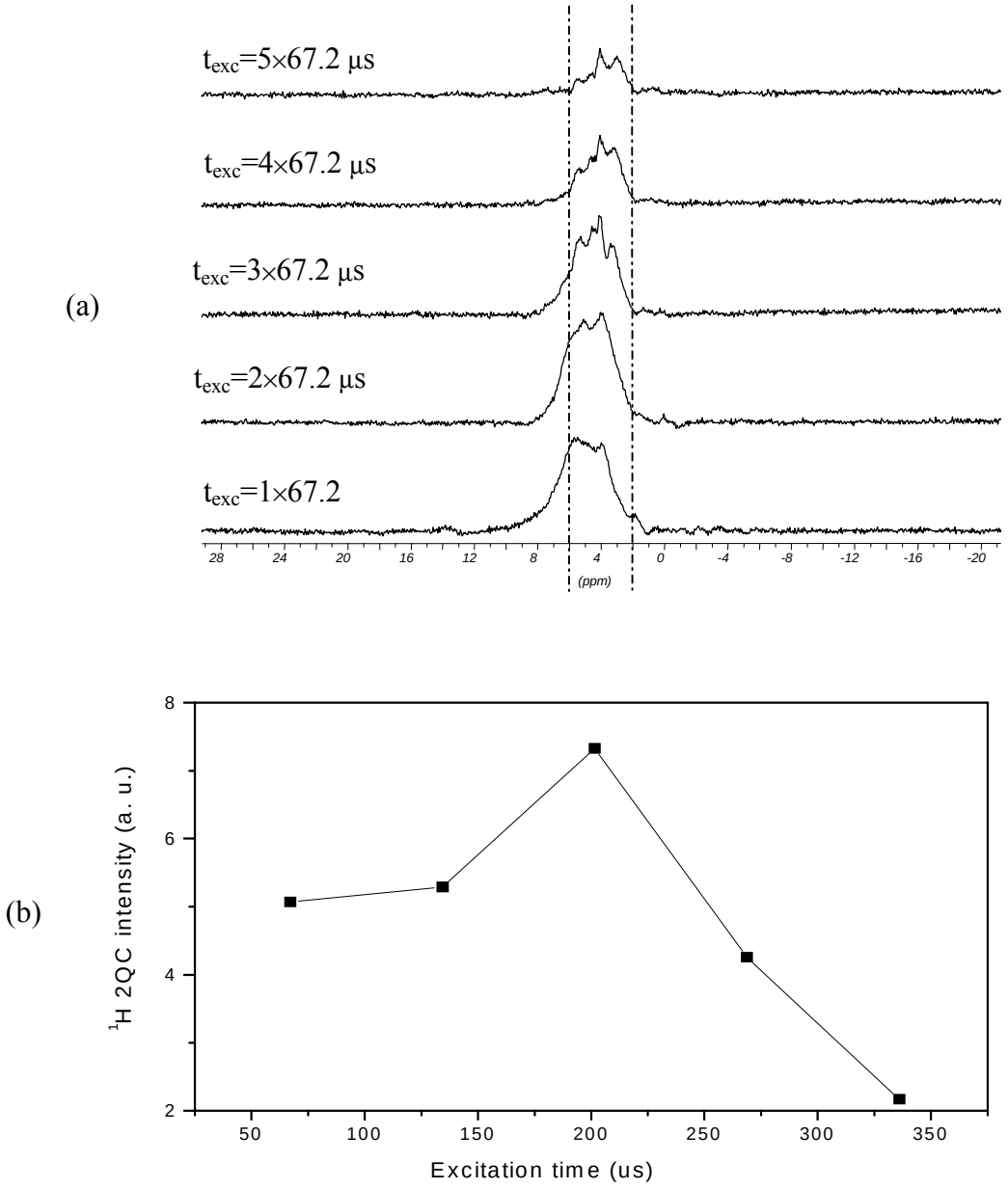

***Figure 6.8**. The ^{1}H-2QC-filtered spectra of the as-received silica gel vs. excitation times (μs) under the same condition as in Figure 6.4. (a) The stack plot of the ^{1}H-2QC-filtered spectra with different excitation time. (b) The development of the ^{1}H 2QC vs. the excitation time.*

In order to study the properties and behaviour of the silanol groups on the silica gel surface, the effect of the water molecules must be eliminated first. The removal of the physically adsorbed water from the silica surface was carried out in different ways as described in experimental section. The obtained ^{1}H spectra of these treated samples are discussed as follows.

Sample A

Figure 6.5b shows ^{1}H spectra of sample A. Like the ^{1}H one-pulse spectrum (Figure 6.5b, top) the ^{1}H-0QC-filtered spectrum (Figure 6.5b, middle) has two resolved peaks together with an unresolved broad low-field shoulder: one peak resonates at 1.8 ppm, another resonates at 3.13 ppm, the unresolved broad shoulder resonates at a range from 1 - 8 ppm. As before, these resonances can be assigned to the isolated silanols, water molecules and the hydrogen-bonded silanols.

Compared with the ^{1}H-0QC-filtered spectrum, the two resolved peaks in the ^{1}H-0QC-filtered spectrum do not show up in the ^{1}H-2QC-filtered spectrum (see Figure 6.5b, bottom). One new peak which resonates at 2.15 ppm with a broad unresolved low-field shoulder is observed in the recorded ^{1}H-2QC-filtered spectrum. The new peak and the low-field shoulder may be assigned to proton resonances from silanol groups which were involved in different hydrogen-bonding environments, the hydrogen-bonding may be due to the bridging of the isolated silanol groups with the remained water molecules or due to the neighbouring silanol groups.

Sample B

The ^{1}H spectra of sample B are shown in Figure 6.5c. The stack mode of the ^{1}H even-order MQC-filtered spectra are plotted in Figure 6.9a, in which the different order coherences are denoted by n = i (i = 0, 2 and 4). The ^{1}H-0QC- and 2QC-filtered spectra are each deconvoluted into three peaks, i.e., one peak at 1.6 ppm, another at 1.8 ppm, and the third at ~2.6 ppm, which may be assigned to the single silanol groups, geminal silanol groups, and the hydrogen-bonded silanol groups, respectively, as shown in Figure 6.9b and 6.9c. The deconvolution results are given in Table 6.2. Comparing the ^{1}H-0QC- and 2QC-filtered spectra in Figure 6.6b and 6.6c, one finds that the relative content of the single silanol is changed from 26% to 16%. This change may suggest that there are two type of single silanols which have the same chemical shift but with different mobilities, i.e., the isolated single silanol groups which are located on the same (111) face according to the β-cristobalite model and the vicinal silanol groups which are located at the intersections of the different (111) faces which are concavely intersected.

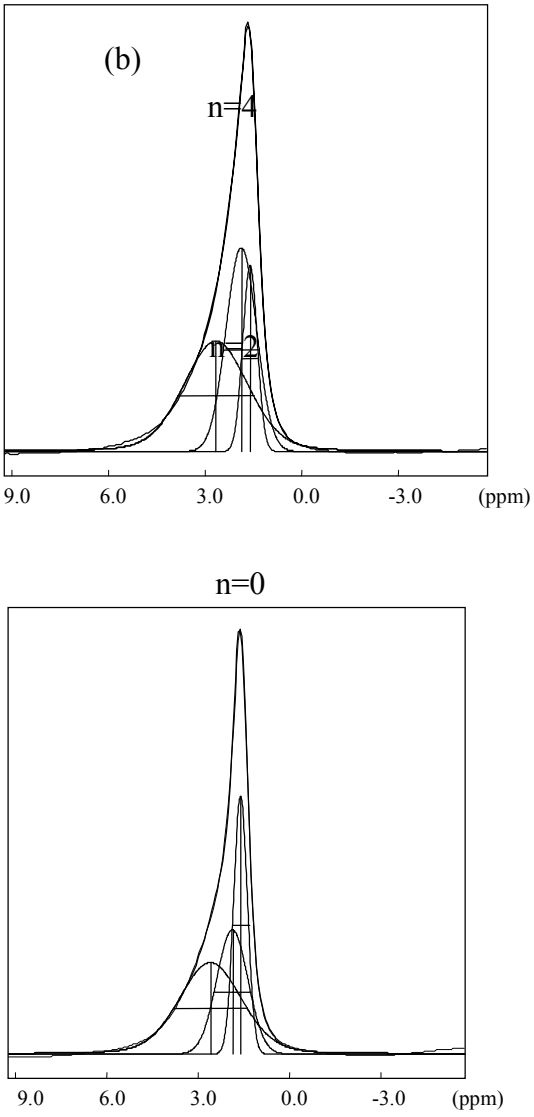

***Figure 6.9**. The ^{1}H even-order MQC-filtered spectra of sample B which was dehydrated at 120°C under nitrogen atmosphere for 64 hours. The spectra were recorded by using the eight-pulse sequence under MAS with an excitation time of 244 μs. The length of the 90° pulse was 4 μs. The synchronization of the eight-pulse sequence with the rotation ($t_r=4t_c$) was used under the MAS frequency of 4098 Hz. (a) The spectra are plotted in stack mode. (b) The deconvolution of the ^{1}H-0QC-filtered spectrum. (c) The deconvolution of the ^{1}H-2QC-filtered spectrum.*

The former can be involved into the 0QC but cannot be involved into the 2QC due to the great separation between the nearest proton pairs. The latter can be involved into both the 0QC and the 2QC. The relative content of each silanol group can be calculated from relative integral intensities of the individual peaks in the deconvoluted ^{1}H-0QC- and 2QC-filtered spectrum: the amount of the geminal silanol groups is 28 %, that of the vicinal single silanol groups is up

to 16 × 28 /37 = 12 %, the quantity of the isolated single silanol groups is (26 % - 12 %) = 14 %, and the hydrogen-bonded silanol groups is 45 %.

***Table 6.2**: The deconvolution results of the ^{1}H-0QC- (Figure 6.9b) and 2QC-filtered (Figure 6.9c) spectra of sample B which was dehydrated at 120°C under N_2 for 64 hours.*

	Chemical shift (ppm)	Full line width at half-height (ppm)	Gauss character of the Gauss/Lorentz line (%)	Relative content (%)
^{1}H 0QC	1.60	0.53	1.00	26
	1.87	1.20	1.00	28
	2.59	2.41	0.80	45
^{1}H 2QC	1.60	0.52	1.00	16
	1.87	1.10	1.00	37
	2.65	2.34	0.80	46

Sample C

The ^{1}H spectra of sample C are shown in Figure 6.5d, the static plot of the ^{1}H even-order MQC-filtered spectra of sample C are represented in Figure 6.10. The ^{1}H-0QC- and 2QC-filtered spectra were deconvoluted using the Bruker WINFIT program as shown in Figure 6.10b and 6.10c, respectively. The deconvoluted results are given in Table 6.3. Both of them can be well fitted into three peaks, i.e., one at 1.65 ppm, another at 1.80 ppm and the third at 2.55 ppm. These three peaks may be assigned as single, geminal and hydrogen-bonded silanol groups, respectively.

Comparing Figure 6.10b and c, the relative intensity of these three peaks was changed in the ^{1}H-0QC- and 2QC-filtered spectra. The peak intensity of the single silanol groups was decreased from 52 % to 28 %, whereas the relative intensity of the geminal silanol groups was increased from 39 % to 51 % and the relative intensity of the hydrogen-bonded silanol groups

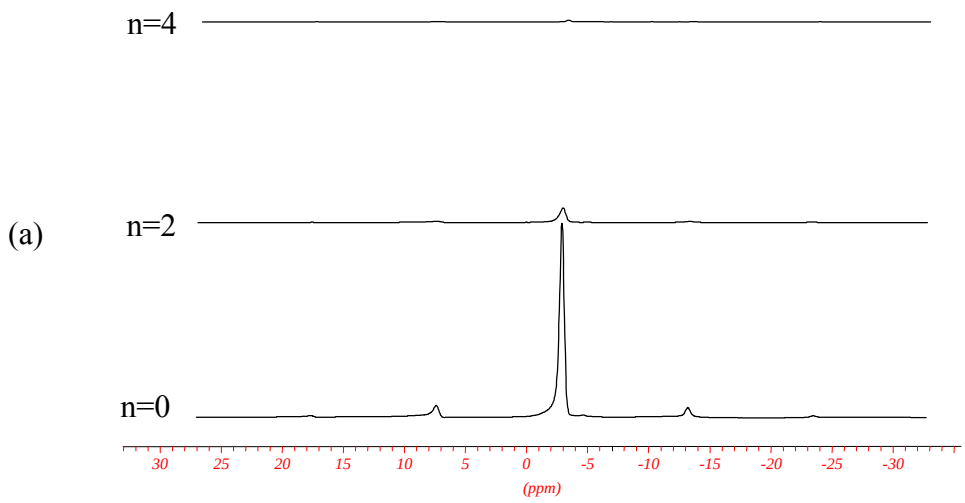

(b) (c)

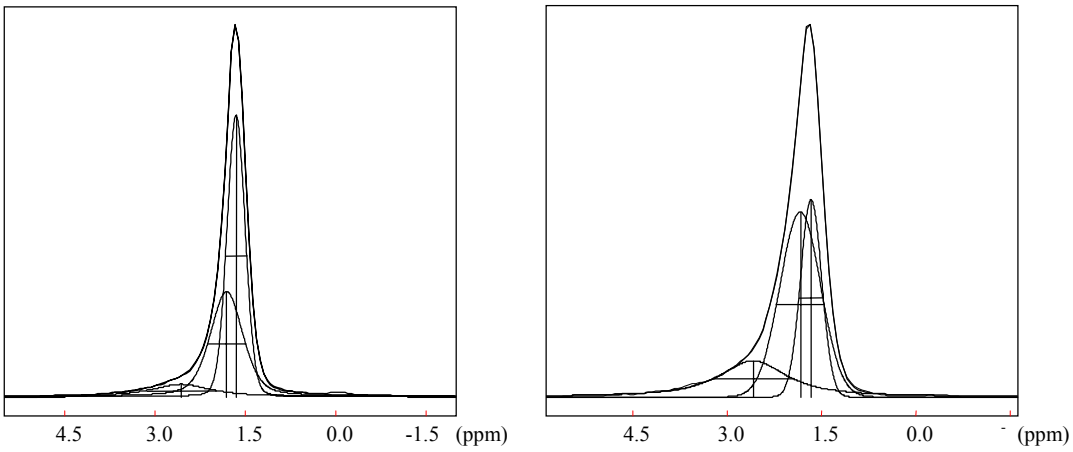

Figure 6.10 *The ^{1}H even-order MQC-filtered spectra of sample C. The spectra were recorded under MAS frequency of 4098 Hz with an excitation time of 244 μs in the condition of $t_r=4t_c$. the duration 90° pulses was 4 μs. The stack mode of the ^{1}H-MQC-filtered spectra are plotted in (a). The deconvolutions of ^{1}H-0QC- and 2QC-filtered spectra are represented in (b) and (c), respectively.*

was increased from 9 % to 21 %. The drop of the relative content of the single silanol groups from the ^{1}H-0QC- to 2QC-filtered spectrum means that there are two kinds of single silanol groups at the dehydroxylated silica surface, i.e., the mobile single silanol groups are located on the same (111) face of the ß-cristobalite structure which are involved in the 0QC but not in the 2QC, and the motionally restricted vicinal single silanol groups are located on different (111) faces of the ß-cristobalite structure, which are involved both in the 0QC- and 2QC-filtered spectra.

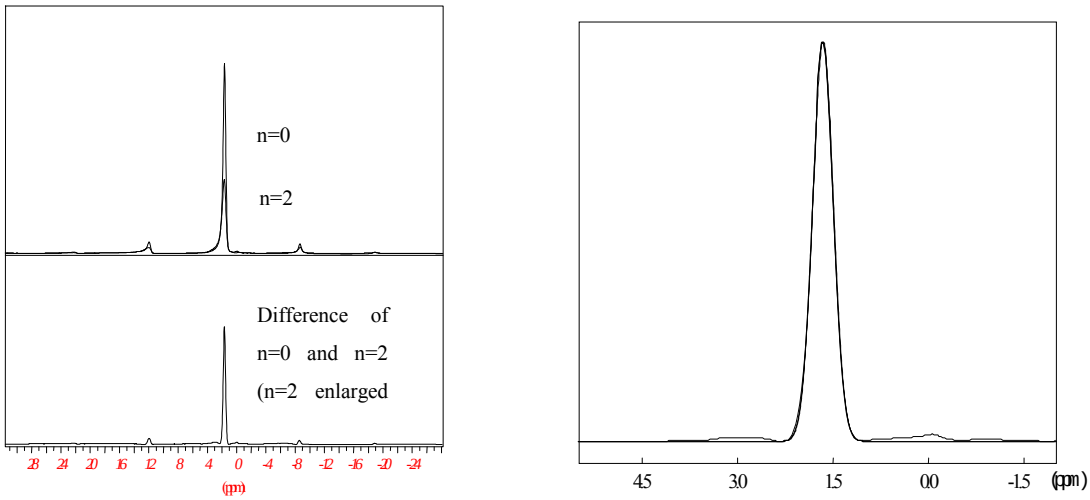

Figure 6.11. *The ^{1}H difference spectrum of 0QC- and 2QC-filtered spectra of sample C (left) and the deconvolution of the subtracted spectrum (right).*

Table 6.3 *The results of deconvolution of the ^{1}H-0QC- and 2QC-filtered spectra of Figure 6.7b and c.*

	Chemical shift (ppm)	Full line width at half-height (ppm)	Gauss character of the Gauss/Lorentz line (%)	Relative content (%)
^{1}H-0QC	1.64	0.35	1.00	52
	1.80	0.63	1.00	39
	2.55	1.15	0.10	9
^{1}H-2QC	1.65	0.39	1.00	28
	1.82	0.76	1.00	51
	2.57	1.28	0.10	21

The relative quantities of each silanol group can be calculated from the relative intensities of the individual peaks in the deconvoluted ^{1}H-0QC- and 2QC-filtered spectra: the amount of the geminal silanol groups is 39 %, that of the vicinal single silanol groups is up to 28 × 39 /51 = 21 %, the quantity of the isolated single silanol groups is (52 % - 21 %) = 31 %, and the amount of residual hydrogen-bonded silanol groups is 9 %.

The same conclusion can also be obtained by subtracting the ^{1}H 2QC spectrum, which is enlarged 5.19 times from the ^{1}H 0QC spectrum, as shown in Figure 6.11. The subtracted spectrum can be well fitted using one Gaussian line at 1.65 ppm with a linewidth of 0.38 ppm, which can be ascribed to the free single silanol groups, i.e., the isolated single silanol groups on the silica gel surface after dehydroxylation at 500°C under vacuum for 20 hours. They are apart from each other beyond the distances which are needed for them to be involved in the 2QC on the experimental time scale.

6.3.3 Discussion and conclusions

For an easy discussion and comparison, the assignments of different species on the silica gel surface are tabulated in Table 6.4. Based on the ß-cristobalite model which was described in the introduction, we can explain the above-mentioned experimental results.

On the surface of the as-received silica gel mobile water molecules dominate the ^{1}H one-pulse (see Figure 6.5a and table 6.7) and resonate at 3.6 ppm. By filtering out the contribution of these mobile molecules by the multiple-pulse sequence, the structured monolayer water molecules were revealed and detected via the ^{1}H double-quantum coherences. This leads to resonances at 3.1 –3.3 ppm, 3.9 – 4.1 ppm, 4.3 – 4.5 ppm and 5.05 – 5.5 ppm. In this case all the silanol groups are hydrogen-bonded through the physically adsorbed water molecules. There are no isolated silanol groups on the surface.

By dehydration of the sample at 100°C under air atmosphere, most of the physically adsorbed water molecules are removed from the surface. The isolated silanol groups (1.8 ppm) are

Table 6.4. *The assignments of different species on the silica surface.*

		As-received	A	B	C
water	mobile	3.6 ppm	3.13 ppm	no	no
	structured	3.1-3.3 ppm		no	no

	monolayer	3.9-4.1 ppm 4.3-5.5 ppm 5.05-5.5 ppm			
silanols	Hydrogen-bonded	1 – 8 ppm	2.15 ppm	2.6 ppm	2.6 ppm
	isolated	unresolved	1.8 ppm	1.6 ppm (single silanols) 1.6 ppm (vicinal silanols) 1.8 ppm (geminal silanols)	1.6 ppm (single silanols) 1.6 ppm (vicinal silanols) 1.8 ppm (geminal silanols)

revealed after dehydration. Hydrogen-bonded silanol groups (2.15 ppm), produced by either the residual water molecules or the neighbouring silanol groups, together with a small amount of residual physically adsorbed water (3.13 ppm), are left on the surface. They can be detected and discriminated by the ^{1}H-MQC-filtering experiment. Due to the interference of the residual water molecules, it is not possible to discriminate between the isolated single, vicinal and geminal silanol groups.

By dehydration of the original sample at 120 °C under a nitrogen atmosphere for 64 hours, the physically adsorbed water molecules are completely removed from the silica surface, the silanol groups that were hydrogen-bonded to these water molecules become isolated. So the isolated single, vicinal and geminal silanol groups, together with hydrogen-bonded silanol groups are left on the surface. They can be quantitatively analysed by ^{1}H-MQC-filtered-MAS-NMR: the isolated single silanol groups which are located on the same (111) face according to the ß-cristobalite model resonate at 1.6 ppm and amount to 14%; the vicinal silanols which are located on different (111) faces resonate at 1.6 ppm and are up to 12%; the hydrogen-bonded silanol groups which are produced by the neighbouring silanol groups resonate at 2.6 ppm (45%).

By dehydroxylation of the original sample at 500°C under vacuum for 20 hours, all physically adsorbed water molecules together with most of the hydrogen-bonded silanol groups are removed from the silica surface by dehydration and condensation. At the same time, a fraction of the hydroxyl groups (most of them are the vicinal single and geminal silanol groups) are also removed from the surface by the condensation. This is the reason that the relative content of the geminal silanol groups with respect to the single silanol groups decreases after dehydroxylation under 500°C, compared with that of sample B. So the detected single isolated (1.6 ppm, 31%) and vicinal silanol groups (1.6 ppm, 21%) and geminal silanol groups (1.8

ppm, 39%), together with some residual hydrogen-bonded silanol groups (9%), resulted from the neighbouring silanol groups reflect that are left on the surface after dehydroxylation.

4 References

(1) J. B. Peri, J. Phys. Chem. **70**, 2937 (1966).

(2) A. J. Van Roosmalen, and J. C. Mol. J. Phys. Chem. **82**, 2748 (1978).

(3) A. P. Legrand, H. Hommel, A. Tuel, A. Vidal, H. Balard, E. Papirer, P. Levitz, M. Czernichowski, R. Erre, H. Van Damme, J. P. Gallas, J. F. Hemidy, J. C. Lavalley, O. Barres, A. Burneau, and Y. Grillet., Adv. Colloid Interface Sci. **33**, 91 (1990).

(4) G. E. Maciel, P. D. Ellies, In NMR techniques in Catalysis, A. T. Bell, A. Pines, Eds., Marcel Dekker: New York, **1994**, p231.

(5) S. Leonardelli, L. Facchini, C. Fretigny, P. Tougne, and A. P. Legrand, J. Am. Chem. Soc. **114**, 6412 (1992).

(6) C. Doremieux-Morin, L. Heeribout, C. J. Dumousseaux, J. Fraissard, H. Hommel, and A. P. Legrand, J. Am. Chem. Soc. **118**, 13040 (1996).

(7) G. E. Maciel, C. E. Bronnimann, R. C. Zeigler, I-S. Chuang, D. R. Kinny, E. A. Keiter, In The Colloid Chemistry of silica, H. E. Bergna Ed., Advances in Chemistry Series 234, American Chemical Society: Washington, DC, **1994**, p269.

(8) B. C. Gerstein, M. Pruski, and S. –J. Hwang, Anal. Chem. Acta **283**, 1059 (1993).

(9) R. K. Iler, The chemistry of silica: solubility, polymerization, collid and surface properties, and biochemistry, A Wiley-Interscience Publication, John Wiley & Sons,**1979.**

(10) K. K. Unger, Porous Silica: its properties and use as support in column liquid chromatography, Elsevier Scientific Publishing Company, **1979**.

(11) I-Ssuer Chuang and G. E. Maciel, J. Am. Chem. Soc. **118**, 401 (1996).

(12) J. J. Fripiat and J. Uytterhoeven, J. Phys. Chem. **66**, 800 (1962).

(13) M. L. Hair, Infrared Spectroscopy in Surface Chemistry, Marcel Dekker, New York, **1967**.

(14) W. Noll, K. Damm and R. Fauss, Kolloid-Z. **169**, 18 (1969).

(15) I. –S. Chuang, D. R. Kinny, C. E. Bronnimann, R. C. Zeigler, and G. E. Maciel, J. Phys. Chem. **94**, 4189 (1990).

(16) F. J. Feher, D. A. Newmann, and J. F. Walzer, J. Am. Chem. Soc. **118**, 13040 (1996).

(17) G. E. Maciel and D. W. Sindorf, J. Am. Chem. Soc. **102**, 7606 (1980).

(18) D. W. Sindorf and G: E. Maciel, J. Phys. Chem. **86**, 5208 (1982).

(19) E. Maciel, Encyclopedia of Nuclear Magnetic Resonance, ed. by D. M. Grant and R. K. Harris, **1996**, 4370-4386.

(20) C. E. Bronnimann, R. C. Zeigler, G. E. Maciel, J. Am. Chem. Soc. **110**, 2023 (1988).

(21) I. –S. Chuang, D. R. Kinney, and G. E. Maciel, J. Am. Chem. Soc. **115**, 8693 (1993).

(22) D. R. Kinny, I.-S. Chuang, and G. E. Maciel, J. Am. Soc. **115**, 6786 (1993).

(23) K. Overloop and L. Van Gerven, J. Magnet. Reson. Series A **101**, 147 (1993):

(24) J. –B. d'Espinose de la Caillerie, M. Raouf Aimeur, Y. El Kortobi, and A. Pierre Legrand, J. Colloid Interface Sci. **194**, 434 (1997).

(25) A. Bogdan, M. Kulmala, B. Gorbunov, and A. Kruppa, J. Colloid Interface Sci. **177**, 79 (1996).

(26) Y. Ba, Ph.D. Thesis, Gerhard-Mercator University of Duisburg, **1995**.

(27) D. A. Lathrop and K. K. Gleason, Macromolecules **26**, 4652 (1993).

Chapter 7. Phase selection of polymers by double-quantum filtered MAS NMR

In this chapter, ^{1}H-2QC-filtered-^{13}C-MAS-NMR spectroscopy is used to distinguish and probe the different phases in polymers. The investigated materials include one semicrystalline homopolymer, two copolymers, and two polymer blends. It will be shown that the three-pulse sequence under MAS with a short excitation time can be employed to generate ^{1}H 2QC from the rigid phases, and that the time-reversible eight-pulse sequence can be used to excite ^{1}H 2QC from the mobile, usually amorphous domains.

7.1 Experimental

Samples

The investigation of the following polymer materials is described in this chapter:

(1) Semicrystalline polyoxymethylene (DELRIN® 100) is commercially available from DuPont de Nemours (Germany) GmbH. For NMR measurements the granular sample was first melted at 200°C and then pressed into a bar form, then scraped into small pieces using a scalpel and filled into a 7 mm MAS rotor. Another commercial semicrystalline polyethylene will be investigated in great detail in the next chapter.

(2) The poly(butylene terephthalate)-co-poly(tetramethylene oxide) (PBT/PTMO) copolymer, is from DSM Research B. V., Geleen, The Netherlands. It has the following properties: block length, 2000 g/mol; the amount of PTMO, 60 wt%; the number average degree of polymerization, $\overline{p}_n$(PTMO) = 27.7 and $\overline{p}_n$(PBT) = 6.5. For the NMR measurement the sample was injection-moulded into a bar form and cut into 4×4×10 mm block and loaded into a 7 mm zirconia rotor.

(3) The ethylene-propylene-diene-terpolymer (EPDM) is from HÜLS AG, Germany (BUNA AP437). Ethylidene norbornene is used for cross-links. The double bond content is 3 DB/1000 C. The ethylene content is 70 %. For the NMR measurement the powder sample was directly loaded into a 7 mm zirconia rotor.

(4) The polymer blend of isotactic polypropylene (iPP, Vestolen P7000 from Hüls AG, Marl) with a 95 % isotactic structure and EPDM consists of 60 % (volume) iPP and 40 % EPDM.

(5) The polymer blend of the PBT/PTMO copolymer and EPDM with a 50/50 composition was also studied in this chapter.

NMR measurements

All NMR measurements were carried out on a Bruker ASX-400 spectrometer operating at 400 MHz and 100 MHz for ^{1}H and ^{13}C, respectively. A Bruker double-bearing CP MAS 7 mm probe was used.

To generate ^{1}H double-quantum coherences, two different pulse sequences, i.e., the three-pulse sequence and the eight-pulse sequence, were employed. For obtaining high resolution the multiple pulse sequences were combined with magic angle rotation. The three-pulse sequence with a short excitation time (Figure 4.3) and the eight-pulse sequence with a long excitation time (Figure 4.11b) can excite double-quantum coherences from rigid and amorphous domains, respectively. The 90° pulse length was 5 μs. An eight-step phase cycling in the preparation period with respect to mixing period was used to select the double-quantum coherences in both cases. For saving experiment time and for simplicity we kept the evolution time t_1 constant in both pulse sequences: in the three-pulse sequence we fixed t_1=5 μs, in the eight-pulse sequence experiments we set t_1=0. In the detection period, the ^{1}H-2QC-filtered-^{1}H-1QC was detected via ^{13}C through cross-polarization (Figure 4.12). The high-resolution ^{13}C spectra are observed. Other detailed parameters are given in the results and discussion section.

7.2 Results and Discussions

7.2.1 Semicrystalline polymer: Polyoxymethylene (POM)

Polyoxymethylene (POM) is a semicrystalline polymer with chain structure $(-CH_2-O-)_n$, made by the polymerization of formaldehyde. The chemical composition and the highly crystalline structure of the homopolymer offer a unique combination of physical properties, not available with metals or most other plastics. Since its introduction in 1960 by DuPont, it has been widely used around the world in many applications, such as in the automotive, appliance, construction, hardware, electronic, and consumer goods industry.

Polyoxymethylene has two crystal modifications: the trigonal and the orthorhombic forms. The trigonal form is stable at ambient temperature, with the chains arranged in a 9/5 helical conformation mode[1,2]. Within a single crystal only helices with the same handedness are existent, with the right or left handedness equally probable. From melt crystallized POM has a spherulitic structure, containing crystalline lamellae and amorphous phases. The lamellae are about 100 Å, in which the molecular chains are folded[2].

Normally the heterogeneity can be probed through measuring of the spin relaxation properties of different domains, such as T_1, $T_{1\rho}$ and T_2. These measurements reflect the different chain mobilities in different phases. As a new method, we will illustrate in this section that double-quantum filtered MAS NMR can be well used to study the heterogeneity in semicrystalline polymers.

The high-resolution ^{13}C NMR spectrum of POM has been first studied by Veeman et al.[3] by means of the proton-decoupled magic-angle-spinning (MAS) technique with and without cross-polarization (CP). They found that the trigonal POM has a singlet line at about 90 ppm with a line width of 3.7-5.7 ppm depending on the MAS frequency. The ^{13}C T_1 and $T_{1\rho}$ measurements showed[3] the coexistence of two phases: a crystalline phase having short $T_{1\rho}$ (0.5-3 ms) and long T_1 (>>10 s) and an amorphous phase having long $T_{1\rho}$ (17.5 ms) and short T_1 ($\leq$1 s). Cholli et al.[4] used a modified CP MAS method to separate the amorphous and crystalline phases. They found that the amorphous peak appeared at about 1 ppm downfield compared to the crystalline peak. Kurosu et al.[5] investigated the ^{13}C CP MAS spectra of trigonal POM in various samples. They observed a peak centered at 88.5 ppm, which can be simulated by two Lorentzian lines centered at 88.5 ppm and 89.4-91.5 ppm (depending on the crystallinity of the samples), the former and the latter being ascribed to the crystalline and amorphous phases, respectively.

Figure 7.1 shows the ^{13}C spectra of DELRIN® 100. The deconvoluted spectra are represented in Figure 7.2 and the deconvolution results are given in Table 7.1.

Fig. 7.1a is the ^{13}C spectrum of DELRIN® 100 recorded using the simple CP MAS pulse sequence. It consists of one peak at about 88 ppm with a downfield shoulder centered at about 89 ppm. The resonance at 88 ppm comes from the carbons in rigid crystalline phases with their chains having a gauche conformation, and the shoulder peak comes from the carbons in mobile amorphous phases.

The ^{13}C detected ^{1}H double-quantum coherence filtered spectrum is shown in Fig. 7.1b. The three-pulse sequence with an excitation time of 5 μs was used to generate the ^{1}H double-quantum coherences from the crystalline phases which have strong proton dipolar couplings. The proton spin pairs with smaller dipolar couplings in the amorphous domains do not experience enough time to become fully aware of each other and are not involved in the ^{1}H 2QC, thus the signals from the amorphous domains are rejected under this condition. For comparison, the spectrum in Figure 7.1b is enlarged and replotted together with the spectrum of Figure 7.1a (see Fig. 7.1d). It is obvious that the downfield shoulder in Fig. 7.1a has disappeared here (see Fig. 7.1d). The spectrum of Figure 7.1b can be well fitted with two peaks (see Fig. 7.2b and Table 7.1): one peak at 87.8 ppm and the other at 88.6 ppm. They might be assigned as the inequivalent carbon atoms from -CH_2- units in the crystal phase of the trigonal lattice as suggested by Kobayashi[6], the resonance at 88.6 ppm coincides with that of the crystal signal in the ordinary trigonal POM, while the resonance at 87.8 ppm corresponds to the highly ordered crystal phases in the trigonal POM.

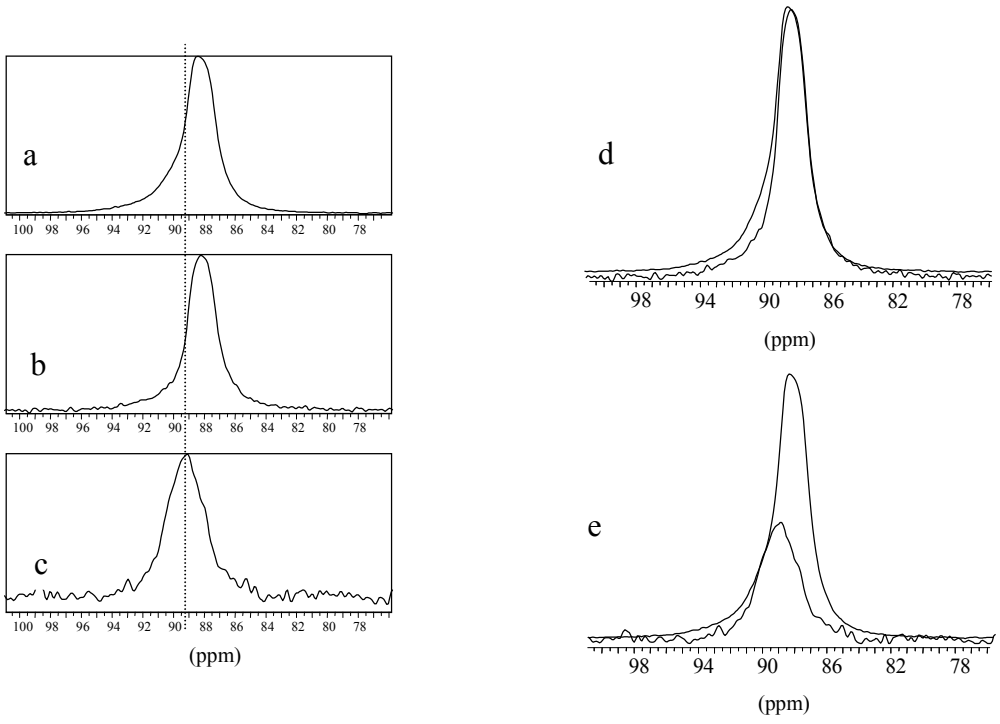

Figure 7.1. *^{13}C spectra of DELRIN® 100 recorded under CP MAS with a MAS frequency of 5 kHz and a contact time of 2 ms, the recycle time was 3 s. (a) ^{13}C CP MAS spectrum; (b) ^{13}C detected ^{1}H-2QC-filtered spectrum recorded by using the three-pulse sequence with an excitation time of 5 μs; (c) ^{13}C-detected-^{1}H-2QC-filtered spectrum recorded by using the eight-pulse sequence with an excitation time of 200 μs; (d) comparison of*

spectrum (a) and (b) which are normalized to the same height; (e) comparison of spectrum (a) and (c). The dashed line in the left column emphasizes the peak positions in the different spectra.

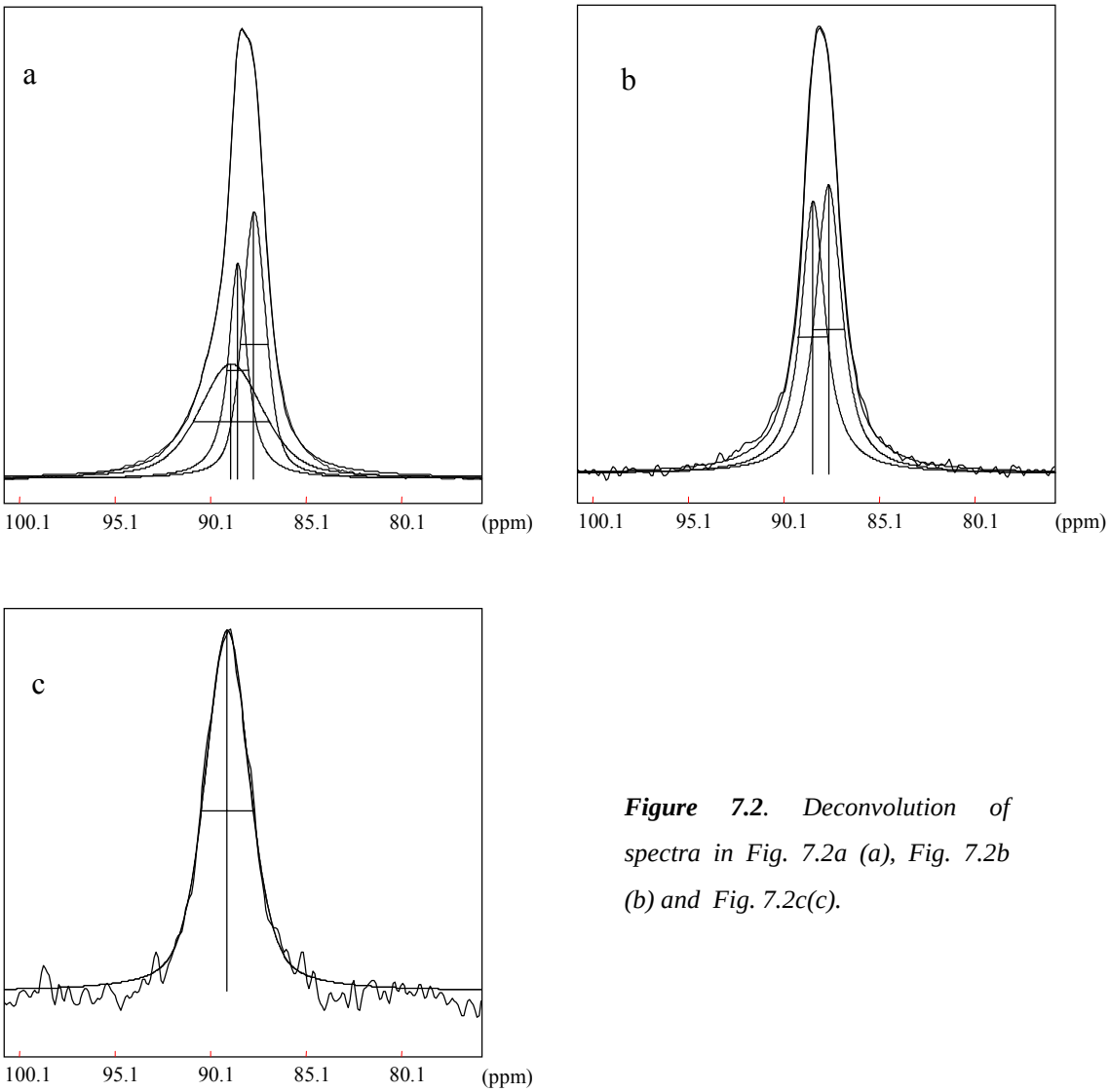

***Figure 7.2**. Deconvolution of spectra in Fig. 7.2a (a), Fig. 7.2b (b) and Fig. 7.2c(c).*

***Table 7.1**. The deconvolution results of Figure 7.2.*

Figure no.	phase	chain conformation	chemical shift (ppm)	width at half height (ppm/Hz)	Gauss factor	relative content (%)
Fig. 7.2a	crystalline	gauche	87.8	1.5/146.9	0.5	34.8
	crystalline	gauche	88.7	1.1/114.7	0	26.0
	amorphous	trans	89.0	4.0/399.5	0.5	39.1
Fig. 7.2b	crystalline	gauche	87.8	1.6/161.0	0.15	54.0
	crystalline	gauche	88.6	1.4/143.9	0	46.1
Fig. 7.2c	amorphous	trans	89.2	2.7/274.7	0.55	100.0

For observing amorphous phases, the time-reversible eight-pulse sequence with an excitation time of 200 μs was used. Under this condition, the signals from the rigid crystalline domain are relaxed due their short ^1H T_2 time and thus eliminated from the filtered spectrum. The double-quantum coherence filtered spectrum is illustrated in Figure 7.1c, one broad peak centered at 89.22 ppm (see Fig. 7.2c and table 7.1) is obtained. Compared with the normal CPMAS spectrum in Figure 7.1a, the upfield resonances are obviously absent in the detected spectrum (see Fig. 7.1e). This difference is also perceivable through comparison of the peak positions of the different spectra: the dashed line in the left column in Figure 7.1 clearly shows this difference.

7. 2. 2 Some elastomers and copolymers

As a further application, we have employed the three-pulse sequence and the eight-pulse sequence to two kinds of elastomers: one is an ethylene-propylene-diene-terpolymer (EPDM), and the other is a poly(butylene terephthalate)-co-poly(tetramethylene oxide) PBT/PTMO copolymer.

7. 2. 2. 1 Ethylene-propylene-diene-terpolymer (EPDM)

Ethylene-propylene-diene-terpolymer (EPDM) contains a saturated backbone and unsaturated termonomer in the side chain of the molecule. The saturated backbone accounts for its excellent weatherability and ozone resistance, and the unsaturated termonomer permits direct sulphur cure as well as chemical modification. It is an important industrial material. The properties of EPDM are largely determined by the saturated nature of the backbone, the relative amounts of ethylene, propylene and diene, as well as the molecular weight. Other factors such as molecular weight distribution, composition distribution, and type of diene also affect the product properties. Normally three types of diene are used for cross-links: ethylidene norbornene (ENB), dicyclopentadiene (DCPD) and 1.4-hexadiene (HD). Ethylidene norbornene (ENB) is used in the EPDM in this study. This EPDM has the following structure:

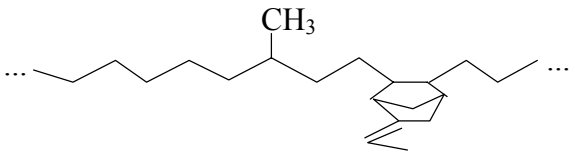

It is a semicrystalline copolymer, the crystallinity[7] is about 28 % (determined from the wide-angle-X-ray-diffraction). The ^{13}C spectra of BUNA AP437 are illustrated in Figure 7.3. Figure 7.3a is the simple ^{13}C CP MAS spectrum, the peaks can be assigned according to literature[8-11] and the assignments are listed in Table 7.2. For simplicity, the primary, secondary and tertiary carbons are represented by P, S and T, respectively. The Greek subscripts indicate the displacements of the interested carbons relative to the nearest tertiary carbons in both directions along the polymer chains. As an example, the unit structure of $T_{\alpha\beta}$ and $S_{\alpha\beta}$ are illustrated as follows:

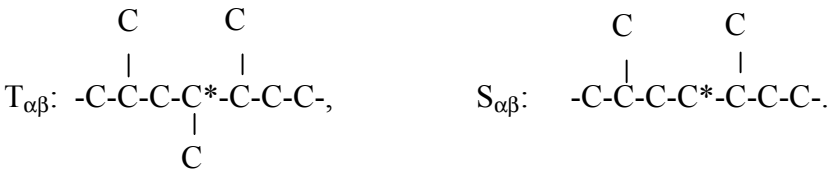

Figure 7.3b is the ^{13}C-detected-^{1}H-2QC-filtered spectrum. The three-pulse sequence with an excitation time of τ = 5 μs was used to generate the ^{1}H double-quantum coherences from the rigid, crystalline domain, as discussed before. The signals are dominated by the resonances at 33.1 ppm (62.3%) and at 31.0 ppm (29.8%), which mainly arise from the PE (polyethylene)-sequence, i.e., $S_{\delta\delta}$, $S_{\beta\gamma}$, and $T_{\delta\delta}$, $T_{\gamma\delta}$ sequences. There are also some small contributions from the other sequences: the resonance at 20.2 ppm (3.8%) comes from the sequences of $P_{\alpha\alpha}$, $P_{\beta\beta}$, $P_{\beta\gamma}$, $P_{\beta\delta}$, the resonance at 39.5 ppm (4.2%) comes from the chain ends containing more than six methylene units[9].

Figure 7.3c shows the ^{13}C-detected-^{1}H-2QC-filtered spectrum using the time-reversible eight-pulse sequence. The spectrum was recorded under MAS frequency of 5 kHz with an excitation time of 200 μs. Compared with the spectrum in Figure 7.3b, the signals are mainly from the mobile sequences in EPDM. The dominating resonance at 30.8 ppm (51.1%) is from the $S_{\delta\delta}$, $S_{\beta\gamma}$ sequences in EPDM.

For direct comparison, the spectra in Figure 7.3 are normalized to the same height and plotted together in the top part of Figure 7.4, the differences of the compared spectra are given in the bottom part of Figure 7.4. The differences between the normal CPMAS spectrum and the

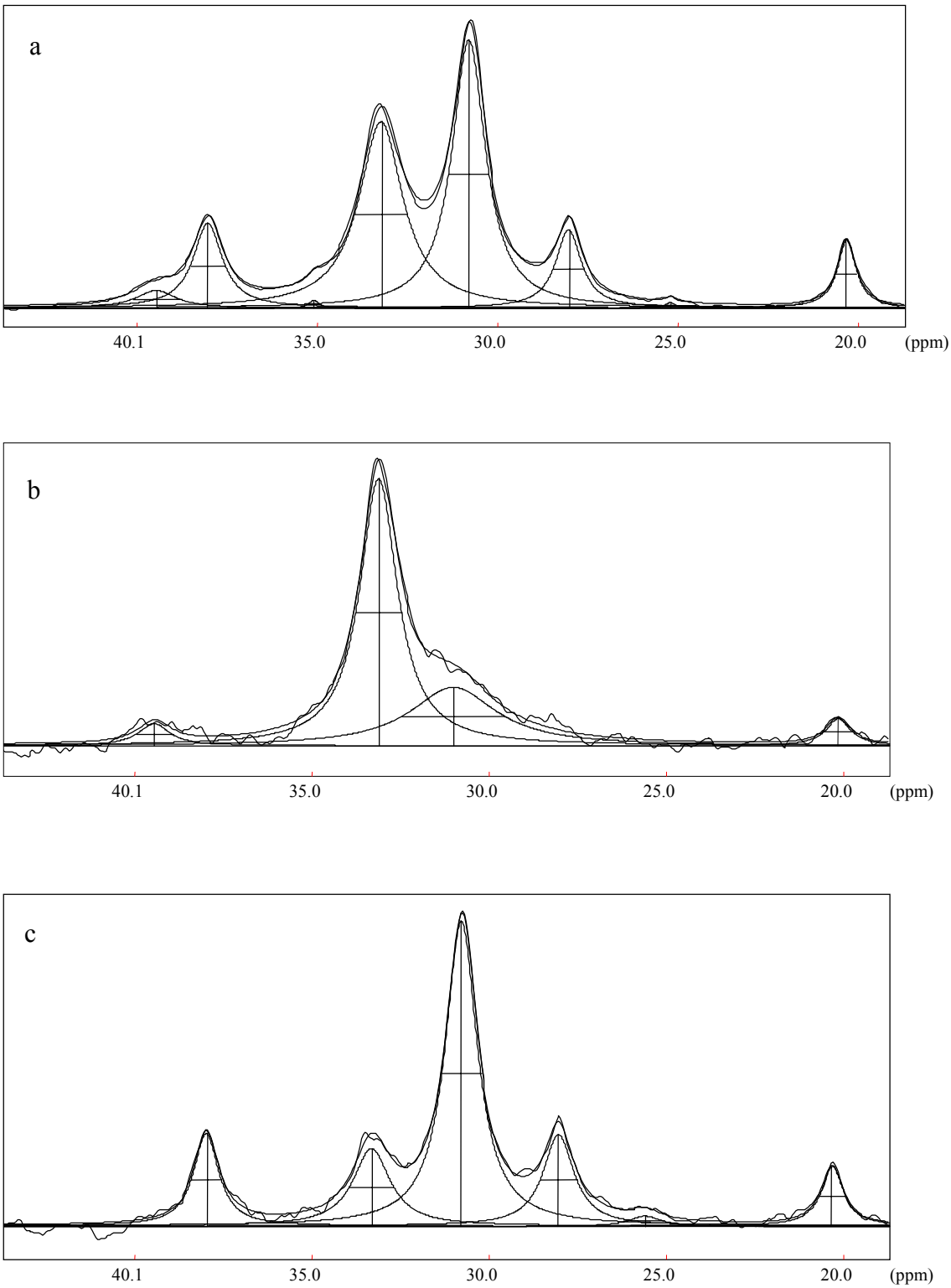

Figure 7.3. *The ^{13}C spectra of EPDM recorded with the following parameters: MAS frequency 5kHz, contact time 1 ms, recycle time 3 s, 90° pulse duration 5 μs. (a) The simple CPMAS spectrum, (b) ^{1}H 2QC filtering under the three-pulse sequence, (c) ^{1}H 2QC filtering under the eight-pulse sequence.*

***Table 7.2**: The results of deconvolution and the assignments of spectra in Figure 7.3.*

Figure no.	block type	chemical shift (ppm)	width at half height (ppm)	relative content (%)
Fig. 7.3a	$P_{\alpha\alpha}$, $P_{\beta\beta}$, $P_{\beta\gamma}$, $P_{\beta\delta}$	20.34	0.61	5.1
	$S_{\beta\beta}$	25.22	0.29	0.2
	$S_{\beta\gamma}$, $S_{\beta\delta}$, $S_{\beta\beta}$	28.04	0.86	8.6
	$S_{\delta\delta}$, $S_{\beta\gamma}$	30.81	1.13	38.3
	$T_{\delta\delta}$, $T_{\gamma\delta}$	33.25	1.48	24.4
	$S_{\alpha\beta}$	35.11	0.32	0.3
	$S_{\alpha\delta}$, $S_{\alpha\gamma}$	38.06	0.97	10.3
	*	39.49	1.32	2.8
Fig. 7.3b	$P_{\alpha\alpha}$, $P_{\beta\beta}$, $P_{\beta\gamma}$, $P_{\beta\delta}$	20.17	0.83	3.8
	$S_{\delta\delta}$, $S_{\beta\gamma}$	31.02	2.94	29.8
	$T_{\delta\delta}$, $T_{\gamma\delta}$	33.13	1.29	62.3
	*	39.47	1.06	4.2
Fig. 7.3c	$P_{\alpha\alpha}$, $P_{\beta\beta}$, $P_{\beta\gamma}$, $P_{\beta\delta}$	20.34	0.76	6.5
	$S_{\beta\gamma}$, $S_{\beta\delta}$, $S_{\beta\beta}$	28.05	1.13	15.5
	$S_{\delta\delta}$, $S_{\beta\gamma}$	30.80	1.1	51.1
	$T_{\delta\delta}$, $T_{\gamma\delta}$	33.33	1.27	15.0
	$S_{\alpha\delta}$, $S_{\alpha\gamma}$	38.00	0.86	12.0

* According to Cheng et al.[10] this peak may be assigned as the following chain ends:

$$-CH_2-CH_2-CH_2-CH_2-CH_2-CH_2-CH_2-CH_2-CH_2-\underset{\displaystyle CH_3}{\underset{|}{CH}}-CH_2-CH_3$$

2QC-filtered spectrum are clearly illustrated in Figure 7.4.

From above, one can see that the BUNA AP437 is heterogeneous with respect to chain mobility. The copolymer EPDM has at least two distinguishable phases, i.e., crystalline and amorphous domains. The mobile, amorphous domain can be detected using the time-reversible eight-pulse sequence. The ^{13}C-detected-^{1}H-2QC-filtered spectrum has main resonances at 28.05 ppm (15%), 30.80 ppm (51.1%) and 33.33 ppm (15%). The rigid,

crystalline domain can be selected by using the three-pulse sequence. The observed ^{13}C spectrum is then dominated by the resonances at 31.0 ppm (29.8%) and 33.13 ppm (62.3%).

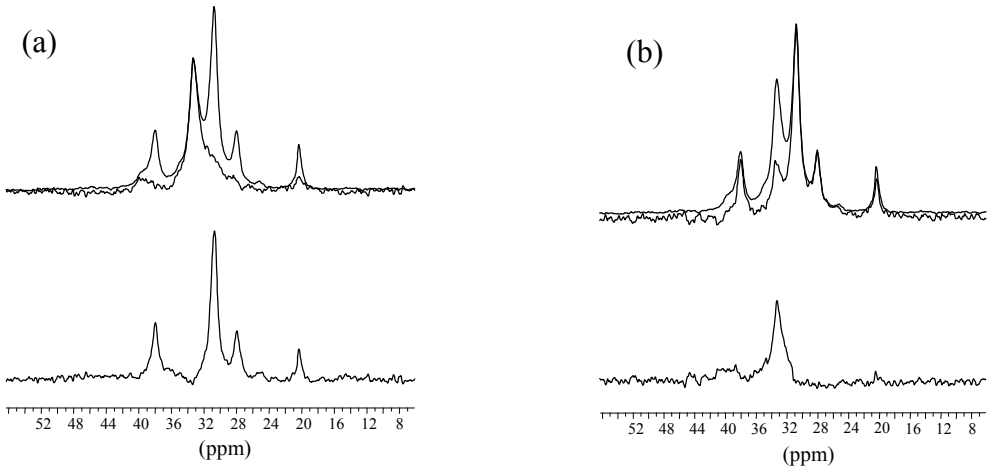

Figure 7.4*. Comparison of the ^{13}C spectra from Figure 7.3a and 7.3b (a), and from Figure 7.3a and 7.3c (b). Top: the spectra are normalized to the same height and plotted together for comparison. Bottom: the difference of the top spectra.*

7. 2. 2. 2 Poly(butylene terephthalate)-co-poly(tetramethylene oxide) PBT/PTMO copolymer.

Poly(butylene terephthalate)-co-poly(tetramethylene oxide) PBT/PTMO copolymer is another example of a copolymer. It contains hard segments (PBT blocks) and soft segments (PTMO blocks) in the molecular chains. The soft segments impart elastomeric character to the copolymers, whereas the hard segments form thermally reversible noncovalent networks, analogous to the covalent cross-links in elastomers.

Figure 7.5 shows ^{13}C spectra obtained from the copolymer PBT/PTMO using cross-polarization (CP) combined with the magic-angle-spinning (MAS). Figure 7.5a is the simple CPMAS spectrum. The peaks can be assigned as follows[12,13]: the 65.5 ppm peak arises from the -OCH_2- groups of PBT blocks; the 71 ppm peak is from the -OCH_2- groups of PTMO blocks; the line at 27.3 ppm with an upfield shoulder is assigned to the resonances of the internal methylene groups of PTMO and PBT blocks; the resonances at 164.5 ppm, 134.2 ppm and 130.8 ppm/129.6 ppm belong to the carbonyl carbons, the nonprotonated aromatic carbons and the protonated aromatic carbons, respectively.

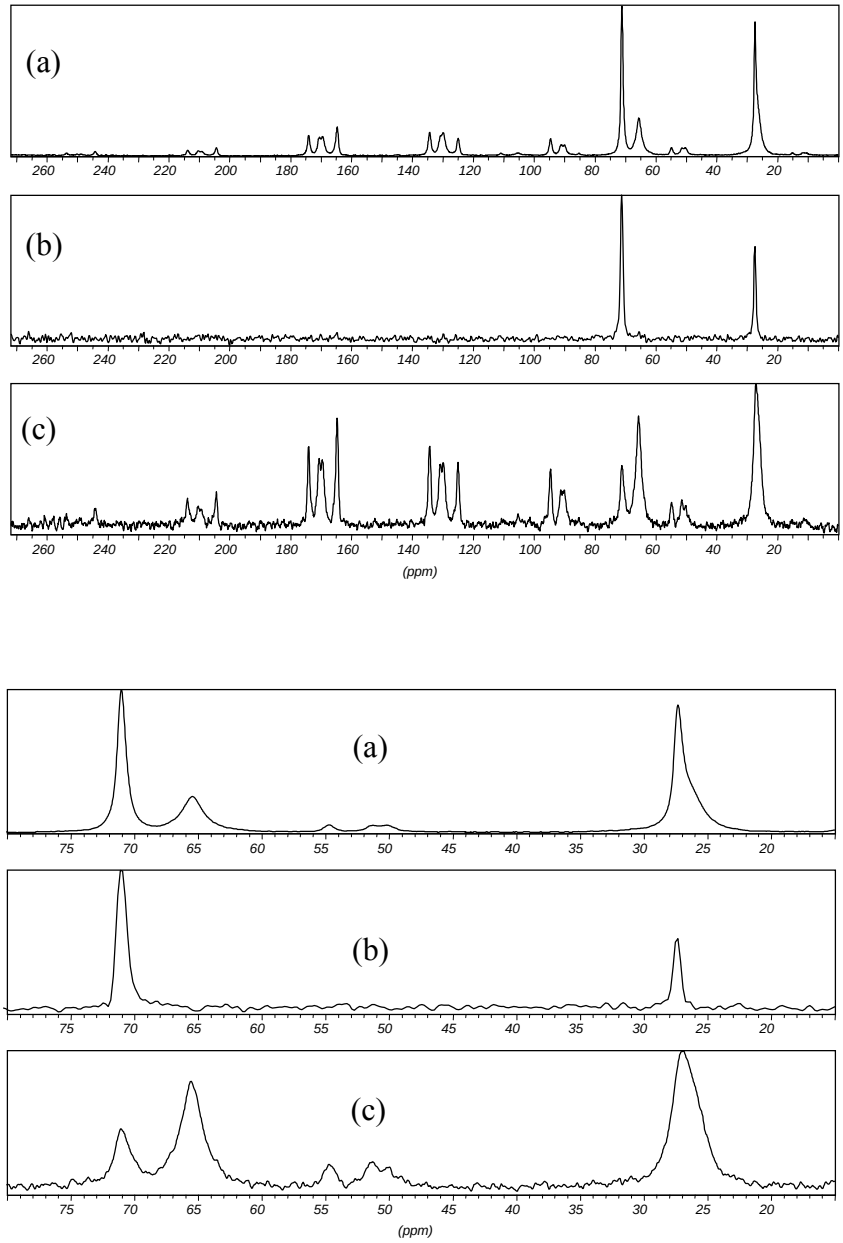

***Figure 7.5**. The ^{13}C spectra of PBT/PTMO copolymer. All the spectra were recorded under a MAS frequency of 4 kHz and a CP contact time of 1 ms. Top: the whole chemical shift range of the spectra are shown. Bottom: the expanded spectra containing only the resonances from the –OCH_2- and –CH_2- groups are shown. (a) ^{13}C CPMAS spectrum, (b) ^{13}C-detected-^{1}H-2QC-filtered spectrum, recorded under the effect of the eight-pulse sequence with an excitation time of 250 μs, the pulse sequence was synchronized with the rotation of the rotor in the condition of $t_r = 2\ t_c$, (c) ^{13}C-detected-^{1}H-2QC-filtered spectrum recorded under the effect of the three-pulse sequence with an excitation time of 5 μs.*

Figure 7.5b shows the ^{13}C-detected-^{1}H-2QC-filtered spectrum (eight-pulse sequence). Under long enough excitation time, in this case the excitation time is 250 μs, the signal from the rigid domains are relaxed during the excitation period due to the ^{1}H short T_2 time, so the

obtained signals reflect the amorphous domains. From Figure 7.5b (top) one can observe that the ^{13}C signals from the aromatic carbons are completely eliminated in the ^{13}C-detected-^{1}H-2QC-filtered spectrum obtained by using the eight-pulse sequence, so we will only discuss the ^{13}C signals from the $–OCH_2-$ and $–CH_2-$ groups. For comparison, the spectra in Figure 7.5 (top) are expanded in Figure 7.5 (bottom) containing only the ^{13}C resonances from the $–CH_2-$

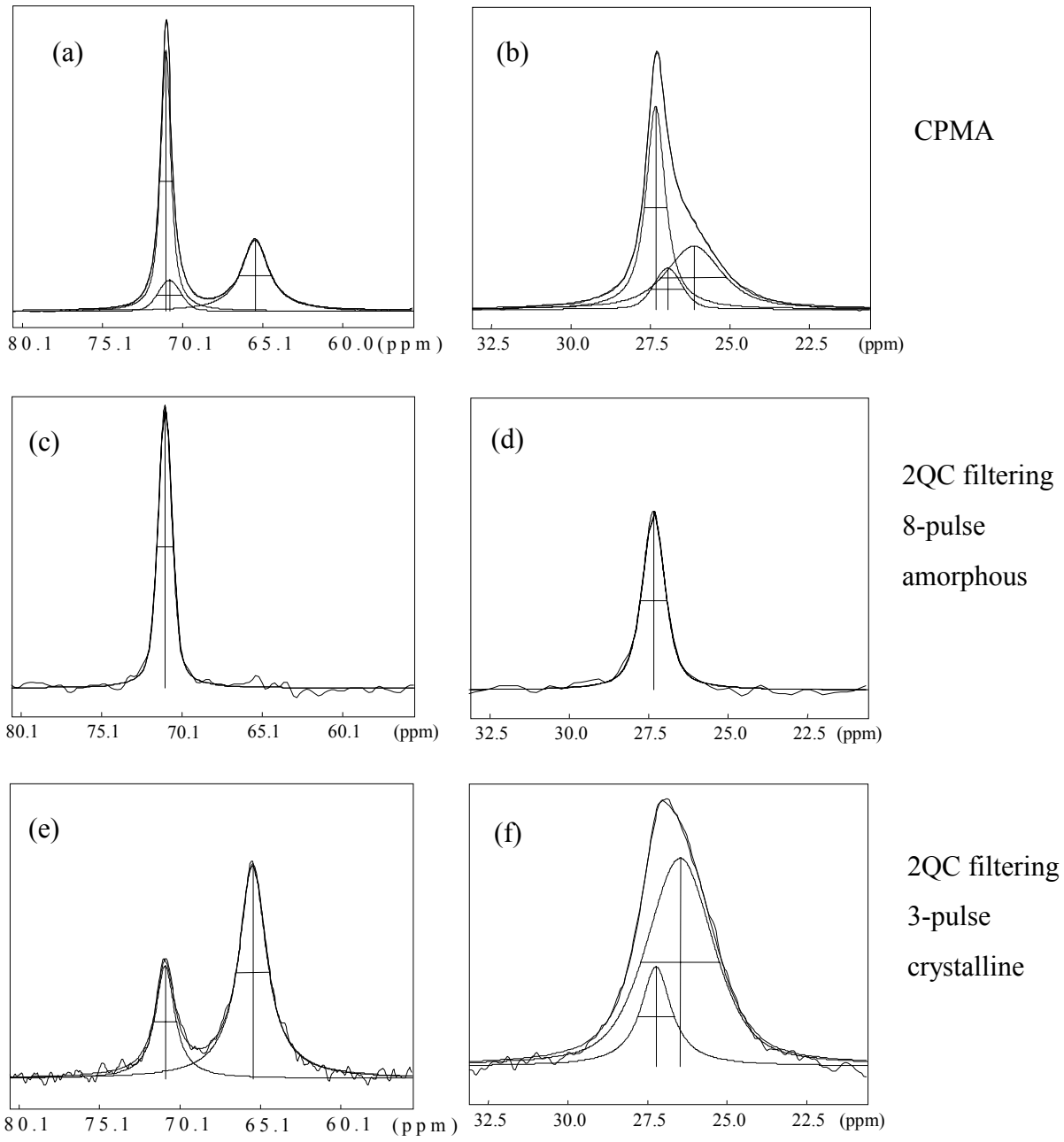

Figure 7.6. *Deconvolution of the spectra in Figure 7.5. The left column shows the ^{13}C spectra of $–OCH_2-$ groups, in the right column are the ^{13}C spectra of $–CH_2-$ groups. (a) and (b) are the ^{13}C spectra of CPMAS, (c) and (d) are the ^{13}C-detected-^{1}H-2QC-filtered spectra recorded under the effect of the eight-pulse sequence with an excitation time 250 μs, (e) and (f) are the ^{13}-detected-^{1}H-2QC-filtered spectra recorded under the effect of the three-pulse sequence with an excitation time 5 μs.*

Table 7.3. *The deconvolution results of Figure 7.6.*

Fig. No.	Block type	Carbon type	Chemical shift (ppm)	Linewidth at half height (ppm)	Relative content (%)
Fig. 7.6a	PBT	-OCH_2-	65.5	2.0	38
	PTMO	-OCH_2-	70.9	1.8	11
			71.1	0.8	51
Fig. 7.6b	PBT	-CH_2-	26.1	2.1	41
	PTMO	-CH_2-	27.0	1.0	11
			27.3	0.7	48
Fig. 7.6c	PTMO	-OCH_2-	71.0	1.0	100
Fig. 7.6d	PTMO	-CH_2-	27.4	0.7	100
Fig. 7.6e	PBT	-OCH_2-	65.6	2.1	74
	PTMO	-OCH_2-	71.0	1.5	26
Fig. 7.6f	PBT	-CH_2-	26.5	2.6	75
	PTMO	-CH_2-	27.2	1.3	25

and –OCH_2- groups. The peaks were deconvoluted as shown in Figure 7.6 using the Bruker WINFIT program, and the deconvoluted results are tabulated in Table 7.3.

First, we make a closer examination of the change of the ^{13}C signals from the –OCH_2- groups as shown in the left column in Figure 7.6 and Table 7.3. The ^{13}C CP MAS spectrum can be deconvoluted into three peaks (see Fig. 7.6a): two peaks (one resonates at 71.1 ppm with a line width at half height of 0.8 ppm, the other resonates at 70.9 ppm with a line width at half height of 1.8 ppm) can be assigned as the ^{13}C resonances of the –OCH_2- groups from the mobile and the motionally restricted PTMO blocks (see below); the third peak at 65.5 ppm with a linewidth at half height of 2.0 ppm is the ^{13}C response from the –OCH_2- groups of the PBT blocks[11]. The mobile –OCH_2- groups are present in the PTMO rich domains, while the motionally restricted PTMO blocks are found in a mixture phase of PBT/PTMO blocks, where the mobility of the PTMO blocks are affected by the rigid PBT blocks.

Figure 7.6c is the ^{13}C-detected-^{1}H-2QC-filtered spectrum, which was recorded using the eight-pulse sequence. Under this condition, the signals from the rigid phases are relaxed due to the too long ^{1}H T_2 during the excitation period and filtered out, and only the signals from

the mobile PTMO blocks are passed. The 71.0 ppm peak with a width at half height of 1.0 ppm (see Figure 7.6c and Table 7.3) corresponding to -OCH_2- groups of mobile PTMO blocks is clearly selected and separated from the rigid domains of copolymer PBT/PTMO.

Figure 7.6e shows the ^{13}C detected ^{1}H 2QC (from the rigid domains of PBT/PTMO) filtered spectrum, which was obtained by using the three-pulse sequence. In this case, i.e., with a short excitation time 5 μs, the proton spin pairs with a smaller dipolar coupling from the mobile PTMO chains have not enough time to become correlated with each other, thus the signals from the mobile phases are eliminated. The acquired spectrum contains two peaks: the peak at the position of 71.0 ppm with a width at half height of 1.5 ppm is the ^{13}C resonance of the –OCH_2- groups from the motionally restricted PTMO blocks; the other at position of 65.6 ppm with a width at half height of 2.1 ppm is the ^{13}C resonance of the –OCH_2- groups from the rigid PBT blocks. Compared with Figure 7.6a, the relative ratio of the integrated intensities of -OCH_2- groups from PBT blocks and those from PTMO blocks are drastically changed in Figure 7.6e due to the elimination of the mobile PTMO units: in Figure 7.6a the relative ratio of the integrated intensity of -OCH_2- groups from PBT and those from PTMO blocks is 38/62, while this ratio is increased to 74/26 in Figure 7.6e (see Table 7.3). The resonances in Figure 7.6e may arise from rigid carbons in the PBT-richer domains or phases, which have a mixture of PBT and motionally restricted PTMO blocks. It may be regarded as PBT/PTMO interfaces[12].

The existence of two kinds of PTMO phases was also proved by ^{1}H and ^{13}C $T_{1\rho}$, and T_{CH} (contact time for cross-polarization) measurements[12]. All these relaxation time measurements showed that the -OCH_2- resonance of PTMO gives a biexponential behaviour. This suggests that there are two different types of PTMO blocks: the mobile PTMO units form the continuous domain or phase, while the motionally restricted PTMO blocks together with the hard PBT segments are localized in a rigid PTMO phase.

The same analysis can be made to the spectra in the right column of Figure 7.6. The line shape in Figure 7.6b can be deconvoluted into three peaks: two ^{13}C resonances at 27.3 ppm and 27.0 ppm are from the methylene –CH_2- groups of mobile and motionally restricted PTMO blocks, respectively, and one resonance at 26.1 ppm is from the PBT blocks. Figure 7.6d is the ^{13}C-detected-^{1}H-2QC-filtered spectrum recorded under the time-reversible eight-pulse sequence, the ^{13}C resonance at 27.4 ppm represents the signal from the mobile PTMO blocks. Figure 7.6f is the ^{13}C-detected-^{1}H-2QC-filtered spectrum obtained by using the three-pulse sequence.

It shows two ^{13}C resonances at 27.2 ppm and 26.5 ppm, which can be assigned to the motionally restricted PTMO blocks and PBT blocks, respectively.

7.2.3 Application of ^{1}H-2QC-filtered-MAS-NMR to polymer blends

Above we have studied a homopolymer and copolymers. In this section, we will simply illustrate the application of the double-quantum filtered MAS NMR to two polymer blends: one is iPP/EPDM with a composition of 60/40 (volume), the other is (PBT/PTMO)/EPDM with a composition of 50/50 (volume).

7.2.3.1 iPP/EPDM blend

Figure 7.7 shows the ^{13}C spectra of the polymer blend iPP/EPDM with a composition of 60/40 (volume). Figure 7.7a is the ^{13}C CP MAS spectrum. The spectrum reflects the contributions from both components of the blend. It can be deconvoluted into 9 peaks. The deconvoluted peak positions, linewidths and assignments are given in Table 7.4.

Figure 7.7b is the ^{13}C-detected-^{1}H-2QC-filtered spectrum recorded by using the three-pulse sequence with an excitation time of 5 μs. The ^{13}C resonances are mainly from the isotactic polypropylene matrix or phases. The peaks which resonate at 22.9 ppm, 26.7 ppm, and 44.6 ppm can be assigned [14-16] to the methyl, methine and methylene groups of the α-crystalline in iPP. There is only a small contribution from the rigid components in EPDM which resonate at 31.3 ppm (2.3 %, mainly coming from $S_{\delta\delta}$ and $S_{\beta\gamma}$ sequences) and 33.1 ppm (11.1 %, mainly coming from $T_{\delta\delta}$ and $T_{\gamma\delta}$ sequences). This means that EPDM has parts with a similar chain mobility as those of iPP. It would be interesting to know whether the rigid parts of iPP and EPDM are mixed on a molecular level. Further spin diffusion and double-quantum experiments are needed to verify this.

Figure 7.7c is the ^{13}C-detected-^{1}H-2QC-filtered spectrum. The spectrum can be deconvoluted into five peaks (the deconvoluted peak positions and assignments are given in Table 7.4) which arise from the mobile EPDM sequence. There is no contribution from iPP. This means that according to this filter, all chains of iPP are considered to be rigid.

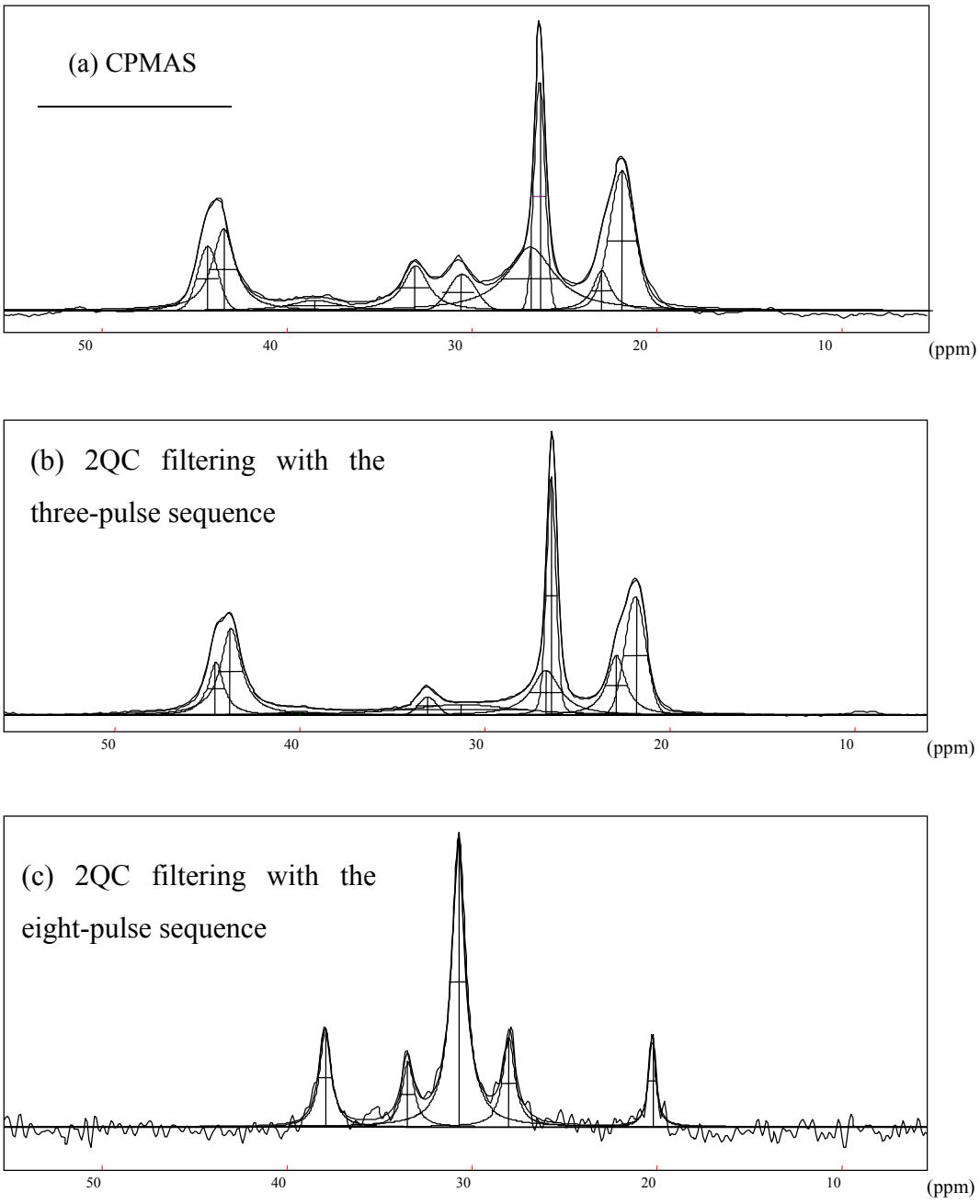

Figure 7.7. The ^{13}C spectra of polymer blend iPP/EPDM with a composition of 60/40 (volume). The spectra were recorded under a MAS frequency of 3.5 kHz with a contact time of 1 ms. (a) CPMAS spectrum, (b) ^{13}C-detected-^{1}H-2QC-filtered spectrum recorded by synchronizing the time-reversible eight-pulse sequence with MAS, the excitation time was 286 μs, (c) ^{13}C-detected-^{1}H-2QC-filtered spectrum recorded by using the three-pulse sequence with an excitation time of 5 μs.

Table 7.4*. The deconvolution results of Figure 7.7.*

Fig. No.	assignments		chemical shift (ppm)	width at half height (ppm)	relative content (%)
Fig. 7.7a	iPP	methyl	21.9	1.6	19.9
		methyl	23.0	1.1	5.4
		methine	26.4	0.7	13.2
		methine	26.9	3.13	22.9
		methylene	43.6	1.5	14.4
		methylene	44.4	1.3	6.7
	EPDM	$S_{\delta\delta}$, $S_{\beta\gamma}$	30.8	1.7	5.2
		$T_{\delta\delta}$, $T_{\gamma\delta}$	33.2	1.6	8.6
		$S_{\alpha\delta}$, $S_{\alpha\gamma}$	38.6	3.1	3.8
Fig. 7.7b	iPP	methyl	21.8	1.3	17.1
		methyl	22.9	1.2	11.2
		methine	26.4	0.6	17.2
		methine	26.7	1.8	13.0
		methylene	43.8	1.3	18.1
		methlyene	44.6	1.0	8.1
	EPDM	$S_{\delta\delta}$, $S_{\beta\gamma}$	31.3	7.1	2.3
		$T_{\delta\delta}$, $T_{\gamma\delta}$	33.1	1.2	11.1
		*(see Table 7.2)	40.1	3.1	1.7
Fig. 7.7c	EPDM	$P_{\alpha\alpha}$, $P_{\beta\beta}$, $P_{\beta\gamma}$, $P_{\beta\gamma}$	20.3	0.5	8.2
		$S_{\beta\gamma}$, $S_{\beta\delta}$, $S_{\beta\beta}$	28.1	0.8	13.8
		$S_{\delta\delta}$, $S_{\beta\gamma}$	30.8	0.9	53.5
		$T_{\delta\delta}$, $T_{\gamma\delta}$	33.6	0.8	10.0
		$S_{\alpha\delta}$, $S_{\alpha\gamma}$	38.0	0.7	14.6

7.2.3.2 (PBT/PTMO)/EPDM blend

Figure 7.8 shows the ^{13}C spectra of the polymer blend (PBT/PTMO)/EPDM with a composition of 50/50 (vol.). The spectra including all resonances are shown in the left column of Figure 7.8, while the aliphatic carbon ranges are expanded and shown in the right column of Figure 7.8.

Figure 7.8a is the ^{13}C CP MAS spectrum. It consists of all the contributions from the two components. This can be clearly observed in the resonance range of 20 – 40 ppm. In this range all the ^{13}C resonances from the EPDM domains overlap with those from the methylene $–CH_2-$ groups in the PBT/PTMO copolymer.

Figure 7.8b is the ^{13}C-detected-^{1}H-2QC-filtered spectrum recorded by using the three-pulse sequence with an excitation time of 5 μs. In this situation, the filtering effect of the three-pulse sequence is the same as in the case of the pure PBT/PTMO copolymer discussed in section 7.2.2.2: the ^{13}C resonances from the more mobile PTMO blocks or domains together with those from EPDM are totally filtered out, and only the resonances from the motionally restricted PTMO blocks and PBT blocks are observed and selected. There is no contribution from EPDM in the filtered spectrum. This is obvious by comparison of the resonance range of 20 – 40 ppm in Figure 7.8a and b.

Figure 7.8c is the ^{13}C-detected-^{1}H-2QC-filtered spectrum which was recorded by synchronizing the time-reversible eight-pulse sequence with MAS. Under this condition, the ^{1}H 2QC were excited only from the more mobile domains, those from the rigid PBT blocks together with the motionally restricted PTMO blocks are eliminated due to the short ^{1}H T_2 time. Comparing this spectrum with that in Figure 7.8b, one can deduce that the signals are mainly from the mobile PTMO blocks with only a small portion from EPDM. This observation indicates that the mobile PTMO block sequences and some EPDM chains in the blend of (PBT/PTMO)/EPDM have the same mobility. The ratio of the integrated intensities of them is 68/32.

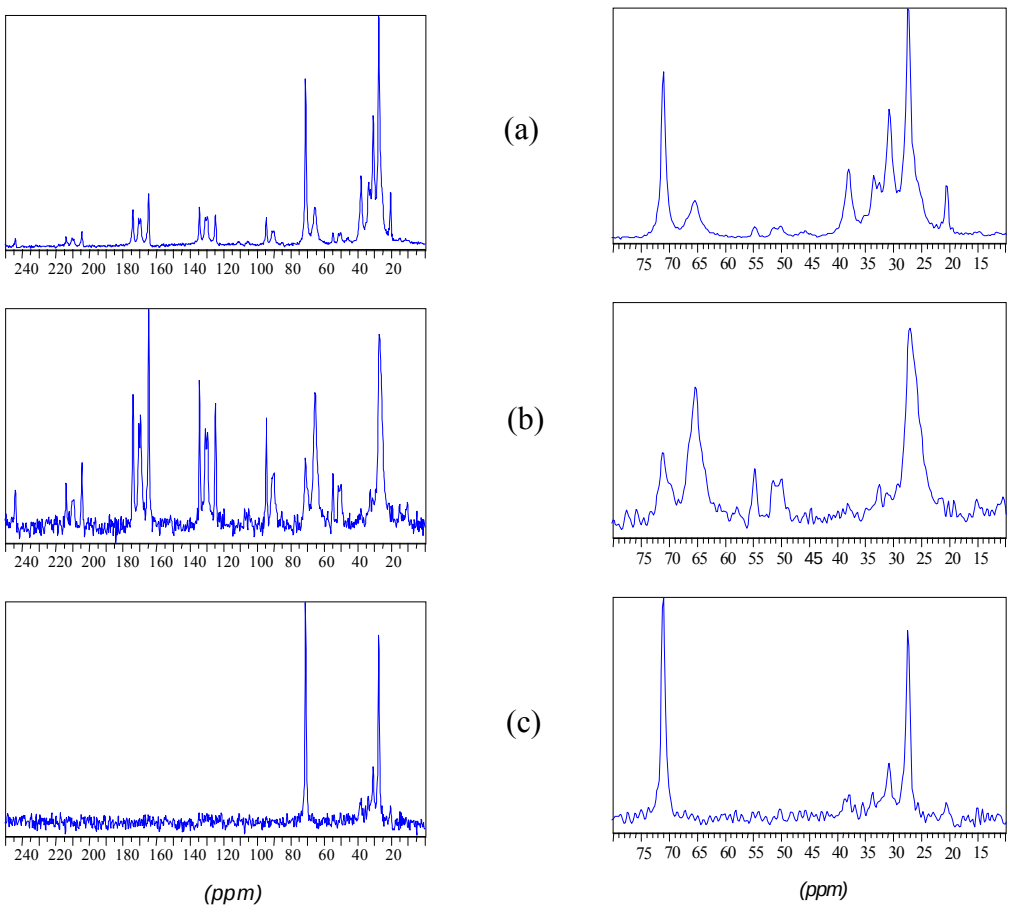

***Figure 7.8**. The ^{13}C spectra of polymer blend of (PBT/PTMO)/EPDM with a composition of 50/50 (vol.). The spectra were recorded under the MAS frequency of 4 kHz. Other parameters are as follows: the contact time for cross-polarization was 1 ms, the 90° pulse duration was 5 μs, and the recycle time 3 s. (a) The ^{13}C CP MAS spectrum. (b) The ^{13}C-detected-^{1}H-2QC-filtered spectrum recorded under the three-pulse sequence with an excitation time of 5 μs. (c) The ^{13}C-detected-^{1}H-2QC-filtered spectrum, which was recorded by synchronizing the time-reversible eight-pulse sequence with MAS, the excitation time was 250 μs.*

7.3 Conclusions

The following conclusions can be drawn from the above experiments:

(1) The two pulse sequences can be complementarily used to separate and select spectra from different domains with different proton dipolar interactions and molecular mobilities. The three-pulse sequence with a proper short excitation time (5 μs) generates ^{1}H double-quantum coherences from the more rigid or crystalline domains of the investigated polymers. The time-reversible eight-pulse sequence with a proper long excitation time (about 200 to 290 s),

synchronized with the rotation, can excite ^{1}H double-quantum coherences from the amorphous or mobile phases of polymers.

(2) The combination of ^{1}H 2QC filtering and ^{13}C detection is a necessary technique for getting high resolution spectra from the strongly proton dipolar coupled spin-1/2 solid polymers.

(3) Semicrystalline polyoxymethylene such as DELRIN®100 can be investigated using these two pulse sequences. Two domains are observed: the crystalline domains have a ^{13}C resonance at 88 ppm, while the amorphous domains have a ^{13}C resonance at 89 ppm.

(4) The heterogeneity of elastomers such as EPDM, and copolymers such as PBT/PTMO, as well as the polymer blends such as iPP/EPDM and (PBT/PTMO)/EPDM, can be well studied by these two pulse sequences.

References

(1) M. L. Huggins, J. Chem. Phys. **13**, 37 (1945).

(2) A. P. M. Kentgens, Dissertation, University of Nijmegen, The Netherlands, **1987**.

(3) W. S. Veeman, E. M. Menger, W. Ritchey, E. de Boer, Macromolecules **12**, 924 (1979).

(4) A. L. Cholli, W. M. Ritchey, J. L. Koening, Spectrosc. Lett. **16**, 21 (1983).

(5) H. Kurosu, T. Yamanobe, I. Ando, Chem. Phys. **116**, 391 (1987).

(6) M. Kobayashi, M. Murano and A. Kaji, Macromolecules **23**, 3051 (1990).

(7) K. Schaefer, PhD thesis, Gerhard-Mercator University of Duisburg, Germany, 1991.

(8) C. J. Carman, R. A. Harrington, and C. E. Wilkes, Macromolecules **10**, 536 (1977).

(9) H. N. Cheng. Macromolecules **17**, 1950 (1984).

(10) H. N. Cheng and D. A. Smith, Macromolecules **19**, 2065 (1986).

(11) I. Tritto, Z. –Q. Fan, P. Locatelli, M. C. Sacchi, and I. Camurati, M. Galimberti, Macromolecules **28**, 3342 (1995).

(12) A. Schmidt and W. S. Veeman, Macromolecules **31**, 1652 (1998).

(13) L. W. Jelinski, Joseph J. Dumais, A. K. Engel, Macromolecules **16**, 403 (1983).

(14) R. A. Komoroski, High Resolution NMR Spectroscopy of Synthetic Polymers in Bulk, VCH, 1986.

(15) M. A. Gomez, H. Tanaka, A. E. Tonelli, Polymer **28**, 2227 (1987).

(16) S. Saito and Y. Moteki, M. Nakagawa, F. Horii, and R. Kitamaru, Macromolecules **23**, 3256 (1990).

Chapter 8. The application of MQ NMR to polyethylene

8.1 Introduction

Semicrystalline polyethylene is structurally heterogeneous. Its bulk structure contains chain-folded crystalline lamellae that are typically 5-40 nm thick and separated by non-crystalline regions. Depending on the treatment and thermal history, two crystal modifications can be formed, i.e., with an orthorhombic and monoclinic structure. In both crystalline structures the main methylene $–CH_2-$ chains are in an all-trans conformation but the chain packing is different[1].

Solid state NMR[2-7] has been extensively used to study the structure of polyethylene and has revealed the basic heterogeneity of its morphology via multicomponent line shapes and relaxation characteristics. It has been found by ^1H broad-line NMR investigations that samples crystallized from the melt generally consist of three regions: The crystalline region with molecular chains oriented perpendicular to the faces of the lamellae, the noncrystalline interfacial region with limited molecular mobility, and the noncrystalline interzonal region with liquid-like molecular mobility. The combination of dipolar-decoupling (DD), magic-angle spinning (MAS) and cross-polarization (CP) techniques permits one to detect chemical shifts and magnetic relaxation parameters that are directly related to the chain conformation and dynamics in each phase of the structure under investigation.

Concerning the interface, there are many reports about the existence of an interfacial region between the crystalline and the amorphous phase, but the interpretation of the peak position and the line shape are not the same among many research groups. Kitamaru and co-workers[8] investigated the T_{1C} relaxation behaviour of HDPE. They found that there are three different carbon T_{1C} values for the orthorhombic crystalline domains. They also found a downfield shoulder on the amorphous line and assigned it to the interfacial region. Horii and co-workers[9] put forward a model as shown in Figure 8.1, in which the interfacial region is defined as a transition region where the conformation is gradually randomized from the surface to the crystallites. The crystalline lamellae with a thickness of 8.6 nm are covered with the interfacial overlayer, and such lamellae are dispersed in a somewhat disordered fashion in the continuous amorphous phase.

Cheng et el.[10] found that the carbons in the interfacial region resonate at 32.9-33.0 ppm, the same chemical shift as the carbons in crystalline domains.

By using the ^{13}C detected ^{1}H MQ MAS NMR, Ba[11] observed two different phases, i.e., a motionally restricted phase and a liquid-like phase, in the noncrystalline regions.

By using the inversion-recovery cross-polarization MAS technique, Hillebrand[12] found that two types of all-trans chains in orthorhombic crystalline domains are present, which give two overlapping carbon-13 lines with different line widths and different relaxation times.

In this chapter we will investigate the HDPE phase structure using the MQ MAS NMR together with other solid state NMR methods.

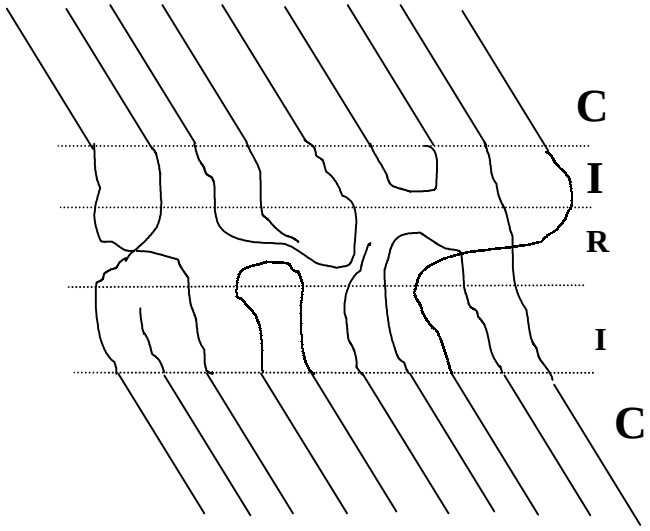

Figure 8.1*. Molecular-level structure models for HDPE: C, crystalline; I, interfacial; R, rubbery. There are crystalline, crystalline-amorphous interfacial, and rubbery amorphous components.*

8.2 Experimental

Sample

HDPE is commercially available from HÜLS AG, Germany. It has the following properties: crystalline melt temperature is 131-135°C; density at 23°C is 0.959 g/cm3; number average molecular weight is M_n = 10,500, and weight average molecular weight is M_w = 100,000.

For the NMR measurement the granular sample was first melted at 200°C and pressed into bars, then machined into a cylinder and inserted into the 7 mm and 4 mm Zirconia rotor.

NMR measurements

The HDPE sample was investigated on a Bruker ASX-400 spectrometer, which operates at 400 MHz and 100 MHz for ^{1}H and ^{13}C, respectively. In these experiments, the ^{1}H and the ^{13}C spectra were recorded with both the 4 mm and 7 mm probe head. The time-reversible eight-pulse sequence and the three-pulse sequence were used to excite the MQC. For getting high-resolution ^{1}H and ^{13}C spectra, the multiple-pulse sequences, both the three-pulse and the time-reversible eight-pulse sequence, were combined with sample rotation around the magic angle. The experimental condition and the parameters are given in the figure captions.

8.3 Results and discussions

8.3.1 ^{1}H spectra of HDPE

The ^{1}H NMR characteristics of HDPE are determined almost entirely by the dipolar couplings between the protons. These interactions, and their manifestation in terms of resonance line shapes, relaxation times, etc., depend primarily on the spatial distribution of the protons (i.e., structure) and on the nature of thermally activated motions which modulate these spatial arrangements of the spins.

The general ^{1}H NMR dipolar line-shape problem is of a many-body nature and is not soluble in analytical terms. For spins arranged in small groups there are analytical expressions for line shapes, but generally, the ^{1}H NMR absorption approximates an unresolved peak, often with Gaussian character. The half-height width, or root second moment, $M_2^{1/2}$, of this absorption reflects the root-mean square local dipolar magnetic field experienced by a typical proton. The root-mean-square local field reflects two properties of the materials. Firstly, it reflects its structure via the dependence of the local field on the spatial distribution of the spins. Secondly, it reflects motions occurring at rates which are sufficient to average the dipolar couplings. Thus, in a heterogeneous solid polymer such as HDPE, above its glass transition temperature, ^{1}H spectra are expected to consist of superpositions of components with different linewidths and shapes.

8.3.1.1 ^{1}H single-quantum coherences

8 A. Static HDPE sample

Figure 8.2a shows the static ^{1}H spectrum of HDPE, it may be viewed as a superposition of a broad line with a half-height width of 63 kHz (with a relative amount of 88%) and a narrow line with a half-height width of 10.7 kHz (with a relative amount of 12%). The former can be ascribed to the ^{1}H resonance from more rigid, ordered or crystalline regions, and the latter can be attributed to the ^{1}H resonance from more mobile amorphous regions.

9 B. Rotating HDPE sample

Figure 8.2b shows ^{1}H spectra of HDPE with different MAS frequencies from MAS = 2,000 Hz to MAS = 14,881 Hz. Figure 8.2c shows an enlarged centerband of Figure 8.2b as a function of the MAS frequency. It can be noted that, with increasing sample spinning speed, the static ^{1}H spectrum is more and more affected by the sample spinning and separated into a centerband and a series of sidebands which appear at the integer multiples of ω_R. By further increasing the MAS frequency, more and more anisotropic interactions and rigid components are affected by the sample spinning. With the MAS frequency of 14,881 Hz, the broad signal is completely converted into a resolved centerband and sidebands (see Figure 8.2b). By closer examination of the line shape and intensity of the sideband at the fast spinning condition of MAS = 14,881 Hz, two features can be noted: on the one hand, the first

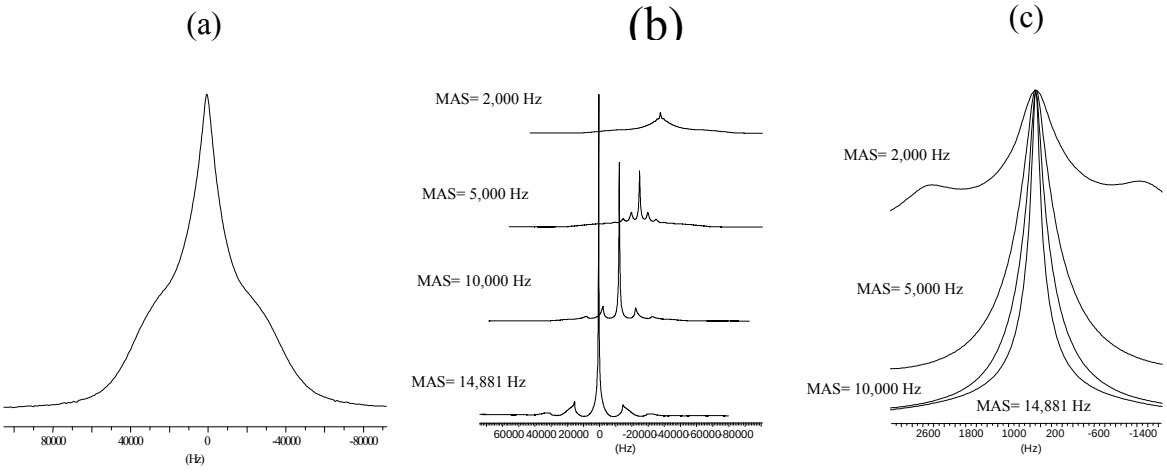

***Figure 8.2**. The ^1H spectra of HDPE which were recorded by using a 4 mm Bruker MAS probe head and a single 90° pulse, the duration of the 90° pulse was 3.5 μs. (a) The static spectrum, (b) the spectra with different MAS frequencies from MAS = 2,000 Hz to MAS = 14,881 Hz, (c) the first-order centerband of the spectra in (b) is spread out and plotted together.*

order sideband has an asymmetric shape which is different from that of the centerband, which may reflect the contributions of the isolated sub-spin systems, such as two- and three-spin system, to the spectrum; on the other hand, the intensity of the –1 order sideband is greater than that of the +1 order sideband, this indicates that the corresponding static ^1H spectrum may have an asymmetric line shape. Indeed, VanderHart[13] obtained an axially symmetric static ^1H spectrum under the ^1H homonuclear decoupling by using the BR-24 pulse sequence with a cycle time of 108 μs. The intensity of the centerband of the spectrum increases with increasing MAS frequency (see Figure 8.2c), at the same time the width of the centerband decreases with increasing MAS frequency (see Figure 8.2b and c).

8.3.1.2 ^1H multiple-quantum filtered spectra

To further investigate the properties of HDPE, the ^1H multiple-quantum filtering experiments are carried out both on the static and the magic angle spinning samples. Both the three-pulse and the time-reversible eight-pulse sequence are used to excite the ^1H MQC.

A. Static HDPE sample

First we used the simplified 1D three-pulse sequence with different excitation times to pump the MQC from the static HDPE sample. An eight-step phase cycling was used to select the ^1H-2QC-filtered spectra. The spectra with different excitation times are shown in Figure 8.3. For comparison, the single pulse spectrum is also presented in Figure 8.3. It is observed that, the three-pulse sequence can be effectively used as a dipolar filter. With a short excitation time of τ = 5.5 μs, the obtained ^1H double-quantum filtered spectrum in Figure 8.3 consists of two superposed Gaussian components: the dominating broad component corresponds to the ^1H resonance from the rigid domains, whereas the small narrow component may be attributed to the ^1H resonance from the amorphous or motionally restricted interphases. Under the intermediate excitation time (τ = 20 - 30 μs) the ^1H 2QC can be produced from both the crystalline and the amorphous phases. Under the long excitation time ($\tau \geq$ 30 μs) the ^1H 2QC

can be generated only from the amorphous phases, the rigid phases are filtered out. So, using the three-pulse sequence, MQC can be selected and excited from different domains by using a suitable excitation time.

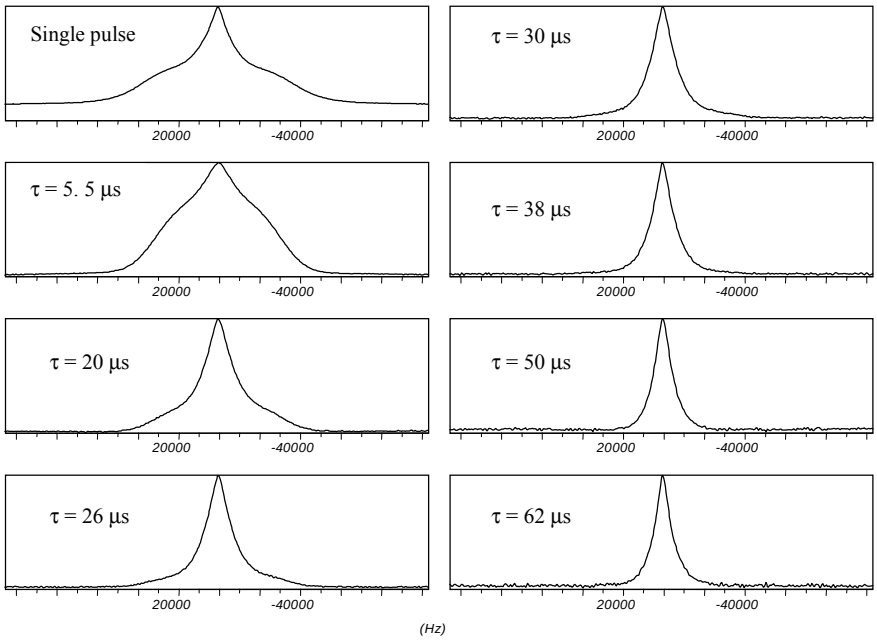

Figure 8. 3*. The static ^{1}H-2QC-filtered spectra of the HDPE sample with different excitation times (μs) under the effect of the three-pulse sequence. The spectra were recorded by using a Bruker 4 mm MAS probe head, the 90° pulse duration was 3.5 μs, the dead time was 4.5 μs, the recycle delay time was 3 s, the excitation time τ is given near the spectrum.*

Above we have demonstrated the dipolar filter properties of the three-pulse sequence, now we examine the properties of the ^{1}H MQC under the effect of the time-reversible eight-pulse sequence. Figure 8.4 shows the static ^{1}H-MQC-filtered spectra. In obtaining these spectra, a series of experiments were performed, in which the phase of the excitation pulse sequence φ was incremented with a phase increment of $\Delta\varphi = 22.5°$ with respect to that of the reconversion pulse sequence in each successive experiment, so the highest order observed is 8 and the multiple-quantum coherences of order n_i acquire an additional phase shift of $n_i\Delta\varphi$ for each experiment. The evolution time period was kept constant, i.e. t_1 was set to $t_1 = 0$. The delay time after the mixing time was set to $t_d = 1$ μs.

Figure 8.4a is the stack plot of the ^{1}H-MQC-filtered spectra, the n = 2 and n = 4 filtered spectra are a sum of the n = +2 and n = -2, and of the n = +4 and n = -4 filtered spectra, respectively. The same series of the spectra are normalized to the same height and replotted in

a separate mode in Figure 8.4b for comparison of the line shape of the different ^{1}H-MQC-filtered spectra. Figure 8.4c and d show the ^{1}H-2QC- and the enlarged ^{1}H-4QC-filtered spectra. Figure 8.4e presents the comparison of the static single 90° pulse spectrum with the

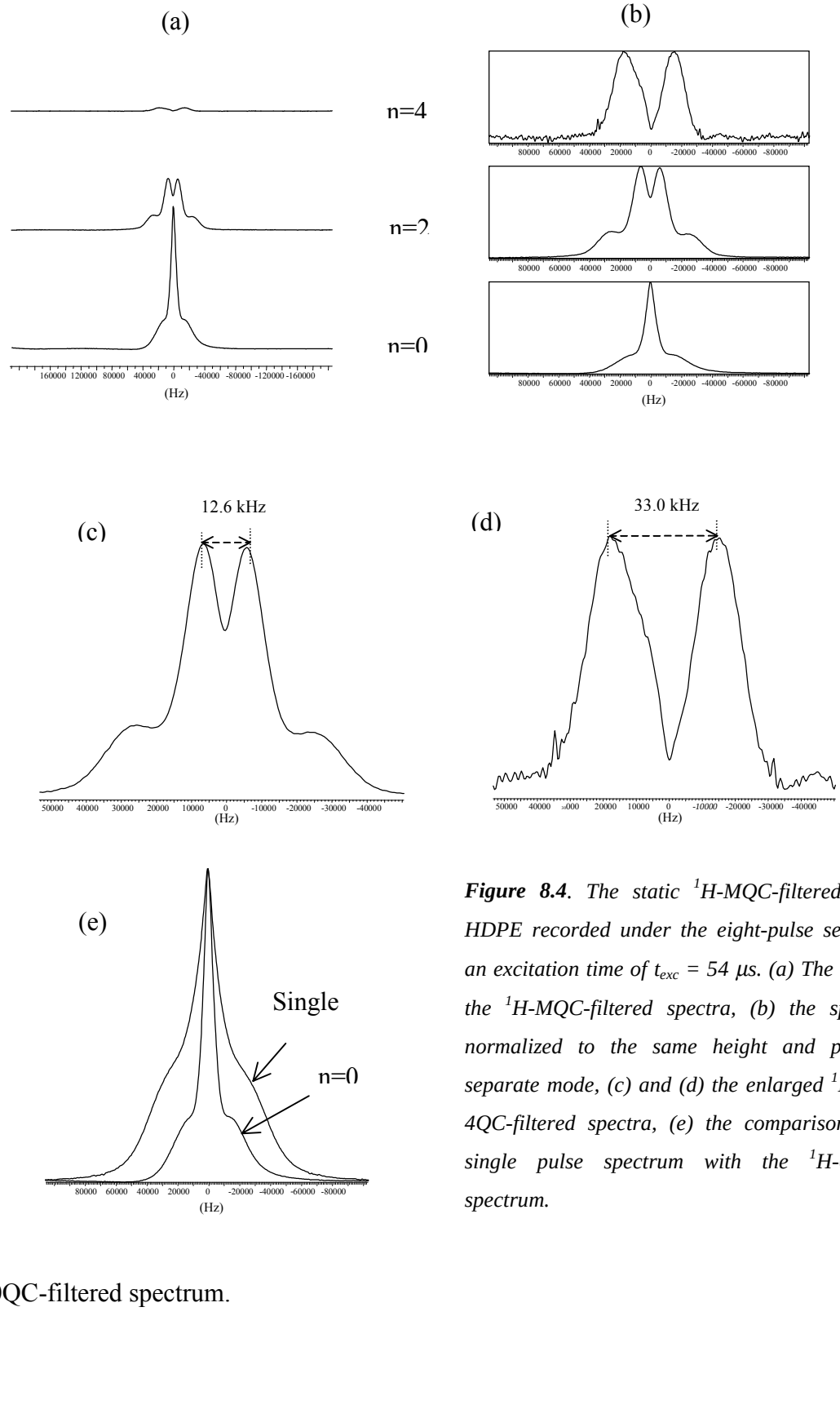

Figure 8.4*. The static ^{1}H-MQC-filtered spectra of HDPE recorded under the eight-pulse sequence with an excitation time of t_{exc} = 54 μs. (a) The stack plot of the ^{1}H-MQC-filtered spectra, (b) the spectra were normalized to the same height and plotted in a separate mode, (c) and (d) the enlarged ^{1}H-2QC- and 4QC-filtered spectra, (e) the comparison of the ^{1}H single pulse spectrum with the ^{1}H-0QC-filtered spectrum.*

^{1}H-0QC-filtered spectrum.

Compared with the static ^{1}H single pulse spectrum, the ^{1}H-0QC-filtered spectrum has changed both its line shape and the relative contents of its components (see Figure 8.4e and Table 8.1). The single pulse spectrum consists of two Gaussian lines: one broad line with a width at half height of 63 kHz (with a relative content of 88 %) and a narrow line with a width at half height of 10.7 kHz (with a relative content of 12 %). The ^{1}H-0QC-filtered spectrum can also be simulated with two Gaussian lines: one broad line with a width at half height of 41.5 kHz (with a relative content of 70.5 %) and a narrow line with a width at half height of 6.9 kHz (with a relative content of 29.5 %). Both the linewidth and the relative content of the broad line in the ^{1}H-0QC-filtered spectrum have been reduced compared to those of the ^{1}H single pulse spectrum. This can be accounted for by the dipolar filter property of the time-reversible eight-pulse sequence. During the excitation process of the eight-pulse sequence with an excitation time of 54 μs, the proton spins from the most rigid component (usually having a T_2 value of 8 ~12 μs) of the HDPE are relaxed during the excitation time period and are not affected by the pulse sequence. What is affected by the time-reversible eight-pulse sequence are the proton spins whose inverse dipolar couplings are greater than the cycle time of the multiple-pulse sequence t_c. In this sense, to change the cycle time is equal to change the strength of the dipolar filter. Increasing excitation time has two effects: on the one hand, more and more rigid components are filtered out due to the T_2 process; on the other hand, more and more spins with intermediate and small dipolar couplings are correlated with increasing excitation time.

The ^{1}H 2QC can be excited from the two-spin, four-spin, six-spin, and higher number of even-spin clusters according to the selection rule of the eight-pulse sequence in this case. So the ^{1}H-2QC-filtered spectrum which has a Pake doublet pattern with a separation of $\Delta\nu$ = 12.6 kHz (see Figure 8.4c) has contributions from all these components, in addition to the intra- and interchain interactions. According to the relationship between the splitting and the dipolar coupling of the like spin pair, $\Delta\nu = 1.5\ \omega_D$, one can obtain an average dipolar coupling constant ω_D = 8.4 kHz, it corresponds to a separation of the proton spin pair of $r_{H\text{-}H}$ = 2.44 Å. This may arise from the proton spin pair between the intra- and inter-chain -CH_2 – groups. According to Hillebrand[12], the protons from the nearest neighbouring –CH_2- groups in the same chain have distances of 2.358 Å and 2.823 Å, while the nearest distance between protons in different chains is 2.724 Å. So it seems that the time-reversible eight-pulse sequence can be used to excite ^{1}H 2QC from protons of the intra- and interchains nearest neighbouring –CH_2- groups.

The ^{1}H-4QC-filtered spectrum is shown in Figure 8.4d. It has two horns with a separation of 33.0 kHz. At first sight, it is like a pseudo Pake doublet pattern with a splitting of 33.0 kHz. In fact, it is not a real doublet. This can be explained by the following arguments. Under the effect of the time-reversible eight-pulse sequence, the proton spins are becoming correlated via the dipolar coupling. According to the selection rule of the eight-pulse sequence, a correlation of at least five proton spins is needed to form ^{1}H 4QC. The formation of the product operator, $I_1I_2I_3I_4I_5$, can develop in different ways depending on the spin topologies. One possible process leads to $D_{12}D_{23}D_{34}D_{45}$, as depicted in Figure 4.7(a), another possible process leads to $D_{12}D_{13}D_{14}D_{15}$, as depicted in Figure 4.7(b), where D_{ij} is the dipolar coupling constant between two neighbouring proton spins i and j. So the intensity of the ^{1}H-4QC-filtered spectrum is proportional to the products of the dipolar couplings, i.e.,

$$I \propto <\prod_{i\neq j=1}^{5}\sin(\frac{3}{2}D_{ij}\tau_{exc})\times\prod_{i\neq j=1}^{5}\sin(\frac{3}{2}D_{ij}\tau_{mix})>, \qquad (8.1)$$

where i = 1, 2, 3, 4, 5, and the symbol < > represents the powder average. As previously discussed in chapter 5 (see section 5.2.1), the dipolar coupling D_{ij} has an angular term $(3\cos^2\Theta_{ij}-1)$, where Θ_{ij} is the angle between the internuclear vector r_{ij} of the two spins and the external magnetic field B_0. An ensemble of isolated two-spin pairs, where the direction of the internuclear vector r_{ij} of the two proton spin pairs, i.e., the Θ_{ij} values, are randomly distributed, gives a Pake doublet pattern spectrum under the effect of a single rf pulse. A powder sample where many strongly dipolar coupled spin pairs are present, such as in the HDPE sample, gives a Gaussian featureless spectrum. According to Lacelle[14], some anisotropy in the growth of the multiple spin correlations is expected due to this angular dependence of the dipolar coupling constant. For constant distances of the protons inside a spin pairs, the growth process in the direction with angles satisfying $0° \leq \Theta \leq 35.3°$ and $144.7° \leq \Theta \leq 180°$, is expected to be greater than for those with $35.3° < \Theta < 144.7°$. Based on this argument, it can inferred that the generation and growth of the 1H 4QC in the static HDPE sample is orientation dependent and anisotropic.

For further study of the properties of the static HDPE sample, the behaviour of the ^{1}H-MQC-filtered spectra with increasing excitation time is investigated. Figure 8.5, 8.6 and 8.7 show the behaviour of the ^{1}H-0QC-, 2QC- and 4QC-filtered spectra with increasing excitation time from τ_{exc} = 54 μs to τ_{exc} = 498 μs. The line width change of the ^{1}H 0QC, the splitting of the ^{1}H 2QC, and the spacing of the two horns in the ^{1}H-4QC-filtered spectra with increasing excitation time are given in Table 8.1. One can observe as a general phenomenon of these ^{1}H-

MQC-filtered spectra that the integral intensity and the line width of the ^{1}H-0QC-, 2QC- and 4QC-filtered spectra decrease with increasing excitation time. This means that under the

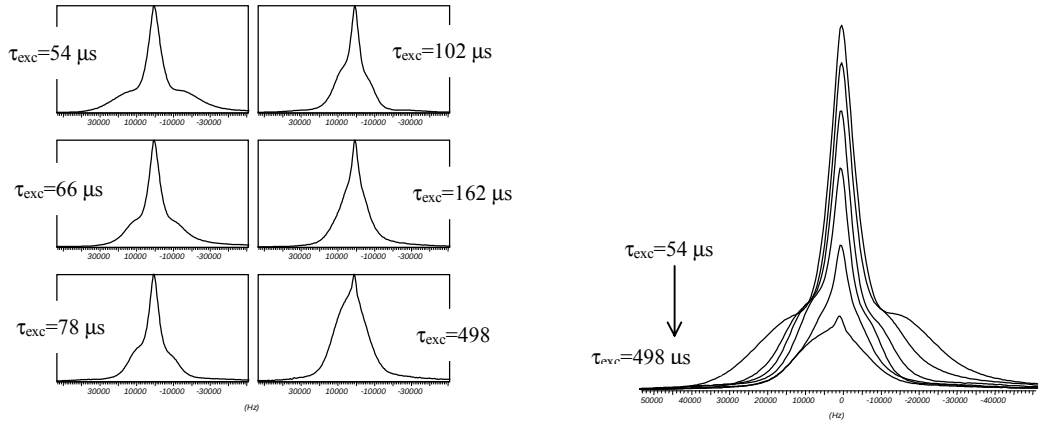

(a) (b)

Figure 8.5*. The ^{1}H-0QC-filtered spectra with increasing excitation time, the spectra were recorded under the same parameters as in Figure 8.4. (a) The spectra are normalized to the same height and plotted in a separate mode, (b) the same series of the spectra in (a) are plotted in an overlay mode, the arrow indicates the increasing direction of excitation time.*

Table 8.1. *The line widths and relative contents of the two components in the ^{1}H-0QC-filtered spectra, the doublet splittings of the ^{1}H-2QC-filtered spectra, and the pseudo doublet splittings of the ^{1}H-4QC-filtered spectra.*

	0QC-filtered spectra	2QC-filtered spectra	4QC-filtered spectra
τ_{exc}=54 μs	41.5 kHz (70.5 %) 6.9 kHz (29.5 %)	12.6 kHz	33.0 kHz
τ_{exc}=66 μs	29.3 kHz (69.35 %) 5.8 kHz (30.65 %)	9.4 kHz	24.4 kHz
τ_{exc}=78 μs	23.5 kHz (76.25 %) 4.8 kHz (23.75 %)	7.7 kHz	16.7 kHz
τ_{exc}=102 μs	19.1 kHz (85.58 %) 3.8 kHz (14.42 %)	4.9 kHz	8.5 kHz
τ_{exc}=162 μs	18.3 kHz (80.74 %) 3.8 kHz (19.26 %)	9 kHz (full width at half height)	14.0 kHz (full width at half height)
τ_{exc}=498 μs	20.2 kHz (95.55 %) 2.3 kHz (4.45 %)		

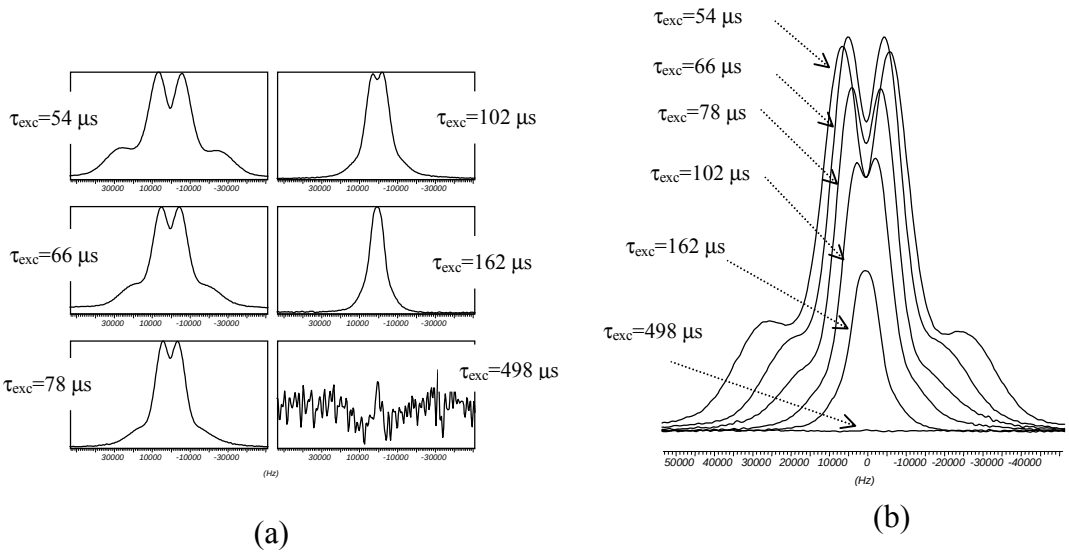

(a) (b)

Figure 8.6. *The ^{1}H-2QC-filtered spectra with increasing excitation time. (a) The spectra are normalized to the same height and plotted in a separate mode, (b) the same series of spectra in a are plotted in a overlay mode.*

(a) (b)

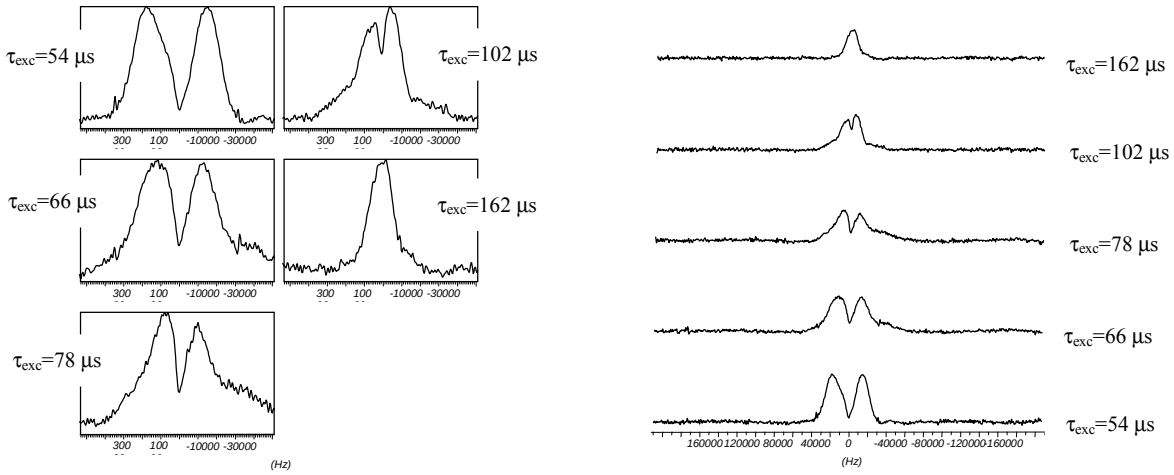

Figure 8.7*. The ^{1}H-4QC-filtered spectra with increasing excitation time. (a) The spectra are normalized to the same height and plotted in a separate mode, (b) the same series of the spectra in (a) are plotted in a stack mode.*

effect of the eight-pulse sequence with an excitation time of τ_{exc} = 54 μs, the maximum intensity of the build-up of the ^{1}H 2QC and 4QC has already been passed, so that with increasing excitation time, the intensities decrease.

In addition, spin diffusion can also affect the ^{1}H-MQC-filtered spectra of HDPE. As discussed in section 5.2.1.2, the spin diffusion process and its effect on the ^{1}H-MQC-filtered spectra can be detected through the variation of the delay time t_d which is inserted between the mixing period and the last read out pulse. The effect of spin diffusion on the ^{1}H MQC filtration in HDPE is shown in Figure 8.8 and in Table 8.2. It is noted that the sharp line form of the ^{1}H-MQC-filtered spectra reflecting the molecular structure has been gradually smeared out with increasing spin diffusion time. The narrow line of the ^{1}H-0QC-filtered spectrum is broadened and its relative content is increased (see Table 8.2). For example, the narrow line (with a linewidth of 6.9 kHz and a relative content of 29.5 %) of the ^{1}H-0QC-filtered spectrum at t_d = 1 μs has broadened to 10.4 kHz (with a relative content of 61.2 %) at t_d = 500 μs. At the same time the broad line of the same spectrum has dropped its relative content from 70.5 % at t_d = 1 μs to 38.8 % at t_d = 500 μs. Spin diffusion via dipolar flip-flop process accounts for this change. A similar change has also occurred to the ^{1}H-2QC- and 4QC-filtered spectra.

From the above-mentioned results and discussions, we can obtain the following conclusions. Although most of the rigid components of the coupled proton spins in the static HDPE sample are relaxed and filtered out under the effect of the time-reversible eight-pulse sequence due to

the long cycle time (in our case, we had a minimum cycle time of t_c = 54 μs by using a 4 mm MAS probe head), the obtained ^{1}H-MQC-filtered spectra give structural and motional information. The observed ^{1}H-0QC-filtered spectrum consists of one broad and one narrow line which correspond to the rigid and amorphous components, respectively. The generated ^{1}H-2QC-filtered spectrum has a Pake doublet pattern, the distance between the contributing spin pairs can be calculated through the splittings. Due to the strong dipolar couplings (~22.4 kHz), the proton spin pair of the methylene –CH_2- groups (with a separation of 1.76 Å between the two proton spins) from the rigid domains can not be affected by the eight-pulse sequence, its contribution is relaxed during the excitation process. What is affected by the eight-pulse sequence, are the intra- and interchain proton spin pairs from different neighbouring –CH_2- groups in the crystalline domains, as well as the proton spin pair of the methylene groups from the interphases and the amorphous components, where the dipolar couplings are attenuated by the molecular and chain motions. The ^{1}H-4QC-filtered spectrum has two horns with a separation of 33.0 kHz, it results from the direction dependent and anisotropic growth of the ^{1}H 4QC. The line widths of all the ^{1}H-MQC-filtered spectra are narrowed with increasing excitation time, this means that both the motionally restrained and mobile components have a distribution of dipolar coupling constants.

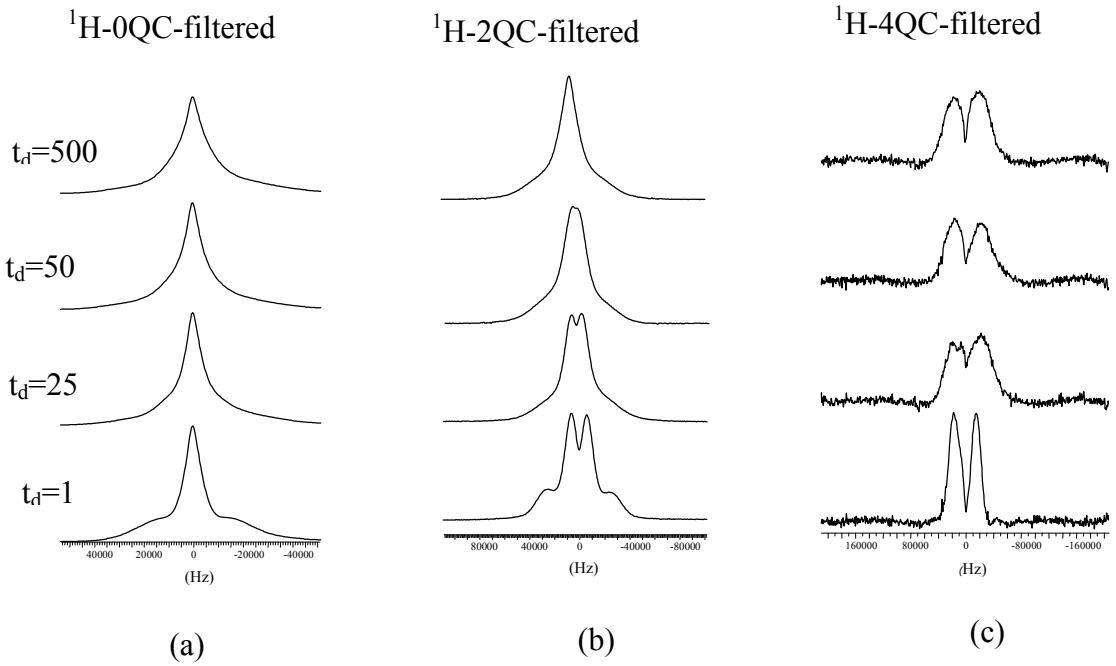

Figure 8.8*. The effect of spin diffusion on the ^{1}H-0QC- (a), 2QC- (b), and 4QC-filtered spectra. All the spectra were recorded by using the time-reversible-eight-pulse sequence with an excitation time of τ_{exc} = 54 μs, the delay time t_d was varied from t_d = 1 μs to t_d = 500 μs.*

Table 8.2*. The effect of the spin diffusion on the linewidth and relative content of the ^{1}H 0QC, doublet splittings of the ^{1}H-2QC, and pseudo doublet splittings of the ^{1}H-4QC-filtered spectra.*

	^{1}H-0QC-filtered spectra	^{1}H-2QC-filtered spectra	^{1}H-4QC-filtered spectra
t_d = 1 μs	41.5 kHz (70.5 %) 6.9 kHz (29.5 %)	12.6 kHz	33.0 kHz
t_d = 25 μs	42.3 kHz (44.6 %) 7.8 kHz (55.4 %)	8.1 kHz	37.0 kHz
t_d = 50 μs	39.0 kHz (44.3 %) 8.3 kHz (55.7 %)	52.8 kHz (61.5 %) 17.0 kHz (38.5 %)	37.4 kHz
t_d = 500 μs	40.6 kHz (38.8 %) 10.4 kHz (61.2 %)	54.9 kHz (54.9 %) 14.1 kHz (45.1 %)	37.8 kHz

B. **Rotating HDPE solid**

To get high resolution ^{1}H spectra, we combined the three-pulse sequence and the eight-pulse sequence with magic angle sample spinning.

In the case of the three-pulse sequence, an eight-step phase cycling was adopted to select the ^{1}H 2QC. One finds that when the evolution time is short, i.e., when the evolution time was not synchronized with the sample rotation, then the centerband and sidebands of the recorded ^{1}H-2QC-filtered spectra are no longer in absorption mode. The intensities of the sidebands and the centerband are governed by a number of factors[15] such as off-resonance values, chemical shift tensor magnitudes, and relative orientations.

In order to get the pure phase spectra, it is necessary to synchronize the evolution time with the sample rotation in order to eliminate the rotor modulation of the active Hamiltonian during the evolution time period[16-19]. Figure 8.9 shows the ^{1}H-2QC-filtered spectra with different evolution times $n\omega_R$, where n is an integer number and ω_R the sample rotation frequency. We observed that the sideband linewidth of the ^{1}H-2QC-filtered-^{1}H-SQC spectra are narrowed with increasing evolution time, compared to those of the single 90° pulse spectrum. This can be elucidated as follows: at long evolution time, the multi-spin 2QC have decayed, and only the two-spin 2QC are remained. All the obtained spectra then have a pure phase. Compared

with the single pulse spectrum, the relative intensity of the centerband in the ^{1}H-2QC-filtered spectrum has decreased. The width of the sidebands and the centerband are narrowed with increasing evolution time.

In the case of the eight-pulse sequence, due to the self-time reversible property[20,21], the eight-pulse sequence must be synchronized with the sample rotation for effectively exciting the ^{1}H MQC. Figure 8.10 (a) shows the ^{1}H-MQC-filtered spectra plotted in a stack mode. The comparison of the ^{1}H-0QC-filtered spectrum with the ^{1}H single pulse spectrum is shown in Figure 8.10 (b), where the spectra are normalized to the same height and plotted together, the centerband and the first order sidebands are enlarged and inserted in (c) and (d), respectively. The centerband and the sidebands of the ^{1}H-0QC-filtered spectrum are drastically narrowed compared with those of the ^{1}H single pulse spectrum.

The behaviour of the ^{1}H-MQC with increasing excitation time was also investigated. The acquired ^{1}H-0QC- and 2QC-filtered spectra are exhibited in Figure 8.11 and 8.12, respectively. Analogous to the static cases under effect of the time-reversible eight-pulse sequence, the intensity and linewidth of the ^{1}H-0QC- and 2QC-filtered spectra are decreased with increasing excitation time. Although the height of the ^{1}H-2QC-filtered spectrum at τ_{exc} = 2×67.2 μs is higher than that at $\tau_{exc} = 1 \times 67.2$ μs, the integral intensity of the latter is greater than the former. The linewidth of the ^{1}H-0QC. and 2QC-filtered spectra is gradually narrowed with increasing excitation time. This is due to the dipolar filter effect of the eight-pulse

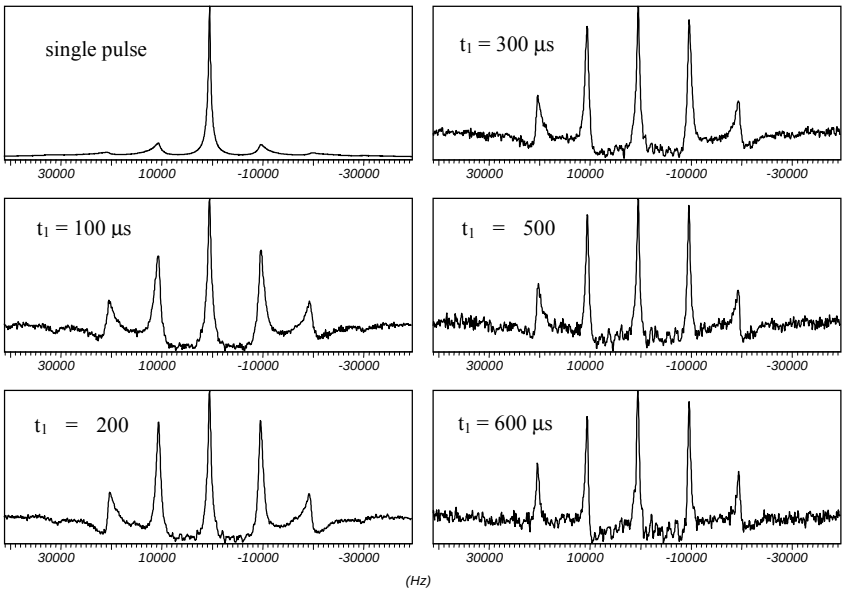

Figure 8. 9*. The ^{1}H-2QC-filtered spectra with the same excitation time of 6 μs under magic angle spinning when the evolution times were synchronized with the rotation.*

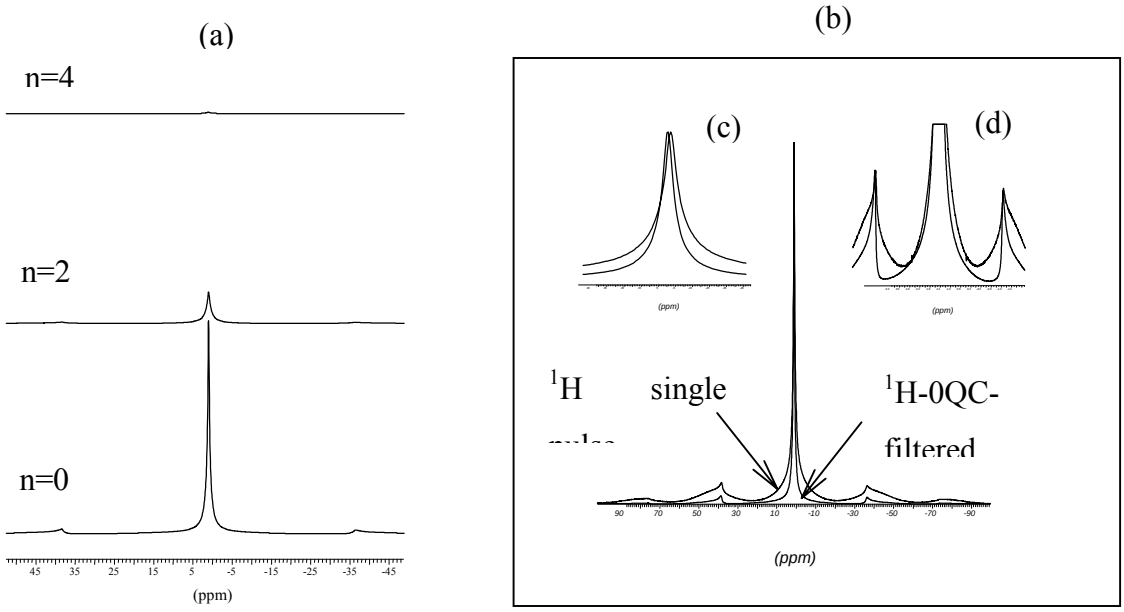

Figure 8.10. *The ^{1}H-MQC-filtered spectra of HDPE under a MAS frequency of 14,881 Hz. The spectra were recorded by using the eight-pulse sequence with an excitation time of τ_{exc} = 67.2 μs, which was synchronizd with the sample rotation under the condition of $t_r = t_c$. (a) The ^{1}H-MQC-filtered spectra are plotted in a stack mode, (b) the comparison of the ^{1}H-0QC-filtered spectrum with the ^{1}H single pulse spectrum, the centerband and first-order sidebands are enlarged and inserted in (c) and (d), respectively.*

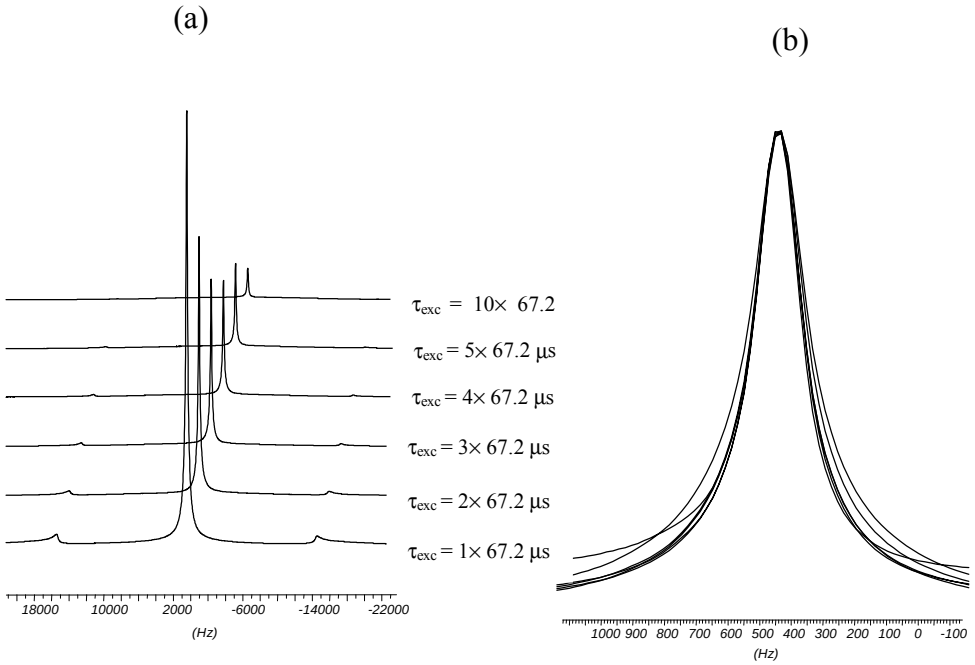

Figure 8.11. *The ^{1}H-0QC-filtered spectra versus the excitation time. The spectra were recorded with the same condition as in Figure 8.10. (a) The spectra are plotted in a stack mode, (b) the same series of spectra are normalized to the same height.*

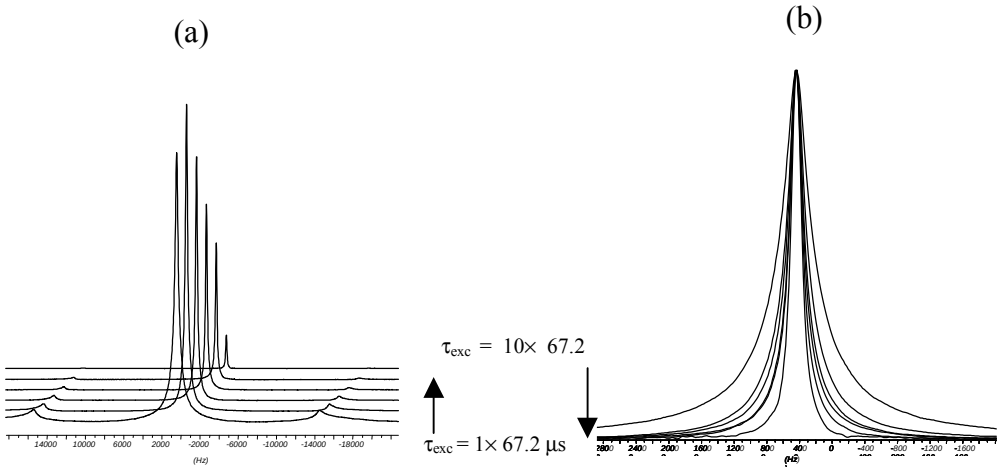

Figure 8.12. *The ^{1}H-2QC-filtered spectra versus the excitation time under the time-reversal eight-pulse sequence. The experimental parameters are the same as in Figure 8.10. (a) The spectra are plotted in a stack mode, (b) the same series of the spectra are normalized to the same height. The arrow indicates the direction of the increasing the excitation time.*

sequence: with increasing excitation time, more and more rigid components are filtered out, so the intensity and linewidth of the 0QC- and 2QC-filtered spectra is decreased and narrowed with increasing excitation time.

8.3.2 ^{13}C spectra of HDPE

In the previous section we have shown the ^{1}H spectra of HDPE, in this section we will discuss the ^{13}C spectra of HDPE. Due to the fact that the ^{13}C nucleus occurs at a natural abundance of only 1.1 % and has a small magnetic moment (about one-fourth of the proton), the dipolar ^{13}C–^{13}C coupling can be neglected. Unlike ^{1}H NMR spectra, ^{13}C NMR spectra suffer neither from a narrow dispersion of chemical shifts nor from extensive homonuclear spin-spin coupling, so high-resolution ^{13}C NMR spectra can be expected.

8.3.2.1 Static HDPE sample

Figure 8.13 shows the static ^{13}C spectra of HDPE, all the spectra were recorded with a contact time of 2 ms and under high power heteronuclear (^{1}H) decoupling. Figure 8.13 (a) is the simple cross-polarization ^{13}C spectrum, it has contributions from both the crystalline and amorphous phases. Figure 8.13 (b) and (c) are the ^{13}C detected ^{1}H 2QC- and 3QC-filtered spectra recorded by using the three-pulse sequence with an excitation time of 5 μs. The spectra reflect the asymmetric chemical shift tensor of carbon-13 from the crystalline domains, which has the principal values of σ_{11} = 50.6 ppm, σ_{22} = 36.3 ppm, and σ_{33} =11.6 ppm. Figure 8.13 (d) is the ^{13}C-detected-^{1}H-2QC-filtered spectrum obtained by using the time-reversible eight-pulse sequence with an excitation time of 120 μs, the axially symmetric line shape represents the carbon-13 signal from the amorphous phases where the chains can execute rotational and wobbling motions[11].

8.3.2.2 Rotating HDPE sample

Figure 8.14 shows the ^{13}C CPMAS spectra of HDPE. Fig. 8.14 (a) is a simple ^{13}C CP MAS spectrum, it consists of one peak centered at 33 ppm with an upfield shoulder centered at 31 ppm (the peak at 33 ppm can be further decomposed into three peaks as shown by the thin

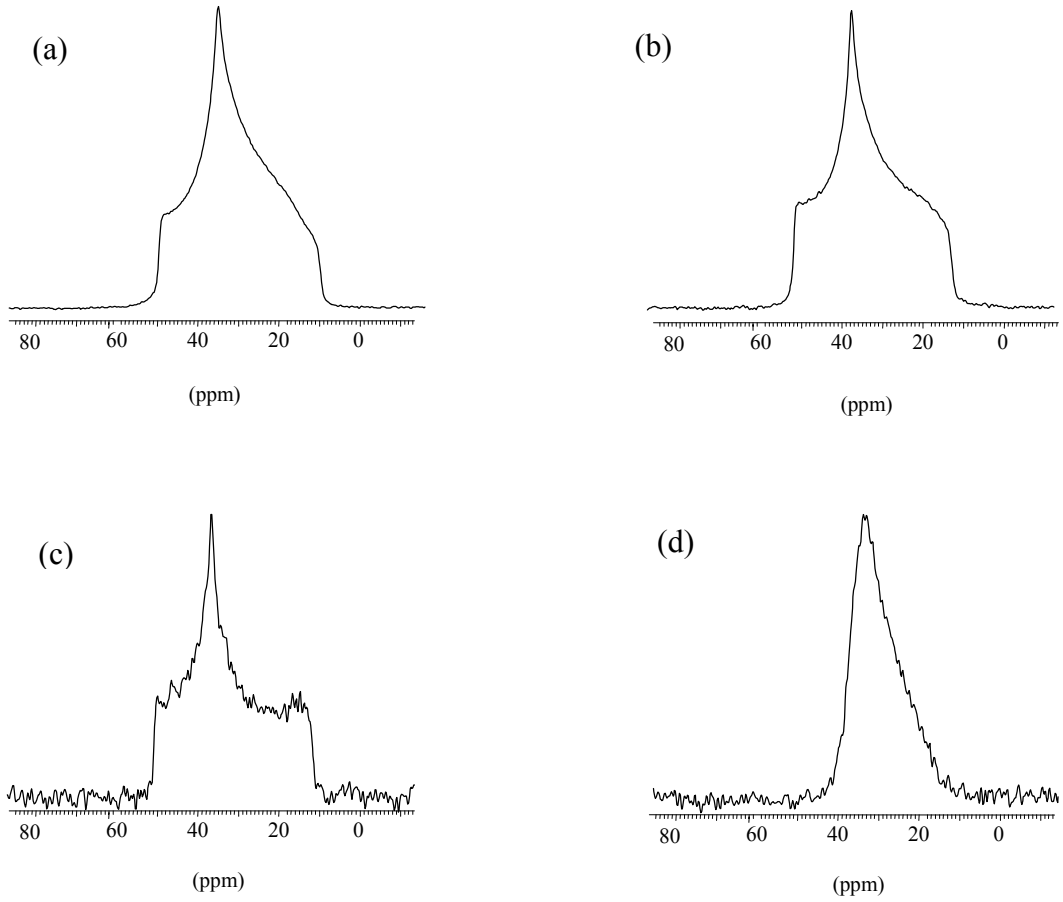

Figure 8.13. *^{13}C spectra of a static HDPE sample. (a) Simple ^{13}C cross-polarization spectrum, (b) ^{13}C-detected-^{1}H-2QC-filtered spectrum using the three-pulse sequence with an excitation time of τ_{exc}=5 μs, (c) ^{13}C-detected-^{1}H-3QC-filtered spectrum using the three-pulse sequence with an excitation time of τ_{exc} =5 μs, (d) ^{13}C-detected-^{1}H-2QC-filtered spectrum using the eight-pulse sequence with an excitation time of 120 μs.*

lines). They can be assigned according to VanderHart[22] to crystalline (33 ppm) and amorphous (31 ppm) carbons of the main methylene -CH_2- chains, respectively. The chemical shift difference between the crystalline and amorphous phases can be explained with the intrachain γ-gauche effect[23], in addition to the differences in the intermolecular packing of amorphous and crystalline chains. In the crystalline phases, the chains are constrained by the lattice to adopt the all-trans, planar zigzag conformation, while in the amorphous phases, the chains are free from the conformational constraints imposed by the crystalline lattice and are conformationally disordered, with an appreciable portion of the chains in the gauche conformation. So the different conformational environments experienced by the crystalline and amorphous carbons, is the reason that they have different chemical shifts. The amorphous carbons having mixed trans and gauche conformations are expected to be shielded upfield

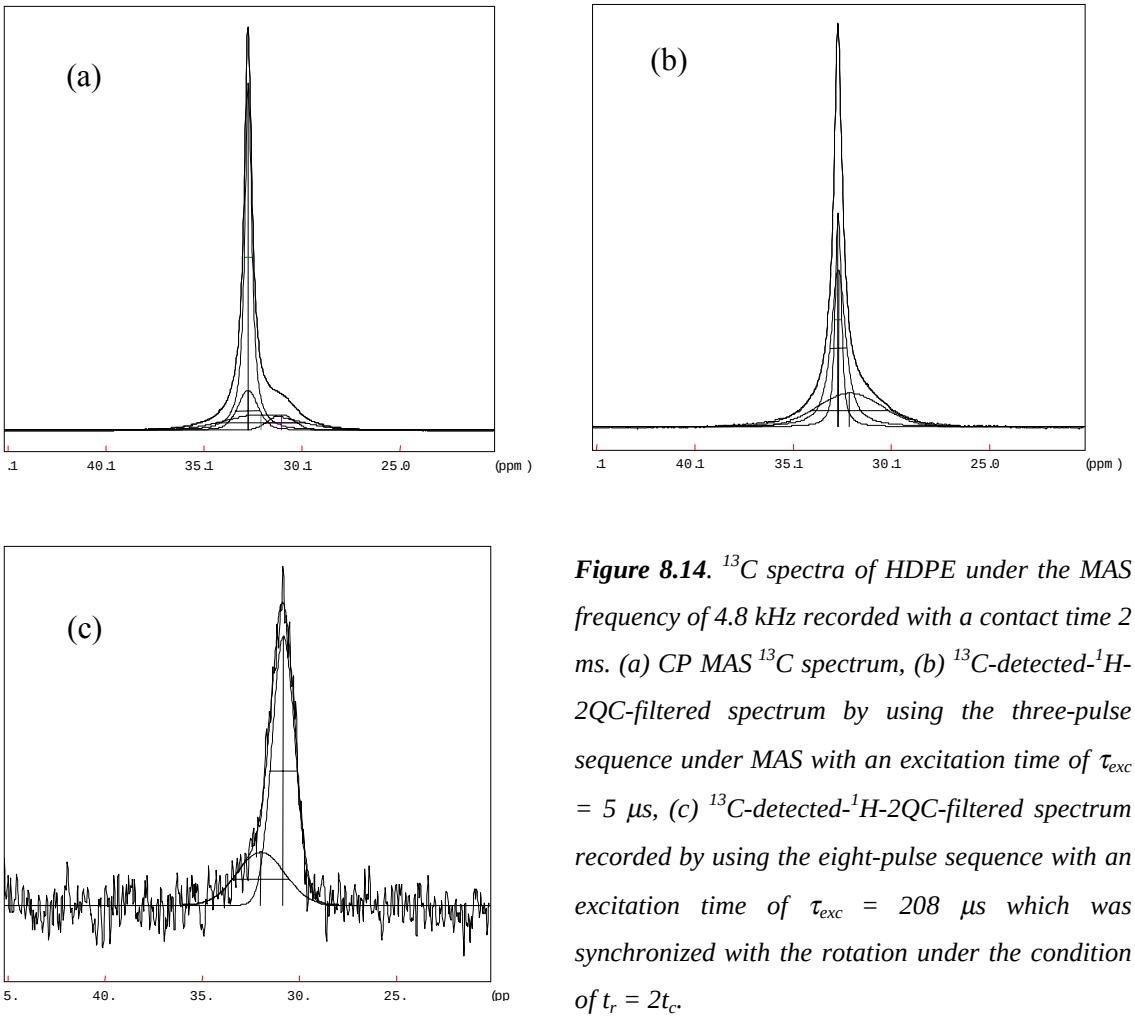

Figure 8.14. *^{13}C spectra of HDPE under the MAS frequency of 4.8 kHz recorded with a contact time 2 ms. (a) CP MAS ^{13}C spectrum, (b) ^{13}C-detected-^{1}H-2QC-filtered spectrum by using the three-pulse sequence under MAS with an excitation time of τ_{exc} = 5 μs, (c) ^{13}C-detected-^{1}H-2QC-filtered spectrum recorded by using the eight-pulse sequence with an excitation time of τ_{exc} = 208 μs which was synchronized with the rotation under the condition of $t_r = 2t_c$.*

Table 8.3. *The results of the deconvolution.*

Figure no.	phase	conformation	chemical shift (ppm)	width at half height (ppm)	Gaussian factor	relative content (%)
Fig. 8.14a	crystalline	all-trans	32.82	0.41	0.0	57.50
	crystalline	all-trans	32.84	1.22	0.6	15.65
	interphase	more-trans	32.19	4.55	1.0	19.8
	amorphous	more-gauche	31.14	1.60	1.0	7.01
Fig. 8.14b	crystalline	all-trans	32.80	0.36	0.3	24.31
	crystalline	all-trans	32.80	0.87	0.2	44.53
	interphase	more-trans	32.21	3.90	1.0	31.16
Fig. 8.14c	interphase	more-trans	32.07	2.90	1	29.16
	amorphous	more-gauche	30.90	1.40	1	70.84

compared to the all-trans crystalline carbons.

Figure 8.14(b) illustrates the ^{13}C detected ^{1}H 2QC (excited from the crystalline domains with an excitation time of 5 μs using the three-pulse sequence) filtered spectrum, which can be deconvoluted into three lines with different full width at half height (see Table 8.3). Two lines have the same chemical shift of 32.80 ppm but have different line widths at half height of 0.36 ppm (24.31 %) and of 0.87 ppm (44.53 %), respectively; one very broad line having a linewidth at half height of 3.90 ppm (31.16 %) resonates at 32.21 ppm. According to previous work[12,24,25], we can ascribe the two lines at 32.80 ppm to the all-trans methylene -CH_2- chains in the orthorhombic phases but with different mobilities: the narrower line comes from the perfectly packed all-trans -CH_2- chains, while the broader one results from the -CH_2- chains also in an all-trans conformation, but which can undergo 180° jumps around the chain axis with a frequency of kHz or more [9,12]. The broad line at 32.21 ppm can be contributed to the -CH_2- chains which are located at the interphase between the crystalline and the amorphous phases.

Figure 8.14c shows the ^{13}C-detected-^{1}H-2QC-filtered spectrum excited from the amorphous domains of HDPE by the time-reversible eight-pulse sequence with an excitation time of 208 μs which was synchronized with the sample rotation under the condition of $t_r = 2t_c$. Under the eight-pulse sequence with a long excitation time (208 μs), the rigid domain signals should be suppressed due to their very short ^{1}H T_2 (usually 8-12 μs) value, the obtained ^{1}H double-quantum filtered signals should only come from the mobile carbons. Two kinds of mobile carbons are observed in Figure 8.26c (see Table 8.3): one line resonates at 30.9 ppm, the other one resonates at 32.07. The former may come from the mobile carbons in the amorphous phases, while the latter may come from the mobile carbons located in the interphase between the crystalline and amorphous phases and having a more trans conformation.

There are many reports[26-28] that suggest the existence of an interphase. The reason for this is that the great difference of the chain conformations between crystalline and amorphous phases, imposes constrains on the boundary between them. We know that the molecular chains in amorphous domains, having mixed trans-gauche conformations, may undergo low-frequency librational motions which are in the range of 10-100 kHz[29]. So we could imagine that, close to the surface of the crystalline domains, the chain mobility is retarded or restricted compared to that of the amorphous chain. The chains near crystalline domains possess more trans conformation, away from the crystalline surface the chains have more degrees of freedom and take more gauche conformations. This means that the line at 32.07 ppm may

come from the more-trans chains that are located in the interphases. The same T_{1c} values of interphase and amorphous domains were also found by Kitamuru[27]. All this suggests that there is an interphase between the crystalline and amorphous domains. The mobile methylene chains with a more-trans conformation with a resonance at 32 ppm are located close to the crystalline surface, most of the mobile chains with a mixture of trans-gauche conformations and having a resonance at 31 ppm are present in the amorphous domains.

The use of the time-reversible eight-pulse sequence under fast MAS combined with an other selection method, such as dipolar dephasing, IRCP, spin-diffusion, to select and discriminate the different phases of HDPE and to get high-resolution was performed. Figure 8.15 shows the results. The high-resolution ^{13}C-detected-^{1}H-MQC-filtered spectra can be obtained under the fast MAS condition by using the eight-pulse sequence with a short excitation time (see Figure 8.15a, here $\tau_{exc} = 1 \times 72$ μs). In this case, the ^{1}H MQC are generated from both the crystalline and the amorphous phases. Like the ^{1}H-detected-^{1}H-MQC-filtered spectra discussed before, most of the rigid signals are filtered out due to the T_2 process, this can be clearly seen through comparison of the simple CPMAS spectrum 1 with the ^{13}C-detected-^{1}H-0QC-filtered spectrum 2 in Figure 8.15f, where the numbers from 2 to 6 correspond to the ^{1}H-0QC-filtered spectra from (a) to (e) and all the spectra are normalized to the same height. A further filtering of the rigid signal can be achieved through increasing excitation time. This is illustrated in Figure 8.15b, where the excitation time is doubled to $\tau_{exc} = 2 \times 72$ μs compared to that in Figure 8.15a. Through combination with the inversion-recovery cross-polarization (IRCP) method with an depolarization time of 25 μs, the crystalline signal in Figure 8.15a can be completely filtered out, and only the amorphous signal remains in the ^{13}C-detected-^{1}H-MQC-filtered spectra as presented in Figure 8.15c. Figure 8.15d gives another example to suppress the crystalline signal from Figure 8.15a. By inserting a dipolar dephasing time of $t_d = 20$ μs before the cross-polarization, the rigid signal is decayed away.

As discussed above, due to the filter effect, one can not get the signal from the very rigid domains (where the ^{1}H T_2 is short) by using the eight-pulse sequence. This shortcoming can be overcome through combination with the spin-diffusion method, as illustrated in chapter 5. Figure 8.15e shows this effect, the spectra were recorded using the same parameters as in Figure 8.15a, except inserting a spin-diffusion time of $t_d = 100$ ms before the last read pulse. Comparing the ^{13}C-detected-^{1}H-0QC- and 2QC-filtered spectra in Figure 8.15a and e, one can tell which line results from which domains. For clear observation, the spectra are

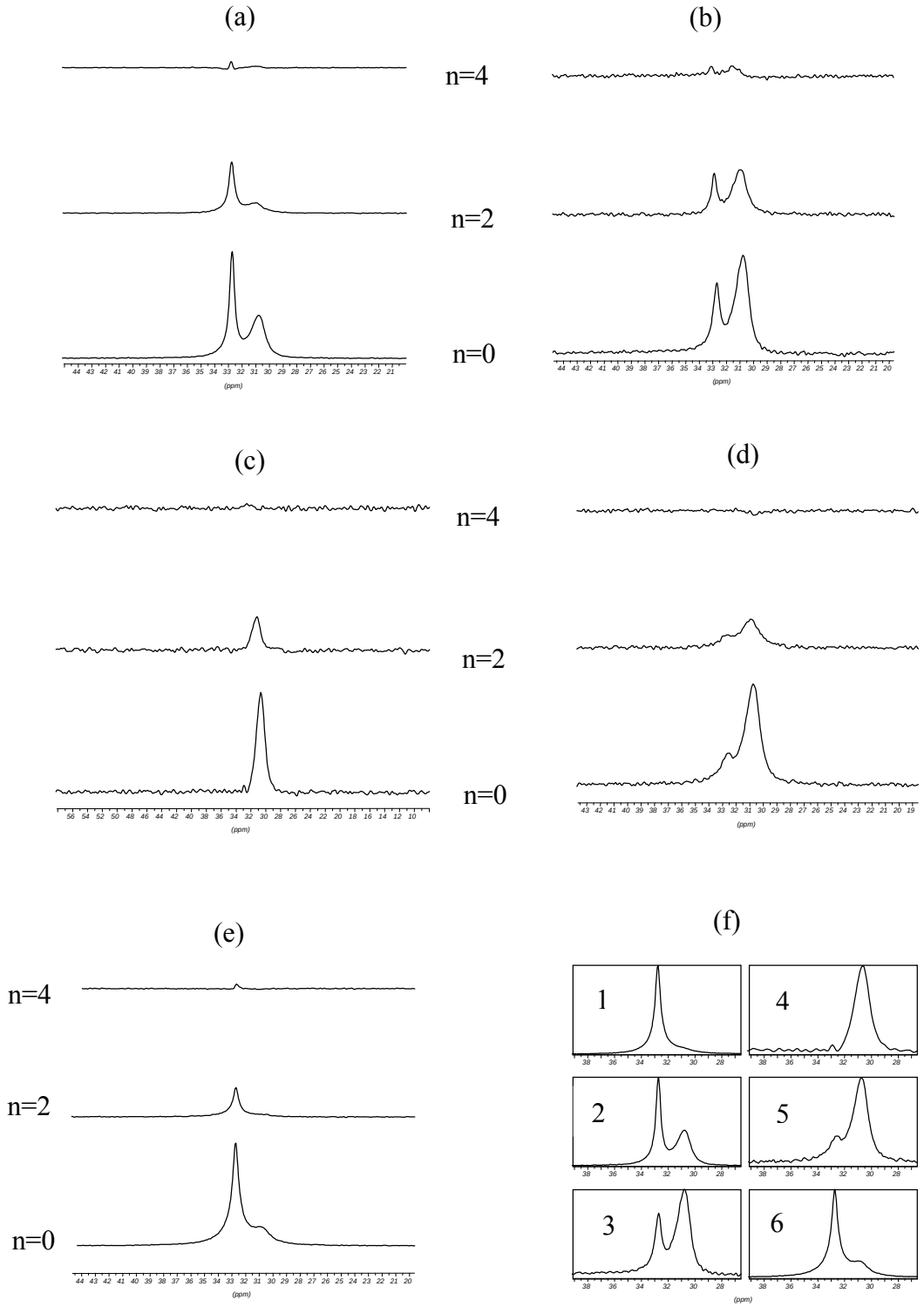

Figure 8.15. *^{13}C-detected-^{1}H-MQC-filtered spectra of HDPE under the eight-pulse sequence synchronized with the rotation in a condition of $t_r = t_c$. The MAS frequency is 13889 Hz, the contact time is 500 μs, the 90° pulses are 3.5 μs. (a) Excitation time is $\tau_{exc} = 1 \times 72$ μs, (b) excitation time is $\tau_{exc} = 2 \times 72$ μs, (c) the same parameters as in (a) except for using IRCP ^{13}C detection, (d) the same parameters as in (a) except for inserting a dipolar dephasing time $t_d = 20$ μs before detection, (e) the same parameters as in (a) except with a spin-diffusion time of $t_d = 100$ ms before detection, (f) comparison of the ^{13}C single pulse spectrum with the ^{13}C- detected-^{1}H-0QC-filtered spectra, where the numbers from 2 to 6 correspond to the 0QC-filtered spectra from (a) to (e).*

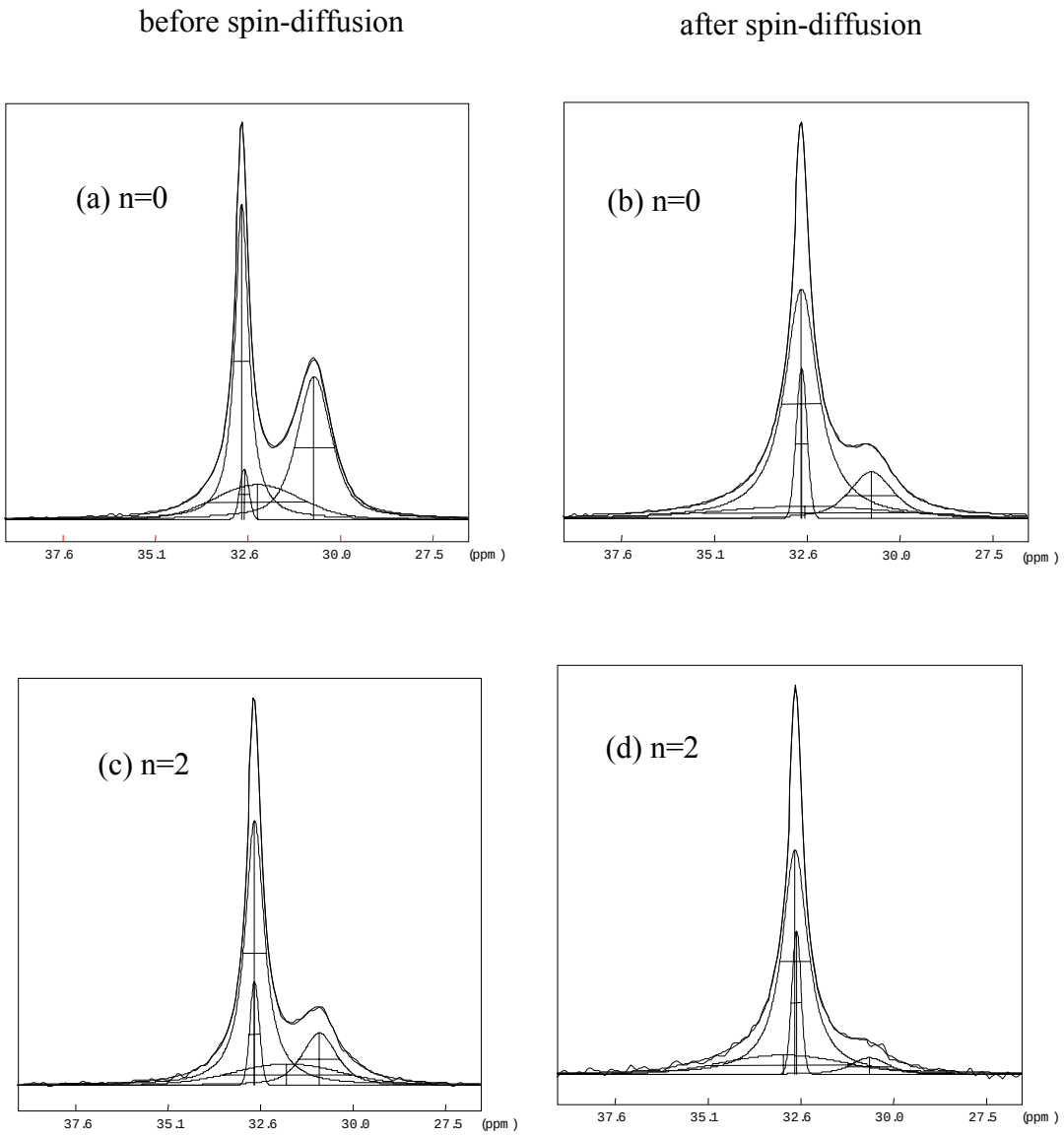

Figure 8.16*. The comparison of the ^{13}C-detected-^{1}H-0QC- and 2QC-filtered spectra before (left column) and after (right column) the spin-diffusion in Figure 8.15 a and e.*

deconvoluted into four peaks as before and shown in Figure 8.16 and the results are tabulated in Table 8.4.

The relative amount of the chains with different mobilities in amorphous domains can be obtained through comparison of the ^{13}C-detected-^{1}H-0QC- and 2QC-filtered spectra with a certain excitation time. For instance, in the case of the excitation time $\tau_{exc} = 1 \times 72$ μs, the relative contribution of the amorphous peaks decreases from 37.8 % in the ^{1}H-0QC-filtered spectrum to 17.1 % in the ^{1}H-2QC-filtered spectrum (comparing Figure 8.16 a and c). This

means that the chains in the amorphous domains have different mobilities, the signals from more mobile chains are filtered out in the ^{1}H-2QC-filtered spectrum, so the relative content of the two type chains in the amorphous domains can be calculated as follows: the total contribution of the mobile carbons is 37.77% in CPMAS spectrum (Fig. 8.16a), while the contribution of the restricted carbons is 17.12% in the ^{1}H-2QC-filtered spectrum (Fig. 8.16c) so the contribution of the more mobile carbons is (37.77%-17.12%) = 20.65%.

Table 8.4*. The results of the deconvolution.*

Figure no.	phase	conformation	chemical shift (ppm)	width at half height (ppm)	Gaussian factor	relative content (%)
Fig. 8.16a	crystalline	all-trans	32.73	0.44	0.0	39.94
	crystalline	all-trans	32.67	0.29	1.0	2.84
	interphase	more-trans	32.31	2.72	0.9	19.45
	amorphous	more-gauche	30.77	1.09	0.4	37.77
Fig. 8.16b	crystalline	all-trans	32.72	1.08	0.0	63.41
	crystalline	all-trans	32.72	0.34	1.0	9.37
	interphase	more-trans	32.63	5.50	0.9	12.72
	amorphous	more-gauche	30.83	1.39	0.4	14.50
Fig. 8.16c	crystalline	all-trans	32.72	0.63	0.0	57.06
	crystalline	all-trans	32.73	0.30	1.0	7.36
	interphase	more-trans	31.85	3.48	0.9	18.46
	amorphous	more-gauche	30.97	1.11	0.4	17.12
Fig. 8.16d	crystalline	all-trans	32.72	0.83	0.0	64.71
	crystalline	all-trans	32.69	0.29	1.0	10.26
	interphase	more-trans	33.03	3.91	0.9	19.12
	amorphous	more-gauche	30.71	1.17	0.4	5.90

The spin diffusion process can be observed by comparing the ^{13}C-detected-^{1}H-0QC-filtered spectra before and after the spin-diffusion in Figure 8.16. One can note that the relative contributions of the amorphous and interphase peak decrease, while the crystalline peaks increase. This indicates that the flow of the spin magnetization is from amorphous and

interphase to crystalline domains. The spin-diffusion dynamics will be further illustrated later in this chapter.

8.3.3. ^{1}H WISE (the ^{1}H Wideline Separation) experiment

In the previous sections, the heterogeneity of HDPE was studied by the ^{1}H- and ^{13}C-detected-^{1}H-MQC-filtration method. In this section, the relation between the ^{1}H and ^{13}C spectra is correlated through the WISE experiment.

In the WISE experiment, the ^{1}H-^{1}H dipolar coupling is allowed to be active during the evolution period, and the ^{1}H line shapes of individual components in heterogeneous samples such as HDPE can be observed. The pulse sequence of the WISE experiment can be written as: (^{1}H) $\pi/2 - t_1$ – acquisition, it consists of a ^{1}H 90° pulse followed by an incremented proton evolution time (t_1), after which the proton magnetization is transferred to ^{13}C via Hartman-Hahn cross-polarization. Then the ^{13}C signal is detected in the detection period under high power heteronuclear decoupling. The result is a 2D spectrum that correlates ^{13}C chemical shifts with ^{1}H-^{1}H dipolar broadened powder patterns, i.e., slices at individual ^{13}C resonances in a 2D data set reveal the ^{1}H line widths of the protons that are dipolar coupled to the particular ^{13}C.

Figure 8.17 shows the ^{1}H WISE 2D ^{1}H – ^{13}C correlated spectrum recorded under a MAS frequency of 10 kHz. From the contour plot of the ^{1}H WISE 2D ^{1}H – ^{13}C correlated spectrum (see Figure 8.17a), one can see that there are two different ^{13}C components: the crystalline domains resonate at 32.8 ppm, it has a narrow linewidth due to the perfect packing of the molecular chains with all-trans conformations. The corresponding ^{1}H spectrum is very broad due to the strong proton dipole-dipole interactions; the amorphous component resonates at 31 ppm which has a broad linewidth due to the broad distribution of the conformations of the molecular chains. The corresponding ^{1}H spectrum is narrow due to the molecular motions which attenuate and average the dipolar interactions. From Figure 8.17b one can see another feature of the ^{1}H spectra of the crystalline domains: ^{1}H spinning sidebands are superposed onto a broad line, this suggests that there are two distinguishable components with different mobilities: the rigid crystalline component has very strong dipolar couplings which can not be affected by the magic angle spinning at 10 kHz, while another crystalline component apparently can be affected by MAS. This agrees with the previous work[12,31], i.e., there are two

detectable ^{13}C components in the orthorhombic modification of HDPE sample. The crystalline ^{13}C broad line may correspond to the ^{1}H sidebands and centerband, while the crystalline ^{13}C narrow line may correspond to the ^{1}H broad line.

For comparison, the WISE experiment is also performed by using a Bruker 7 mm probe head under a low MAS frequency of 3 kHz. The acquired spectrum is presented in Figure 8.18. Figure 8.18a is the contour plot of the ^{1}H WISE 2D ^{1}H – ^{13}C correlated spectrum. Figure 8.18b shows the ^{1}H spectra of slices at A_1, A_2 and A_3 corresponding to the ^{13}C resonances at 32.8 ppm, 32.2 ppm and 31 ppm, respectively. It is evidence that there are three different domains, i.e., crystalline, interphase and amorphous in heterogeneous HDPE sample.

(a)

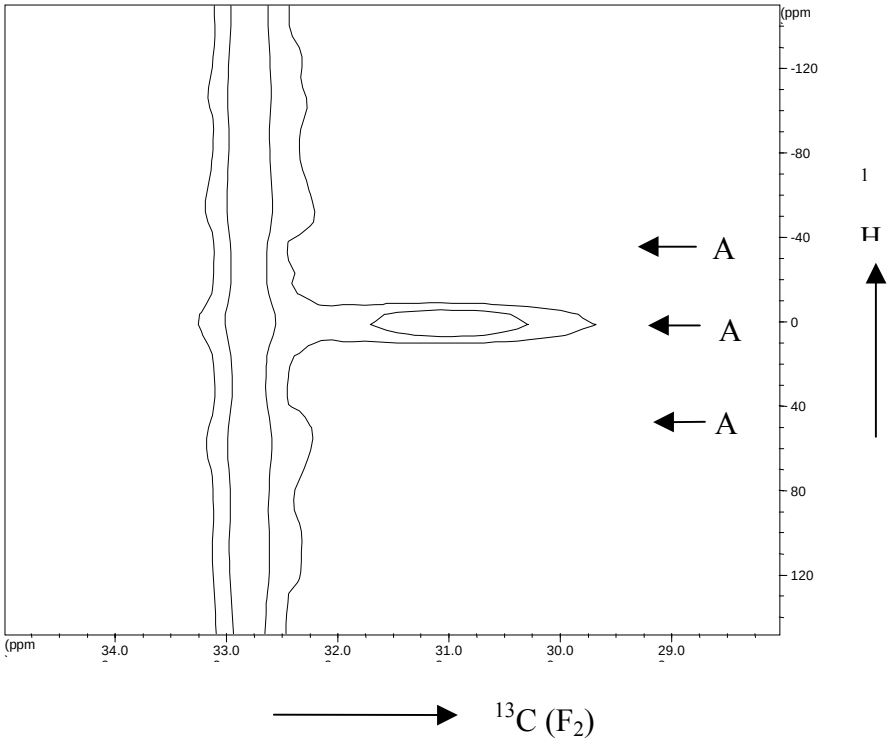

(b) (c)

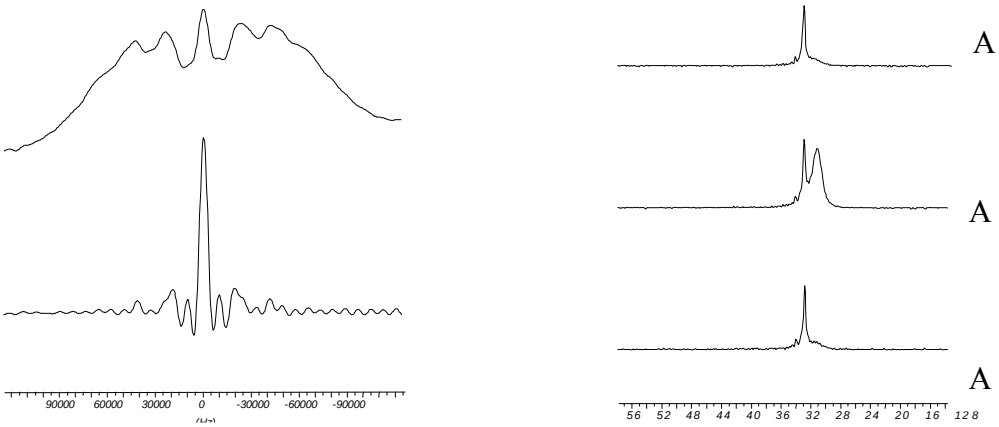

Figure 8.17. *The ^{1}H WISE (wideline separation) 2D ^{1}H – ^{13}C correlated NMR spectrum. The spectrum was recorded under a MAS frequency of 10 kHz. TPPI method was used in the F_1 dimension. (a) The contour plot of the ^{1}H –^{13}C correlated spectrum, (b) the ^{1}H spectra of the crystalline and amorphous domains, (c) the ^{13}C spectra of slices at A_1, A_2 and A_3 in (a).*

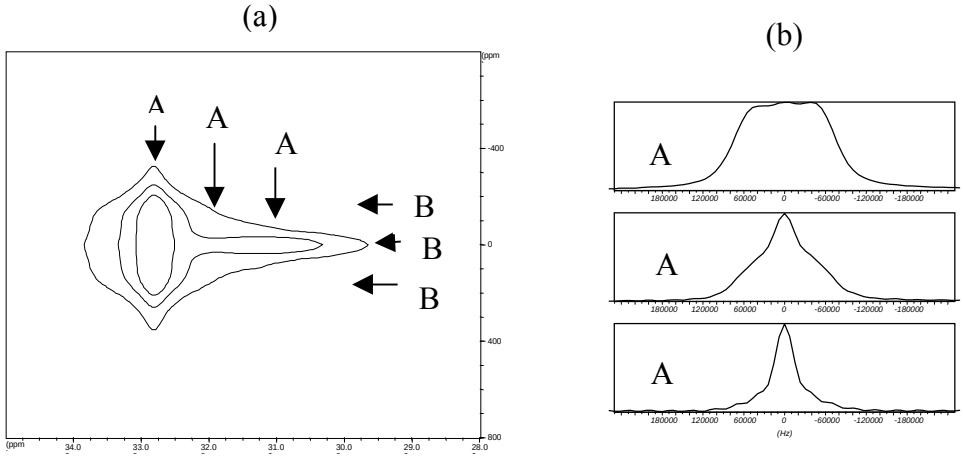

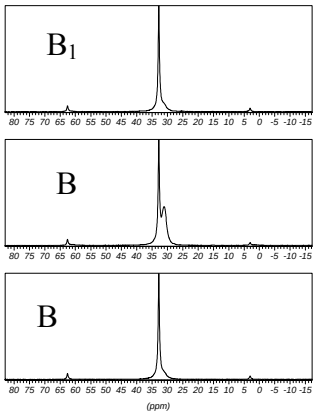

Figure 8.18. *The ^{1}H WISE 2D ^{1}H – ^{13}C NMR spectrum recorded under a MAS frequency of 3 kHz. (a) The contour plot of the spectrum, (b) the ^{1}H spectra of the slices A_1, A_2 and A_3. (c) the ^{13}C spectra of slices B_1, B_2 and B_3.*

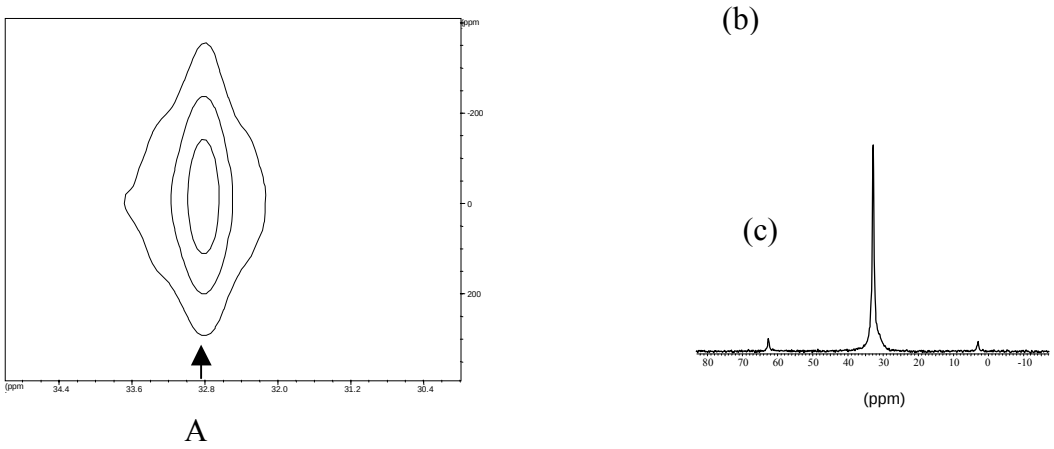

Figure 8.19. *^{1}H 2QC 2D ^{1}H – ^{13}C correlated spectrum. The 2D three-pulse sequence with an excitation time of 5 μs was used. (a) The contour plot of the spectrum, (b) ^{1}H 2QC spectrum, (c) ^{13}C spectrum.*

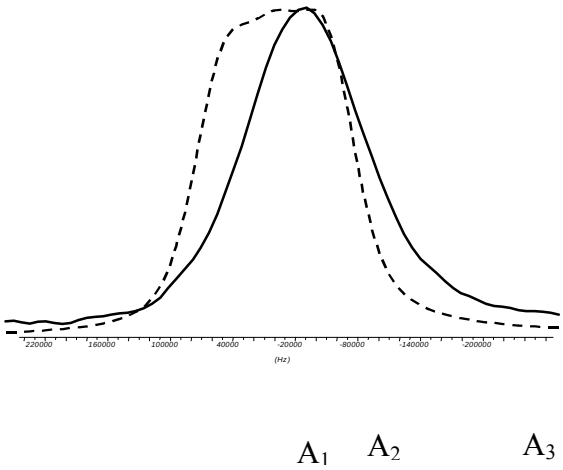

Figure 8.20. *Comparison of the ^{1}H SQC and 2QC spectra. The dotted line is the ^{1}H SQC spectrum, and the solid one is the ^{1}H 2QC spectrum.*

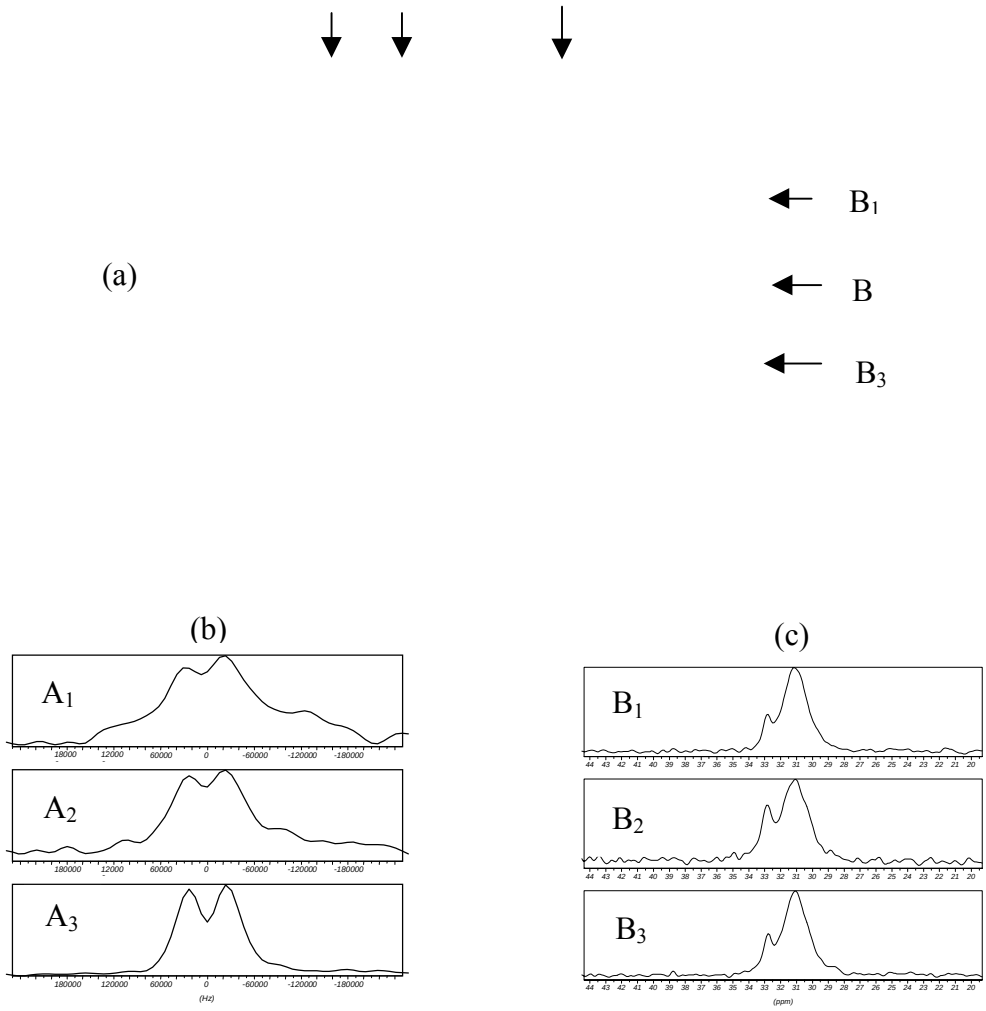

Figure 8.21. *^{1}H 2QC 2D ^{1}H – ^{13}C correlated spectrum. The 2D three-pulse sequence with an excitation time of 25 μs was used. (a) The contour plot of the spectrum, (b) ^{1}H 2QC spectra of slices at A_1, A_2 and A_3, (c) ^{13}C spectra of slices at B_1, B_2 and B_3.*

Figure 8.19 shows the ^{1}H 2QC 2D ^{1}H – ^{13}C correlated spectrum. The ^{1}H 2QC spectrum of slice A corresponding to the ^{13}C resonance at 32.8 ppm is shown in Figure 8.19b. Compared with the ^{1}H SQC in Figure 8.18b(A_1) (see Figure 8.20), the line width of the ^{1}H 2QC spectrum is clearly narrowed.

Figure 8.21 is the ^{1}H 2QC 2D ^{1}H – ^{13}C correlated spectrum recorded by using the same parameters as in Figure 8.19 but with an excitation time of 25 μs. Figure 8.21a is the contour plot, the ^{1}H 2QC spectra of slices A_1, A_2 and A_3 corresponding to the ^{13}C resonances at 32.8 ppm, 32.2 ppm and 31 ppm, are shown in Figure 8.21b. The ^{13}C spectra of slices at B_1, B_2 and B_3 are presented in Figure 8.21c. From ^{13}C spectra, one can note that with an excitation time

of 25 μs, the crystalline signal are drastically suppressed, so the ^{1}H 2QC are generated from the interphase and amorphous domains in this case.

10 8.3.4. ^{13}C detected ^{1}H MQC dynamics of HDPE

11 8.3.4.1 ^{13}C detected ^{1}H spin diffusion

Spin-diffusion is a general phenomenon in a strongly dipolar coupled homonuclear spin system. It can be used to determine the domain sizes and shapes of heterogeneous materials such as HDPE. Magnetization in a particular type of domain can be selectively destroyed by applying NMR pulses while there is still sufficient magnetization remaining in the other type of domain. Then the magnetization in the latter is allowed to transfer to the former by the spin-diffusion process via the dipolar flip-flop process. The recovery of the magnetization associated with the former domain as a function of the transfer time will reflect the size and shape of the latter domain.

The ^{1}H spin-diffusion process in HDPE can be easily followed by using the ^{13}C detected ^{1}H 2QC filtration method. In doing so, a delay time[30] t_d is inserted after the mixing period in both the three-pulse and the eight-pulse sequences. The three-pulse sequence with a short excitation time can be used to select the magnetization from rigid domains and suppress the magnetization from mobile, amorphous domains. The diffusion of the magnetization from the rigid domains to the amorphous domains can then occur via the dipolar flip-flop interactions. The eight-pulse sequence can be used to select the magnetization from the amorphous domains and eliminate that from the crystalline domains. The spin diffusion from the amorphous domains to the crystalline domains can then be investigated. As an example, Figure 8.22 illustrates the ^{13}C detected ^{1}H spin-diffusion process (from amorphous to crystalline) using the simplified 1D eight-pulse sequence of the ^{1}H 2QC filtration method and varying the time t_d from 5 μs to 100 ms. Initially the amorphous together with some interfacial magnetization is selected by using an excitation time of τ_{exc} = 208 μs with a short t_d time of 5 μs. By diffusion of magnetization from the amorphous into the crystalline phase during the diffusion time, the intensity of the amorphous phase signal gradually decreases and that of the crystalline phases progressively increases with increasing diffusion time.

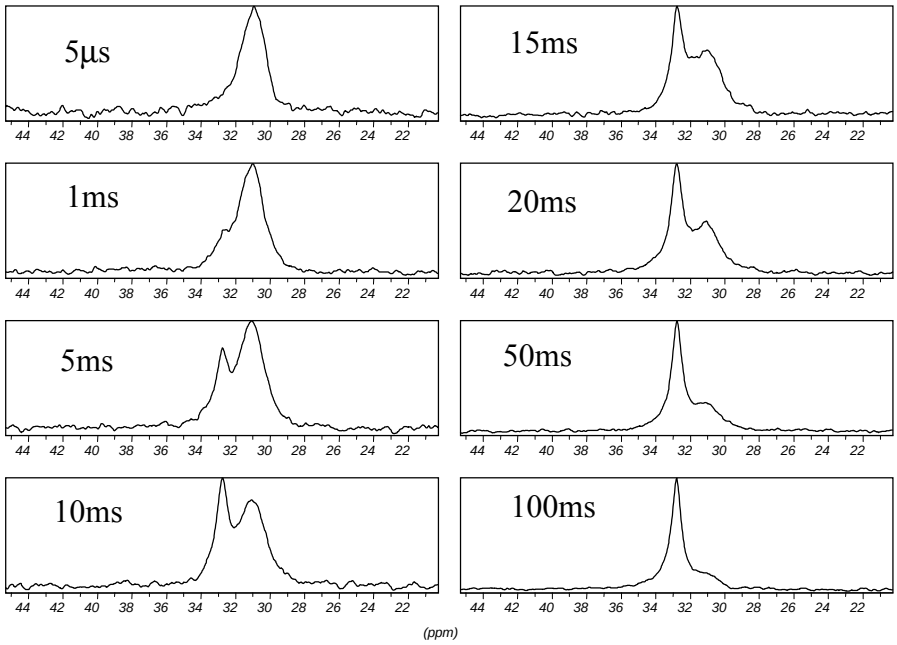

Figure 8.22. *^{13}C detected ^{1}H spin-diffusion process in HDPE.*

8.3.4.2 The ^{13}C detected ^{1}H 1QC dipolar evolution

As discussed in chapter 4, the formation of the multiple-spin single-quantum coherences has an intimate relation with the generation of the MQC. Here we investigate the dipolar relaxation behaviour of the multiple-spin 1QC of the different domains in HDPE.

To observe the generation and development of the multiple-spin single-quantum coherences in HDPE, the ^{1}H dipolar dephasing experiment was carried out. The pulse sequence can be described as follows: first a 90° pulse is applied to the ^{1}H spins, the resulting ^{1}H transverse magnetization is then allowed to dephase under the dipolar interaction. The dipolar modulated ^{1}H transverse magnetization is cross-polarized to ^{13}C and finally detected under high power ^{1}H heteronuclear decoupling. Through the observation of the relaxation behaviour of the ^{1}H transverse magnetization, i.e., the indirect detection of the generation of the multiple-spin single-quantum coherences, we can study the spin dynamics of HDPE in different phases.

Figure 8.23 is the stack plot of the ^{13}C detected ^{1}H dipolar dephasing spectra of HDPE. The spectra, from bottom to top, correspond to the dipolar dephasing times from t = 0 μs to t = 200 μs. These spectra can be well fitted with four peaks with different peak positions and line widths. Two of the deconvoluted spectra, corresponding to the dipolar dephasing times of t = 5 μs and t = 20 μs, are shown in Figure 8.24. They have the following features: two peaks

have the same chemical shifts at 32.8 ppm but with different linewidths, one has a width at half height of 0.2 ppm and the other has a width of 0.5 ppm, they can be assigned to the crystalline narrow (cr-n) and crystalline broad (cr-b) lines according to previous work[12,25]; one broad peak with a linewidth ranging from 1.8 ppm to 3.0 ppm resonates in the range of 31.2-33.0 ppm, it can be assigned to the interphase carbons; the last peak with a linewidth of about 1.2-1.8 ppm resonates at the position of 31.0 ppm, it represents the carbons from the amorphous domains. The change of the integral intensities of the four lines with increasing dipolar dephasing time are fitted and plotted in Figure 8.25.

A closer examination of the dipolar evolution of the crystalline phase shows that the intensity of the crystalline peak (cr-b) oscillates with a damped cosine function. The cr-b peak can be well fitted with the following equation (see Figure 8.25a):

$$I = I_{01} \exp(-t^2/2T_2^2) + I_{02} \cos(2\pi\omega t) \exp(-t/T_2') , \quad (8.3)$$

with the parameters: T_2=8.2 ± 1.3 μs, T_2' = 9.4 ± 0.7 μs, ω = 21.5 ± 3.2 kHz and I_{01}/I_{02}=46/54.

The cr-n peak can be fitted with a damped oscillating cosine function (see Figure 8.25b):

$$I = I_0 \exp(-t^2/2T_2^2) \cos(2\pi\omega t), \quad (8.4)$$

with the parameter values: T_2 = 11.3 ± 0.6 μs, ω = 16.9 ± 0.5 kHz.

The interphase peak has a distribution of resonance frequencies, for short decay times, the peak resonates at about 33 ppm with a width of 3 ppm, after 13 μs ^{1}H decay time, the peak position changes upfield to 31.2-31.8 ppm with a width of about 3 ppm. It can be fitted with the equation:

$$I=I_{01}\exp(-t/T_2)+I_{02}\exp(t/T_2')\cos(\omega t), \quad (8.5)$$

with the following parameter values: T_2 = 9.7 ± 0.8 μs, T_2' = 33.9 ± 20.4 μs and ω = 1.23 ± 0.04 kHz. For short decay times (< 50 μs), i.e., within the first half revolution period of the rotor (MAS frequency is 10 kHz), the interphase peak decays in a monoexponential fashion with a T_2 time of 9.7 μs. It is dominated by the decay of the ^{1}H transverse magnetization

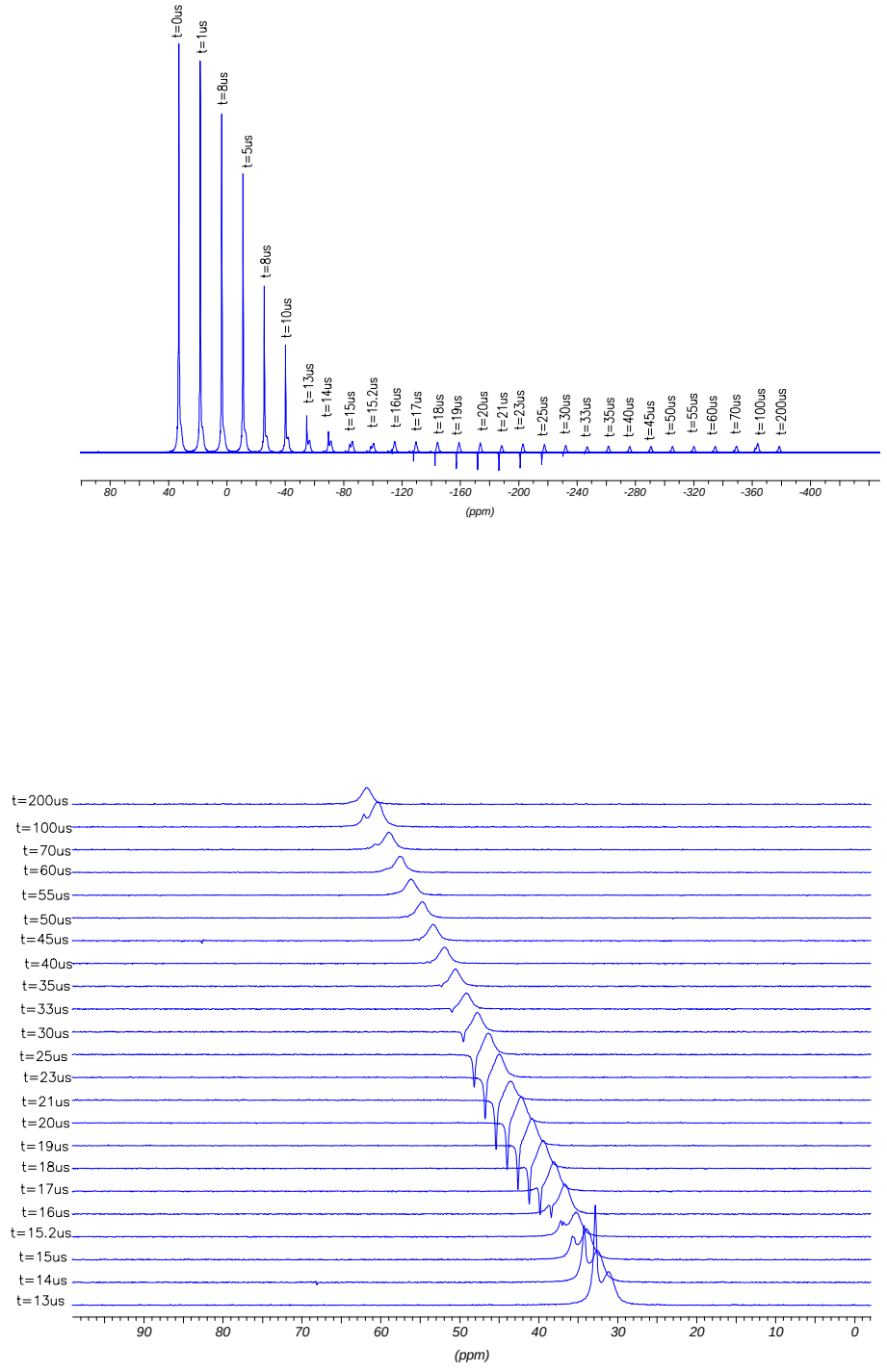

Figure 8.23. *The stack plot of the ^{13}C detected ^{1}H dipolar dephasing spectra of HDPE with increasing dipolar dephasing time. The spectra were recorded by using a Bruker 4 mm MAS probe head under a MAS frequency of 10 KHz, the 90° pulses were 3.5 μs.*

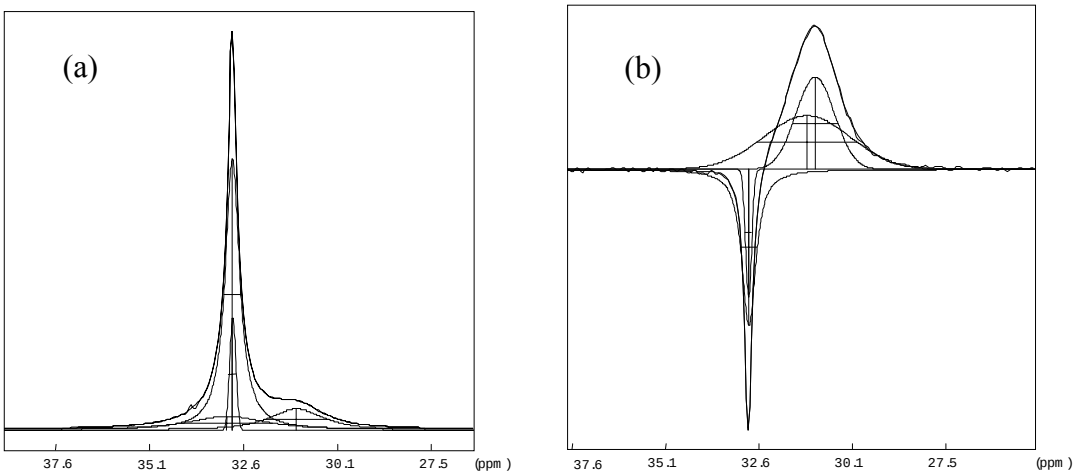

***Figure 8.24**. The deconvolution of some spectra from Figure 8.35. (a) t = 5 μs, (b) t = 20 μs.*

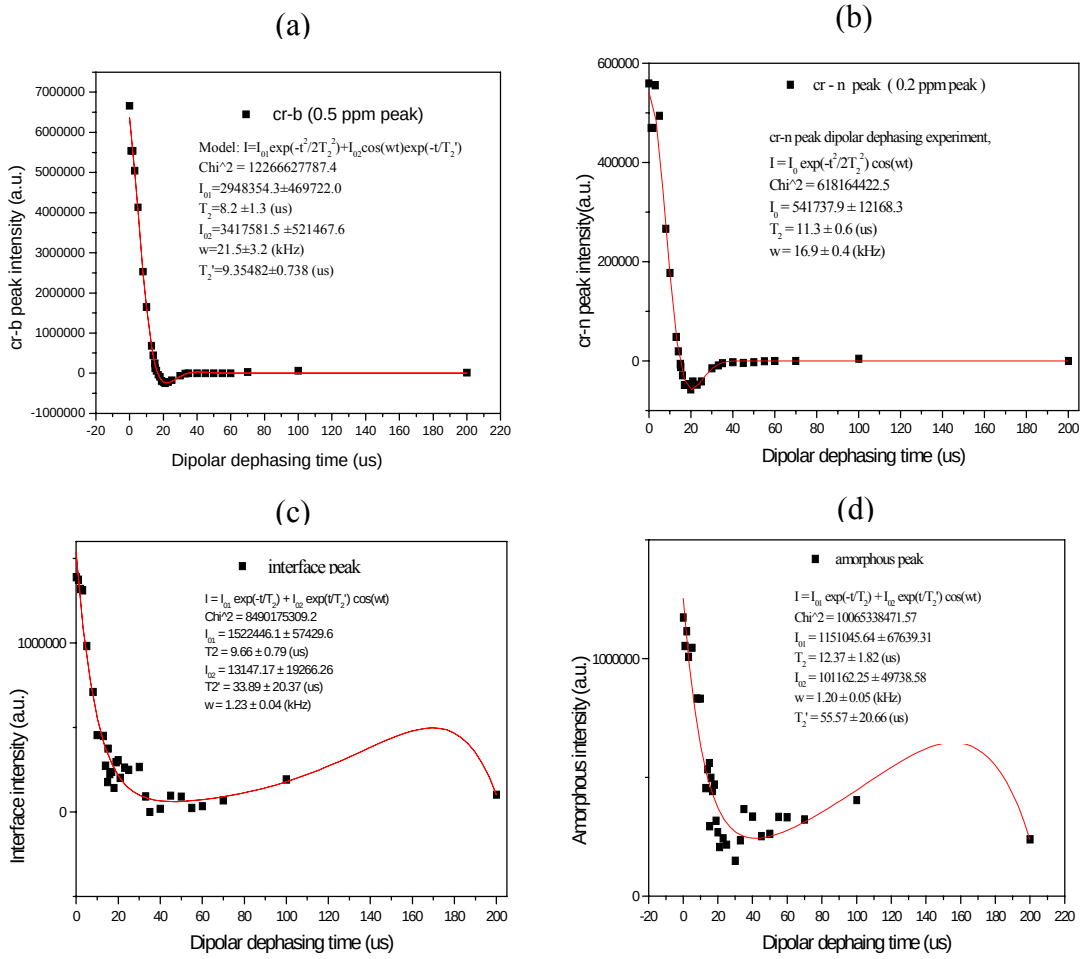

***Figure 8.25**. The fitted peaks: (a) cr-b; (b) cr-n; (c) interphase; and (d) amorphous. The filled diamonds are the integrated intensities, the solid lines represent the fitted curve.*

resulting from the homo- and inhomogeneous interactions, such as ^{1}H-^{1}H, ^{1}H-^{13}C dipolar coupling and the ^{1}H chemical shift anisotropy. Then in the second half revolution period of the rotor, the intensity of the ^{1}H signal increases again with further increasing of the dipolar dephasing time, due to the refocusing of the inhomogeneous part of the interactions.

The amorphous peak can be fitted by using the same formula as that of the interphase (see equation (8.5)) with the results: T_2=12.4 ± 1.8 μs, ω=1.20 ± 0.05 kHz, $T_2^{'}$=55.6 ± 20.7 μs. From the fitted results, one can see that the ^{1}H dipolar dephasing behaviour of the cr-b peak is a superposition of the function $I_{01}\exp(-t^2/2T_2^2)$ and the damped cosine function $I_{02}\cos(2\pi\omega t)\exp(-t/T_2^{'})$. The cr-n peak follows the damped pattern $I_0\exp(-t^2/2T_2^2)\cos(2\pi\omega t)$. The pattern of $I_0\exp(-t^2/2T_2^2)$ suggests[32] that the decay of the ^{1}H transverse magnetization (SQC) is modulated by the strong homonuclear ^{1}H-^{1}H and heteronuclear ^{13}C-^{1}H dipolar couplings. The oscillating phenomenon may come from the follow two origins: one origin is the offset effect, the other is the spin dynamics or rotational echo of the spin clusters.

In view of the spin dynamics, the oscillating pattern of the ^{1}H 1QC may suggest the existence of the proton spin clusters. The oscillating frequencies have a relation with the dipolar interactions between the proton spin pairs from the intra- and interchains of the HDPE molecules.

8.4 Conclusion

From above the results and discussions, the following conclusions can be drawn:

(1) The three-pulse sequence and the time-reversible eight-pulse sequence can be complementarily used to study the heterogeneity of semicrystalline polyethylene. The former is suitable for excitation of the ^{1}H MQC from the more rigid domains, the latter is more effective in generating ^{1}H MQC from the amorphous domains. Both the ^{1}H- and ^{13}C-detected-^{1}H-MQC-filtration method can be used to select and detect the different domains with different mobilities by varying the excitation time.

(2) In the case of the ^{1}H-detected-^{1}H-MQC-filtered spectra, the linewidth of the 0QC- and 2QC-filtered spectra of HDPE are continuously narrowed with increasing excitation time. This means that there is a distribution of dipolar coupling constants for each original distinguished domain. High-resolution of the ^{1}H-MQC-filtered spectra as well as the ^{1}H-2QC spectrum of HDPE can be obtained through the suitable combination of the pulse sequence with magic angle spinning.

(3) In the case of the ^{13}C-detected-^{1}H-2QC-filtered spectra, three domains (i.e., crystalline, interphase, and amorphous domains) in HDPE can be distinguished. Together with other methods, such as IRCP, dipolar dephasing, individual domains can be selected and investigated.

(4) The ^{1}H and ^{13}C relations in HDPE can be correlated through the 2D ^{1}H WISE NMR experiment.

References

(1) L. Mandelkern. An introduction to macromolecules, 2nd ed. Springer, New York, **1983**.

(2) V. J. McBrierty, and D. C. Douglass, Phys. Rep., **63**, 63 (1980).

(3) V. J. McBrierty and D. C. Douglass, J. Polym. Sci. Macromol. Rev., **16**, 295 (1981).

(4) O. Phaovobul, J. Loboda-Cackovic, H. Cacovic, and R. Hosemann, Makromol. Chem. **175**, 2991 (1974).

(5) K. Bergmann, J. Polym. Sci. Phys. Ed, **16**, 1611 (1978).

(6) H. G. Zachmann, J. Polym. Sci. Polym. Symp., **43**, 111 (1973).

(7) J. B. Smith, A. J. Manuel, and I. M. Ward, Polymer, **16**, 57 (1975).

(8) R. Kitamaru, F. Horii, and K. Murayama. Macromolecules **19**, 636 (1986).

(9) F. Horii, H. Kaji, H. Ishida, K. K. Kuwabara, K. Masuda, T. Tai, J. Mol. Str. **441**, 303 (1998).

(10) J. Cheng, M. Fone, V. N. Reddy, K. B. Schwartz, H. P. Fischer, and B. Wunderlich, J. Polym. Sci. Part B: Polym. Phys. 32, 2683 (1994).

(11) Y. Ba, Ph.D. Dissertation 1995, Gerhard-Mercator University of Duisburg, Germany.

(12) L. Hillerbrand, Dissertation **1997**, Gerhard-Mercator University of Duisburg, Germany.

(13) J. R. Havens and D. L. Vanderhart, J. Magn. Reson**. 61**, 389 (1985).

(14) S. Lacelle, Adv. Magn. Opt. Reson. **16**, 173 (1991).

(15) E. M. Menger, S. Vega, and R. G. Griffin, J. Am. Chem. Soc. **108**, 2215 (1986).

(16) H. Geen, J. J. Titman, J. Gottwald, H. W. Spiess, Chemical Physics letters **227**, 79 (1994).

(17) J. Gottwald, D. E. Demco, R. Graf, H. W. Spiess, Chemical Physics Letters **243**, 314 (1995).

(18) H. Geen, J. J. Titman, J. Gottwald, and H. W. Spiess, J. Magn. Reson., Series A **114**, 264 (1995).

(19) U. Friedrich, I. Schnell, D. E. Demco, H. W. Spiess, Chemical Physics letters **285**, 49 (1998).

(20) B. H. Meier and W. L. Earl, J. Chem. Phys. **85**, 4905 (1986).

(21) B. H. Meier and W. L. Earl, J. Am. Chem. Soc. **109**, 7937 (1987).

(22) W. L. Earl, D. L. VanderHart. Macromolecules **12**, 762(1979) .

(23) A. E. Tonelli, NMR spectroscopy and Polymer Microstructure: The Conformational Connection, VCH, **1989**.

(24) A. Schmidt, Diplomarbeit, 1994, University of Duisburg, Germany.

(25) L. Hillerbrand, A. Schmidt, A. Boltz, M. Hess, W. S. Veeman, R. J. Meier, G. van der Velden, Marcromolecules **31**, 5010 (1998).

(26) L. Mandelkern, Chematracts-Macromolecular Chemistry, **3**, 347 (1992).

(27) R. Kitamaru, F. Horii, and K. Murayama, Macromolecules **19**, 636 (1986).

(28) C. Choi, L. Bailey, A. Rudin, M. M. Pinter, J. Polym. Sci: Part B: Polym. Phys. **35**, 2551 (1997).

(29) T.T.P. Cheng and B. C. Gerstein. J. Appl. Phys. **52(9),** 5517 (1981).

(30) Y. Ba and J. A. Ripmeester, J. Chem. Phys., **108**, 8589 (1998).

(31) D. G. Cory and W. M. Ritchey, Macromolecules **22**, 1611 (1989).

(32) L. B. Alemany, D. M. Grant, T. D. Alger, and R. J. Pugmire, J. Am. Chem. Soc. **105**, 6697(1983).

(33) U. Haeberlen, High Resolution NMR in Solids, Suppl. 1, Academic Press, New York, 1976.

Summary

The thesis describes the investigation of high-resolution MQ MAS NMR in rigid spin-1/2 systems. Formerly, MQC techniques were mainly applied to systems of small molecules, the newly developed MQC technique in this thesis, the ^{1}H-MQC-filtered-MAS-NMR method, can be well applied to study the heterogeneity of inorganic and organic materials, such as silica gel, homopolymers, copolymers and their blends.

In this thesis two multiple-pulse sequences were adopted: the three-pulse and the time-reversible eight-pulse sequence. The former has the advantage that the cycle time, i.e. the excitation time can be adjusted to arbitrary values, therefore it can be used to generate ^{1}H MQC in coupled spin-1/2 systems for a wide range of dipolar interactions, especially to pump ^{1}H MQC from a rigid system, such as the crystalline phase of polymers. But it has disadvantages: it is sensitive to chemical shifts and resonance offsets, and has low efficiency in exciting higher order coherences. The latter has higher efficiency in exciting higher order coherences and is not sensitive to chemical shifts and resonance offsets, but it has a long cycle time, so it is only effective when the dipolar interactions are not strong such as in the amorphous phase of polymers.

First the multiple-quantum behaviour, such as the effects of the excitation time and the spin-diffusion process on the ^{1}H MQC development, the dipolar evolution of the ^{1}H MQC, the effect of the finite pulse on the MQC generation, were investigated and demonstrated by using a model polycrystalline compound: adamantane.

The ^{1}H-MQC-filtration-MAS-NMR was successfully applied to study the silica gel surface. In this case the time-reversible eight-pulse sequence, synchronized with the sample rotation, was used to identify and discriminate the different species on the silica gel surface. For the first time, the single (1.6 ppm) and geminal (1.8 ppm) silanol groups are separated and discriminated by using the ^{1}H-MQC-MAS-NMR technique. Physically adsorbed water (3.6 ppm) and hydrogen-bonded silanol groups (1 – 8 ppm) are present on the surface of the as-received silica gel. Usually the signals of the mobile water molecules and the structured water monolayer overlap. Using the ^{1}H-2QC-filtered-MAS-NMR method, they can be well separated and directly detected. By dehydration of the sample at 100°C under air atmosphere, most of the physically adsorbed water molecules are removed from the surface, the isolated (1.8 ppm) and hydrogen-bonded (2.15 ppm) silanol groups, together with a small amount of

the residual water (3.13 ppm), were left on the surface. By heat treatment of the sample at 120°C under nitrogen atmosphere for 64 hours, the physically adsorbed water molecules are removed from the surface, the single (isolated and vicinal silanol groups) (1.6 ppm) and geminal (1.8 ppm) silanol groups together with the hydrogen-bonded silanol groups (2.6 ppm) are observed on the surface. At the same time, some of the hydroxyl groups (most of them are the vicinal single and geminal silanol groups) are also removed from the surface through condensation. By dehydroxylation of the sample at 500°C under vacuum for 20 hours, the physically adsorbed water molecules together with most of the hydrogen-bonded silanol groups are removed from the silica surface through dehydration and condensation, so the single (isolated and vicinal silanol groups) (1.6 ppm) and geminal (1.8 ppm) silanol groups, together with some residual hydrogen-bonded silanol groups (2.6 ppm) are left on the surface.

1D-^{13}C-detected-^{1}H-double-quantum-filtration-MAS-NMR was successively used to investigate the heterogeneity of polymers, copolymers as well as their blends. The three-pulse sequence with a suitable short excitation time can generate ^{1}H double-quantum coherences from the more rigid or crystalline domains of the investigated polymers, and the eight-pulse sequence with a proper long excitation time can excite ^{1}H double-quantum coherences from the amorphous or mobile phases of polymers. With this method two domains in semicrystalline polyoxymethylene (DELRIN®100) have been observed: the crystalline domains have a ^{13}C resonance at 88 ppm, whereas the amorphous domains have a ^{13}C resonance at 89 ppm. The heterogeneity of elastomers such as EPDM, and the copolymer PBT/PTMO, as well as the polymer blends iPP/EPDM and (PBT/PTMO)/EPDM can also be studied by these two pulse sequences.

The semicrystalline polymer, high density polyethylene, was studied by using the ^{1}H-MQC-filtration-NMR together with other high resolution solid state NMR methods, such as IRCP, dipolar dephasing and WISE. The ^{1}H and ^{13}C detected ^{1}H-MQC-filtration-NMR can be used to select and discriminate the rigid and amorphous domains. In the case of the ^{1}H-detected-^{1}H-MQC-filtering method, the ^{1}H-0QC-filtered-spectra consist of two lines: one broad line corresponds to the rigid component, the other narrow line corresponds to the amorphous component. With increasing excitation times, the intensity of the ^{1}H-0QC- and 2QC-filtered spectra decrease and their linewidths are narrowed. This means that each of the different domains has a distribution of dipolar couplings, i.e., each has a distribution of motional correlation times.

The ^{1}H and ^{13}C spectra are correlated through the ^{1}H WISE experiment. In the amorphous regions, the ^{13}C spectrum is very broad due to the distribution of trans, gauche conformations, the corresponding ^{1}H spectrum has a narrow line due to the averaging out of the dipolar interaction by the molecular motions. In the crystalline regions, the ^{13}C spectrum has a narrow line due to the perfect packing of the molecular chains with all-trans conformation, while the corresponding ^{1}H spectrum has a very broad line due to the strong dipolar interactions between the intra- and inter methylene chains.

The discussion of most experimental results is qualitative rather than quantitative in this thesis, two reasons account for this. Firstly, the research is to find the applications of MQC to materials, therefore many experiments are done for looking for the potential applications. Secondly, many factors affect this technique , e.g. the 90° pulses have a finite length of 3.5 μs and are not real δ pulses, so a quantitative analysis is questionable. However, in theory, this technique can be made more quantitative, e.g. through analysing MQ buildup intensities and MQ sideband patterns one can extract quantitative information on the strength of dipolar coupling and the topologies of the spin system. Another example is that the domain sizes of polymers can be obtained by combination of ^{1}H-MQC-filtration with spin diffusion as illustrated in section 8.3.4.1.

Zusammenfassung

In der vorliegenden Arbeit wird die Untersuchung von Hochauflösungsmehrquanten-(MQ) MAS-NMR an rigiden Spin-1/2-Systemen beschrieben. Die früheren MQ-Kohärenz Techniken wurden hauptsächlich auf Systeme, bestehend aus kleineren Molekülen angewandt. Die in dieser Arbeit neue entwickelte MQ-Kohärenz Technik, die ^{1}H-MQC-filtered-MAS-NMR Methode, kann gut zur Untersuchung von Heterogenitäten in anorganischen und organischen makromolekularen Materialien, wie Kieselgel, Homopolymeren, Copolymeren und deren Blends, verwendet werden.

In dieser Arbeit wurden zwei multiple Pulssequenzen benutzt: eine 3-Puls-, und eine zeitreversible 8-Pulssequenz. Die 3-Pulssequenz hat den Vorteil, daß die Zykluszeit willkürlich lang gewählt werden kann. Deswegen kann sie zur Erzeugung von ^{1}H MQC in gekoppelten ½-Spin Systemen genutzt werden, die einen breiten Bereich von dipolaren Wechselwirkungen besitzen. Diese breiten Bereiche findet man besonders in rigiden Systemen, wie den kristalline Phasen von Polymeren. Aber es gibt auch Nachteile: Die 3-Pulssequenz ist empfindlich für chemische Verschiebungen und „Resonanz Offsets“, und sie hat eine geringere Effektivität bei der Erzeugung der höherrangigen Kohärenzen. Die 8-Pulssequenz hat eine hohe Effektivität bei der Erzeugung dieser Kohärenzen und ist unempfindlich für chemische Verschiebungen und „Resonanz Offsets“. Aufgrund der langen Zykluszeit ist diese Sequenz sehr effektiv, speziell wenn schwach dipolare Wechselwirkungen auftreten, wie z.B. in den amorphen Phasen von Polymeren.

Zuerst wurde das Verhalten der Mehrquanten-Kohärenz, zum Beispiel, der Effekt der Anregungszeit, des Spindiffusion-Prozeßes, der dipolaren Evolution, der finiten Pulse über die MQC Entwicklung anhand der Modellsubstanz Adamatan demonstriert.

^{1}H-MQC-Filtrations-MAS-NMR wurde erfolgreich zur Untersuchung der Kieselgeloberfläche herangezogen. In diesem Fall wurde die zeitlich umkehrbare 8-Pulssequenz, die mit der Rotation der Probe synchronisiert wurde, um unterschiedliche Hydroxidgruppen auf Kieselgeloberfläche zu identifizieren und zu unterscheiden, ausgenutzt. Es ist dabei erstmals gelungen die vicinalen (1.6 ppm) und geminalen (1.8 ppm) Hydroxidgruppen durch ^{1}H-MQC-MAS-NMR Technik zu trennen und zu unterscheiden. Es wurde festgestellt, daß es auf den Oberflächen des unbehandelten Kieselgels physikalisch adsorbiertes Wasser (3.6 ppm) und verbrückte Hydroxidgruppen (1 – 8 ppm) gibt. Gewöhnliche überlappen die Signale von

mobilen Wassermolekülen und die Signale von unmittelbar an der Oberfläche adsorbierten Wassermoleküle. Durch die hier angewandte ^{1}H-2QC-filtered-MAS-NMR Methode können sie gut getrennt und direkt detektiert werden. Durch die Dehydratisierung des Kieselgels bei 100°C unter Luftatmosphäre sind die meisten physikalisch adsorbierten Wassermoleküle von der Oberfläche entfernt worden; nur isolierte (1.8 ppm) und verbrückte (2.15 ppm) Hydroxidgruppen zusammen mit wenigen restlichen Wassermolekülen (3.13 ppm) sind zurückgeblieben. Durch thermische Vorbehandlung des Kieselgels bei 120° unter Stickstoffatmosphäre für 64 Stunden sind alle physikalisch adsorbierten Wassermoleküle von der Oberfläche desorbiert. Zurückgeblieben sind vereinzelte (isolierte und vicinale) Hydroxidgruppen (1.6 ppm) und geminale Hydroxidgruppen (1.8 ppm), sowie mit wasserstoffbrückengebundenen Hydroxidgruppen (2.6 ppm). Gleichzeitig sind auch einige Hydroxidgruppen (zumeist vicinale und geminale Hydroxidgruppen) durch Kondensation eliminiert worden. Durch 20 stündige Dehydroxylierung des Kieselgels bei 500°C unter Vakuum sind die physikalisch adsorbierten Wassermoleküle zusammen mit den meisten wasserstoffbrückengebundenen Hydroxidgruppen durch Dehydration und Kondensation entfernt worden. Auf den Oberflächen sind nur isolierte (1.6 ppm), vicinale (1.8 ppm) und geminale Hydroxidgruppen zusammen mit wenigen wasserstoffbrückengebundenen Hydroxidgruppen (2.6 ppm) verblieben.

Die vereinfachte 1D-^{13}C-detektierte-^{1}H-Doppelquanten-Filtrations-MAS-NMR ist eine erfolgreiche Methode zur Untersuchung der Heterogenität von Homopolymeren und Copolymeren, sowie deren Blends. Die 3-Pulssequenz mit einer geeigneten kurzen Anregungszeit kann die ^{1}H-Doppel-Quanten Kohärenzen aus den rigiden oder kristallinen Domänen der untersuchten Polymere erzeugen. Hingegen kann die 8-Pulssequenz mit einer passenden langen Anregungszeit die ^{1}H-Doppelquanten-Kohärenzen aus der amorphen oder mobilen Polymerphase entwickeln. In Polyoxymethylen (DELRIN®100) wurden zwei verschiedene Domänen beobachtet: die kristallinen Domänen zeigen eine Resonanz bei 88 ppm, wohingegen für die amorphen Domänen eine Resonanz bei 89 ppm beobachtet werden kann. Die Heterogenität der Elastomere, Copolymere und deren Blends, wie zum Beispiel EPDM, PBT/PTMO, und PP/EPDM und (PBT/PTMO)/EPDM, kann mit Hilfe dieser beiden Pulssequenzen untersucht werden.

Das semikristalline Polymer Polyethylen (HDPE) wurde mit ^{1}H-MQC-Filter-NMR und unterschiedlichen Hochauflösung-Festkörper-NMR-Methoden, wie zum Beispiel IRCP, dipolar dephasing und WISE untersucht. Die über ^{1}H und ^{13}C beobachteten ^{1}H-MQC-Filter-

NMR kann dazu genutzt werden, die rigiden und amorphen Domänen zu selektieren und zu unterscheiden. Im Fall der über ^{1}H beobachteten ^{1}H-MQC-Filter Methode bestehen die ^{1}H-0QC-Filter-Spektren aus zwei Banden: einer breiten Bande, die der rigiden Domäne entspricht, und einer schmalen Bande, hervorgerufen durch die amorphe Phase. Mit zunehmenden Anregungszeiten nehmen die Intensitäten der ^{1}H-0QC- und 2QC-Filter-Spektren ab, gleichzeitig werden deren Linienbreiten immer schmaler. Das bedeutet, daß jede einzelne Domäne eine unterschiedliche Verteilung der dipolaren Kopplung hat, d.h., jede Domäne hat eine Verteilung von Bewegungs-Korrelationszeiten. Der Zusammenhang zwischen ^{1}H und ^{13}C wurde über das ^{1}H WISE Experiment korreliert. In der amorphen Region erhält man eine breite ^{13}C Linie aufgrund der unterschiedliche Kettenkonformation. Die entsprechenden Signale in ^{1}H-Spektren sind schmal aufgrund der durch molekulare Bewegung gemittelten dipolaren Wechselwirkungen. In der kristallinen Region erhält man dagegen eine schmale ^{13}C Linie wegen der perfekten Verpackung der molekularen Ketten. Die entsprechende ^{1}H Linie ist sehr breit aufgrund der stärkeren dipolaren Kopplungen zwischen intra- und inter molekularen Ketten.

Die Diskussion der meisten experimentellen Ergebnisse in dieser Arbeit sind mehr qualitativer als quantitativer Natur. Es gibt zwei Gründen dafür: Zunächst dienten die Untersuchung dazu, Anwendungen der MQC an rigiden Materialien zu finden. Aus diesem Grund wurden die meisten Experimente für diese Suche nach brauchbaren Anwendungen durchgeführt. Darüber hinaus wirken viele Faktoren auf diese Technik ein. So sind zum Beispiel die 90°-Pulse nicht infinitisimal kurz, sondern 3.5 μs lang. Deshalb ist die quantitative Analyse fragwürdig. Jedoch kann diese Technik theoretisch quantitative Ergebnisse liefern. Beispielsweise durch die Analyse des Aufbaus der MQ-Intensitäten und der MQ-Seitenbanden-Muster könnte man quantitative Informationen über die Stärke der dipolaren Kopplung und die relative Anordnung der Spinsysteme erhalten. Ein anderes Beispiel ist die Bestimmung der Domänengröße bei Polymeren, durch die Kombination ^{1}H-MQC-Filteration mit Spindiffusion (sehe Sektion 8.3.4.1).

Appendix

The formulas of rotations of the angular momentum operators which are used in chapter 4 are listed as follows[1,2]:

$$\exp(i\phi I_z)\begin{vmatrix} I_x \\ I_y \\ I_z \end{vmatrix}\exp(-i\phi I_z) = \begin{cases} I_x\cos\phi + I_y\sin\phi \\ I_y\cos\phi - I_x\sin\phi \\ I_z \end{cases}$$

$$\exp(i\phi I_x)\begin{vmatrix} I_x \\ I_y \\ I_z \end{vmatrix}\exp(-i\phi I_x) = \begin{cases} I_x \\ I_y\cos\phi + I_z\sin\phi \\ I_z\cos\phi - I_y\sin\phi \end{cases}$$

$$\exp(i\phi I_y)\begin{vmatrix} I_x \\ I_y \\ I_z \end{vmatrix}\exp(-i\phi I_y) = \begin{cases} I_x\cos\phi - I_z\sin\phi \\ I_y \\ I_z\cos\phi + I_x\sin\phi \end{cases}$$

$$\exp(i\phi 2I_{z1}I_{z2})\begin{vmatrix} I_{x1} \\ I_{y1} \\ I_{z1} \end{vmatrix}\exp(-i\phi 2I_{z1}I_{z2}) = \begin{cases} I_{x1}\cos\phi + 2I_{y1}I_{z2}\sin\phi \\ I_{y1}\cos\phi - 2I_{x1}I_{z2}\sin\phi \\ I_z \end{cases}$$

$$\exp[i\phi(I_{x1}+I_{x2})]\begin{vmatrix} I_{x1}I_{y2} \\ I_{y1}I_{x2} \\ I_{z1}I_{z2} \\ I_{z1}I_{x2} \\ I_{x1}I_{z2} \end{vmatrix}\exp[-i\phi(I_{x1}+I_{x2})] = \begin{cases} I_{x1}(I_{y2}\cos\phi + I_{z2}\sin\phi) \\ (I_{y1}\cos\phi + I_{z1}\sin\phi)I_{x2} \\ (I_{z1}\cos\phi - I_{y1}\sin\phi)(I_{x2}\cos\phi - I_{y2}\sin\phi) \\ (I_{z1}\cos\phi - I_{y1}\sin\phi)I_{x2} \\ I_{x1}(I_{z2}\cos\phi - I_{y2}\sin\phi) \end{cases}$$

References

(1) W. S. Veeman, NMR Lecture.

(2) R. R. Ernst, G. Bodenhausen, and A. Wokaum, Principles of Nuclear Magnetic Resonance in One and Two Dimensions, Volume 14 of International Series of Monographs on Chemistry, **1990**, Oxford University Press, New York.

Lebenslauf

Name:	Guangxin Lin
Geburtstag:	21. 05. 1963
Geburtsort:	Wuqiao, Hebei Provinz, VR China
Geschlecht:	männlich
Staatsangehörigkeit:	chinesisch
Familienstand:	verheiratet (ein Kind)

Schulbildung:

9. 1971 - 7. 1976	Besuch der Grundschule in Wuqiao
9. 1976 - 7. 1980	Besuch der Mittelschule in Wuqiao

Studium:

9. 1980 - 7. 1984	Studium im Fachbereich Polymere an der ostchinesische Universität für chemische Technologie, Shanghai.
7. 1988	Abschluß des Studiums mit „The Degree of Bachelor of Engineering“. Das Thema der Bachelor-Degree-Arbeit war: „The manufacturing and properties of phenolic resin based friction materials“.
9. 1985 - 7. 1988	Studium im Fachbereich Polymere an der ostchinesische Universität für chemische Technologie, Shanghai.
7. 1988	Abschluß des Studiums mit „The Degree of Master of Engineering“. Das Thema der Master-Degree-Arbeit war: „ Carbon fiber reinforced machineable phlogopite glass-ceramic composite“.
11. 1995 – 10.1999	Forschungsarbeit zur Erlangung des akademischen Grades eines Doktors an dem Institut für physikalische Chemie an der Universität Diusburg. Das Thema ist: „The Application of Multiple-Quantum MAS NMR to Materials“.

Berufliche Tätigkeit:

7. 1984 - 9. 1985	Forschungstätigkeit an dem Institut für Baumaterial in der chinesischen Provinz Hebei.
7. 1988 - 4. 1993	Lehr- und Forschungstätigkeit im Fachbereich Polymere an der ostchinesische Universität für chemische Technologie, Shanghai.

08. 1994 – 10.1995	Forschungsarbeit an dem Laboratorium für Angewandte Physik an der Universität-GH-Duisburg.
11. 1995 – 10.1999	Forschungsarbeit an dem Institut für physikalische Chemie an der Universität-GH-Diusburg.